

ALMA MATER STUDIORUM – UNIVERSITÀ DI BOLOGNA

DOTTORATO DI RICERCA IN

**Ingegneria Energetica, Nucleare e del Controllo
Ambientale**

Ciclo XXV

Settore Concorsuale di afferenza: 09/C2

Settore Scientifico disciplinare: ING-IND/10

TITOLO TESI

**Experimental and Numerical Analysis of Gas Forced
Convection through Microtubes and Micro Heat
Exchangers**

Presentata da: Yahui Yang

Coordinatore Dottorato

Prof. -Ing. Antonio Barletta

Relatore

Prof. -Ing. Gian Luca Morini

Correlatore

Dr. -Ing. habil. Jürgen J. Brandner

Esame finale anno 2013

*To see a world in a grain of sand
And a heaven in a wild flower,
Hold infinity in the palm of your hand
And eternity in an hour.*

-----William Blake: *Auguries of Innocence*

ABSTRACT

The last decade has witnessed very fast development in microfabrication technologies, which tend to bring about smart and flexible miniaturized systems. Among them are the microfluidic systems in which fluid flow and heat transfer are activated on regions with characteristic dimensions of the order of tens of micrometers. The increasing industrial applications of microfluidic systems call for more intensive and systematic knowledge on this newly emerging field. Especially for gaseous flow and heat transfer at microscale, the applicability of conventional theories developed at macro scale is not yet completely validated; this is mainly due to scarce experimental data available in literature for gas flows. Moreover, some deviations from conventional theory has been reported in the past but not fully explained or justified. The objective of this thesis is to investigate these unclear elements by analyzing forced convection for gaseous flows through microtubes and micro heat exchangers.

Experimental tests have been performed with microtubes having various inner diameters, namely 750 μm , 510 μm and 170 μm , over a wide range of Reynolds number covering the laminar region, the transitional zone and also the onset region of the turbulent regime. The results show that conventional theory is able to predict the flow friction factor when flow compressibility does not appear and the effect of fluid temperature-dependent properties is insignificant. It has been experimentally evidenced that the axial conduction in the solid wall is important at microscale and greatly alters the linear distribution of bulk temperature. The experimental data have been compared with results obtained from numerical simulation.

Numerical simulation has been extensively applied to the design and optimization of a gas micro heat exchanger based on parallel rectangular microchannels. A double-layered microchannel heat exchanger has been designed in order to study experimentally the efficiency of a gas-to-gas micro heat exchanger. This microdevice contains 133 parallel microchannels machined into polished PEEK plates for both the hot side and the cold side. The microchannels are 200 μm high, 200 μm wide and 39.8 mm long. The design of the micro device has been made in order to be able to test different materials as partition foil with flexible thickness. The test rig has been developed by integrating customized pressure and temperature sensors for local measurements within the device. In addition, the packaging of the microchannel layers has been designed in order to reproduce easily various flow arrangements (countercurrent, concurrent and cross flow configurations).

Experimental tests have been carried out for five different partition foils, with various mass flow rates and flow configurations. The experimental results indicate that the thermal performance of the countercurrent and cross flow micro heat exchanger can be strongly influenced by axial conduction in the partition foil separating the hot gas flow and cold gas flow. However, this is not the case for a cocurrent flow micro device, where the partition wall is almost isothermal. It can be concluded from the experimental data that conventional theory is able to predict the performance of the micro heat exchanger as long as the influence of axial conduction is correctly taken into account. The experimental conclusions are further validated by 3D numerical simulation, in which the optimal value of partition foil thermal conductivity has been determined considering different foil thicknesses, flow arrangements and mass flow rates.

ACKNOWLEDGEMENTS

I would like to express deep gratitude to my supervisor Prof. Gian Luca Morini and co-supervisor Dr. Jürgen J. Brandner for guiding me into the fascinating world of microfluidics. Their support, encouragement and inspiration accompanied me throughout my Ph.D. study.

I also want to thank all the colleagues and friends during my work and stay in both Bologna and Karlsruhe. They have made my life full of colours.

My appreciation also goes to Ms. Iris Gerken for her assistance in the construction of the test rig, which helped to keep work progress on schedule. In addition, I would like to thank the microfabrication group at IMVT, Karlsruhe Institute of Technology, for manufacturing and assembling the micro heat exchangers.

The present research has received funding from the European Community's Seventh Framework Programme (ITN-FP7/2007-2013) under grant agreement n ° 215504. The financial support is acknowledged.

Last but not least, I am deeply grateful to my family for their eternal support, especially my wife. This work may have never been finished without her endless love beyond long distance.

TABLE OF CONTENTS

ABSTRACT	i
ACKNOWLEDGEMENTS	iii
TABLE OF CONTENTS	iv
LIST OF FIGURES	viii
LIST OF TABLES	xvi
NOMENCLATURE	xviii
1 Introduction	1
1.1 Background.....	1
1.2 Introduction to flow and heat transfer at microscale	2
1.2.1 Gas flow and heat transfer through microchannels.....	2
1.2.2 Gas flow and heat transfer through micro heat exchangers (microHEXs)	5
1.3 Effects of gas flow and heat transfer at microscale	8
1.3.1 Rarefaction effects	9
1.3.2 Thermal transpiration.....	10
1.3.3 Roughness effects	11
1.3.4 Compressibility effects	12
1.3.5 Longitudinal heat conduction	13
1.3.6 Effects of fluid temperature-dependent properties	14
1.3.7 Viscous dissipation	15
1.3.8 Thermal boundary conditions	16
1.3.9 Experimental accuracy.....	16
2 Measurement Techniques at Microscale	18
2.1 Measurement of microchannel geometry and surface roughness	18
2.2 Pressure measurement at microscale	20
2.3 Temperature measurement at microscale	24
2.4 Flow rate measurement at microscale.....	28
3 Experimental Uncertainties at Microscale	35
3.1 Analysis of experimental uncertainties.....	35
3.2 Experimental uncertainties on friction factor of micro gas flows	36
3.3 Experimental uncertainties on Nusselt number of micro gas flows	47

3.4	Conclusions.....	50
4	Experimental Study on Gas Flow through Microtubes.....	53
4.1	Experimental apparatus.....	53
4.2	Adiabatic gas flow through microtubes	57
4.2.1	Theory on conventional adiabatic flow.....	58
4.2.2	Data reduction for compressible flows	58
4.2.3	Friction factor of adiabatic gas microflow	59
4.3	Heated gas flow through microtubes	62
4.3.1	Friction factor of gas microflow under heated conditions	63
4.3.2	Correction of flow friction factor under heated conditions	66
4.3.3	Laminar-to-turbulent transition.....	70
4.4	Mach number and flow compressibility	72
4.5	Conclusions.....	78
5	Gas Forced Convection through Microtubes	81
5.1	Theory and data reduction	81
5.1.1	Thermal entrance region	81
5.1.2	Thermal boundary conditions	83
5.1.3	The Nusselt number	86
5.1.4	Reduction of experimental data	88
5.1.5	Temperature different between fluid and wall: from macroscale to microscale	89
5.1.6	Measurement of fluid outlet temperature.....	92
5.2	Gas micro convection in laminar and transitional regimes.....	94
5.2.1	Axial distribution of gas bulk temperature	94
5.2.2	Effect of nonlinear temperature distribution on Nusselt number.....	101
5.3	Compressible gas micro convection in transitional and turbulent regimes	105
5.3.1	Compressibility effects in micro convection	105
5.3.2	Estimation of recovery coefficient under adiabatic conditions.....	107
5.3.3	Nusselt number of compressible flows through microtubes.....	113
5.4	Main conclusions of Chapter 5	117
5.5	From microtubes to micro heat exchangers: from fundamentals to application.....	119
6	Design of Micro Heat Exchangers for Gas Flows	121

6.1	Fundamental theory and design pre-calculation	121
6.2	Heat conduction in the solid wall	124
6.3	Influence of manifold configuration on flow distribution	126
6.4	2D simulation of flow distribution and pressure drop	136
6.4.1	Numerical model and Validation of the grid dependence of the results.....	137
6.4.2	Flow distribution and pressure drop of a full layer.....	138
6.5	3D simulation of flow distribution and pressure drop	146
6.6	Conclusions.....	150
7	Experimental Investigation on Gas Flow Micro Heat Exchangers	153
7.1	Description of the experimental apparatus	153
7.2	Data reduction.....	162
7.3	Pressure losses	163
7.4	Axial heat conduction in solid walls.....	165
7.4.1	A novel method to account for wall axial conduction	165
7.4.2	Influence of wall axial conduction on the performance of microHEX.....	168
7.5	Thermal performance of microHEX with balanced flows.....	174
7.5.1	MicroHEX with countercurrent arrangement	175
7.5.1.1	Overall heat transfer coefficient and volumetric heat exchange rate.....	175
7.5.1.2	Heat exchanger effectiveness.....	177
7.5.2	MicroHEX with cross flow arrangement.....	183
7.5.2.1	Calculation of theoretical heat exchanger effectiveness for cross flow.....	183
7.5.2.2	Overall heat transfer coefficient and volumetric heat exchange rate.....	185
7.5.2.3	Heat exchanger effectiveness.....	187
7.5.3	MicroHEX with cocurrent arrangement	192
7.5.3.1	Overall heat transfer coefficient and volumetric heat exchange rate.....	192
7.5.3.2	Heat exchanger effectiveness.....	194
7.5.4	Comparison among different flow arrangements	199
7.6	Thermal performance of microHEX with unbalanced flows.....	204
7.6.1	Conventional theory on unbalanced flow heat exchanger	205
7.6.2	Countercurrent microHEX with unbalanced gas flow.....	206
7.7	Conclusions.....	207

8	Numerical Simulation on Micro Heat Exchangers	211
8.1	Numerical model.....	211
8.1.1	Geometrical construction of numerical model.....	211
8.1.2	Conditions applied to numerical model and computational method	213
8.1.3	Validation of result dependence on grid density of numerical model	214
8.2	Simulation of the double-layered microHEX.....	215
8.2.1	Numerical model.....	215
8.2.2	Temperature distribution.....	217
8.2.3	Effectiveness of the double-layered microHEX	224
8.2.4	Comparison between simulation and experimental data	228
8.3	Simulation of the multi-layered microHEX.....	232
8.3.1	Temperature distribution.....	232
8.3.2	Effectiveness of the multi-layered microHEX.....	236
8.4	Conclusions.....	240
9	Conclusions and Outlook	243
9.1	Conclusions.....	243
9.2	Future work.....	246
	Bibliography	247
	Appendix A	258
	Appendix B	267
	Appendix C.....	269
	Curriculum Vitae	273
	Publications	274

LIST OF FIGURES

Figure 1-1: Experimental correlations of Nusselt number for gas convection through microchannels (except for Gnielinski correlation).	5
Figure 3-1: Two different strategies for pressure measurement in determination of friction factor.	37
Figure 3-2: Influence of each measured parameter with typical uncertainty for a microtube having an inner diameter of 100 μm and a length of 30 mm.....	44
Figure 3-3: Contribution of the pressure and mass flow rate measurements (with uncertainties equal to 0.5% of FS) on the uncertainty of total friction factor.	45
Figure 3-4: Effect of the use of two sets of pressure sensors and mass flow meters (with full scales at $\text{Re}=500$ and $\text{Re}=2300$, respectively) on the total uncertainty of friction factor.	46
Figure 3-5: Comparison of the influence of different strategies for the pressure measurement on the sensitivity coefficients of the inlet, outlet and differential pressure (sensors with a fixed uncertainty ($\pm 0.5\%$ of FS)).	47
Figure 3-6: Sensitivity coefficients of operating parameters linked to the uncertainty of Nusselt number as a function of Reynolds number.	50
Figure 4-1: Geometry of microtube cross sections.	54
Figure 4-2: Schematic layout of the test rig (1- gas source, 2- valve, 3- filter, 4- mass flow controllers, 5- thermocouples, 6- differential pressure sensors, 7- infrared thermal camera, 8- DC heating, 9- absolute pressure sensor).	55
Figure 4-3: Photograph of the test system.	56
Figure 4-4: Friction factor as a function of Reynolds number for adiabatic flow through microtube #1.	60
Figure 4-5: Friction factor as a function of Reynolds number for adiabatic flow through microtube #2.	61
Figure 4-6: Friction factor as a function of Reynolds number for adiabatic flow through microtube #3.	62
Figure 4-7: Friction factor versus Reynolds number under adiabatic and heated conditions for microtube #1.	64
Figure 4-8: Friction factor versus Reynolds number under adiabatic and heated conditions for microtube #2.	65

Figure 4-9: Friction factor versus Reynolds number under adiabatic and heated conditions for microtube #3.	66
Figure 4-10: Correction of the friction factors of heated flow through microtube #1: (a) $m=0$, no correction; (b) $m=1$, correction for macro flow; (c) $m=2$, suitable correction with minor deviation.....	69
Figure 4-11: Correction of friction factor for heated flow.....	70
Figure 4-12: Effect of wall heating on critical Reynolds number of microflows.....	71
Figure 4-13: Average Mach number as a function of Reynolds number for the three microtubes.	73
Figure 4-14: Outlet Mach number as a function of Reynolds number for the three microtubes..	74
Figure 4-15: Pressure drop of the three microtubes versus Reynolds number.	75
Figure 4-16: Friction factor of compressible flow-comparison between experimental data and theoretical/numerical predictions (by using average Ma as suggested).....	76
Figure 4-17: Friction factor and Mach number versus Reynolds number through microtube #3.	77
Figure 4-18: Friction factor of compressible flow-comparison between experimental data and theoretical/numerical predictions (by using outlet Mach number).	78
Figure 5-1: Schematic diagram of thermal entrance region.....	81
Figure 5-2: Dimensionless thermal entry length of the three microtubes as a function of Reynolds number.	83
Figure 5-3: Wall and fluid temperature difference as a function of Reynolds number	91
Figure 5-4: Sketch of microtube outlet section designed for the measurement of exit gas temperature.	92
Figure 5-5: Gas temperature contours in the plenum for: (a) microtube #1 at $Re=1400$ at the entrance of the plenum; (b) microtube #3 at $Re=600$ at the entrance of the plenum.....	93
Figure 5-6: Wall and gas temperatures measured at different Re for microtube #1.....	95
Figure 5-7: Axial gas and wall temperature distribution through microtube #1 at $Re=1400$, under an imposed heating power of 2.8 W.	98
Figure 5-8: Axial gas and wall temperature distribution through microtube #3 at $Re=600$, under an imposed heating power of 0.6 W.	99

Figure 5-9: Experimental Nusselt numbers as a function of the Reynolds number and comparison with Gnielinski [10], Choi <i>et al.</i> [7], Wu and Little [3] and Yu <i>et al.</i> [8] correlations for microtube #1 (a) and microtube #3 (b).	104
Figure 5-10: Gas and wall temperature at the outlet of microtube #1 under adiabatic condition.	108
Figure 5-11: Gas and wall temperature at the outlet of microtube #2 under adiabatic condition.	109
Figure 5-12: Gas and wall temperature at the outlet of microtube #3 under adiabatic condition.	110
Figure 5-13: Mach number at outlet versus Re for three microtubes.	111
Figure 5-14: Recovery coefficient for gas outlet temperature measurement versus Reynolds number.	112
Figure 5-15: Gas and wall temperature at the outlet of microtube #2.	113
Figure 5-16: Nusselt number as a function of Reynolds number for microtube #1.	114
Figure 5-17: Nusselt number as a function of Reynolds number for microtube #2.	115
Figure 5-18: Nusselt number as a function of Reynolds number for microtube #3.	116
Figure 6-1: Schematic of the micro heat exchanger core. (a) double-layered; (b) multi-layered.	121
Figure 6-2: Three flow arrangements achievable in one device.	122
Figure 6-3: Heat exchanger effectiveness in dependence on the wall thermal conductivity (adapted from Stief <i>et al.</i> [147]).	125
Figure 6-4: Configurations of a typical layer to generate an S-type flow (Type A) and a U-type flow (Type B).	127
Figure 6-5: Configurations of a typical layer in the design of Type C and Type D.	128
Figure 6-6: Configurations of a typical layer in the design of Type E.	130
Figure 6-7: Mass flow distribution in the Type A configuration of the manifolds.	132
Figure 6-8: Mass flow distribution in the Type B configuration of the manifolds.	133
Figure 6-9: Mass flow distribution in the Type C configuration of the manifolds.	134
Figure 6-10: Mass flow distribution in the Type D configuration of the manifolds.	135
Figure 6-11: Mass flow distribution in the Type E configuration of the manifolds.	136

Figure 6-12: Flow velocity field in the distribution manifold and microchannels at feeding pressure of 160 kPa (length of microchannel partly displayed, velocity>100 m/s in white region).	138
Figure 6-13: Flow velocity field in the collecting manifold and microchannels at feeding pressure of 160 kPa (length of microchannel partly displayed, velocity>100 m/s in white region).	139
Figure 6-14: Static pressure in the distributing manifold and microchannels at feeding pressure of 160 kPa (length of microchannel partly displayed).	140
Figure 6-15: Static pressure in the collecting manifold and partial length of microchannels at feeding pressure of 160 kPa (length of microchannel partly displayed).	140
Figure 6-16: Mass flow rate of each microchannel under different feeding pressure.	141
Figure 6-17: Pressure distribution at inlet of each microchannel.	142
Figure 6-18: Pressure drop in the distribution manifold (from feeding port to inlet of microchannel).	143
Figure 6-19: Pressure distribution at outlet of each microchannel.	144
Figure 6-20: Percentage of pressure drop in the collecting manifold (from outlet to exhaust port).	145
Figure 6-21: Partial views of 3D geometry of one layer. Microchannels with sidewalls (a); small pillars and feeding port (b).	147
Figure 6-22: Comparison of flow distribution obtained from 2D and 3D models.	148
Figure 6-23: Mass flow distribution obtained from 3D simulation at two different feeding pressures.	149
Figure 7-1: Typical layer (with 133 microchannels) of the micro heat-exchanger (a); in-situ measurement in distribution/collecting manifolds (b) (1- pressure sensor; 2- temperature sensor; 3- pillars. unit: mm).	155
Figure 7-2: A typical layer manufactured in PEEK material with integrated pressure (1) and temperature (2) sensors.	156
Figure 7-3: Exploded schematic of the double-layered microHEX (a: 1- connection of thermocouple; 2- connection of pressure transducer; 3- feeding/venting port of the first fluid; 4- metallic cover; 5- PEEK cover with 133 microchannels; 6- partition foil between two fluids; 7- feeding/venting port of the second fluid) and photograph of the manufactured device (b).	157

Figure 7-4: Schematic layout of the test rig. (1- gas source, 2- filter, 3- flow splitter, 4- valves, 5- mass flow controller, 6- temperature regulator, 7- micro heat exchanger).....	158
Figure 7-5: Photograph of the test system (1- pressure regulator of gas source; 5- mass flow controllers; 6- temperature regulators; 7- micro heat exchanger).....	159
Figure 7-6: Photograph of the micro heat exchanger in test (1- pressure sensors; 2- thermocouples).....	160
Figure 7-7: The double-layered micro heat exchanger (a) and the partition foil (b)	161
Figure 7-8: Pressure drops in different sections of the micro heat exchanger.....	165
Figure 7-9: Effectiveness of a countercurrent double-layered micro heat exchanger with a thick aluminum partition foil (AL100) in comparison with theoretical predictions of Eq. (7.10) (continuous line) and Eq. (7.11) (dashed line).....	168
Figure 7-10: Geometrical parameters of the double-layered microHEX (red color – microchannels for hot flow; blue color – microchannels for cold flow).	169
Figure 7-11: Longitudinal conduction parameter in the previous and present work for gas-to-gas micro heat exchanger (S.S. refers to stainless steel).	171
Figure 7-12: Heat exchanger effectiveness as a function of Reynolds number for different magnitudes of axial conduction parameter.	173
Figure 7-13: Wall conduction parameter by changing the working gases in previous work into water.....	174
Figure 7-14: Heat transfer coefficient of the microHEX as a function of mass flow rate.....	175
Figure 7-15: Volumetric heat exchange rate as a function of mass flow rate.....	177
Figure 7-16: Effectiveness of microHEX with thin stainless steel foil (SS100) in comparison with theoretical prediction.	178
Figure 7-17: Effectiveness of microHEX with thin copper foil (C100) in comparison with theoretical prediction.	179
Figure 7-18: Effectiveness of microHEX with thick copper foil (C500) in comparison with theoretical prediction.	180
Figure 7-19: Effectiveness of countercurrent microHEX with thick PEEK foil (P500).	181
Figure 7-20: Effectiveness of microHEX as a function of mass flow rate for various partition foils.	182

Figure 7-21: Heat transfer coefficient of cross flow microHEX as a function of mass flow rate.	186
Figure 7-22: Volumetric heat exchange rate of cross flow as a function of mass flow rate.....	187
Figure 7-23: Effectiveness of microHEX with thick PEEK foil (P500) in comparison with theoretical prediction.	188
Figure 7-24: Effectiveness of microHEX with thin aluminum foil (AL100) in comparison with theoretical prediction.	189
Figure 7-25: Effectiveness of cross flow microHEX with thin copper foil (C100).....	190
Figure 7-26: Effectiveness of cross flow microHEX with thin stainless steel foil (SS100).....	190
Figure 7-27: Effectiveness of cross flow microHEX with various partition foils.	192
Figure 7-28: Overall heat transfer coefficient of the cocurrent microHEX as a function of mass flow rate.	193
Figure 7-29: Volumetric heat exchange rate versus mass flow rate for cocurrent flow.	194
Figure 7-30: Effectiveness of microHEX with thick PEEK foil (P500) in comparison with theoretical prediction.	195
Figure 7-31: Schematic diagram of local fluid and wall temperature development in cocurrent flow heat exchanger.	196
Figure 7-32: Effectiveness of microHEX with thin aluminum foil (AL100) in comparison with theoretical prediction.	197
Figure 7-33: Effectiveness of cocurrent microHEX with thin stainless steel foil (SS100).	198
Figure 7-34: Effectiveness of cocurrent microHEX with thin copper foil (C100).	198
Figure 7-35: Effectiveness of cocurrent flow microHEX with various partition foils.	199
Figure 7-36: Comparison of effectiveness among three flow arrangements with thick PEEK partition foil (P500).....	201
Figure 7-37: Comparison of effectiveness among three flow arrangements with thin aluminum partition foil (AL100).	202
Figure 7-38: Comparison of effectiveness among three flow arrangements with SS100 foil.	203
Figure 7-39: Comparison of effectiveness among three flow arrangements with C100 foil.....	203
Figure 7-40: Countercurrent flow heat exchanger effectiveness as a function of NTU for various ratios of heat capacity rate.	205

Figure 7-41: Comparison between experimental effectiveness and theoretical prediction for unbalanced flows.	206
Figure 7-42: Experimental values of effectiveness as a function of NTU.....	207
Figure 8-1: A multi-layered micro heat exchanger with hot and cold flows (a) and a typical element from it (b). ($C_1D_1=D_1G_1=G_1H_1=0.1$ mm, $A_1B_1=0.05$ mm, microchannel length $A_1A_2=39.8$ mm)	212
Figure 8-2: 3D model of two microchannels with partition and side walls (a) and schematic display of heat flux (b).....	212
Figure 8-3: A double-layered micro heat exchanger with hot and cold flows (a) and a typical element from it (b). ($D_1G_1=0.1$ mm, $C_1D_1=G_1H_1=0.2$ mm, $A_1B_1=0.05$ mm, channel length $A_1A_2=39.8$ mm)	216
Figure 8-4: 3D model of two microchannels with partition and side walls in the double-layered microHEX.	216
Figure 8-5: Temperature contour on the right vertical symmetric plane ($C_1H_1C_2H_2$) for three different thermal conductivities of partition foil (Black lines indicate the surfaces of solid walls).....	218
Figure 8-6: Temperature contour on the left vertical symmetric wall ($A_1J_1A_2J_2$) for three different thermal conductivities of partition wall.	220
Figure 8-7: Axial temperature distribution for the countercurrent double-layered microHEX with partition foil made of different solid materials (different thermal conductivity).....	222
Figure 8-8: Axial distribution of overall heat transfer coefficient for a countercurrent double-layered microHEX with partition foil made of different materials.....	223
Figure 8-9: Heat exchanger effectiveness for a double-layered microHEX as a function of partition wall thermal conductivity at $Re=550$ (countercurrent flow arrangement).	225
Figure 8-10: Heat exchanger effectiveness as a function of partition wall thermal conductivity at different Reynolds numbers (countercurrent flow arrangement).....	226
Figure 8-11: Heat exchanger effectiveness as a function of partition foil thermal conductivity with different foil thicknesses (countercurrent flow arrangement).....	227
Figure 8-12: Heat exchanger effectiveness versus partition wall thermal conductivity for cocurrent flow arrangement at $Re=100$	228

Figure 8-13: Comparison of heat exchanger effectiveness between simulation and experiment for a countercurrent double-layered microHEX with a balanced mass flow rate of 1.0 kg/h. .	229
Figure 8-14: Velocity vectors at connecting manifolds and central microchannels (channel index: 66-68 out of 133) of the double-layered microHEX (feeding pressure at 500 kPa).	231
Figure 8-15: Temperature contour on the right vertical symmetric plane ($C_1H_1C_2H_2$) for three different thermal conductivities of solid walls (Black lines indicate the surfaces of solid walls).	233
Figure 8-16: Temperature contour on the left vertical symmetric wall ($A_1J_1A_2J_2$) for three different thermal conductivities solid walls.	235
Figure 8-17: Heat exchanger effectiveness as a function of wall thermal conductivity for the multi-layered microHEX with countercurrent flow.	236
Figure 8-18: Heat exchanger effectiveness of a countercurrent multi-layered microHEX with balanced mass flow rates as a function of wall thermal conductivity for air and water flows.	238
Figure 8-19: Comparison on thermal performance between double-layered and multi-layered microHEXs for countercurrent flow arrangement.	239
Figure 8-20: Comparison on thermal performance between double-layered and multi-layered microHEXs for cocurrent flow arrangement.	240
Figure A-1: Correction of the friction factors of heated flow through microtube #2: (a) $m=0$, no correction; (b) $m=1$, correction for macro flow; (c) $m=2$, suitable correction with minor deviation.	270
Figure A-2: Correction of the friction factors of heated flow through microtube #3: (a) $m=0$, no correction; (b) $m=1$, correction for macro flow; (c) $m=2$, suitable correction with minor deviation.	272

LIST OF TABLES

Table 1-1: Experimental study on gas-to-gas microchannel heat exchangers.....	6
Table 2-1: Experimental techniques on measurement of microchannel geometry.....	20
Table 2-2: Experimental techniques on measurement of pressure at microscale.....	24
Table 2-3: Experimental techniques on temperature measurement in microflows.....	28
Table 2-4: Experimental techniques on measurement of gas mass flow rate at microscale.....	34
Table 3-1: Sensitivity coefficients of operating parameters in the calculation of friction factor.	39
Table 3-2: Relative uncertainties of measured quantities in liquid microflows (from Ferguson <i>et al.</i> [121])	40
Table 3-3: Relative uncertainties of measured quantities in gaseous microflows.....	41
Table 3-4: Typical values of experimental parameters for gaseous microflows.....	43
Table 3-5: Sensitivity coefficients of operative parameters for determination of experimental uncertainty in Nusselt number.....	49
Table 4-1: Geometrical characteristics of the tested microtubes	53
Table 4-2: Characteristics and accuracy of instrumentation.....	57
Table 5-1: Calculation of Nusselt number in various flow regimes.....	87
Table 5-2: Dimension of the tubes in comparison and assumed boundary conditions.....	90
Table 5-3: Thermal properties of water and air [133].....	90
Table 5-4: Temperature-dependent thermal properties of nitrogen adopted in numerical simulation.....	96
Table 5-5: Typical ranges of the non-dimensional parameters linked to the main effects for the tested microtubes.....	101
Table 5-6: Value of the fitting parameters obtained for microtube #1($P=1.2$ W) and microtube #3 ($P=0.6$ W).	102
Table 6-1: Prediction of operating conditions and selection of sensors.....	124
Table 6-2: The main characteristics of the 5 types of configurations.....	131
Table 6-3: Validation of grid dependence.....	137
Table 6-4: Uniformity of mass flow rate and pressure distribution in terms of microchannel number from 2D simulation.....	146

Table 6-5: Uniformity of mass flow rate and pressure distribution in terms of microchannel number from 3D simulation.....	150
Table 7-1: Parameters of the micro heat exchangers for fabrication.	153
Table 7-2: Uncertainties in the measurements.....	161
Table 7-3: List of partition foils in the present tests.	162
Table 7-4: Calculation of heat exchanger effectiveness for cross flow (P500 foil).....	185
Table 8-1: Validation of result dependence on grid density.	214

NOMENCLATURE

Roman symbols

Br	Brinkman number	(-)
c_p	Specific heat at constant pressure	(J/kgK)
d	Inner diameter	(m)
D	External diameter	(m)
d_h	Hydraulic diameter	(m)
h	Convective heat transfer coefficient	(W/m ² K)
H	Height of microchannel	(μ m)
k	Thermal conductivity	(W/mK)
L	Microtube total length	(m)
L_h	Microtube heated length	(m)
\dot{m}	Mass flow rate	(kg/s)
Ma	Mach number	(-)
Nu	Nusselt number	(-)
P	Heating power	(W)
Pr	Prandtl number	(-)
q	Heat flux	(W/m ²)
R	Specific gas constant	(J/kgK)
Re	Reynolds number	(-)
s_1	Thickness of microchannel sidewall	(m)
s_2	Thickness of partition wall	(m)
T	Temperature	(K)
U	Overall heat transfer coefficient	(W/m ² K)
\bar{v}	Average bulk flow velocity	(m/s)
W	Width of microchannel	(m)

Greek symbols

δ	Absolute roughness	(m)
ε	Heat exchanger effectiveness	(-)
γ	Specific heat ratio (c_p/c_v)	(-)

λ	Conduction parameter	(-)
μ	Dynamic viscosity	(kg/ms)

Superscript and subscript

adb	adiabatic
e	external surface
f	fluid
h	heated
i	internal surface
in	inlet value
m	mean value
out	outlet value
stg	stagnation
w	wall

Abbreviations

CAD	Computer-aided design
CFD	Computational Fluid Dynamics
2D	Two-dimensional
3D	Three-dimensional
FS	Full Scale
H b.c.	Constant heat flux boundary condition
LIF	Laser-induced Fluorescence
LMTD	Logarithmic mean temperature difference
MEMS	Micro-electro-mechanical System
MFC	Mass flow controller
microHEX	micro Heat Exchanger
microPIV	microscale Particle Image Velocimetry
MTV	Molecular Tagging Velocimetry
NTU	Number of transfer unit
PEEK	Polyether ether ketone
PSMF	Pressure-sensitive Molecular Film
PSP	Pressure-sensitive Paints
RTD	Resistance Temperature Detector
SEM	Scanning Electron Microscope
T b.c.	Constant temperature boundary condition
TFTC	Thin Film Thermocouple

1 Introduction

1.1 Background

In recent years there has been rapid progress in the technology of miniaturization, with devices and systems being scaled down from macrometric sizes to micrometric dimensions [1]. This was not only ignited by extensive engineering and industrial applications with promising market potential, but also stimulated by multidisciplinary research intersecting chemistry, physics, biology, life science, pharmaceuticals and engineering, etc.

To meet various industrial demands, the miniaturization technology has been developed in different specialized branches including microfabrication, microassembly, microcontrol, micromasurement and microprocessing [2]. The achievements in these fields brought about very flexible and smart systems, such as micro-electro-mechanical systems (MEMS), microfluidic devices, lab on a chip (LOC) and micro-total-analysis systems (μ TAS). The typical dimension of these systems ranges from 1000 μm down to 1 μm . In the field of mechanical engineering, the state-of-art technologies enable the operation inside micro mixers, micro heat exchangers, micro reactors, micro pumps, micro turbines, to name just a few. These miniaturized devices often accommodate fluid flow, heat transfer and chemical reaction in order to meet very diverse purposes in different fields of application.

The miniaturization of these devices can give some advantage compared to their conventional-sized counterparts. Such devices are very small and can be flexibly adapted to meet various requirements. Due to small sizes and weights, they offer great mobility and can be integrated to many larger systems. Another benefit is the enhanced heat transfer coefficient brought by small hydraulic diameter and large surface-to-volume ratio. In addition, the momentum and thermal inertia of such devices are greatly reduced. This is quite beneficial for precise control and management of temperature field and fluid concentration, and thus has great potential in industrial applications.

The numerical research on fluid flow and heat transfer at microscale can be considered plentiful. Besides conventional computational fluid dynamics (CFD) solvers, such as ANSYS Fluent, OpenFoam, COMSOL and PHOENICS, many home-developed codes using specific methods are reported in literature to further increase the simulation accuracy (which sometimes

can be too much accurate if compared with the typical measurement accuracy which can be reached in the experimental analysis of microflows) and reduce computational time. However, the experimental data on micro flow and heat transfer are scarce compared with the existing numerical research, mainly due to challenges not only in microfabrication, but also in flow control and measurement at micro scale.

By considering the available experimental data from different research groups, diverging conclusions can be drawn, as the error in measurement can be in some case very large (up to 100% uncertainty in measurement). As pointed out by Morini [3], sometimes the physical behavior can be completely masked by large uncertainties in measurement, and the experimental data do not make any sense and thus lead to wrong conclusions. Furthermore, by observing the published experimental works on single phase flow and heat transfer at microscale, it can be noted that the amount of works in which liquids are used as working fluids surpasses the number of works dealing with gases. The crucial lack of experimental data on gaseous flow and heat transfer at microscale makes some problem to validate the large number of analytical and numerical predictions made in this field. This aspect has been also emphasized in a recent review by Colin [4]. On the other hand, increasingly extensive applications of gaseous microfluidic devices nowadays call for more systematic investigation in this field. More and more extensive applications of these devices are pushed to operate under some extreme conditions, i.e., rarefied flows or highly subsonic flows. Therefore, it will be useful to provide designers and engineers with a reliable reference of gaseous flow and heat transfer features through microfluidic devices. This is also motivating to the present research.

This thesis is dedicated to the investigation of the main features of forced convection for gaseous flows through a single microtube and within microstructured devices like the gas-micro heat exchangers, mainly from an experimental point of view but always with the support of numerical simulation.

1.2 Introduction to flow and heat transfer at microscale

1.2.1 Gas flow and heat transfer through microchannels

In the last years a large amount of experimental analyses has been addressed to the study of the fluid-dynamical and heat transfer characteristics of single-phase flows in microchannels, as

summarized by Rostami *et al.* [5], Morini [3], Hetsroni *et al.* [6] and more recently, by Dey *et al.* [7] and Kandlikar [8].

The pioneering experimental investigation on gas micro flow can be traced back to the work by Wu and Little [9], who explored the flow characteristics of N₂, H₂ and Ar through miniaturized rectangular channels with hydraulic diameter from 40 to 80 μm. They found significant departure of friction factor from classical theory and a very early laminar-to-turbulent transition at Re=900. These abnormal phenomena were attributed by the authors to the large relative roughness in the microchannel wall surface and its asymmetric distribution along the wetted perimeter. Pong *et al.* [10] developed microchannels which had hydraulic diameters of 2 μm with integrated pressure sensors along the flow path. By means of a careful and systematic measurement they found that the pressure distribution of nitrogen and helium flow along the axial direction is not linear. This non-linear pressure distribution was also evidenced in the experimental work by Jang and Wereley [11] even for Reynolds number down to around 100. Harley *et al.* [12] compared experimental results with numerical simulation for subsonic and compressible flow of N₂, H₂ and Ar through microchannels having hydraulic diameters from 1 to 36 μm. Their work verified that the experimental friction factor could be reasonably predicted by conventional theory considering the uncertainties in measurement. In addition, the authors concluded that cross sectional pressure distribution may be considered uniform and the transverse velocity is negligible. On the contrary, the work by Arkilic *et al.* [13] evidenced momentum transfer in the cross section from the central axis to the wall surface for helium flow through microchannels of 2.6 μm in hydraulic diameter. Combining experimental data and numerical simulations, the authors developed expressions for transverse velocity and cross sectional pressure distribution.

Wu and Little [14] also investigated gas convective heat transfer at microscale. They compared the trend of experimental Nusselt number as a function of Reynolds number in laminar, transitional and turbulent regimes with the classical correlations proposed by Sieder and Tate [15], Hausen [16] and Dittus and Boelter [17] evidencing a strong disagreement with these correlations.

Choi *et al.* [18] experimentally analyzed the forced convection of nitrogen flows in silica microtubes having inner diameters between 3 μm and 81 μm. Their experimental results indicated significant departures from classical correlations. The Nusselt number in turbulent flow

was found larger than the prediction of the Dittus-Boelter correlation [17] but not in agreement with the correlation proposed by Wu and Little. In laminar regime Choi *et al.* [18] obtained very low values of Nusselt number in strong disagreement with classical correlations. The authors gave no justification for this and proposed a new correlation by fitting their own experimental data.

Yu *et al.* [19] investigated the convective heat transfer of nitrogen flow in turbulent regime ($6000 < Re < 20000$) through microtubes with inner diameters between 19 μm and 102 μm . They obtained larger values of Nusselt numbers than those predicted by means of conventional correlations.

Hara *et al.* [20] experimentally investigated the convective heat transfer of air flows through square minichannels with hydraulic diameters between 0.3 mm and 2 mm. They reported that Nusselt number in turbulent regime can be larger or smaller than the values predicted from Dittus and Boelter correlation. The deviation depends on the hydraulic diameter and length of the minichannels. In laminar regime, the Nusselt numbers were found to be lower than those obtained by Wu and Little [14].

More recently, Chen *et al.* [21] and Yang *et al.* [22] conducted experimental research on air and carbon dioxide flow heat transfer through microtubes with an inner diameter of 920 μm . The trend of Nusselt number in both laminar and turbulent regimes was found in agreement with the classical correlation by Gnielinski [23], which was proposed for incompressible flow at macro scale. Their experimental results seem to indicate that the heat transfer coefficient is not influenced by the flow compressibility effect even at very large Reynolds numbers.

By analyzing the works of Wu and Little [14], Choi *et al.* [18], Yu *et al.* [19] and Hara *et al.* [20] it turns out that these authors did not try to explain the peculiar trends of their experimental data, or the possible effects that should be considered. In addition, if the results of these research groups are compared among one another, the mismatch among the data appears well evident both in laminar and turbulent regimes, as plotted in Figure 1-1. However, the authors of these experimental works did not make any efforts to provide a physical explanation of these results; they limited their work to collecting the data for new correlations. This “uncritical” behavior is typical in the field of microfluidics as underlined by Morini [3].

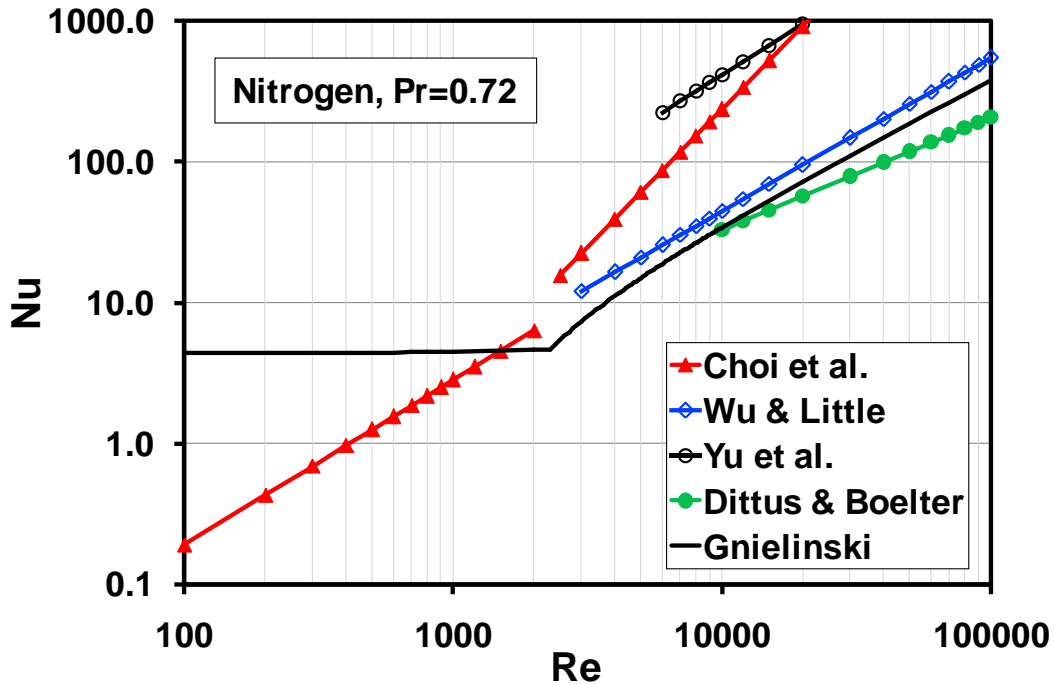


Figure 1-1: Experimental correlations of Nusselt number for gas convection through microchannels (except for Gnielinski correlation).

1.2.2 Gas flow and heat transfer through micro heat exchangers (microHEXs)

Among micro-structured devices, micro heat exchangers are of increasing interest, for their improved heat exchange capacities thanks to very large surface-to-volume ratio [24].

The applied research on micro channel heat exchangers using liquids (mostly deionized water) as working media can be considered extensive, even though some of the results are not univocal. Based on experiments with cross-flow micro heat exchangers, Harris *et al.* [25] found that the volumetric heat transfer in these micro-sized devices is improved at least five times compared to the conventional-sized ones. Improved heat exchanger devices of different microstructure designs and manufactured in metals have been described by Brandner *et al.* [26, 27]. Alm *et al.* [28] reported larger heat transfer coefficients and larger pressure losses in ceramic microchannel heat exchangers available for both countercurrent and cross flow arrangements. Cao *et al.* [29] proposed an experimental correlation for the prediction of the average value of Nusselt number and pressure drop of microchannel heat exchangers. On the contrary, the investigation of Garcia-Hernando *et al.* [30] showed no heat transfer enhancement or higher pressure drop through micro heat exchangers due to the reduced scale of the channels.

More recently, Mathew and Hegab [31] provided a universal correlation to estimate the heat transfer performance of microchannel heat exchangers subjected to external heat flux, regardless of the cross-sectional geometry of the microchannels.

Compared with the research on liquid micro heat exchangers, experimental investigations on these devices subjected to gas flows are quite few. The experimental works available in literature on gas-gas micro heat exchangers are summarized in Table 1-1 in which for each work the range of the main parameters adopted during the tests is shown.

Table 1-1: Experimental study on gas-to-gas microchannel heat exchangers.

Authors	Channel			Materials	Partition wall		Gas species	Flow arrangement
	width (μm)	height (μm)	length (mm)		conductivity ($\text{WK}^{-1}\text{m}^{-1}$)	thickness (μm)		
Bier <i>et al.</i> [32]	100	78	14	copper	401	22	He, N ₂ , Ar	cross flow
Bier <i>et al.</i> [32]	90	75	14	stainless steel	14.7	25	He, N ₂ , Ar	cross flow
Meschke <i>et al.</i> [33]	1500	1500	50	ceramic SiC	125	2000	N ₂	cross flow
Koyama and Asako [34]	300	200	20	stainless steel	15	300	air	cocurrent flow countercurrent flow

The first work on gas micro heat exchangers made of metal was reported by Bier *et al.* [32] for cross flows of helium, nitrogen and argon. The researchers found that in laminar regime the overall heat transfer coefficients are greatly reduced for low mass flow rates. In addition they proposed a homogeneous model to account for the dominant influence of longitudinal heat conduction in the solid wall. As the thermal conduction in metal (copper and stainless steel) overwhelms that in the fluid, actually in such a case the micro heat exchanger works as a temperature mixer between cold and hot flows. This is probably the reason why this model indicated that the thermal performance of the gas micro heat exchangers does not differ between cross flow, cocurrent flow and countercurrent flow; this result is in complete disagreement with the typical behavior of conventional-sized heat exchangers. Accordingly, it was suggested by the authors that, in order to obtain larger heat transfer rates, material of lower thermal conductivity should be used both for microchannel plates and for the shell of micro heat exchanger.

The experimental data by Meschke *et al.* [33] on a ceramic micro heat exchanger also evidenced lower values of heat transfer coefficients with respect to the theoretical predictions based on conventional theory. According to the authors, the reduced heat transfer coefficients

were subjected to strong axial heat conduction in solid wall. In addition, the heat losses due to the heat conduction from the ceramic core to the steel housing were found significant on the thermal performance of the micro heat exchanger. The influence of thermal conduction within the solid wall on the overall thermal performance was so large that the impact of flow arrangement (cross, co-current, counter-current) becomes comparably insignificant, as evidenced by the authors.

Similar conclusion was drawn by Koyama and Asako [34] from experiments with a stainless steel micro heat exchanger. In this work no significant difference in the total thermal performance was found between cocurrent and countercurrent flows. The investigators finally used an isothermal model with T boundary condition (constant wall temperature) to explain their experimental data.

More recently, Kee *et al.* [35] fabricated and tested an alumina micro heat exchanger for gas heat transfer. The device was operated at high temperature range up to 700 °C. They underlined how, due to the limitation of the ceramics fabrication technique, the wall thickness of channels cannot be reduced to the typical sizes of microHEXs made of metal or other material such as polymer. Therefore the thermal performance of the ceramic micro heat exchanger is limited. This work was not listed in Table 1-1 because the researchers used short microchannels with gaps in the flow direction in order to enhance the flow mixing. Thus the physics behind hydrodynamic and thermal behaviors is quite different from the other microdevices.

Another issue raised on micro heat exchangers is the flow distribution among the parallel channels which compose the heat exchanger core. In general, micro heat exchangers are built by using a large number of parallel microchannels for each layer in order to obtain large heat transfer between the hot and cold flows with a limited pressure drop even in the case of large mass flow rates. For this reason, most of the micro heat exchangers described in literature are based on parallel microchannels built on a plate or foil. All the microchannels are connected to the same inlet and outlet manifolds and for this reason they can be modeled as a series of channel in hydraulic parallel. It becomes important to design accurately the inlet and outlet manifolds in order to assure a flow distribution among the parallel channels as uniform as possible. In the work of Bier *et al.* [32] and Meschke *et al.* [33] the issue of flow distribution was not addressed. Koyama and Asako [34] found the experimentally measured pressure drop to be several times higher than prediction, and they considered non-uniform distribution of mass flow as one reason

to this disagreement. However, the exact impact of flow maldistribution on additional pressure drop was not estimated in the work of Koyama and Asako [34].

The flow distribution is very important to micro heat exchangers, because it does not only influence the hydrodynamic behavior, but also changes the thermal behavior of these devices. The optimization of flow distribution was systematically studied by Commenge *et al.* [36] who proposed an approximate pressure drop model. Chein and Chen [37] compared the velocity and temperature distribution along 11 parallel microchannels by changing the positions of distribution/collecting ports. Tonomura *et al.* [38] developed an automatic optimization algorithm which is able to tailor iteratively the shape of distributing/collecting manifold until satisfying flow distribution is obtained. Balaji and Lakshminarayanan [39] proposed a new design of the distribution chamber in order to obtain a uniform flow distribution. In their design the flow enters the distribution chamber from one port while the exhausted flow is collected by two ports. An original analytical model for optimization of flow distribution in a manifold has been reported by Renault *et al.* [40]. The authors demonstrated that their model can be able to calculate the flow distribution faster than the classical CFD simulation without losing too much in accuracy.

The methods described in the works available in the open literature provide convenient guidelines for the design of micro heat exchangers. However, up to now it is difficult to find a systematic way to optimize flow distribution inside multi-layered microchannel heat exchangers, mainly due to the difficulties in compromising among all the parameters in design phase. These parameters include: (i) the dimensions of microchannels (width, height and length), (ii) the shape of distributing/collecting manifolds, (iii) the curvature of manifolds corners, (iv) the length of the connections between the heat exchanger core and manifolds, (v) the position of feeding/exhaust ports, (vi) the direction of inflow/outflow, etc. Furthermore, in practical tests and applications of micro heat exchangers, the parameters mentioned above may be subjected to different types of practical constraints coupled with higher priorities as assembling, working condition, vulnerability to possible damages, pricing and so on.

1.3 Effects of gas flow and heat transfer at microscale

This section addresses the main effects that may be encountered in gaseous flow and heat transfer through microdevices. These effects include:

- 1) Micro effects which require physical reformulation of governing equations and/or boundary conditions when the system is miniaturized from the normal macro dimension, such as rarefaction effects and thermal transpiration;
- 2) Scaling effects which become significant only when the geometrical scale of the system changes from the reference scale, such as roughness effects, flow compressibility, longitudinal wall heat conduction, temperature-dependence of fluid properties and viscous dissipation;
- 3) Practical effects which are not related to the system dimension but are very important to obtain correct and accurate results in practical operations of microdevices, such as thermal boundary conditions and accuracy of experimentation.

These effects will be individually introduced in a very brief way in this section, with emphasis on experimental investigation. However, it should be noted that for gas flow and heat transfer at microscale, several of these effects may co-occur under certain conditions. For example, the roughness effects can be conjugated with flow compressibility. Also the influences of these effects on flow dynamics and heat transfer characteristics will be demonstrated in this section by analyzing their impacts on friction factor and Nusselt number.

1.3.1 Rarefaction effects

The gas rarefaction is characterized by the ratio of the mean free path to the typical dimension of the flow volume. This ratio is called Knudsen number, which is defined by:

$$Kn = \frac{l}{L} \quad (1.1)$$

where l is the gas mean free path and L is the characteristic length of the volume.

The gas flow is classified into different flow regimes in which different governing equations and/or boundary conditions should be applied according to the magnitude of Knudsen number [41]:

1. $Kn < 0.001$. The flow is in continuum regime, and the flow behavior can be exactly described by the Navier-Stokes equations with non-slip boundary conditions.
2. $0.001 < Kn < 0.1$. The flow is in slip regime in which the Navier-Stokes equations are still valid, but the velocity slip and temperature jump on the wall surface should be applied to these equations. In this flow regime the gas is slightly rarefied.

3. $0.1 < Kn < 10$. The flow is in transition regime in which the Navier-Stokes equations are no longer applicable. The gas flow in this regime is moderately rarefied.
4. $Kn > 10$. The flow is in free molecular regime and the occurrence of molecule-wall collision overwhelms that of intermolecular collision. In this regime the flow is highly rarefied.

At microscale, the flow is confined within very small volume and tends to deviate from continuum regime given that the mean free path does not change notably. The effect of gas rarefaction on friction factors (or mass flow rates) and convective heat transfer coefficients has been investigated in a series of papers in the past [4]. The early experimental work of Harley *et al.* [12] showed good agreement with theoretical predictions on slip flow for Knudsen number up to 0.4. Ewart *et al.* [42] experimentally investigated the mass flow rate of gaseous flows in slip regime. Later the authors extended their study to near free molecular regime [43]. Pitakarnnop *et al.* [44] measured the velocity slip of gas flow in both slip and transition regimes. Demsis *et al.* [45] explored the heat transfer coefficient of gas flow in slip regime by applying highly vacuum (very low absolute pressure) flow through tube of constant wall temperature. In general, these works have put in evidence that gas rarefaction is responsible for a decrease of the friction factors along a microchannel (which determines an increase of the gas flow rate for a fixed pressure difference between the inlet and the outlet) and of a decrease of the convective heat transfer coefficients.

1.3.2 Thermal transpiration

While most gas flows at macro scale are driven by an imposed external pressure difference (pressure driven flow), it is possible to generate a flow in rarefied gas by applying an initial temperature gradient along a thin channel while the initial pressure difference between the ends of the channel is set to zero [46]. This phenomenon is known as thermal transpiration or thermal creep, and it has been investigated by many researchers [47, 48] and [49].

The principle of thermal transpiration brought about the idea of Knudsen pump, which is a gas pump with no moving parts and operates under rarefied conditions. In order to have the Knudsen pump operating under low vacuum condition (i.e., near atmospheric condition), the dimension of the thin channel must be small enough, usually at micro or even nano scales. One of the examples is the work by McNamara *et al.* [50], who manufactured a micro-structured

Knudsen pump which is able to operate at atmospheric pressure. The effect of thermal transpiration can modify the value of the mass flow rate along a microchannel especially for low gas pressure and low flow rates. On the contrary, for a gas pressure larger than the atmospheric value ($Kn < 0.01$) the effects due to thermal creep can be considered always as negligible.

1.3.3 Roughness effects

The surface roughness tends to play an important role on the determination of the friction factors in conventional-sized tubes only in turbulent regime; on the contrary, the role of tube roughness on convective heat transfer coefficients is smaller. An indicator of the roughness level of a tube is its relative roughness defined as the ratio between the absolute height of the wall roughness elements and the hydraulic diameter of the channel. For conventional tubes the relative roughness is always lower than 5%. When the relative roughness is lower than $10^{-4}\%$, as indicated by the Moody's diagram, the tube can be considered perfectly smooth. Due to the reduction of the inner diameter, in microchannels the relative roughness can assume very large values, in some cases larger than 5%. In this case the effects of the roughness on the friction factor become evident also in laminar regime.

In order to investigate the influence of roughness effects on pressure drop, Kandlikar and Schmitt [51] manufactured microchannels with different shapes of artificial roughness elements. They found that the surface roughness does not influence the pressure drop in laminar flow as long as the flow area is accurately taken into account by introducing the concept of the "reduced diameter" of the microchannel. Later Tang *et al.* [52] evidenced that conventional laws for the estimation of the friction factors are still applicable for gaseous flow in microchannels if the relative roughness is smaller than 1%.

Surface roughness may also influence the flow transition from laminar regime to turbulent regime. Kandlikar *et al.* [53] tested flows through micro and mini tubes with various surface textures. They found that the pressure drop and the transition to turbulent regime are strongly influenced by the surface roughness. These results are in disagreement with the experimental results obtained by Lorenzini *et al.* [54] for nitrogen flows through microtubes with relative roughness from 0% to 1.0% in which a very weak dependence of the critical Reynolds number on surface roughness was evidenced. In particular, the scattered data points of critical Reynolds

number as a function of either roughness or the ratio of length to diameter (L/d) in the work by Lorenzini *et al.* [55] and Kolh *et al.* [56] suggested no explicit relation among them.

Roughness also plays a role in the heat transfer coefficient of gas micro convection. The pioneering experimental research of Wu and Little [14] showed a strong enhancement of convective heat transfer of nitrogen flow through microtubes due to the presence of a large relative roughness around the inner perimeter of the microchannel and its asymmetric distribution. These results are in disagreement with the 3D numerical investigation of Croce *et al.* [57] which evidenced slight improvement in convective heat transfer with the relative roughness, in agreement with their earlier results obtained by means of a 2D numerical simulation [58]. More recently, the experimental test by Lin and Kandlikar [59] using artificially structured roughness element for microchannels exhibits very strong enhancement (up to 377%) in convective heat transfer.

1.3.4 Compressibility effects

Unlike liquid flow, micro gas flows may become compressible under certain operating conditions. From the point of view of gas dynamics, the flow compressibility can be characterized by the value assumed by the Mach number, which is defined by:

$$Ma = \frac{\bar{v}}{c} \quad (1.2)$$

where c is the speed of sound and \bar{v} is the flow mean velocity associated to the channel cross-section.

For gas flows through circular tubes, Eq. (1.2) can be further expressed by

$$Ma = \frac{\mu Re}{dp} \sqrt{\frac{RT}{\gamma}} \quad (1.3)$$

using the state equation of ideal gas, where μ is the gas dynamic viscosity, Re is the Reynolds number, d is the tube inner diameter, R the gas specific constant, γ the specific heat ratio of the gas considered, and T and p are the gas bulk temperature and pressure. Eq. (1.3) indicates that a larger value of Mach number will be evidenced if the tube inner diameter is reduced, given that the Reynolds number, and gas species and the operating conditions (pressure and temperature) are kept unchanged. This means that the flow compressibility effects are more likely to be encountered at microscale.

The work of Turner *et al.* [60] on nitrogen and air flow through microchannels confirms this aspect. They evidenced a very abrupt increase of the Mach number (from 0.4 to nearly unity) in the last 10% of microchannel length, while the increase of Mach number in the first part of the microchannel was rather mild.

The flow compressibility may result in extra pressure losses in flow direction compared with incompressible flows. In other words, flow compressibility tends to increase the friction factor along a channel. Therefore, there was some research devoted to the modification of traditional correlations for the estimation of the friction factor in order to take into account the flow compressibility. Asako *et al.* [61] developed a correlation between the Poiseuille number and Mach number by solving two-dimensional compressible momentum and energy equation numerically; the numerical correlation was validated by means of specific experimental tests conducted with nitrogen through a series of microtubes having an inner diameter of 150 μm . Another similar relation between the Poiseuille number and Mach number was proposed by Li *et al.* [62] using an analytical method. Tang *et al.* [52] developed an additional experimental correlation in order to consider the compressibility effect by fitting their experimental data.

Another effect due to compressibility is the flow choking, which occurs when the Mach number of the flow reaches unity. A direct consequence of the flow choking, as known from its name, is that the mass flow rate does not increase any more with a further decrease of downstream pressure while the upstream pressure remains fixed [63]. Shi *et al.* [64] studied the behavior of choked flow through a flat minichannel by comparison between experiment and numerical calculation. More recently, Lijo *et al.* [65] concluded that for choked flows the heat transfer coefficient is higher at the exit, which can be due to the scaling effects. Consequently, the authors suggested to use a scaling factor in order to explain the effect caused by flow choking in microtubes.

1.3.5 Longitudinal heat conduction

Longitudinal conduction, also called axial conduction, refers to heat conduction in flow direction. It occurs in both the fluid and the solid wall. The longitudinal conduction in the fluid can play a significant role for fluid with high thermal conductivity, especially for liquid metals. However, for gases which have low thermal conductivities, the fluid axial conduction is

generally negligible compared to the convective heat transfer between fluid and wall. This also applies to gas convective heat transfer at microscale.

The longitudinal conduction in the solid wall becomes important to the heat transfer characteristics of gas flows at microscale, because the walls of the microchannels are generally “thick” if compared with the characteristic dimensions of the channels and they can host a strong conductive heat transfer, either wanted or unwanted. Such problem is generally referred to as conjugated problem in convective heat transfer [66], or simply, wall-fluid conjugated heat transfer. In some cases the heat transfer between the gas and the wall can be seriously modified by the presence of a longitudinal conduction within the solid channel walls. The wall longitudinal conduction can be characterized by a non-dimensional factor, the longitudinal conduction parameter, which is defined as the ratio of the axial conductive heat flux within the solid wall (q_w) and the convective heat flux of the fluid (q_f) [67]:

$$\lambda = \frac{q_w}{q_f} \quad (1.4)$$

This parameter is generally very small for conventional tubes. On the contrary, for microtubes Maranzana *et al.* [68] numerically demonstrated that the conjugate heat transfer can be responsible for an evident change in the axial gas temperature distribution and a remarkable reduction in the convective heat transfer coefficient when the value of longitudinal conduction parameter is larger than 1 %. In presence of strong longitudinal wall conduction, the axial distribution of gas bulk temperature may not be linear any more under H (uniform heat flux) boundary condition. This aspect will be investigated later in more detail in the present study. Furthermore, longitudinal wall conduction tends to have a negative impact on the thermal performance of micro-structured devices accommodating gaseous flows, such as micro heat exchangers and micro reactors, as put in evidence by the analyses of Bier *et al.* [32], Koyama [69] and Meschke *et al.* [33].

1.3.6 Effects of fluid temperature-dependent properties

The influence of fluid temperature-dependent properties (viscosity, density, thermal conductivity and thermal capacity) has been extensively explored for conventional-sized tubes, as reported by Shah and London [70]. Various methods have been proposed in order to take into account the effect of the variation of the fluid properties on friction factors and convective heat transfer

coefficients such as the property ratio method and the reference temperature method, [71]. According to Shah and London [70], for gas flows through conventional tubes the temperature-dependent properties influence the friction factor but have no effect on the Nusselt number.

However, with dimensions of flow geometry downscaled to a few hundred micrometers or smaller, the temperature gradient in the flows can be quite different from that in the conventional flows. As demonstrated by Mahulikar and Herwig [72], for microflows the low Reynolds numbers and permissible high heat fluxes increase the radial and axial gradients of fluid properties. Therefore, the variation of the fluid thermal properties should be considered in the evaluation of the convective heat transfer coefficients, especially for low Reynolds numbers and relatively large wall heat fluxes.

1.3.7 Viscous dissipation

Viscous dissipation, also known as viscous heating, is the energy dissipation caused by the work of shear forces between the flow layers of different velocity. Early in 1951, Brinkman [73] analytically derived the fluid temperature increase due to viscous heating in capillary. As the transverse velocity gradient in flow through microtubes is very high, viscous dissipation may play a critical role. The importance of viscous dissipation in a channel is characterized by the Brinkman number, which is the ratio of heat generated by viscous dissipation and the heat transferred by thermal conduction. The calculation of Brinkman number takes different forms depending on the thermal boundary conditions applied.

The influence of viscous dissipation in microtubes has been widely investigated experimentally by Tso and Mahulikar [74], Judy *et al.* [75], and Celata *et al.* [76], and numerically by Tunc and Bayazitoglu [77], Hadjiconstantinou [78], Koo and Kleinstreuer [79] and van Rij *et al.* [80]. A detailed analysis of the influence of viscous dissipation on temperature distribution can be found in the work by Morini [81] for microchannels with various cross sections. Most of the above research was focused on liquid flows. For high speed gas microflows, the strong viscous dissipation is accompanied by the compressibility effects and the effect of the flow work. The flow work term and the viscous dissipation term have an opposite sign (negative and positive respectively) in the contribution of fluid temperature change. This fact underlines that the viscous dissipation plays the role of a distributed heat source inside the fluid; on the contrary the fluid thermal expansion cools the flow like a distributed heat sink. Since the viscous

dissipation and the fluid thermal expansion are locally proportional to $(\partial v_z / \partial r)^2$ and to v_z respectively, the heat sink (flow work) prevails in the central region of the channel and the heat source (viscous heating) dominates in the wall region. The thermal energy generated mainly near the wall region due to the viscous dissipation is absorbed near the channel central region due to the flow work effect. To some extent it is difficult to individuate the influence of each effect, especially in experimental investigations where only average values are measured.

1.3.8 Thermal boundary conditions

The thermal boundary condition describes or defines the temperature or heat flux conditions on the interface between the fluid and the solid wall. A complete classification of various thermal boundary conditions for conventional tube flows had been summarized decades ago by Shah and London [70] and adapted by Morini [82] for application to microchannels.

Two basic thermal boundary conditions are widely applied by both numerical and experimental researchers: T (uniform wall temperature along the channel) boundary condition and H (uniform wall heat flux along the channel) boundary condition.

However, it is worth to note that experimentally speaking it is not easy to obtain a pure T or H boundary condition due to some effects, such as the conjugate effects at the walls heat losses close to the ends of the cross section, the presence of heat sinks on the channel wall and so on. As an example, by imposing an uniform heat flux on the external surface of a microtube with thick walls (where the conjugate effects are very strong) one obtains a non uniform axial distribution of the heat flux on the microtube inner surface; this means that in this case the H boundary condition cannot be considered completely appropriate in order to model the heat transfer along the microtube. Unfortunately, this point is rarely checked in the design of the experimental test rigs for the analysis of forced convection in microchannels.

1.3.9 Experimental accuracy

While the application of microfluidics offers several benefits for engineering and industrial purposes, the downsizing of the devices brings about challenges in the control of the accuracy of the geometric sizes of the devices and of the measured quantities as well. The accurate control of geometric size of a channel during the process of microfabrication can be problematic. As an example, it is possible to consider the commercial stainless steel microtubes; their inner diameter

may vary dramatically not only in axial direction, but also along circumferential direction on the same cross section and this inaccuracy can deeply influence the experimental results if not accounted for. Another aspect which can have a strong impact on the physical meaning of the experimental results is, of course, the level of accuracy linked to the measurement of the physical quantities. Especially for gaseous flows, the uncertainties of the measurement can be large if compared with conventional flows. As a result, it can be a real challenge to obtain experimentally highly accurate parameters such as the friction factor, Poiseuille number, heat transfer coefficient and Nusselt number, etc.

Therefore, some unexpected experimental results in terms of flow and heat transfer at microscale are only a direct consequence of the large errors which affect the measurements. This is especially evident in the early investigations, made in 80s-90s, where contradictions and deviations can be noticed by comparison between different studies, as reviewed by Morini [3]. In the last period, with the development of the microfabrication technologies and of the measurement techniques at micro scales, the differences in the results from different authors are decreasing.

2 Measurement Techniques at Microscale

In this chapter different measurement techniques proposed for the analysis of pressure drops and heat transfer for gas flows at microscale are analyzed and summarized, including some specific technologies developed recently for the analysis of gas microflows.

2.1 Measurement of microchannel geometry and surface roughness

Measurement of geometric sizes at macro scale is relatively direct and easy to perform with satisfying accuracy. At micro scale it may be challenging. Some methods have been used in order to estimate the inner diameter of microtubes.

Poiseuille [83] in 1840 used mercury to fill glass capillary tubes (down to 15 μm of diameter) of a fixed length in order to determine the average diameter by weighing the tube before and after filling. This technique is very simple and enables an accurate determination of the average flowing area of a microchannel along its whole length. One limitation is that, in order to obtain a good accuracy of the measurement for very small tubes, one has to use very long microtubes. An advantage of this method is that only a precision balance is required to estimate the flowing area.

One interesting development of this technique is based on the accumulation of a heavy liquid (water, mercury, etc) flowing through a microtube under a constant pressure drop, which generates a constant mass flow rate through the channel [61]. If one knows the length of the microchannel, the fluid density and the viscosity (which means that the fluid temperature is known), the cross sectional area of the microchannel can be determined by careful measurement of the liquid weight passing through the microtube over a certain time interval. This technique can be very useful to reduce the uncertainty on the determination of the inner diameter of a microtube as demonstrated by Asako *et al.* [61], who reported an uncertainty of the order of ± 0.2 μm on the inner diameter measurement for a microtube with a nominal diameter of 150 μm ($\pm 0.13\%$). For very small mass flow rates this measurement technique requires very long time to accumulate a certain amount of liquid. As underlined by Asako *et al.* [61], when water is used as test fluid, care must be taken on the estimation of the lost weight due to liquid evaporation during

the experimental tests, which strongly depends on the environmental condition. This aspect can be very critical when lower mass flow rates are generated in smaller microchannels.

Actually, one of the most common methods to measure microchannel dimensions is the scanning electron microscopy (SEM), by means of which it is possible to reconstruct the whole profile of the channel cross section with a high spatial resolution. For axially closed microchannels (e.g. commercial microtubes), this technique is applicable to the inlet and outlet sections only; no information can be obtained on the axial variation of the channel geometry and on the roughness distribution along the channel. This can be a limitation for the correct evaluation of the average channel roughness, because the inlet and the outlet sections may be non-representative of the dominant cross-section along the length due to the cutting which may deform the ends. In this case, only with destructive tests after the experimental investigation can one try to reconstruct the axial trend of the wall roughness and of the cross section by grinding the channel open. Multiple cuts along the channel may prove useless because the action can change the channel's cross section permanently. On the contrary, for open or optically accessible microchannels (like silicon rectangular microchannels bonded with a silicon/glass cover) this technique can be used to check the axial variation of the cross-section and of the roughness on the channel walls before they are closed.

With magnification and image processing, the dimensions of the channel cross section and the topology of the roughness can be determined with good accuracy. Since this technique is convenient and offers satisfying accuracy, it has been employed by many investigators (Tang *et al.* [52], Celata *et al.* [84], Zohar *et al.* [85], Morini *et al.* [86], [87]), as listed in Table 2-1. It is interesting to note that the Poiseuille [83] and Asako *et al.* [61] methods allow to measure directly the average flowing area along the whole length of the microchannel, which is a significant parameter for the evaluation of the friction factor as compared to the algebraic average of the inlet and outlet area obtained by SEM images of the microtube ends.

About the roughness, it is interesting to highlight that in non-circular microchannels made by chemical or ion etching on silicon wafers and sealed with a different material (glass, pyrex, silicon), the distribution of the wall roughness along the wetted perimeter of the channel can be non-uniform at all. However, in this case the measurement of the wall roughness is generally possible by using SEM or profilometers along the channel before sealing.

Another characteristic dimension of the microchannels which must be evaluated for the determination of the pressure drop and convective heat transfer coefficients is the channel length L . For long microchannels, the length L is in general larger than the inner diameter; typical values of the d_h/L ratio drop within the range 0.00001-0.01. In this case, the measurement of length is easier than the measurement of the inner diameter. On the contrary, when the behavior of rarefied gases through microchannel is studied in order to verify the predictions of the mathematical models for transitional and free molecular regimes, very short microchannels must be tested which are characterized by d_h/L ratios close to 1 (Marino [88]). In this case, the measurement of length can become problematic and, as general rule, the characterization of the microchannel by using the hydraulic diameter only is not sufficient.

Table 2-1: Experimental techniques on measurement of microchannel geometry.

Technique	Range	Typical accuracy	References
Accumulation of heavy liquid	150 μm	0.13%	Asako <i>et al.</i> [61]
SEM	0.5-40 μm	1.25-2.00%	Zohar <i>et al.</i> [85]
	133-730 μm	2.00%	Morini <i>et al.</i> [87]
	10-300 μm	0.30-2.98%	Tang <i>et al.</i> [52]
	30-254 μm	2.48-3.67%	Celata <i>et al.</i> [84]

2.2 Pressure measurement at microscale

At macroscale the pressure measurement is usually performed by pressure gauges or transducers [89]. For pressure measurement in microfluidics these traditional methods may still be used if the size of sensing element can be reduced accordingly.

In the experimental works devoted to pressure drop analysis through microchannels, pressure measurement has been carried out: (i) only at the inlet and at the outlet of the channel (Kandlikar *et al.* [53], Asako *et al.* [61], Morini *et al.* [87], Celata *et al.* [84], Tang *et al.* [52], Demsis *et al.* [45]); (ii) and/or along the channel in order to reconstruct the axial distribution (Zohar *et al.* [85], Hsieh *et al.* [90], Jiang and Wereley [11], Turner *et al.* [60], Kohl *et al.* [56]). In the latter case, the knowledge of the axial pressure trend enables to identify special effects, as those related to compressibility and rarefaction, which can play an important role in the determination of the pressure drop. However, in the latter case the microchannel must be specifically provided with

pressure taps along its length. If traditional pressure transducers are used, those are generally placed with care in the manifolds connected to the microchannel inlet and outlet. The presence of these manifolds introduces pressure losses at the inlet and the outlet of the channel.

In order to eliminate the effects of these minor losses the tube cutting method has been proposed by Du *et al.* [91] and other authors (Asako *et al.* [61] and Celata *et al.* [84]). This technique consists of repeating the same mass flow rate conditions of a long tube in a short one having the same inner diameter. In this case, since the effect of the minor losses is approximately identical for both tubes, one can eliminate this effect by subtracting the total pressure drop measured for both tubes. The short and the long tube can be selected from a set of identical tubes, or one can obtain the short one by cutting the long tube. In the latter case, great care must be paid in order to minimize the effect of the cut on the deformation of microchannel geometry. When the selection of the short tube and the long one is made among commercial tubes with the same nominal diameter, Asako *et al.* [61] demonstrated that the real inner diameter may actually vary markedly. In their work only 3 pairs of microtubes with a diameter difference in each pair less than $0.1\ \mu\text{m}$ were selected from precise inner diameter measurement of more than 30 tubes, which have a nominal diameter of $150\ \mu\text{m}$ but actually vary from $148\ \mu\text{m}$ to $154\ \mu\text{m}$. This kind of difference in diameter is stochastic and uncontrollable, which means that with the tube cutting method, the smaller the difference in tube pairs one desires, the larger number of the sample microtubes one has to provide.

However, this method can only be applied correctly when the pressure drop in the tube is linear, as for incompressible flows (liquids or gases under low pressure ratio p_{in}/p_{out}). When the pressure distribution along the channel is not linear, as in the case of compressible and/or rarefied flows, this method is not valid any more. In fact, in this case the effect of the minor losses cannot be eliminated completely, as demonstrated by Morini *et al.* [87]. This means that for gas flows the tube cutting method holds only for low Reynolds numbers, which corresponds to low Mach numbers at the outlet.

When the goal is to determine the axial distribution of the pressure along a microchannel, other techniques can be employed. One of the non-intrusive techniques is the Pressure-Sensitive Paints (PSP). The PSP are optical “molecular-sensors” which enable the measurement of the pressure over a surface. When excited by an outer light source of a certain wavelength, the luminescent molecules coated on the surface of the channel cover will emit luminescence of a

longer wavelength. By appropriate filtering, the emitted luminescence can be detected. The luminescent intensity is sensitive to oxygen molecules near the cover surface. For this reason this technique has been proposed for the analysis of gas flows. Specifically, an increase in the oxygen concentration causes a decrease in the intensity of the luminescence, which is known as oxygen quenching (Huang *et al.* [92] and Liu *et al.* [93]). After calibration, a relation between pressure and luminescent intensity can be established. This non-intrusive measurement technique can provide pressure data with high spatial resolution both along the channel and at the channel entrance and exit. On the other hand, as this technique is based on oxygen quenching, it cannot be applied to test of other pure gases, such as N₂, He, etc. Moreover, the pressure sensitive paint is coated on a transparent cover of microchannel to ensure the direct contact with oxygen and excitation of luminescent molecules from an external light source. It is evident that the main disadvantage of this technique is tied to the shape of the microchannel tested: closed circular or elliptical microtubes make it impossible to coat the pressure sensitive paint onto the inner wall, and passages which do not have a transparent side cannot benefit from this optical technique.

The technique of PSP technique has been applied to the measurement of the pressure distributions in high Knudsen number flows by Liu *et al.* [94] and Bell *et al.* [95]. However, the application of PSP to microdevices is very difficult, because conventional PSPs are very thick ($\cong 5\mu\text{m}$) compared to the dimension of micro-devices owing to the use of polymer binders. Moreover, they do not have sufficient spatial resolution for the pressure measurement of micro-flows due to the aggregation of luminescent molecules in polymer binders as indicated by Mori *et al.* [96].

More recently, for local measurement of pressure in highly rarefied flow Matsuda *et al.* [97] developed a pressure-sensitive molecular film method (PSMF) by using Langmuir-Blodgett technique. Before applying PSMF to micro gas flows, the authors tested the dependence of temperature on pressure sensitivity, which is the main source of the measurement error for this type of pressure sensor. Matsuda *et al.* [97] have demonstrated that their paint composed of Pt (II) Mesoporphyrin IX and arachidic acid showed a small dependence of temperature on the pressure sensitivity. In addition, the authors have demonstrated how, compared with classical PSP method, PSMF method can offer more uniform distribution of pressure sensitivity and an enhanced intensity of luminescence emission.

In order to measure the pressure locally along a microchannel, Kohl *et al.* [56] proposed an optical lever method. The microchannel presents a number of micrometric pressure taps connected to silicon membranes which deform when pressured. The deformation was measured by recording the change in deflection angle of a fixed incident laser targeting the membrane surface. The change in deflection angle was measured by a photodiode sensor which can be precisely moved and positioned. Based on the above principle, an integrated pressure sensor can be produced. The sensitivity of this integrated pressure sensor can be easily adjusted by changing spatial resolution (the distance between the membrane and the photodiode sensor). The uncertainty on the measured pressure ranged from 2.4% to 13.3%.

Since a very precise optical system to test quantitatively the slight slope of the pressurized membrane is involved, the optical lever method requires great labor to adjust the system. Also the cost of this optical system, which includes a laser, a lens and several adjustable stands for precise positioning, is relatively high. In addition, the range of the measurable pressure is limited by the mechanical strength of the membrane material and the channel must be customized for use with this technique.

Micro strain gauge membranes can be employed to sense the pressure induced to the tap from the microchannel. The deformation of the membrane results in the variation of the electrical resistance of the material making up the membrane. Therefore information on pressure can be transformed into an electrical signal, which is usually magnified for better accuracy via a Wheatstone bridge on the membrane, as in the work by Zohar *et al.* [85] and Baviere *et al.* [98]. After careful calibration, a correlation between pressure and voltage in the circuit can be obtained. This micro pressure sensor can be used to test local pressure along the microchannel and has very low temperature sensibility ($\pm 0.011\% \text{ } ^\circ\text{C}^{-1}$), as reported by Baviere *et al.* [98]. The coefficient which links pressure and electrical voltage varies from one membrane to another, and each strain gauge needs to be calibrated individually over a certain pressure range before measurement. Even in this case, the microchannel and the membranes must be specifically designed in order to use this technique.

For liquids through very small microchannel, Celata *et al.* [84] demonstrated that the measurement of the differential pressure along the channel can be linked to the fluid temperature rise between the inlet and the outlet of the channel due to the viscous dissipation. This effect is more evident for fluids having a low specific heat and a large viscosity (i.e. iso-propanol). For

gases, the temperature rise due to the viscous dissipation is compensated by the cooling due to the gas acceleration along the channel. For this reason, this effect is not useful for the determination of the differential pressure along a microchannel for gas flows.

The pressure measurement techniques for gas flows at microscale are summarized in Table 2-2. In this table are also listed the applicable pressure range of each technique and its typical accuracy.

Table 2-2: Experimental techniques on measurement of pressure at microscale.

Technique	Range	Typical accuracy	References
Pressure transducer	0-1.5 MPa	0.25%, 0.50%,	Tang <i>et al.</i> [52], Morini <i>et al.</i> [81], Asako <i>et al.</i> [61]
Tube cutting	-	Minor losses minimized	Asako <i>et al.</i> [61], Celata <i>et al.</i> [84]
Pressure-sensitive paints	From near vacuum to 2 atm.	1 mbar	Huang <i>et al.</i> [92], Liu <i>et al.</i> [93]
Pressure-sensitive molecular film	10^{-2} - 10^4 Pa	-	Matsuda <i>et al.</i> [97]
Micro-strain gauge membrane	0.1 MPa- 0.4MPa	1%	Zohar <i>et al.</i> [85], Baviere <i>et al.</i> [98]
Optical lever	0- 1.4 MPa	2.4% - 13.3%.	Kohl <i>et al.</i> [56]

2.3 Temperature measurement at microscale

Traditional temperature measurement technique can be considered well developed, including thermocouples, thermistors, infrared thermal imaging, temperature indicators, semiconductor junction sensors, optical fiber temperature sensors, etc. [89]. This section describes the applicability of the traditional techniques to micro scale and the emerging newly developed techniques for microscale temperature measurement.

The measurement of the bulk fluid temperature along a microchannel cannot be performed directly without large disturbance of the fluid flow. Suspended micro temperature sensors within microchannels have been proposed in the past, as reported in an interesting review paper by Nguyen [99]. The first prototypes of suspended sensors made by Petersen *et al.* [100] and Lammerink *et al.* [101] demonstrated that, the fully integration between this kind of temperature

sensors and the microchannels was possible but the influence of these sensors on the fluid flow was not negligible at all.

In order to avoid disturbance on the fluid flow, in many cases only the wall temperature along the channel is measured by means of integrated temperature sensors. The direct determination of the fluid bulk temperature can be obtained only at the inlet and at the outlet sections of the channel by using specific manifolds. Sometimes, the thermal inertia of the temperature sensors placed at the walls of the microchannel is larger or comparable to that of the channel walls. In this case, the presence of the sensors can modify the temperature distribution along the wall.

Nowadays microfabrication offers a large variety of devices to achieve local temperature measurements. In the following a summary of the most interesting temperature microsensors developed in the last years is given with the indication of the main advantages and drawbacks of each one.

The first kind of temperature microsensors which can be integrated in microchannels are the micro resistance temperature detectors (μ RTDs). This type of temperature sensors is widely used in microtechnology devices firstly because it is easy to make and has a linear response. The functioning principle of μ RTD is the same as the classical RTD in which the temperature-dependent electrical resistivity of a material is used in order to estimate the temperature. Vittoriosi *et al.* [102] integrated an array of thermopiles with μ RTDs along the length of a microchannel in order to measure the local temperature of gas flows. In this work it was foreseen to investigate the local thermal behavior of rarefied gas flows by taking advantage of the flexibility in integrating μ RTD arrays to microfluidic systems.

Thin film thermocouples (TFTCs) are active elements which use the Seebeck effect to measure the temperature of a two-metal junction. Microfabrication of TFTCs can be more or less complex depending on the existing material constraints for the specific microdevice needed. Zhang *et al.* [103] proposed a chromel thin film thermocouple embedded on a Ni substrate and demonstrated that their behavior is similar to the standard K-Type thermocouples. The Seebeck coefficient of this TFTCs was $40.6 \mu\text{V}\cdot\text{C}^{-1}$, in agreement with the standard value of this coefficient for the classical K-Type thermocouples. However the challenge in microfabrication of this type of micro-components is linked to the surface quality (especially roughness) of the thin film layers which can strongly influence the stability of these temperature microsensors [104].

With the aim to take advantage of the CMOS (Complementary metal–oxide–semiconductor) compatibility process (integration, low cost) an alternative for the temperature microsensors are the Semiconducting sensors (SCs) which use Polysilicon active elements. Bianchi *et al.* [105] present a state of art of integrated smart temperature SCs sensors like MOS transistors, bipolar transistors and diodes. The use of MOS transistors as temperature sensors needs the use of the transistors in weak inversion in order to obtain a linear relation between temperature and their electrical parameters even if some limitations due to leakage currents at high temperature can exist [106].

Even if, up to now, CMOS technologies are not so frequently used in microfluidics applications, SC sensors could have in the future a wide range of applications in this field due to their flexibility and to their high scale of integration that enables to expand the single sensor to a large array. For example, Han and Kim [107] have developed a 32×32 diodes (1024 diodes) array for measuring the temperature distribution on a small surface ($8\text{mm} \times 8\text{mm}$). Their calibration experiment evidenced the linear output temperature signal of this array in the range of $0\text{--}100^\circ\text{C}$ with an accuracy of $\pm 0.5^\circ\text{C}$.

In many technical works appeared in the open literature the temperature measurement of micro flows was obtained by using classical sensors like thermocouples or Platinum RTD. Bavière *et al.* [108] measured the temperature along a rectangular channel by arranging four thermocouples uniformly in line with the channel axis. The thermocouples were planted in blind holes $500\ \mu\text{m}$ from the channel wall surface. To predict the temperature of wall surface a correlation was presented based on calibrating experiment and the temperature measured by thermocouples a constant distance away from the wall surface. This approach provides an indirect way to obtain the local temperature of wall surface along the whole channel, which makes it possible to analyze the heat transfer characteristics locally in microchannels. However, the existence of these holes near the channel walls may alter the temperature distribution inside the wall because they cause heterogeneous thermal conductivity in the solid wall.

Demsis *et al.* [45] investigated the convective heat transfer coefficient in a counter flow, tube-in-tube heat exchanger. Two ports perpendicular to the axis of the microchannel were machined and connected to inlet section of the inner tube 35 mm before the heated section, one for the measurement of temperature and the other for pressure. The measurement of outlet pressure and temperature was proposed in the same way through two ports 35 mm after the heated section.

The risk of this technique is linked to the erroneous evaluation of the fluid outlet temperature. In fact, if the part of tube between the end of the heated section and the outlet side port is not thermally insulated with care, the fluid temperature decreases along this part and the temperature recorded at the exit side port can be very different to the fluid temperature at the end of the heating section. The side ports may disturb the main stream inside the tube. This kind of side ports can be readily applied to non-circular microchannels or circular microtubes with relatively large inner diameter. However, if the inner diameter is very small, i.e. below 0.3 mm, it becomes difficult to manufacture these side ports.

Besides thermocouples or diodes arrays which provide single or multipoint measurement of temperature, some specific optical techniques have been used for the measurement of a two dimensional temperature field at micrometric scales, such as liquid crystal thermography (Muwanga *et al.* [109]), infrared thermography (Mosyak *et al.* [110]), temperature sensitive paints (Liu and Sullivan [93]), microscale particle image velocimetry (microPIV, Hohreiter *et al.* [111]) and laser-induced fluorescence (LIF, Sakakibara and Adrian [112]). The most important constrain of these optical techniques is that these methods can be successfully applied only in the cases in which the external surface of the test section is not thermally insulated.

Table 2-3 summarizes the different techniques applied in micro flows in the recent years. It can be noticed that the accuracy and full range of measurement vary greatly from one method to another.

Table 2-3: Experimental techniques on temperature measurement in microflows.

Technique	Range	Typical accuracy	References
Thermopile with μ RTD	up to 77 °C	± 1.5 °C	Vittoriosi <i>et al.</i> [102]
Thermocouples (directly, at inlet and outlet)	0-400 °C	0.17%, 0.25%	Tang <i>et al.</i> [52], Morini <i>et al.</i> [87]
Thermocouples (indirectly, along microchannel)	0-400 °C	systematic error reduced by around 0.8 °C	Baviere <i>et al.</i> [108]
Thermocouples (directly, after inlet and before outlet)	0-400 °C	inlet and outlet effects minimized	Demsis <i>et al.</i> [45]
Infrared thermography	50-130 °C	sensitivity: 0.1 °C	Mosyak <i>et al.</i> [110]
Liquid crystal thermography	43-50 °C	1.1-1.5 °C	Muwanga <i>et al.</i> [109]
Temperature sensitive paint	10-100 °C	sensitivity: 1% °C ⁻¹	Liu <i>et al.</i> [93]
μ PIV	0-100 °C	± 3 °C	Hohreiter <i>et al.</i> [111]
LIF	depends on fluorescence type	± 1.4 °C	Sakakibara and Adrian [112]

2.4 Flow rate measurement at microscale

There exist many measurement methods for the determination of volumetric and/or mass flow rate based on various physical principles. Different flowmeters have been designed and applied in the industry uses, such as differential pressure flowmeters, variable area flowmeters, impeller flowmeters, electromagnetic flowmeters, ultrasonic flowmeters, thermal mass flow meters, etc., to name a few. The functioning principles of these conventional devices are well stated in a lot of text books [89].

Switching to microscale, the flow rate through a microchannel can be measured directly by means of appropriate instruments (mass or volumetric flow meters) or in an indirect way by checking the value assumed by other measurable quantities, like pressure, forces, weight, volume, temperature or a combination of these quantities. As a rule of thumb, it is possible to use a commercial mass or volumetric flow meter for gas flows only if the gas mass flow rate through

a microchannel is larger than 10^{-8} kg/s (0.1 Nml/min¹). On the contrary, for very low mass flow rates ($<10^{-8}$ kg/s) indirect methods can be considered more reliable in order to determine the flow rate with low values of uncertainty.

Commercial flow meters for gas flows can be divided in two groups: volumetric flow meters and mass flow meters. The volumetric flow meters give an indication of the flow rate not influenced by the fluid tested; the mass flow meters, on the contrary, can be used only with the fluid for which they have been calibrated.

The sensors of the commercial gas flow meters can be classified as non-thermal flow sensors and thermal flow sensors. The first kind of sensors is based on the mechanical working principle by means of which the flow rate can be measured indirectly by:

- 1) drag force (i.e. using silicon cantilevers);
- 2) pressure sensors (i.e. using capacitive and/or piezoresistive pressure sensors);
- 3) using the Coriolis principle.

The main disadvantage of the non-thermal flow sensors is linked to the dependence of the force, pressure difference and Coriolis force on the density of the working fluid. Since the gas density depends on the gas temperature, a temperature compensation is a compelling need for this kind of sensors.

As indicated by Nguyen [99], the thermal flow sensors employed in the commercial flow meters can be classified as follows:

- 1) thermal mass flow sensors which measure the effect of the flowing fluid on a hot body (micro hot-wire and micro hot-film sensors);
- 2) thermal mass flow sensors which measure the asymmetry of temperature profile around a micro heater which is modulated by the fluid flow (calorimetric sensors);
- 3) thermal mass flow sensors which measure the delay of a heat pulse over a known distance (time-of-flight sensors).

The most popular sensors among the commercial flow meters are the calorimetric sensors: this kind of flow meter is able to predict the mass flow rate through the sensor by means of the following balance equation:

¹ Nml/min refers to 1 normal liter (at a standard pressure of 101.325 kPa and temperature of 0 °C) of gas flow per minute.

$$\dot{m} = \frac{Q_{th}}{c_p (T_{b,out} - T_{b,in})} \quad (2.1)$$

which puts in evidence how the gas mass flow rate can be determined by means of two local measures of bulk temperature ($T_{b,out}$ and $T_{b,in}$) and the knowledge of the heat power (Q_{th}) transferred to the gas by the heater.

By using microfabrication, this kind of thermal mass flow sensor can be directly integrated in a microchannel. Schöler *et al.* [113] have shown as two classic Pt RTDs and a microheater made on a glass substrate can be directly integrated on a SU-8 epoxy resist microchannel ($50\mu\text{m} \times 15\mu\text{m} \times 8000\mu\text{m}$). As demonstrated by Kim and Kim [114] by using a capacitive mass flow sensor using two K-Type TFTC ($150\mu\text{m} \times 150\mu\text{m}$) associated to a PDMS microchannel ($800\mu\text{m} \times 800\mu\text{m} \times 4\text{cm}$), the accuracy of this kind of mass flow meters can be strongly influenced by the position and the thermal insulation of the micro-sensor.

When the gas mass flow rates through microchannels are very low ($<10^{-8}$ kg/s), commercial flow meters are not suitable anymore because of high level of uncertainty. In addition, accurate measurements of mass flow rate in microchannels are challenging for gas flows, which have a density very sensitive to the operating pressure and temperature fluctuations.

For very low flow rates, the determination of the gas flow rate can be done by using the general expression of the mass flow rate as the change of mass over time:

$$\dot{m} = \frac{dm}{dt} \quad (2.2)$$

If the gas can be considered as an ideal gas, the mass flow rate can be always expressed as follows:

$$\dot{m} = \frac{p}{RT} \frac{dV}{dt} + \frac{V}{RT} \frac{dp}{dt} - \frac{pV}{RT^2} \frac{dT}{dt} \quad (2.3)$$

It can be noted from Eq. (2.3) that if two of the three variables (volume, pressure and temperature of the gas) are kept constant while the third one is monitored during the experiment, the mass flow rate of the gas can be determined. This provides the basic insights into mass flow rate measurement of gas. In practice, it is impossible to keep two of the three variables strictly unchanged, so great efforts are made to minimize the fluctuation of the nominally unchanged variables to determine the mass flow rate as accurately as possible. These fluctuations are usually the main source of errors for low mass flow rate measurement of gas microflows.

Based on Eq. (2.3) several techniques have been proposed for the determination of the mass flow rate lower than 10^{-8} kg/s. In the droplet tracking technique the gas volumetric flow rate is measured by introducing the outflow gas into a pipette, in which the gas pushes a droplet to move forward. By recording the position of the droplet versus time under the assumption of constant pressure and temperature, the velocity of the droplet can be determined and knowing the diameter of the pipette the mass flow rate of gas can be calculated. In this case, Eq. (2.3) can be rewritten as:

$$\dot{m} = \frac{p}{RT} \frac{dV}{dt} = \frac{p}{RT} \frac{\pi d_{pip}^2}{4} \frac{d\Delta l}{dt} \quad (2.4)$$

where d_{pip} is the diameter of the pipette and Δl is the distance the droplet moves during a certain time interval. This technique does not require expensive measurement meters and can be performed by using multiple microchannels. The lowest mass flow rate that can be measured with this technique depends on the specific setups and on the maximum number of microchannels tested in parallel. As rule of thumb, the lowest value of the mass flow rate that can be measured by using the droplet tracking technique is of the order of 10^{-10} kg/s. However, it is possible to measure lower mass flow rate if hundreds of identical microchannels are used in parallel in test section. This is the case of Shih *et al.* [115] who measured the mass flow rate of helium at the order of 10^{-12} kg/s, which is the same order measured by Ewart *et al.* [42] with nitrogen. Colin *et al.* [116] obtained the mass flow rate down to the order of 10^{-13} kg/s for helium, while Celata *et al.* [84] reached flow rates of the order of 10^{-8} kg/s for the same type of gas with this technique. However, it is technically difficult to maintain a constant moving speed for the droplet using this method. Another problem is the accurate measurement of the pipette inner diameter, which weighs most in determining the mass flow rate, as shown in Eq. (2.4).

If gas flow is accumulated in a tank for a certain time interval, there will be a pressure rise in the tank during the flow. Given that the pressure in the tank is under reasonable control and not very high, the expansion of the tank or the increase in its volume can be safely neglected. In this case Eq. (2.4) becomes:

$$\dot{m} = \frac{V}{RT} \frac{dp}{dt} - \frac{pV}{RT^2} \frac{dT}{dt} \quad (2.5)$$

If the second term in the right-hand side of Eq. (19) is very small compared to the first one (i.e. <1%) it can also be dropped away. In this way the mass flow rate can be determined by

careful measurement and recording of pressure rise versus time inside the tank. This is usually referred to as constant volume technique. Based on this principle, Ewart *et al.* [43] built an experimental set-up in which the outlet of the microchannel is connected to a large tank. The lowest mass flow rate measured with this technique was reported of the order of 10^{-13} kg/s [43]. The volume of the tank should be carefully chosen so that the pressure change is both detectable by pressure sensor and at the same time small enough to remain a nearly constant mass flow rate. Great care should also be paid to the temperature fluctuation of the gas as it is compressed into the tank, so that the temperature change can be neglected, which greatly simplifies the calculation of mass flow rate.

Arkilic *et al.* [13] used a two-tank, modified constant-volume accumulation technique to measure the mass flow rate of gas through microchannel. In this case, Eq. (2.5) is not sufficient for calculating the mass flow rate, as both upstream and downstream pressures vary during the experiment. In fact during the test one tank is used to accumulate the gas flowing out of the microchannel and the other one remains in steady state which provides a pressure reference. Pressure difference between the two tanks is measured instead of the measurement of absolute pressure for the determination of mass flow rate, as given by:

$$\dot{m} = \frac{V}{RT} \frac{dp}{dt} - \frac{\Delta p V}{RT^2} \frac{dT}{dt} \quad (2.6)$$

where Δp is the pressure difference between the reference tank and the flow tank. As the two tanks are well connected before the flow starts, this quantity is 0 at the beginning. Due to the relatively small mass flow rate of gas flow through microchannels, when the flow finishes the pressure difference can be very small, quite several orders of magnitude smaller than the absolute pressure as in Eq. (2.6). Therefore, the sensitivity of mass flow rate to the tank temperature fluctuation is reduced by several orders, and the tank for gas accumulation can be reasonably regarded as isothermal during the experiment. In addition, this technique requires that the two tanks have identical temperature and undergo the same thermal fluctuations, which can be realized by a good design, arrangement and thermal insulation of the tanks. For this reason, in the work by Pitakarnnop *et al.* [44] the whole setup was thermally regulated with Peltier modules to maintain a constant temperature.

This method provided data for mass flow rates of an order of 10^{-11} kg/s and a sensitivity as low as 7×10^{-15} kg/s (Arkilic *et al.* [117]) was reported; Pitakarnnop *et al.* [44] developed a new

setup for gas microflows in which the constant volume method for mass flow rate measurement was implied to both the upstream and downstream flow. This offers a double measurement and provides possibility to compare the measured results for the same flow. Their measured values of mass flow rates were as small as to 7.1×10^{-14} kg/s.

To achieve a constant mass flow rate with this technique, the pressure difference between the two tanks should increase linearly with time during the experiment. As the outlet of the microchannel is directly connected to the tank, the outlet pressure changes gradually and cannot be positively controlled. As a result, the inlet pressure should be very carefully adjusted with the passage of time to achieve a linear increase of pressure difference between the two tanks. This is very difficult to achieve in practice. Thus, the process of gas flow in the microchannel becomes time-dependent with this method.

In order to complete this review, it is possible to highlight that the most sensitive technique for the gas detection and for the measurement of very low mass flow rates in microchannels is based on mass spectrometry and it has been presented by Tison in 1993 [118]. Tison developed a specific setup to measure gaseous capillary leak rates ranging from 10^{-6} mol/s down to 10^{-14} mol/s. A series of complex operation steps are involved in the test so that the final determination of flow rate is dependent on the ratio of measured quantities instead of their absolute values, which reduces the sensitivity of possible fluctuations (temperature, pressure and so on) and expands the measurement to very low range of mass flow rate. However, due to the complexity of this method, the application of this method to technical measurements in microchannels still remains challenging. It could be quite promising for the measurement of rarefied gases through microchannels where in transitional and free molecular flow regimes the mass flow rates can be extremely low.

Besides the above techniques, it is also possible to determine the mass flow rate by integrating the velocity profile coupled with fluid density over the cross section. The velocity profile can be obtained by applying μ PIV or molecular tagging velocimetry (MTV) to the microchannel.

To summarize the main points highlighted in this section for each technique, Table 2-4 shows the most important methods proposed for gas flow rate measurement at microscale. For each technique, the typical ranges for which they have been applied are shown together with the typical values of uncertainty. The data in Table 2-4 may be employed during the design of a new

test rig in order to select the best measurement techniques with the aim to minimize the overall uncertainty on the derived quantities, as will be discussed in detail in the next chapter.

Table 2-4: Experimental techniques on measurement of gas mass flow rate at microscale.

Technique	Range	Typical accuracy	References
Commercial Flow meters	50000-0.05 Nml/min	0.6% , 1%, 2%	Morini <i>et al.</i> [87], Celata <i>et al.</i> [84], Tang <i>et al.</i> [52]
Droplet tracking	$\sim 10^{-8}$ kg/s $\sim 10^{-10} - 10^{-13}$ kg/s (hundreds of parallel microchannels)	9.64% (calculated) 3-4 %	Celata <i>et al.</i> [84] Shih <i>et al.</i> [115], Ewart <i>et al.</i> [42], Colin <i>et al.</i> [116]
Single tank constant volume	$\sim 10^{-13}$ kg/s	4.5%	Ewart <i>et al.</i> [43], Pitakarnnop <i>et al.</i> [44]
Two-tank constant volume	$\sim 10^{-11}$ kg/s	-	Arkilic <i>et al.</i> [13], Arkilic <i>et al.</i> [117]
Mass spectrometry method	$4 \times 10^{-17} - 4 \times 10^{-8}$ kg/s	1-8%	Tison [118]

3 Experimental Uncertainties at Microscale

The uncertainties of measurement cannot be avoided in the experimental determination of micro flow friction factor and heat transfer coefficient, no matter what measurement technique has been applied. Therefore, in this chapter the experimental uncertainties will be discussed deeply in order to know how the accuracy of friction factor and Nusselt number are related to each specific measurement in the experimental tests.

3.1 Analysis of experimental uncertainties

Let us assume that a physical parameter is a function of a series of measurable variables; it can be expressed as $f = f(x_1, x_2, \dots, x_n)$, in which the single measurable variable x_i is characterized by a known absolute measurement uncertainty δx_i which corresponds to the relative uncertainty $\frac{\delta x_i}{x_i}$. Based on the theory of uncertainty propagation [119], the absolute uncertainty of this physical parameter can be calculated by

$$\delta f = \sqrt{\sum_{i=1}^n \left(\frac{\partial f}{\partial x_i} \right)^2 (\delta x_i)^2 + 2 \sum_{i=1}^n \sum_{j=i+1}^n \frac{\partial f}{\partial x_i} \frac{\partial f}{\partial x_j} \text{cov}(x_i, x_j)} \quad (3.1)$$

where $\text{cov}(x_i, x_j)$ is the covariance between variables x_i and x_j . If x_i and x_j are independent, their covariance is 0; if the two variables are correlated, their covariance has a non-zero value. Fortunately, in experiment the singly measured variables can be considered as independent, which greatly reduces the complexity of calculation. Even with such simplification, it is also important to notice that the measurable variables might be correlated by the instrumentation used in the experimental setup (i.e. the use of the same pressure sensor or temperature sensor and so on) and/or by the room conditions (via data acquisition system). However, this kind of correlation is relatively weak (i.e. Agilent 34420A digital multimeter for data acquisition has a slight sensitivity of the magnitude of 0.0008% with regard to room temperature) and can be either negative or positive, which tends to balance out the total contribution to the overall

uncertainty of the function f . For these reasons, in the following discussion the measurable variables will be considered independent to each other. Consequently, Eq. (3.1) can be simply expressed as the following for the total relative uncertainty of f :

$$\frac{\delta f}{f} = \sqrt{\left(\frac{\partial f}{\partial x_1} \frac{x_1}{f}\right)^2 \left(\frac{\delta x_1}{x_1}\right)^2 + \left(\frac{\partial f}{\partial x_2} \frac{x_2}{f}\right)^2 \left(\frac{\delta x_2}{x_2}\right)^2 + \dots + \left(\frac{\partial f}{\partial x_n} \frac{x_n}{f}\right)^2 \left(\frac{\delta x_n}{x_n}\right)^2} \quad (3.2)$$

3.2 Experimental uncertainties on friction factor of micro gas flows

For isothermal and compressible flow along a circular tube, the friction factor can be calculated as [120]:

$$f = \frac{d_h}{L} \left[\frac{(p_{out} + \Delta p)^2 - p_{out}^2}{RT_b \left(\frac{4\dot{m}}{\pi d_h^2}\right)^2} - 2 \ln \frac{p_{out} + \Delta p}{p_{out}} \right] \quad (3.3)$$

where Δp is the pressure drop along the tube, p_{out} the pressure at the tube outlet, \dot{m} is mass flow rate, d_h is the tube hydraulic diameter, L is the tube length, T_b the fluid bulk temperature, and R the specific gas constant.

In Eq. (3.3) it is evident that the value of friction factor is directly linked to six measurable quantities:

$$f = f(d_h, L, \dot{m}, T_b, \Delta p, p_{out}) \quad (3.4)$$

Following the principle of uncertainty propagation in Eq. (3.2), one can obtain the expression of the relative uncertainty of friction factor as:

$$\frac{\delta f}{f} = \sqrt{k_1^2 \left(\frac{\delta D_h}{D_h}\right)^2 + k_2^2 \left(\frac{\delta L}{L}\right)^2 + k_3^2 \left(\frac{\delta T}{T}\right)^2 + k_4^2 \left(\frac{\delta \Delta p}{p}\right)^2 + k_5^2 \left(\frac{\delta p_{out}}{p_{out}}\right)^2 + k_6^2 \left(\frac{\delta \dot{m}}{\dot{m}}\right)^2} \quad (3.5)$$

where the sensitivity coefficients, k_1, k_2, \dots, k_6 , which show how the uncertainty of each measurable parameter contributes quantitatively to the uncertainty of friction factor, are listed in Table 3-1 for both incompressible and compressible flows.

The analytical expression of these coefficients can be mathematically calculated as:

$$k_i = \left| \frac{\partial f}{\partial x_i} \frac{x_i}{f} \right| \quad (3.6)$$

The detailed deduction of these expressions is not given here but can be found in Appendix A for both incompressible and compressible flows. The magnitudes of these sensitivity coefficients depend on the flow conditions applied in the experimental test, for example, incompressible flow or compressible flow.

It should be noted that different measurement strategies can also result in different expressions for the calculation of these coefficients. In Table 3-1 the calculation of the coefficients is compared for two basic measurement strategies, namely Strategy #1 (the use of one differential pressure sensor between microchannel inlet and outlet and one absolute pressure sensor at the outlet) and Strategy #2 (the use of two absolute pressure sensors at the inlet and at the outlet of the microchannel), which are schematically shown in Figure 3-1. Of course, other combinations of pressure sensors are possible.

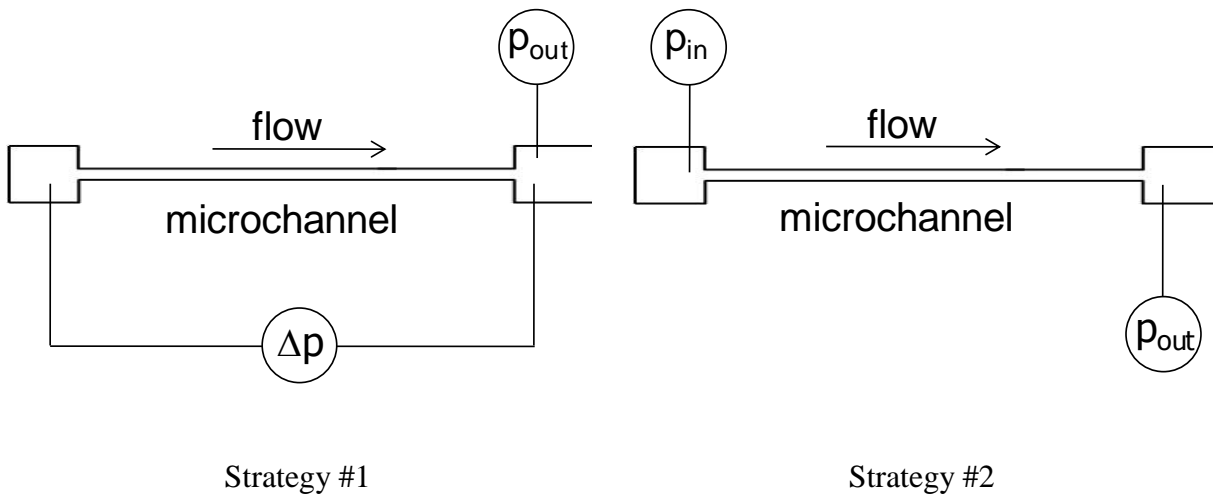


Figure 3-1: Two different strategies for pressure measurement in determination of friction factor.

Eq. (3.5) highlights that the relative uncertainty of the friction factor is more sensitive to the measured variables which are associated to larger sensitivity coefficients and the largest one dominates the total relative uncertainty. Specifically, the accuracy of microchannel diameter measurement has the greatest weight in the determination of the friction factor uncertainty, followed by mass flow rate and pressure (for compressible flows) measurement, while the accuracy of length and temperature measurement is comparatively less important. This analysis

suggests that for accurate calculations of the friction factor, the measurement of the channel diameter is of crucial importance: even a small error will induce a large error in the calculated quantity.

When compressibility effects become important and for very low mass flow rates ($<10^{-8}$ kg/s), uncertainty in flow rate measurements becomes large; as explained in the previous section, in these cases the flow rate is not directly measured but it is calculated with Eq. (2.3) as a function of temperature, pressure and volume of the system: this increases the influence of such quantities measurement on the total uncertainty of the friction factor.

It can also be noted from Table 3-1 that, for incompressible flows and compressible flows with low pressure drop, the uncertainty of friction factor can be directly calculated from the accuracy of each measurement, without knowing the absolute values of the measured parameters. On the contrary, for compressible flows with comparatively large pressure drop (which is usually the case in microchannels), the friction factor uncertainty depends on the absolute values of the following experimental parameters:

$$\alpha = \frac{\Delta p}{p_{out}}, \quad \beta = \frac{2D_h}{fL} \quad (3.7)$$

in which Δp is the pressure drop along the whole microchannel, p_{out} is the outlet pressure, f is the friction factor and L is the total length of the microchannel.

Table 3-1: Sensitivity coefficients of operating parameters in the calculation of friction factor.

Sensitivity coefficients	Incompressible flow	Compressible flow (negligible α^1)	Compressible flow (non-negligible α^1) Strategy #1	Compressible flow (non-negligible α^1) Strategy #2
k_1 (diameter)	5	5	$5 + 4\beta \ln(1 + \alpha)$	$5 + 4\beta \ln(1 + \alpha)$
k_2 (length)	1	1	1	1
k_3 (temperature)	0	1	$1 + \beta \ln(1 + \alpha)$	$1 + \beta \ln(1 + \alpha)$
k_4 (pressure drop or inlet pressure)	1	1	$1 + \frac{\alpha}{2 + \alpha} - \beta \frac{\alpha}{1 + \alpha} + \beta \left(1 + \frac{\alpha}{2 + \alpha} \right) \ln(1 + \alpha)$	$2 + \frac{2}{\alpha^2 + 2\alpha} - \beta + 2\beta \left(1 + \frac{1}{\alpha^2 + 2\alpha} \right) \ln(1 + \alpha)$ (for p_{in} instead of Δp)
k_5 (outlet pressure)	0	1	$\frac{1}{1 + \frac{\alpha}{2}} + \beta \left[\frac{2}{2 + \alpha} \ln(1 + \alpha) + \frac{\alpha}{1 + \alpha} \right]$	$\frac{2}{\alpha^2 + 2\alpha} [1 + \beta \ln(1 + \alpha)] - \beta$
k_6 (mass flow rate)	2	2	$2 + 2\beta \ln(1 + \alpha)$	$2 + 2\beta \ln(1 + \alpha)$

¹ $\alpha = \Delta p / p_{out} = (p_{in} - p_{out}) / p_{out}$; $\beta = 2D_h / (fL)$

In order to complete the calculation of uncertainty on friction factor, the uncertainties of practical measurements on channel dimension, pressure, temperature and mass flow rate are required. In Table 3-2 the declared uncertainties on measurements reported by Ferguson *et al.* [121] who analyzed critically a series of experiments with liquid microflows are summarized, in order to have a reference for the comparison with the measurements for gas microflows. It is interesting to note that the typical values of the friction factor uncertainties vary from 5.4% to 11.8% and, in many papers, the most important uncertainty, related to the inner diameter, was not declared. In these works the flow was adiabatic and in many cases the temperature of the test flow was not checked.

Table 3-2: Relative uncertainties of measured quantities in liquid microflows (from Ferguson *et al.* [121])

Authors	Geometry			Pressure (%)	Mass flow rate (%)	Re (%)	Friction factor (%)
	<i>d</i> (%) (circular)	<i>h, w</i> (%) (rectangular)	<i>L</i> (%)				
Li <i>et al.</i> [122]	2	-	0.1	1.5	2	-	-
Liu and Garimella [93]	-	-	3.9	0.25	1.01	10.5	11.8
Wu and Cheng [123]	1.83	-	0.37	0.68	1.69	-	-
Mala and Li [124]	2	-	0.2	2	2	3	9.2
Judy <i>et al.</i> [75]	2.5	2.5-5	-	0.25	-	-	-
Chen <i>et al.</i> [125]	-	-	-	2	5	10.5	5.4
Celata <i>et al.</i> [84]	-	-	-	-	7	5	7
Peng <i>et al.</i> [126, 127]	-	-	-	1.5	2.5	8	10

Table 3-3 reports a collection of declared uncertainties for gaseous microflows measured using the techniques summarized in Chapter 2. By comparing the data of Table 3-2 with those of Table 3-3, it can be noted that for gas flows the uncertainty on the friction factor can be larger than 12%. This is mainly due to smaller dimensions of the tested microchannels (less than 150 μm generally) and larger uncertainties on mass flow rate measurement. In fact, very low flow

rates and small values of pressure are applied in these experiments in order to obtain large values of Knudsen number (large rarefaction effects).

By observing the total uncertainties of the friction factor quoted in Table 3-3, it should be noted that in many experimental work the data for the uncertainty analysis are not complete. As a result, it is impossible to know the real value of the uncertainty linked to the experimental friction factors.

Table 3-3: Relative uncertainties of measured quantities in gaseous microflows.

Authors	Geometry			Pressure (%)	Temperature (%)	Mass flow rate (%)	Re (%)	Friction factor (%)
	<i>d</i> (%) (circular)	<i>h, w</i> (%) (rectangular)	<i>L</i> (%)					
Ewart <i>et al.</i> [42]	1.39	-	-	1.5	0.02	4.5 (const. volume); 4.2 (drop tracking)	-	-
Celata <i>et al.</i> [84]	2.48-3.67	-	-	-	-	-	-	19 (flow meter); 27 (pipette)
Asako <i>et al.</i> [61]	0.13	-	0.003	0.42	-	0.98	-	12.5
Tang <i>et al.</i> [52]	0.3-2.98	-	0.02-0.07	0.25	0.17	2	4.5	5.9
Morini <i>et al.</i> [87]	2	-	0.3	0.5	0.25	0.5-0.6	3	10
Ewart <i>et al.</i> [43]	-	<i>h</i> : 2.13; <i>w</i> : 0.20	1.06	0.5	0.02	4.5	-	-
Zohar <i>et al.</i> [85]	-	<i>h</i> : 2; <i>w</i> : 1.25	-	< 1	< 1	< 8.5	-	-
Hsieh <i>et al.</i> [90]	-	<i>h</i> : 1; <i>w</i> : 1	-	0.7	0.04	4.0	1.46	1.82
Maurer <i>et al.</i> [128]	-	<i>h</i> : 2; <i>w</i> : 1	1	2	-	2	-	-
Turner <i>et al.</i> [129]	-	-	-	-	-	-	4.9	4.8
Colin <i>et al.</i> [116]	-	<i>h</i> : 2.23-18; <i>w</i> : 0.58-1.4	0.2	-	-	-	-	-
Pitakarnnop <i>et al.</i> [44]	-	<i>h</i> : 5.3; <i>w</i> : 1.4	0.2	0.5	0.2	4 (const. volume); 3.1 (drop tracking)	-	-
Araki <i>et al.</i> [130]	triangle and trapezoid <i>d_h</i> : 3.23	-	0.2	5.13	-	2.2	-	10.9

The typical values of temperature, pressure and mass flow rate for these works are listed in Table 3-4, together with the range of Reynolds numbers investigated. It is interesting to highlight that in the experimental works with Reynolds numbers larger than 10, the compressibility effects can be evidenced and analyzed. On the contrary, in order to study the rarefaction effects, the Reynolds number should generally be smaller than 10 (very low mass flow rate). In fact, in order to study the gas rarefaction effects, small channels (usually less than 20 μm in hydraulic diameter) and low pressure (less than 0.1 bar) should be applied. Under these conditions the values of the mass flow rate are very low (10^{-14} – 10^{-6} kg/s) and specific techniques like the droplet tracking method or the gas accumulation have to be employed to calculate the Reynolds number accurately.

Table 3-4: Typical values of experimental parameters for gaseous microflows.

Authors	Geometry and size (μm)	Length (mm)	Pressure (kPa)		T (K)	Mass flow rate (kg/s)	Re
			Inlet	outlet			
Ewart <i>et al.</i> [42]	circular d : 25.2	53	1.22-12.11	0.25-2.47	297	$0.02-2 \times 10^{-10}$	0.0018-2.5
Celata <i>et al.</i> [84]	circular d : 30-254	50-91	up to 1,000	100	-	-	0.8-500
Asako <i>et al.</i> [61]	circular d : 150	30-50	300	190	300	4×10^{-6}	1508-2188
Morini <i>et al.</i> [87]	circular d : 133-730	200-1000	-	-	-	-	100-5000
Tang <i>et al.</i> [52]	circular and rectangular d_h : 10-300	27.5-100	-	100	295	-	3-6200
Ewart <i>et al.</i> [43]	rectangular h : 9.38; w : 492	9.4	0.060-115.47	0.012-32.65	-	0.0049 -22.5×10^{-10}	-
Zohar <i>et al.</i> [85]	rectangular h : 0.5 and 1; w : 40	4	up to 400	100	-	$1.5-6 \times 10^{-9}$	-
Hsieh <i>et al.</i> [90]	rectangular h : 50; w : 200	24	2.7-64.63	0.68-13.19	300	0.88×10^{-8} - 40.9×10^{-8}	2.6-89.4
Maure <i>et al.</i> [128]	rectangular h : 1.14; w : 200	10	140-500	48-100	296	6×10^{-12} - 5×10^{-10}	0.001-0.07
Colin <i>et al.</i> [116]	rectangular h : 0.5-4.5; w : 20, 50	5	-	65-200	294	4×10^{-13} - 2×10^{-9}	-
Pitakarnnop <i>et al.</i> [44]	rectangular h : 1.88; w : 21.2	5	up to 300	2-50	299	8×10^{-14} - 2×10^{-11}	-
Araki <i>et al.</i> [130]	triangular and trapezoidal d_h : 3.92-10.3	15 and 25	-	100	295	0.2×10^{-10} - 1.0×10^{-10}	0.042-4.19

It is not explicit in Table 3-1 how the accuracy of each measurement influences the accuracy of friction factor at various mass flow rates or Reynolds numbers. In order to give some numerical example, the influence of sensitivity coefficients of the six measurable quantities (inner diameter, microtube length, temperature, total pressure drop, outlet pressure and mass flow rate) on the uncertainty of friction factor is investigated quantitatively for gas flow through

a 100 μm microtube with a length of 30 mm. The flow is assumed to be compressible, isothermal and in the laminar regime, and the gas is discharged to the atmosphere. The typical values of uncertainty for each measurement are selected in reference of the data quoted in Table 3-4; we have assumed an uncertainty of 2% for inner diameter measurement, 0.3% for length measurement, 0.25% for temperature measurement, 0.5% for pressure measurement and 2% for mass flow rate measurement.

Figure 3-2 shows the influence of each measurement on the uncertainty of friction factor. It can be seen that the accuracy of friction factor is most sensitive to the measurement of inner diameter, which results in an uncertainty of more than 10% in friction factor. This contribution grows gradually with the increase of Reynolds number. The importance of mass flow rate measurement takes the second place and a 2% inaccuracy results in an error of 4-5.5% in friction factor. Compared with diameter and mass flow rate, the influence of measurement for other quantities (pressure drop, outlet pressure, length and temperature) on the accuracy of friction factor is small.

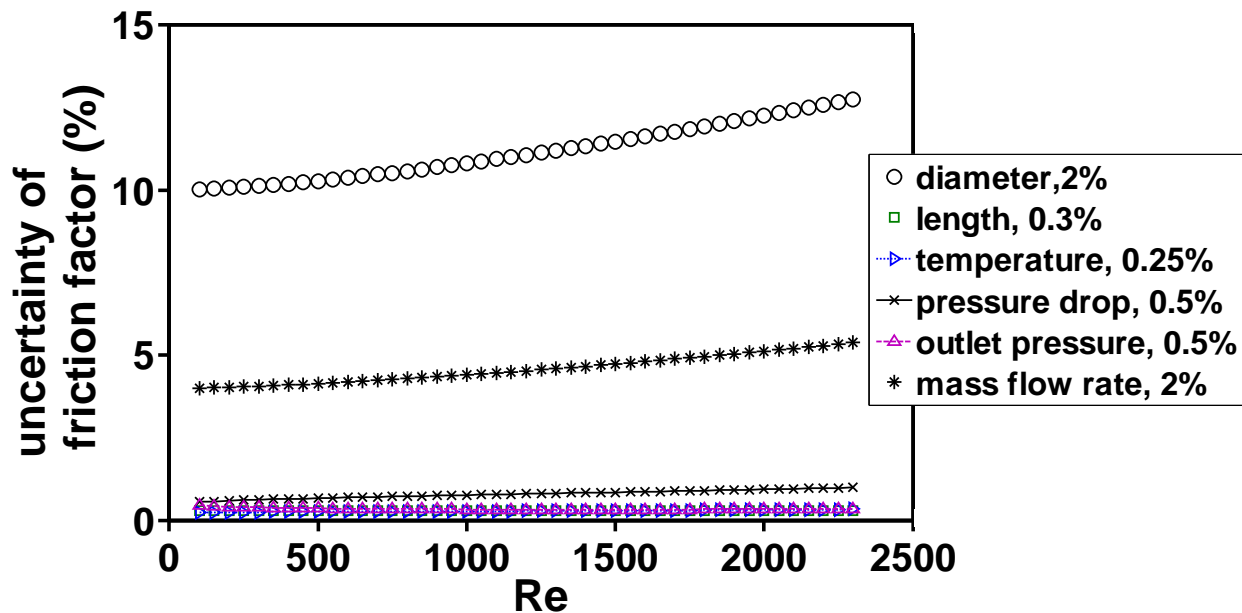


Figure 3-2: Influence of each measured parameter with typical uncertainty for a microtube having an inner diameter of 100 μm and a length of 30 mm.

In practice, the uncertainty propagation is more complicated than the previous simulation in which constant values of relative uncertainty for each measured quantity are assumed. During a specific test round for isothermal flow, the mass flow rate and pressure drop change as the

imposed Reynolds number increases or decreases. This causes non-constant relative uncertainty in the measurement of these two quantities, because the measurement is less accurate if the measured quantity is far from the full scale (FS) of the meter. The rest four quantities, namely, inner diameter, microtube length, temperature and outlet pressure, remain almost constant (here it is assumed that the gas is discharged directly into the atmosphere).

To further explore this effect, it is assumed that the absolute uncertainties in the measurement of pressure drop and mass flow rate are constantly 0.5% of the full scales (FS). In addition, we assume that the relative pressure and mass flow rate reach the full scales at a Reynolds number of 2300.

Figure 3-3 shows the single contribution of the uncertainty of these two parameters to the uncertainty of friction factor. The total uncertainty of friction factor is calculated from the changing uncertainties of pressure drop and mass flow rate, as well as the constant uncertainties of inner diameter (2%), length (0.3%), outlet pressure (0.5%) and temperature (0.25%). It can be seen that for low Reynolds number (< 500), or more generally when the measured values are far from the full scale, the uncertainty of friction factor becomes very large. Sometimes this leads to unreasonable results in microfluidics experiments.

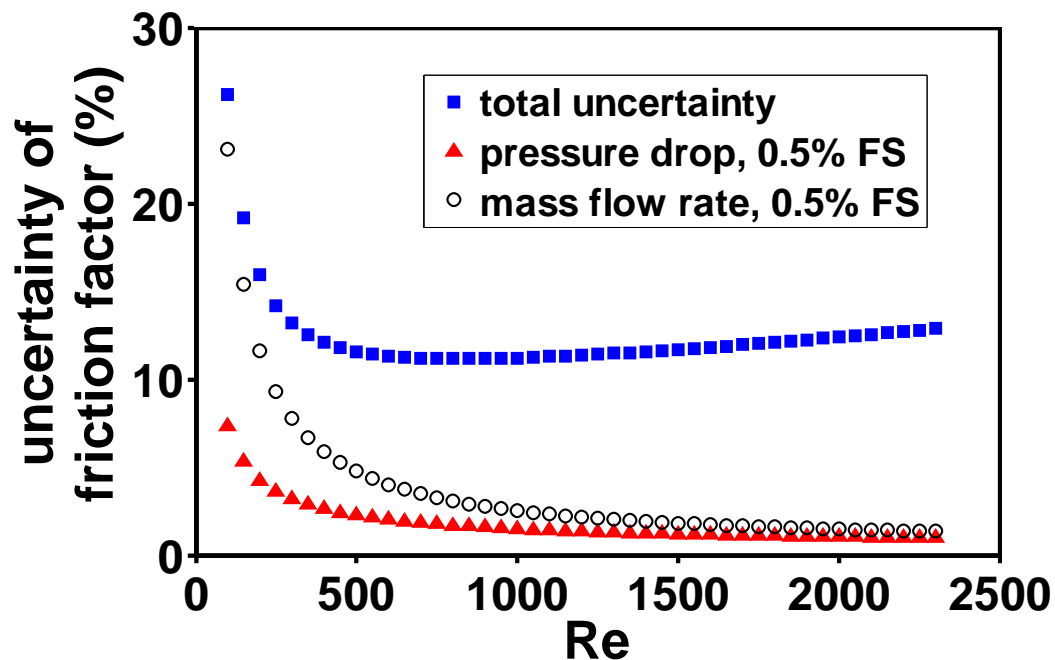


Figure 3-3: Contribution of the pressure and mass flow rate measurements (with uncertainties equal to 0.5% of FS) on the uncertainty of total friction factor.

In order to control the uncertainty during experimental tests over a wide range of Reynolds numbers, it becomes mandatory to use a series of measurement devices with different full scale (FS) values. An example is given in Figure 3-4, where two sets of measurement devices with different full scales are employed for different ranges of Reynolds numbers. The first set of pressure sensor and mass flow meters reach their full scales at $Re=500$ and the second set reach the FSs at $Re=2300$.

By comparing the magnitudes of the uncertainties in Figure 3-4 with those in Figure 3-3, it is evident that by using of two sets of devices having different full scales it is possible to control the uncertainty of friction factor under 14% for Reynolds number from 100 to 2300. If more sets of measurement devices are employed in the experiment, the uncertainty of the friction factor can be lower. However, there should be a balance between the controlled accuracy and the financial and labor inputs in the design of the experiment.

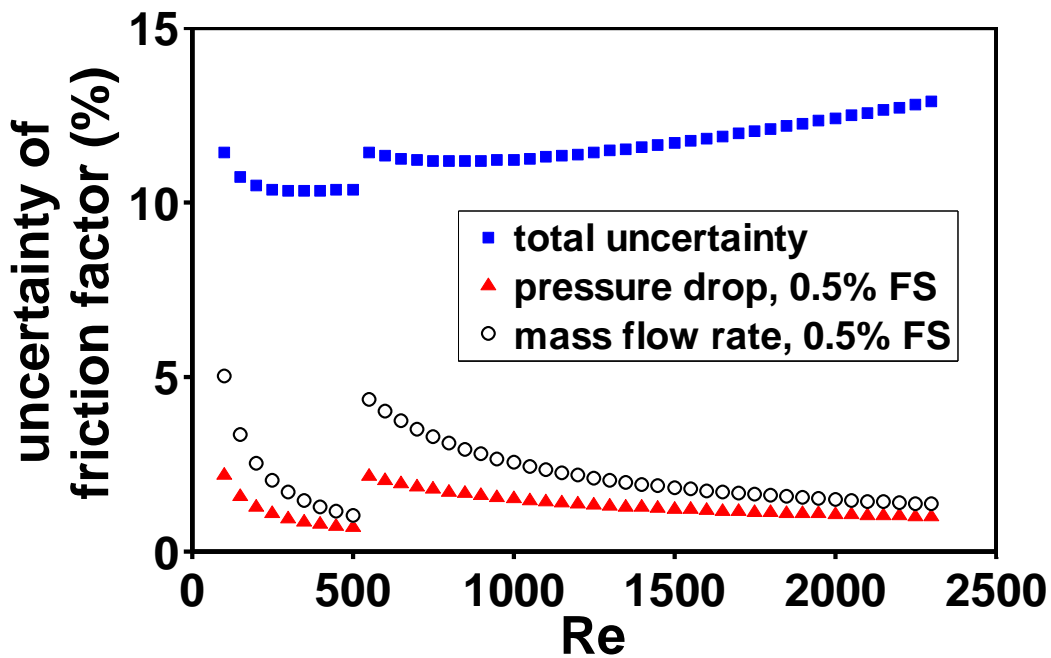


Figure 3-4: Effect of the use of two sets of pressure sensors and mass flow meters (with full scales at $Re=500$ and $Re=2300$, respectively) on the total uncertainty of friction factor.

As shown in Table 3-1, using pressure sensors of identical uncertainty but different strategies of pressure measurement may result in a different accuracy for friction factor. In this sense, an “a-priori” uncertainty analysis can serve as a useful design tool for microfluidics experiment as underlined in [131].

Figure 3-5 indicates that if the inlet and outlet pressure are measured (Strategy #2) for the determination of the friction factor in a compressible gas microflow, the sensitivity coefficients for uncertainty of friction factor will be very large at lower Reynolds number compared with the measurement of pressure drop and outlet pressure (Strategy #1). It is evident that for Reynolds number larger than 500, it is more advisable to choose an absolute pressure sensor with a higher accuracy for the inlet section in order to reduce the total uncertainty of friction factor.

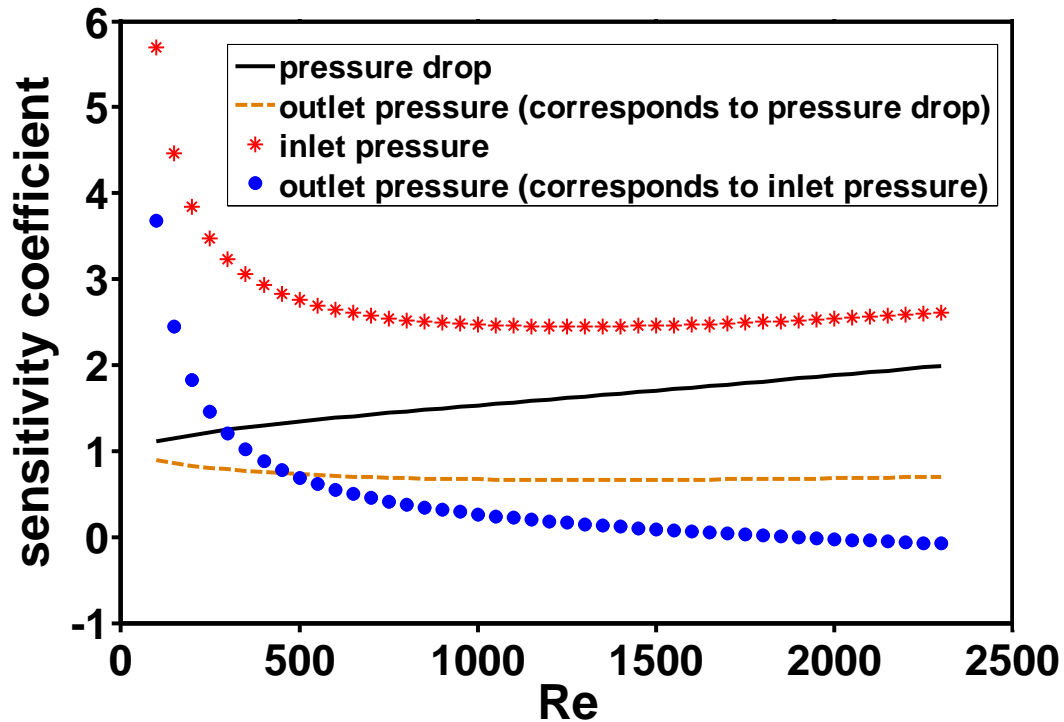


Figure 3-5: Comparison of the influence of different strategies for the pressure measurement on the sensitivity coefficients of the inlet, outlet and differential pressure (sensors with a fixed uncertainty ($\pm 0.5\%$ of FS)).

Uncertainty analysis can be also used to check the validity of the results published in the literature; sometimes discrepancies from theoretical predictions can be traced back to the use of inaccurate instrumentation in the measurements.

3.3 Experimental uncertainties on Nusselt number of micro gas flows

Regarding thermal analysis at microscale, measurement errors may become a major concern when the dimension of test rigs and the magnitudes of the operative parameters are

comparatively small. Therefore, a sensitivity analysis is performed here in order to quantitatively examine the dependence of Nusselt number on the measured parameters.

While the detailed physical deduction for the expression of Nusselt number is discussed in Chapter 5, the value of Nusselt number can be experimentally determined by

$$Nu = \frac{\dot{m}c_{pf}}{\pi\lambda_f L} \frac{T_{out} - T_{in}}{T_w - \frac{T_{out} + T_{in}}{2}} \quad (3.8)$$

where c_{pf} is the thermal capacity of the fluid and λ_f is the thermal conductivity of the fluid. For sake of simplicity, it is assumed in Eq. (3.8) that the effects of fluid temperature-dependent properties are not important.

From Eq. (3.8) it is evident that the value of Nusselt number is related to the following operating variables during specific test:

$$Nu = Nu(L, \dot{m}, T_{out}, T_{in}, T_w) \quad (3.9)$$

The experimental determination of Nusselt number involves direct measurements of the flow length (microtube length), mass flow rate, fluid bulk temperature at inlet and outlet, as well as wall temperature of the microtube. By applying the theory of uncertainty propagation [119], the relative uncertainty on Nusselt number can be expressed as:

$$\frac{\delta Nu}{Nu} = \sqrt{(k_1)^2 \left(\frac{\delta L}{L}\right)^2 + (k_2)^2 \left(\frac{\delta \dot{m}}{\dot{m}}\right)^2 + (k_3)^2 \left(\frac{\delta T_{b,out}}{T_{b,out}}\right)^2 + (k_4)^2 \left(\frac{\delta T_{b,in}}{T_{b,in}}\right)^2 + (k_5)^2 \left(\frac{\delta T_w}{T_w}\right)^2} \quad (3.10)$$

where the sensitivity coefficients, k_1, k_2, \dots, k_5 , show how the uncertainty of each measurable parameter contributes quantitatively to the total uncertainty on the Nusselt number. The theoretical expressions of these coefficients are listed in Table 3-5. The details of analytical deduction are attached in Appendix B.

Table 3-5: Sensitivity coefficients of operative parameters for determination of experimental uncertainty in Nusselt number.

Sensitivity coefficients	Operating parameters	Expressions
k_1	microtube length	1
k_2	mass flow rate	1
k_3	bulk temperature at the outlet	$\frac{T_{out}(T_w - T_{in})}{\left(T_w - \frac{T_{out} + T_{in}}{2}\right)(T_{out} - T_{in})}$
k_4	bulk temperature at the inlet	$\frac{T_{in}(T_w - T_{out})}{\left(T_w - \frac{T_{out} + T_{in}}{2}\right)(T_{out} - T_{in})}$
k_5	wall temperature of the microtube	$\frac{T_w}{T_w - \frac{T_{out} + T_{in}}{2}}$

Figure 3-6 shows the trends of these coefficients over a wide range of Reynolds number (700-4000) for gas flow heat transfer through microtubes. It can be noted that the uncertainty on the Nusselt number strongly depends on the accurate measurement of the gas outlet temperature, which prominently surpasses the significance of the uncertainty on the measurements of gas inlet temperature, wall temperature, length and mass flow rate in both laminar and transitional regimes. When the flow is no longer laminar, there is a steeper increase of the sensitivity coefficient for outlet and inlet gas temperature measurement, with the latter being the stronger.

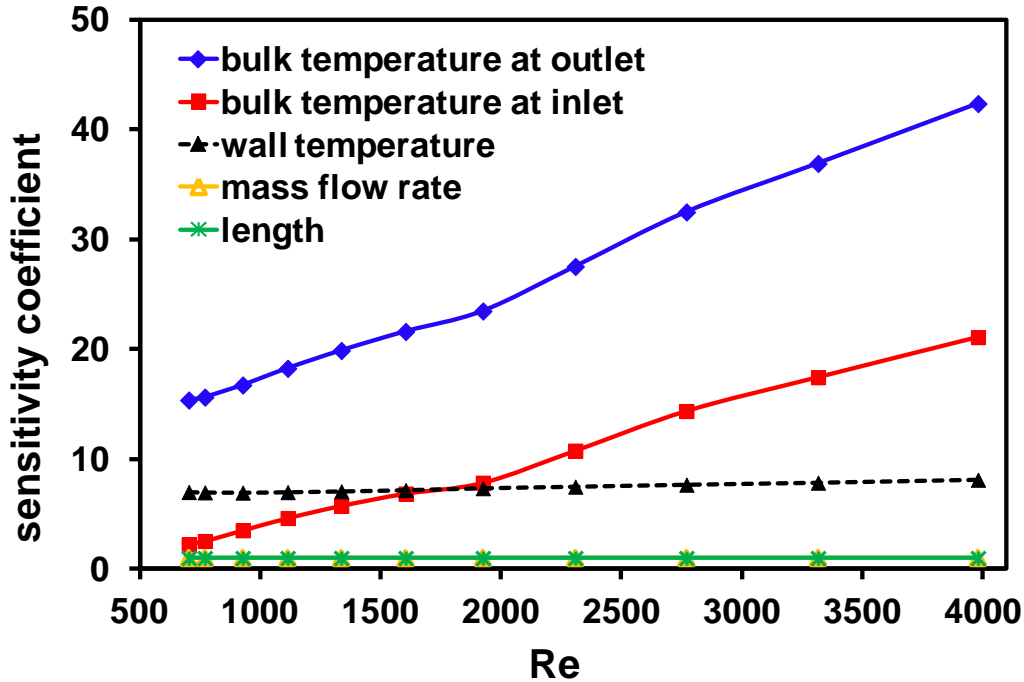


Figure 3-6: Sensitivity coefficients of operating parameters linked to the uncertainty of Nusselt number as a function of Reynolds number.

The curves in Figure 3-6 suggest that, to accurately determine the Nusselt number from experimental data, the accuracy of fluid temperature measurements must be as high as possible, especially in the exit section. However, the accuracy of the exit bulk temperature is not merely related to the uncertainty intrinsic to the thermocouples used in the tests, but is also influenced by the way in which temperature is measured (plenum geometry, position of the temperature sensor in the plenum, existence of an unheated stretch between the plenum and the last electrode, etc.). A detailed examination on the influence of outlet temperature measurement is stated in Section 5.1.6.

3.4 Conclusions

In this chapter the propagations of experimental uncertainties of the friction factor and the Nusselt number are analyzed in a systematic way. It has been pointed out that the uncertainties of all the measurements involved in one single test do not contribute equally to the uncertainties of the friction factor or the Nusselt number, but are characterized by various sensitivity coefficients. It has been demonstrated in the analysis how the values of these sensitivity coefficients vary depending on both the measurement strategies and the experimental conditions. The typical

values of measurement uncertainties on channel size, pressure, temperature and mass flow rate are compared by extracting experimental data from a series of papers published in recent years both for liquid and gas flows through microchannels.

Based on the complete calculation of uncertainties of the friction factor and the Nusselt number, it turns out that the accuracy of diameter measurement is essential to the accuracy of the friction factor, while the accuracy of fluid outlet temperature measurement is most critical for accurate determination of the Nusselt number. The analysis and conclusions of this chapter will be used to design the test rig with expected accuracies and to estimate accurately the uncertainties of experimental data obtained from the test rig, which will be detailed in the next chapters.

4 Experimental Study on Gas Flow through Microtubes

4.1 Experimental apparatus

An experimental campaign to characterize the behavior of nitrogen flow through commercial stainless steel microtubes has been conducted. The main geometrical characteristics of the microtubes are summarized in Table 4-1, where d is the average inner diameter of microtube, D the external diameter, δ the roughness of the wall surface, and L the length of microtube.

Table 4-1: Geometrical characteristics of the tested microtubes

Microtube	d (μm)	D (μm)	δ (μm)	L (m)	δ/d (%)	L/d
#1	750	1588	4	0.5	0.53	667
#2	510	1588	3	0.2	0.60	392
#3	170	1588	3	0.1	1.76	588

Three commercial stainless steel microtubes (*Upchurch*) having different inner diameters and the same outlet diameter (1/16") have been selected for the experiment, as shown in Figure 4-1. The reduction in microtube inner diameters enables to compare and check the influence of scaling effects on the frictional characteristics of the flow. It is important to bear in mind that the real inner diameter of a microtube may deviate greatly from the nominal values declared by the manufacturer. This is especially true for microtubes with inner diameters smaller than 200 μm . An inaccurate determination of the microtube inner diameter will easily lead to wrong experimental results [132]. Therefore in this work the inner diameters of the three microtubes were carefully checked. Firstly, the configurations of the microtube end sections were imaged with SEM (Scanning Electron Microscope) at high resolution, and the diameter information was extracted by using a fitting of the images. Then the hydraulic diameter averaged along the microtube length was further checked by means of experimental tests on the friction factor in laminar regime; in fact, the experimental results accumulated in the recent years on friction

factors in microtubes confirm that the Poiseuille law is still valid for incompressible flows at microscale. Since the friction factor is inversely proportional to the fifth power of hydraulic diameter for incompressible gas flow in laminar regime, the value of friction factor is highly sensitive to the hydraulic diameter of the tube and can be used in order to verify the inner diameter determined by SEM. In this work the microtube hydraulic diameter was finely tuned until experimental friction factors in laminar regime well agree with the Poiseuille law for low Reynolds numbers where the gas flow can be considered incompressible. This method can be very accurate as long as the experiment is carefully carried out and it provides the values of hydraulic diameter averaged over the whole length of microtube, taking into account the possible deformation of local cross section along the microtube. The hydraulic diameters of the tested microtubes determined by using this method are equal to 750 μm , 510 μm and 170 μm respectively, while the values declared by the manufacturer are 750 μm , 500 μm and 175 μm , respectively. It is interesting to note that the relative difference between the declared values and the measured ones is equal to 0% (microtube #1), +2% (microtube #2) and -2.9% (microtube #3); these differences are within the uncertainty declared by the manufacturer.

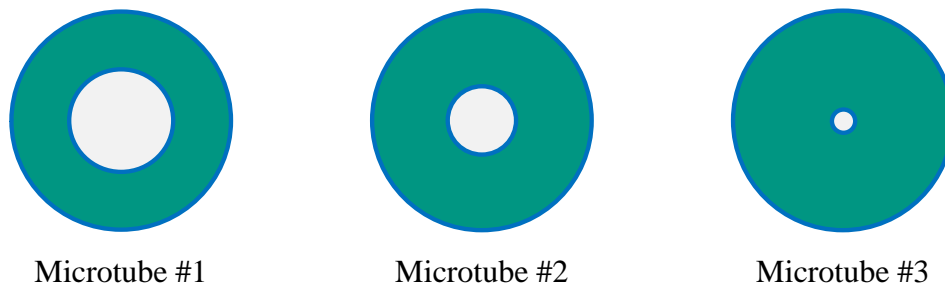


Figure 4-1: Geometry of microtube cross sections.

The microtubes are mounted on the test rig schematically shown in Figure 4-2. Nitrogen is stored in a high pressure flask (200 bar) (1) and it is expanded using a valve (2) to approximately 10 bar and ambient temperature before entering in a 7 μm particle filter (3, *Hamlet*) used to prevent possible impurities from clogging the microchannels or the mass flow controllers. A three-way valve directs the flow to the proper flow sensor, as the facility is equipped with three *Bronkhorst EL-Flow E7000* operating in the 0-5000 Nml/min (4a), 0-500 Nml/min (4b) and 0-50 Nml/min (4c) ranges respectively. The mass flow controllers can impose an expected mass flow rate by means of a computer-steered valve which makes an indirect regulation of the pressure at the inlet of the microtube. The test section (5) allows the test of tubes of varying lengths (from 1

to 100 cm) and variable inner diameters, providing they have the same external diameter, namely 1/16". After exiting the microtube, the gas is vented to the atmosphere. The total pressure drop between the inlet and the outlet of the microtube is measured by a differential pressure transducer (6, *Validyne DP15*). To measure the temperature distribution along the external surface of the microtube, five calibrated K-type thermocouples are glued to the outer surface of the microtube using an electrically non-conductive epoxy resin. In addition, at the inlet and outlet of the channel two additional K-type thermocouples are carefully inserted into the plena. An infrared thermo-camera can be also used (7, *AVIO TVS 200EX*) to check all the possible thermal bridges of the test section and to measure the external temperature of the tube wall. The temperature of the external wall of the microtube can be varied from the room value up to 100 °C by using the Joule effect made by means of an imposed electrical current with a programmable DC power supply (8, *HP6032A*). An absolute pressure sensor (9, *Validyne AP42*) is used to monitor the ambient pressure at the exit of the test rig. The microtube can be thermally insulated at the external surface (Armaflex®, $k_{ins}=0.035$ W/mK) and enclosed in an insulated box in order to decouple the test section from the thermal conditions existing in the room. The photograph of the test equipment is shown in Figure 4-3.

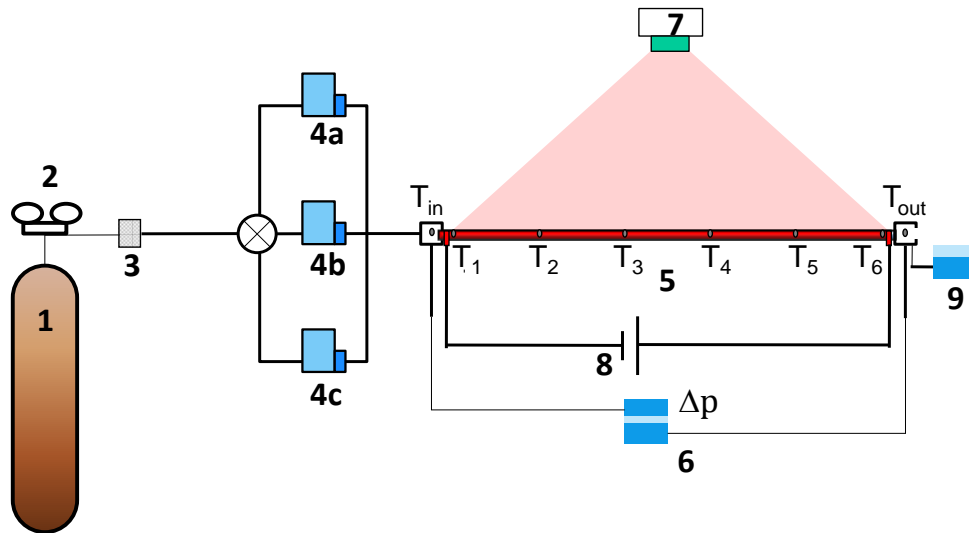


Figure 4-2: Schematic layout of the test rig (1- gas source, 2- valve, 3- filter, 4- mass flow controllers, 5- thermocouples, 6- differential pressure sensors, 7- infrared thermal camera, 8- DC heating, 9- absolute pressure sensor).



Figure 4-3: Photograph of the test system.

To assess the accuracy of the experimental measurements, the uncertainty associated to each measurement device used in the test rig is reported in Table 4-2. The uncertainty on the inner diameter evaluated through SEM imaging is of the order of $\pm 2\%$; the uncertainty on the microtube length is of the order of $\pm 0.3\%$. The roughness of the microtubes is deducted by superimposing a best-fitting circle over the corresponding tube contours in the SEM images. By applying these data to the equations in the uncertainty analysis demonstrated in Chapter 3, the relative uncertainty of friction factor in the present experiment is calculated to be 3-14% and the uncertainty of Nusselt number ranges between 8% and 33%.

Table 4-2: Characteristics and accuracy of instrumentation.

Instrument	Range (0-FS)	Accuracy
Flowmeter (Bronkhorst EL-Flow E7000)	0-5000 (Nml/min)	± 0.6 % FS
	0-500 (Nml/min)	± 0.5 % FS
	0-50 (Nml/min)	± 0.5 % FS
Differential pressure transducer (Validyne DP15)	0-35 (kPa)	± 0.5 % FS
	0-86 (kPa)	
	0-220 (kPa)	
	0-860 (kPa)	
	0-1440 (kPa)	
Thermocouple (K type)	0-200 (°C)	± 0.25 % FS

In this test rig the gas pressure is measured by using a capacitance sensor (*Validyne DP15*) which is able to work with a series of replaceable membranes each one with a fixed full scale value. In the laboratory 23 membranes with specific FSs are available, and three mass flow controllers with different FSs are used. The purpose is to reduce the measurement uncertainties by selecting the appropriate FS of the differential pressure sensors and of the flow controllers for each test. This selection is performed by a pre-calculation which takes into account the value assumed by the fluid thermal physical properties by the dimension of the microtubes (inner diameter and length) and by the range of the tested Reynolds number. All the measurement devices are chosen to work within 10-90% of the full scales to ensure their precision and functionality.

A Labview code has been developed in order to impose a fixed heating of the tube, to control the ongoing of the experiment, to check if a steady state (in terms of flow rate, pressure and temperature) has been reached between two consecutive measurements, and transfer and record all the measured data in specific files.

4.2 Adiabatic gas flow through microtubes

The first set of experimental tests was carried out under adiabatic condition, where there is no heating from the metallic wall. If the effects of flow compressibility are insignificant, the flow is isothermal under this condition.

4.2.1 Theory on conventional adiabatic flow

The pressure drop of conventional flow in a pipe can be calculated by the Darcy-Weisback equation:

$$\Delta p = f \frac{L}{d} \frac{\rho \bar{v}^2}{2} \quad (4.1)$$

where f is the Darcy-Weisback friction factor, also called as drag coefficient, L is the pipe length, d the inner diameter, ρ the density of the fluid and \bar{v} the average bulk velocity of the flow.

The Reynolds number can be calculated as follows:

$$Re = \frac{\rho \bar{v} d}{\mu} \quad (4.2)$$

where μ is the dynamic viscosity of the fluid.

According to the Hagen–Poiseuille law, the friction factor for a fully developed incompressible flow in laminar regime in a pipe can be expressed by the following if the flow is isothermal:

$$f = \frac{64}{Re} \quad (4.3)$$

Eq. (4.3) indicates that the friction factor for laminar flow is only related to the Reynolds number, and is not influenced by the surface roughness of the pipe. This is true up to values of the relative roughness of 5%.

For turbulent flow through smooth pipes, the Blasius equation applies for $3000 < Re < 10000$:

$$f = 0.3164 Re^{-0.25} \quad (4.4)$$

For conventional turbulent flow through rough pipes or at larger Reynolds number, there are well developed equations to calculate the pressure drop or friction factor, for example the Colebrook equation. Details can be found in a lot of text books, such as in [133].

4.2.2 Data reduction for compressible flows

For compressible flows the Reynolds number may change significantly between inlet and outlet. In this work the Reynolds number is defined in terms of measured quantities as follows:

$$Re = \frac{4\dot{m}}{\pi d \mu} \quad (4.5)$$

where \dot{m} is the mass flow rate, d the inner diameter of the tube, and μ the dynamic viscosity of the fluid.

For isothermal compressible flow, the calculation of friction factor by Eq. (3.3) can be rewritten as the following by using the inlet pressure and the pressure drop:

$$f = \frac{d}{L} \left[\left(\frac{1 - \left(1 - \frac{\Delta p_n}{p_{in}}\right)^2}{\left(\frac{4\dot{m}\sqrt{RT_b}}{\pi d^2 p_{in}}\right)^2} \right) - 2 \ln \left(\frac{1}{1 - \frac{\Delta p_n}{p_{in}}} \right) \right] \quad (4.6)$$

where Δp_n is the net pressure drop along the tube, p_{in} the pressure at the tube inlet, T the fluid bulk temperature, and R the specific gas constant. Eq. (4.6) is also used for non-isothermal flow by averaging the bulk temperature between inlet and outlet for estimation of gas properties.

The net pressure drop (Δp_n) in Eq. (4.6) is determined by the measured total pressure drop after subtracting the minor losses at the inlet and outlet plenums:

$$\Delta p_n = \Delta p_{total} - \Delta p_{in} - \Delta p_{out} \quad (4.7)$$

The minor pressure losses are caused by the variation of flow area (sudden expansion at the inlet plenum and sudden contraction at the outlet plenum). These losses can be calculated by:

$$\Delta p_{in} = p_{in'} - p_{in} = \frac{K_{in}}{2} \left(\frac{\dot{m}}{A} \right)^2 \left(\frac{RT}{p_{in'}} \right) \quad (4.8)$$

$$\Delta p_{out} = p_{out} - p_{out'} = \frac{K_{out}}{2} \left(\frac{\dot{m}}{A} \right)^2 \left(\frac{RT}{p_{out}} \right)$$

where $p_{in'}$ is the pressure in the inlet plenum, $p_{out'}$ the pressure in the outlet plenum, p_{out} the pressure at the outlet of the tube, A the flow area of the tube. The coefficient K_{in} is 1.5 and K_{out} is 1.0 in agreement with the indication of the conventional theory [134].

4.2.3 Friction factor of adiabatic gas microflow

The characteristics of nitrogen flow through microtubes under adiabatic condition were experimentally investigated in order to check the validity of classical theory developed for flow at macro scale.

Figure 4-4 shows the relation between friction factor and Reynolds number for adiabatic nitrogen flows through microtube #1, which has an inner diameter of 750 μm . It is evident that classical theory of Poiseuille law is able to well predict the friction factor of flow in laminar regime ($\text{Re} < 2300$). The critical Reynolds number is around 2700, which is within the conventional transitional region ($\text{Re} = 2000\text{--}4000$) valid for conventional flows. For Reynolds number larger than 4000, there is good agreement between the experimental data and the Blasius prediction for turbulent flow through smooth pipes. The relative roughness of microtube #1 is 0.53%, and it can be considered hydraulically smooth.

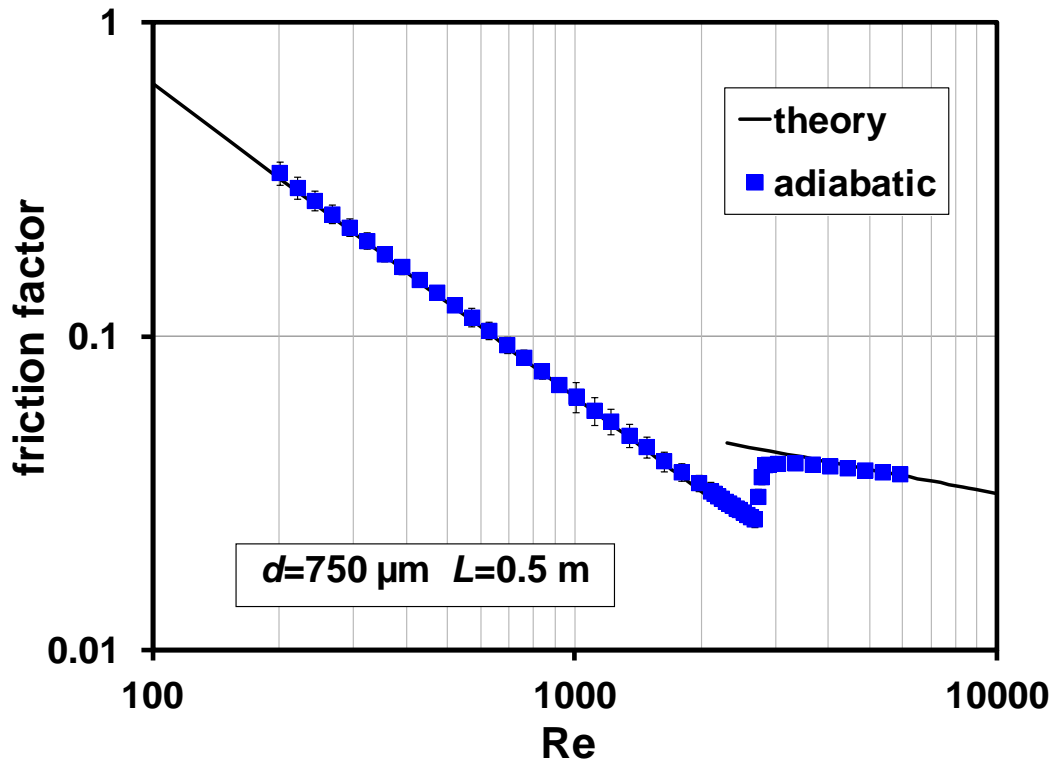


Figure 4-4: Friction factor as a function of Reynolds number for adiabatic flow through microtube #1.

When the microtube inner diameter is reduced from 750 μm to 510 μm , the experimental uncertainties is greatly increased with the same testing apparatus, as shown by the error bars indicated in Figure 4-5. This fact highlights the significant influence on the experimental accuracy of the friction factor of the microtube inner diameter as demonstrated in Section 1.3.9. By comparing the experimental data with the conventional theory, Figure 4-5 further confirms

that no new theory or correlations are needed for the prediction of the frictional characteristics of adiabatic gas flows through microtubes either in laminar regime or in turbulent regime.

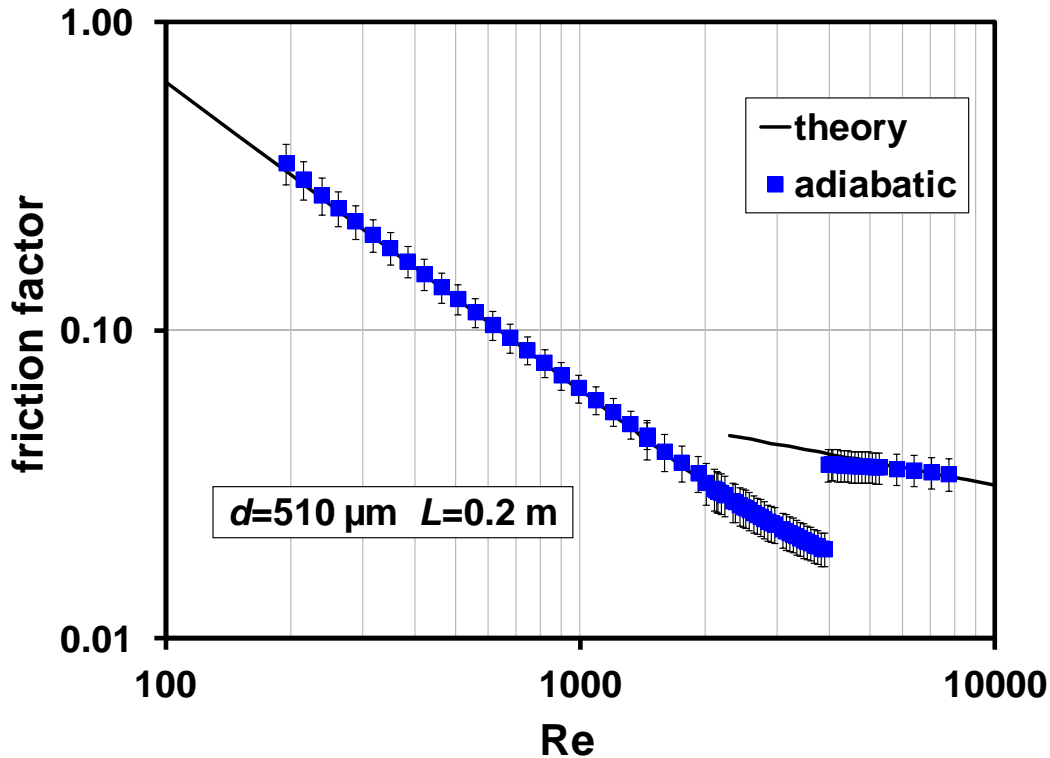


Figure 4-5: Friction factor as a function of Reynolds number for adiabatic flow through microtube #2.

The friction factor of nitrogen flow through the smallest microtube (microtube #3, inner diameter 170 μm) is plotted in Figure 4-6 as a function of Reynolds number and compared with the conventional laws for laminar and turbulent regime. When the Reynolds number is smaller than 1000, the experimental friction factor can be still precisely predicted by the Poiseuille law, considering the experimental uncertainties associated to the data points. For Reynolds numbers larger than 1000 in laminar regime, a deviation from the classical theory is evidenced for adiabatic flow through microtube #3. As it will be fully explained in Section 4 this trend can be understood if the compressibility effects due to the high Mach numbers reached for $\text{Re} > 1000$ are taken into account in the analysis. In turbulent regime, especially for $\text{Re} > 4000$, it can be noted that the value of experimental friction factor is larger than the values indicated by the Blasius equation. This is due in part to the compressibility effects and in part to the large value of the relative roughness which characterizes the microtube #3 (2%).

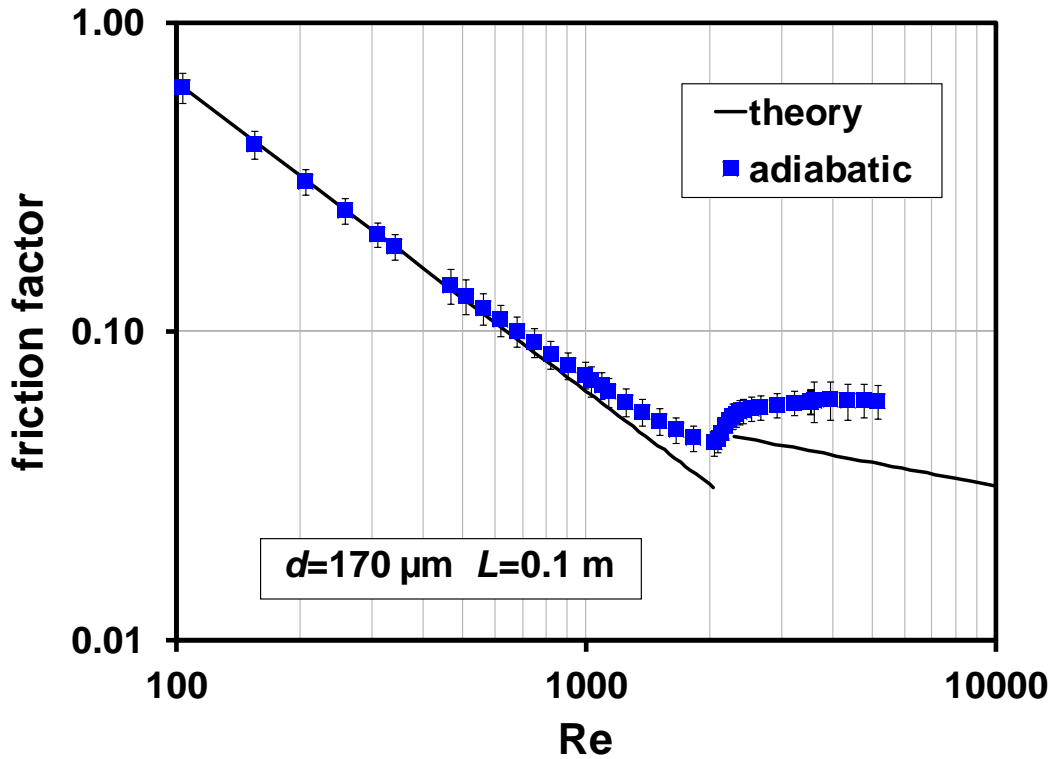


Figure 4-6: Friction factor as a function of Reynolds number for adiabatic flow through microtube #3.

4.3 Heated gas flow through microtubes

In this section the impact on the friction factor of an imposed wall temperature along the tube larger than the gas temperature is investigated. The temperature difference between the walls and the gas changes the value of the gas thermophysical properties close to the walls and can determine a variation of the frictional characteristics of the flow.

As discussed in Section 1.3.6, when a temperature gradient at the wall appears the effects of the variation of the fluid temperature-dependent properties should not be negligible. In particular, two properties can change the frictional behaviour of a fluid in a microtube: its viscosity and its thermal conductivity. For engineering applications, in order to calculate the friction factors in a tube when a large temperature difference between the tube walls and the gas flow is present, the designers generally employ correlations based on analytical solutions from constant property or experimental data obtained with small temperature differences and then apply some kind of correction to account for property variations. The correction methods proposed for this aim are usually based on: (i) the property ratio method and (ii) the reference temperature method. For

gases, the viscosity, thermal conductivity and density are functions of the absolute temperature. Since the principle of fluid temperature-dependent properties is similar for various gases, the reference temperature method is suggested in order to take into account the property variations in the classical correlations. For circular tubes, Shah and London [67] suggested the following equations for the modification of the friction factors for gas flows under non-isothermal conditions:

$$\frac{f}{f_{cp}} = \left(\frac{T_w}{T_{b,m}} \right)^m$$

$$\begin{aligned} (\text{heating}) \quad m = 1 \quad \text{for} \quad 1 < \frac{T_w}{T_{b,m}} < 3 \\ (\text{cooling}) \quad m = 0.81 \quad \text{for} \quad 0.5 < \frac{T_w}{T_{b,m}} < 1 \end{aligned} \quad (4.9)$$

The subscript *cp* means that the quantity is evaluated by using the constant properties hypothesis, T_w is the wall temperature and $T_{b,m}$ is the mean value of the bulk temperature along the tube. Eq. (4.9) has been deduced by using conventional-sized tubes but it has not been checked up to now in a systematic way for gas flows through microtubes.

4.3.1 Friction factor of gas microflow under heated conditions

The three commercial stainless steel microtubes described before have been used in an experiment in which the average temperature of the microtube wall was carefully imposed along the tube (at 45 °C, 65 °C and 85 °C) for a large range of Reynolds numbers in order to investigate the influence of temperature-dependent properties on the friction factor, covering laminar, transitional and turbulent regimes.

The friction factors as a function of the Reynolds number obtained by imposing three different values of the wall temperature along microtube #1 are compared in Figure 4-7 with the values obtained under adiabatic condition, as well with the predictions of the conventional laws. It is evident that in laminar regime, the friction factor tends to increase with the wall temperature. This effect is in agreement with the indication of Eq. (3.9) where $f > f_{cp}$ when $T_w > T_{b,m}$. For instance, for heated flow through microtube #1 with Reynolds number being 842 and wall average temperature equal to 85 °C, the friction factor is 21% larger than that for unheated flow. In this case the experimental uncertainty of friction factor is of the order of 4.4%, which is much

lower than the measured difference in terms of friction factor due to the temperature difference between the tube wall and the gas.

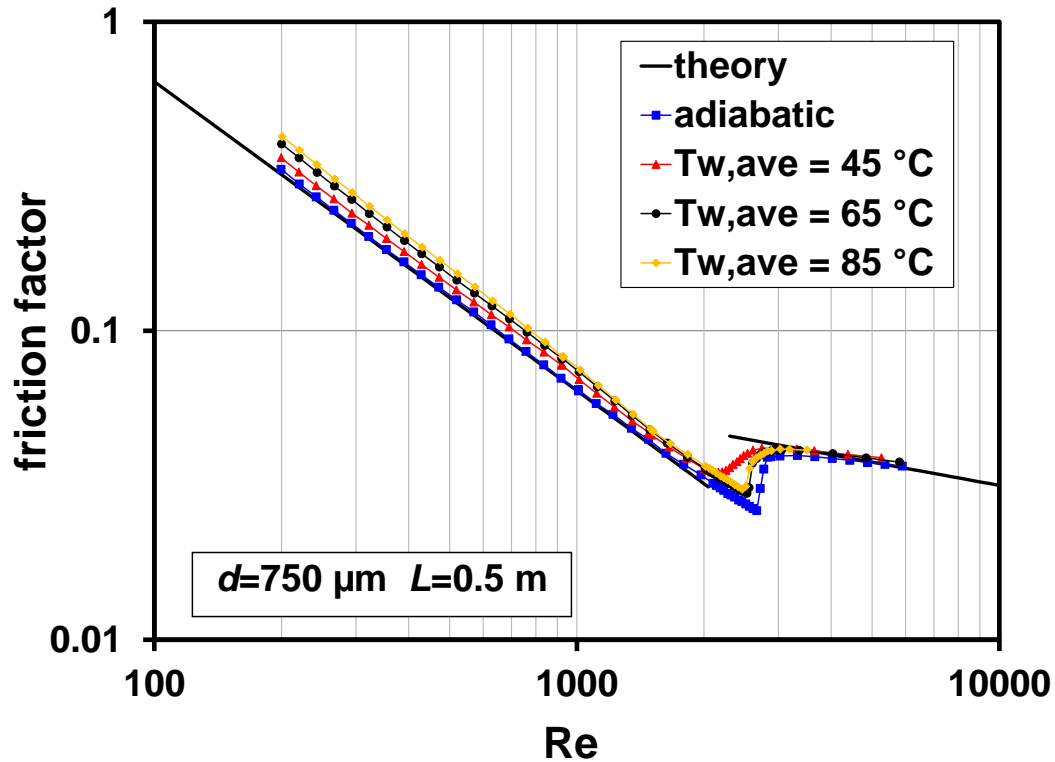


Figure 4-7: Friction factor versus Reynolds number under adiabatic and heated conditions for microtube #1.

The error bars linked to the experimental friction factors are not indicated in order to improve the readability of the plotting. The maximum relative uncertainty of friction factor is 10%, which is encountered at the lowest mass flow rate during experiment.

In turbulent regime, however, the values of friction factor under heated condition converge to that without heating, and the influence of temperature-dependent properties on friction factor becomes slight and negligible. This is most probably attributed to intensive temperature mixing caused by the turbulence in the flow.

Similar trends are evidenced by heated flows through microtube #2 and microtube #3, as shown in Figure 4-8 and Figure 4-9, respectively. In laminar regime the higher the wall temperature, the larger the friction factor is. On the other hand, in turbulent regime this difference disappears. This further indicates that the correction for variable properties effect may not be necessary in turbulent regime, as in the correlation given by Shah and London [67], which covers all the flow regimes.

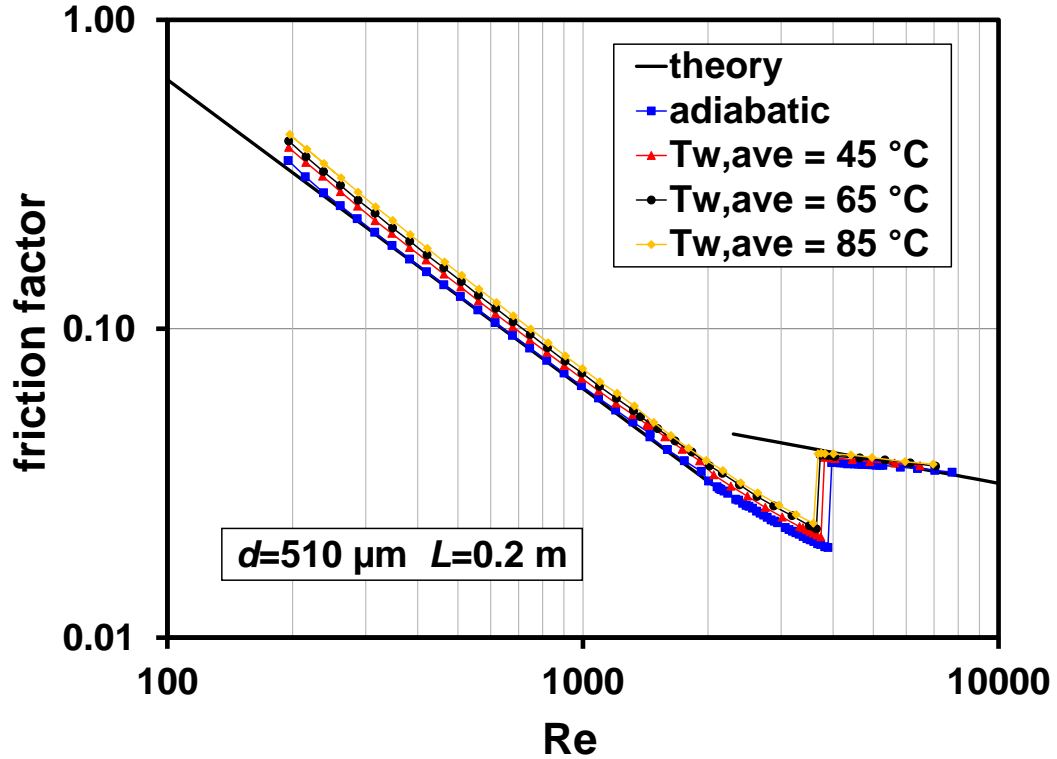


Figure 4-8: Friction factor versus Reynolds number under adiabatic and heated conditions for microtube #2.

In heated flows through the smallest microtube (inner diameter $170\text{ }\mu\text{m}$) it is evident that all the plottings of friction factor versus Reynolds number begin to depart gradually from the straight lines at Reynolds numbers larger than 1000. This phenomenon is already observed under adiabatic conditions and it can be explained by taking into account the gas compressibility as in a next section will be discussed.

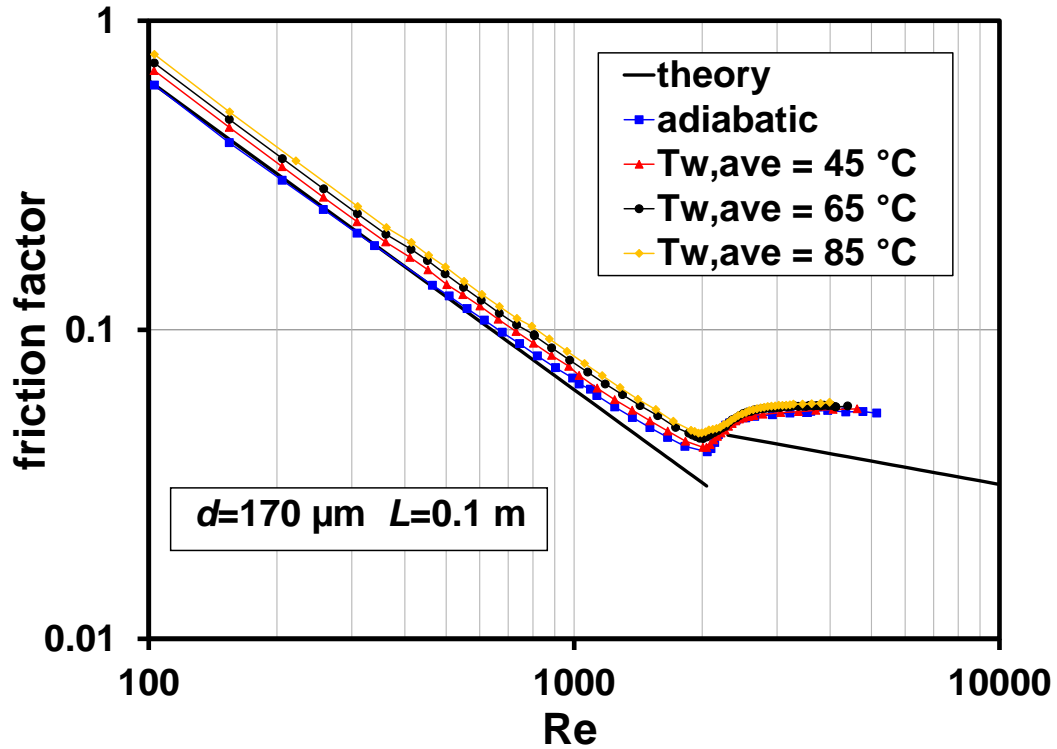


Figure 4-9: Friction factor versus Reynolds number under adiabatic and heated conditions for microtube #3.

4.3.2 Correction of flow friction factor under heated conditions

The results shown in the previous graphs highlight how for heated flow in laminar regime, the effect of temperature-dependent properties leads to a significant departure of the friction factors from the values obtained under isothermal conditions. In this section the validity of the friction factor correction proposed from non-isothermal flows for conventional tubes will be checked by applying Eq. (4.9) suggested by Shah and London [67] to the experimental data obtained for our microtubes.

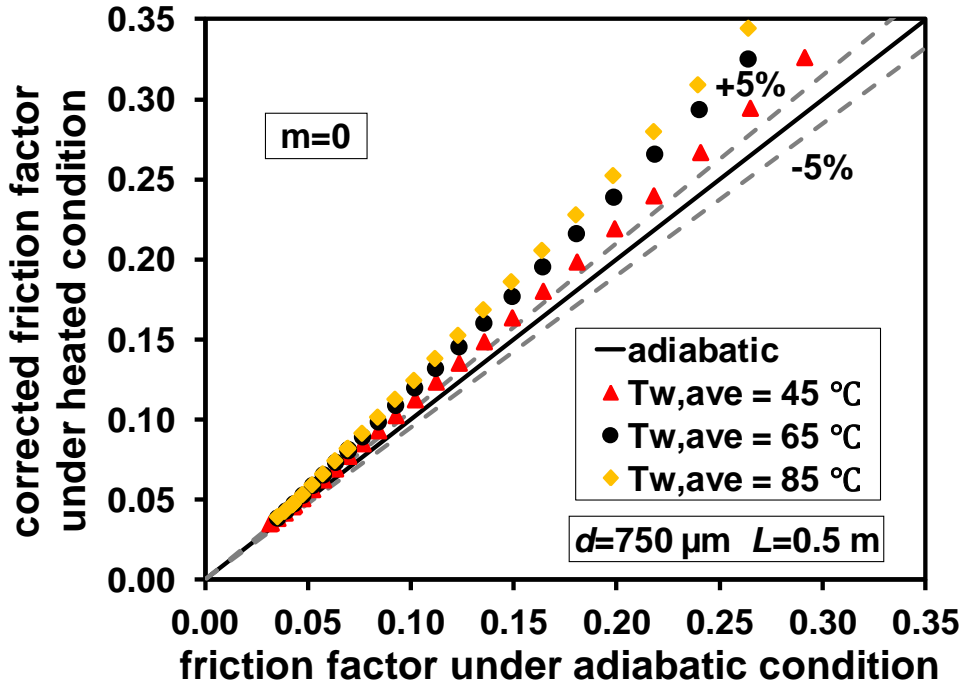
Firstly, in Figure 4-10(a) the experimental friction factors obtained for microtube #1 under non-isothermal conditions are compared with the friction factors obtained under isothermal conditions. It can be noted that the uncorrected friction factors obtained under non-isothermal conditions are generally out of $\pm 5\%$ of the values obtained at the same Reynolds number under isothermal condition. Therefore, a correction is needed in order to account for the effects of temperature-dependent properties.

It should be mentioned that for microtube #1 and microtube #2, as well as the flows through microtube #3 at $Re < 1000$, the compressibility effects are insignificant as the Mach number is small ($Ma < 0.3$). Therefore, under adiabatic conditions these flows are strictly isothermal.

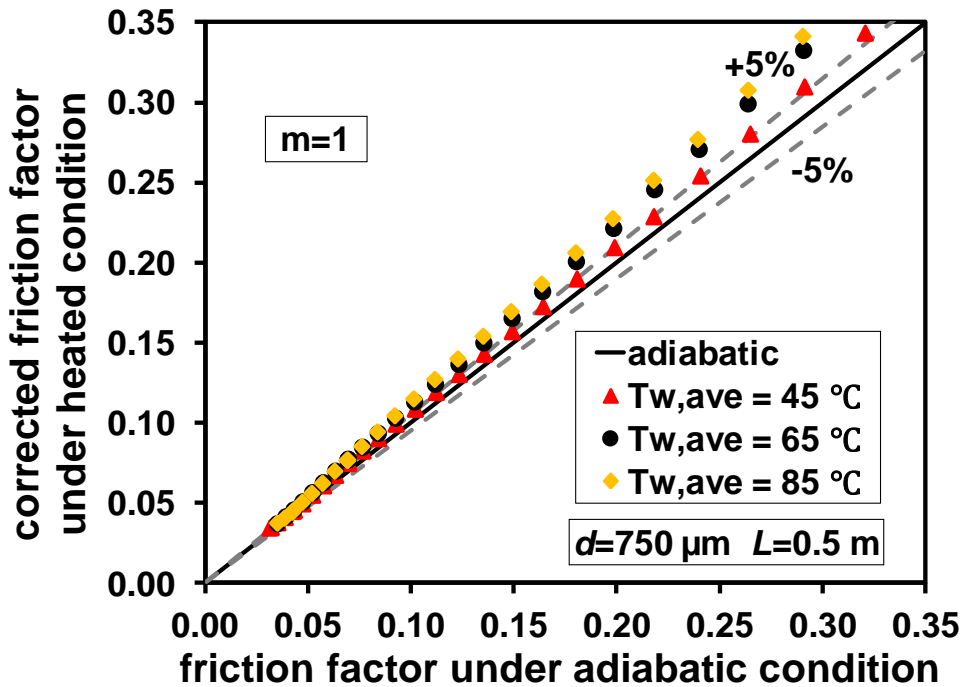
In Figure 4-10(b) the friction factors determined for microtube #1 under non-isothermal conditions have been corrected by using Eq. (4.9) with an exponent $m=1$, which is the value suggested by Shah and London [67] for gas flows through conventional non-isothermal tubes. With $m=1$ only a small number of the total data points differ for $\pm 5\%$ with respect to the values of the friction factors obtained under isothermal conditions. This means that the classical correction of the friction factor validated for conventional pipes is insufficient in order to correct the friction factors for gas flows through commercial microtubes.

The need of a larger exponent for the correction of friction factors in non-isothermal microtubes can be justified theoretically, if one takes into account that the bulk temperature gradient along flow direction can be very large for gas microconvection in laminar regime. Especially for microtube #3, the average bulk temperature gradient is of the order of 1000~1200 K/m within the range of Reynolds number shown in Figure 4-9. Furthermore, the gas temperature gradient in radial direction may also account for the larger correction factor. Consequently, larger values of correction factor were applied to all the data points of the three microtubes under different wall temperature, until all the corrected values fall within $\pm 5\%$ range of adiabatic flows, which leads to the use of an exponent in Eq.(4.9) $m=2$. By observing Figure 4-10(c), it is evident that $m=2$ works well in the case of microtube #1, where the corrected friction factor matches perfectly with the data obtained in adiabatic conditions.

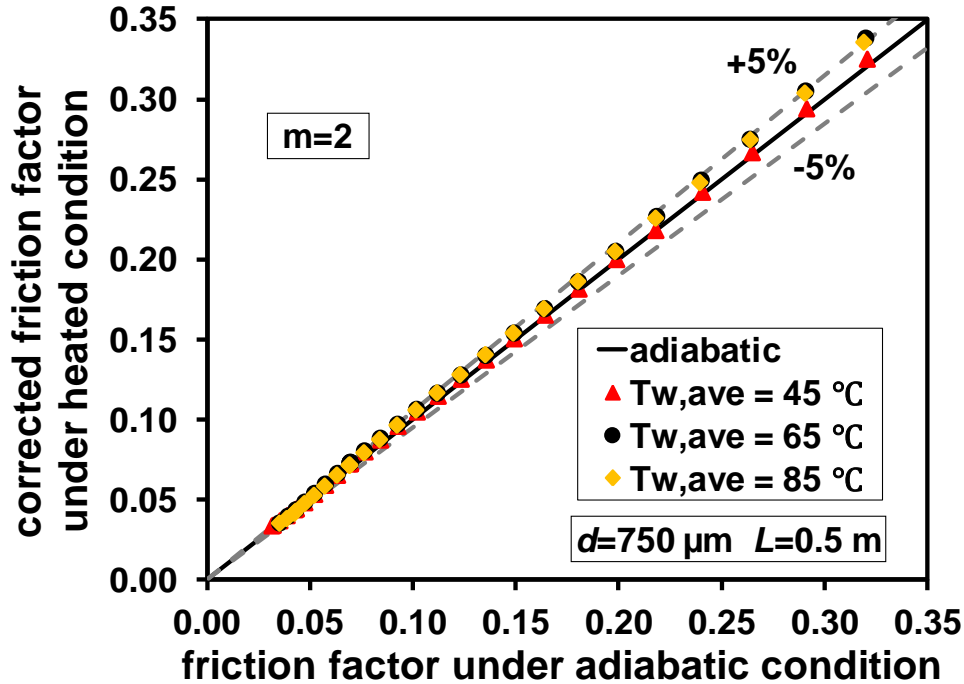
The corrected results with $m=0, 1$ and 2 for the other two microtubes are placed in Appendix C, which shows that an exponent of $m=2$ is more suitable especially when the size of the microtube is smaller, such as in the case of microtube #3.



(a)



(b)



(c)

Figure 4-10: Correction of the friction factors of heated flow through microtube #1: (a) $m=0$, no correction; (b) $m=1$, correction for macro flow; (c) $m=2$, suitable correction with minor deviation.

Figure 4-11 shows a result of corrected friction factor by using Eq. (4.9) with m equal to 2 for laminar gas flow through microtube #3 with different wall average temperature. After being corrected, the friction factors of heated flow are exactly in line with that of the unheated (isothermal) flow. This conclusion also applies to microtube #1 and #2 except for the fact that in these two microtubes the compressibility effect is negligible in laminar regime as the Mach number is very small.

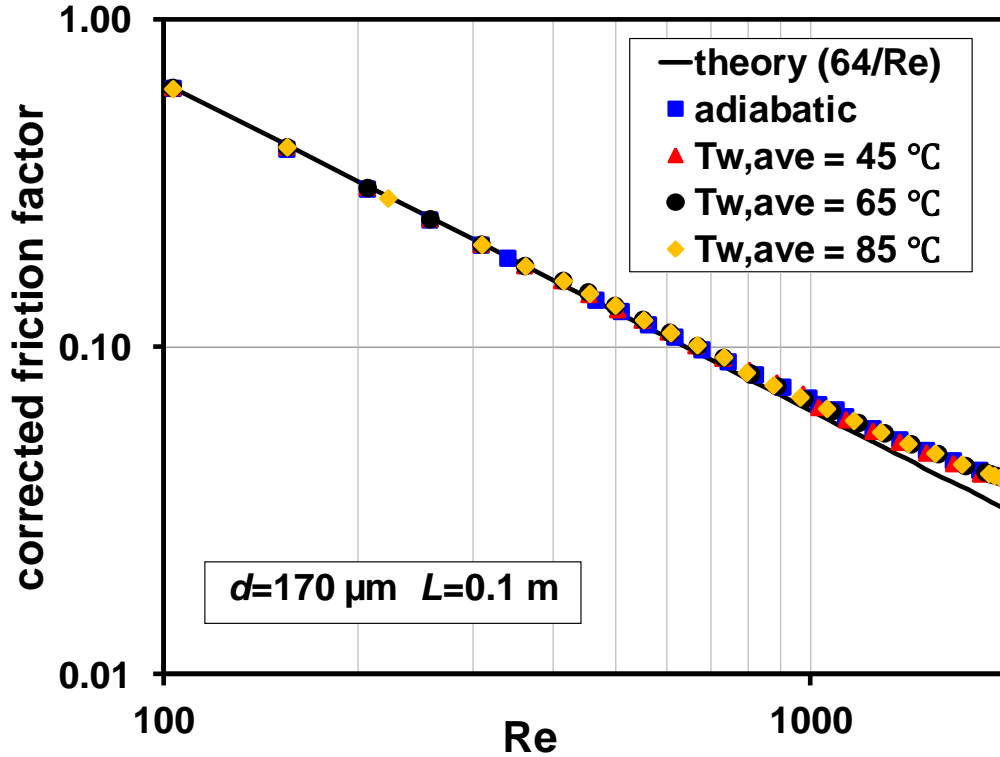


Figure 4-11: Correction of friction factor for heated flow.

4.3.3 Laminar-to-turbulent transition

It can be interesting to check whether the non-isothermal conditions affect the occurrence of flow transition when the Reynolds number approaches the end of laminar regime and continues to increase. Figure 4-12 shows the critical Reynolds number which corresponds to the beginning of transitional regime, as a function of the wall temperature for the three microtubes used in these experimental tests. It can be seen that for microtube #2 and #3 there is very weak dependence of the critical Reynolds number on the wall temperature, which means that the variation of the fluid properties due to the temperature difference between wall and gas does not affect the Reynolds number in correspondence of which the laminar-to-turbulent transition occurs.

However, for microtube #1 with a wall temperature of 45 °C the critical Reynolds number is noticeably lower and seems to be “irregular” compared with the other points in Figure 4-12. It is generally difficult to justify this behaviour if only temperature is considered. By observing the curves in Figure 4-7 it can be noted that the transition mode for this temperature is significantly different from the others. More specifically, the gas flow through microtube #1 at wall

temperature of 45 °C experiences a gradual transition, while the transition becomes quite abrupt if the wall temperature is maintained at 85 °C; this difference is intrinsically linked to the meta-stable nature of the laminar-to-turbulent transition.

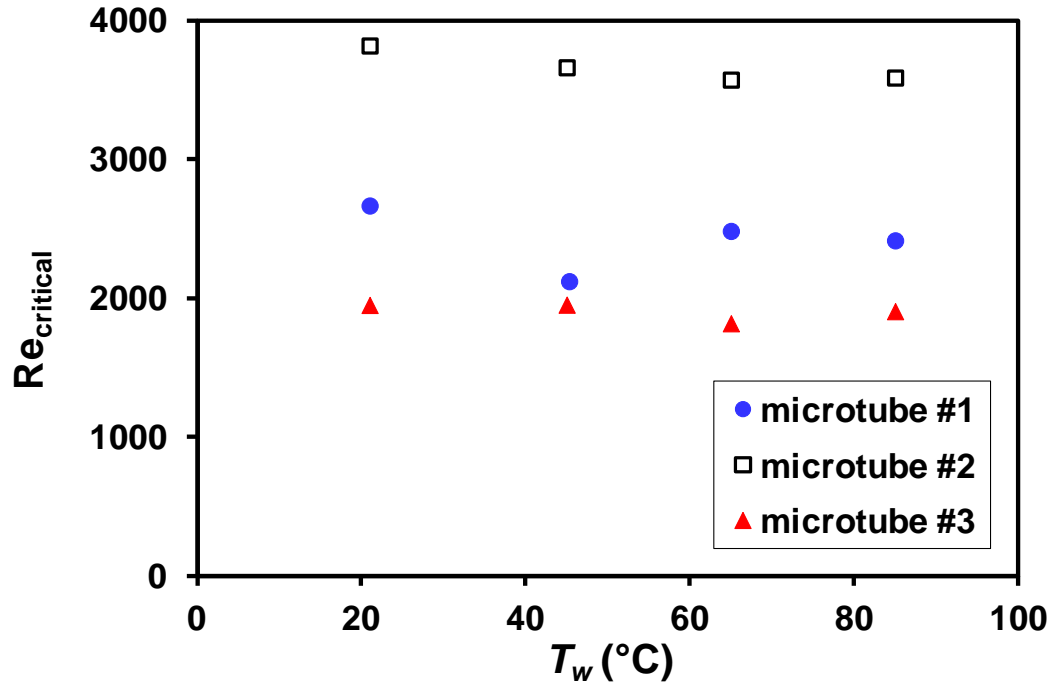


Figure 4-12: Effect of wall heating on critical Reynolds number of microflows.

In the earlier work by Colebrook *et al.* [135] for conventional flows and recent study by Morini *et al.* [136] for microflows, two different transition modes were reported: smooth laminar-to-turbulent transition and abrupt laminar-to-turbulent transition, which are evidenced also in the present work for microtube #3 and microtube #2, respectively. In addition, for the transition of heated flow through microtube #1 at wall temperature of 65 °C and 85 °C, it can be noted that the friction factor first increases suddenly and then there is a gradual growth until to the highest value, which combines the features of the two modes aforementioned and is thus regarded as abrupt-to-smooth transition. No transition which first experiences smooth and then abrupt transition was observed.

Smooth transition begins early (at around $Re=1900$) and the duration in terms of Reynolds number is large ($\Delta Re > 500$). While in abrupt transition, the linear relation between friction factor and Reynolds number seems to have an “inertia” which tends to slow the transition until Reynolds number becomes sufficiently large. Then the friction factor bursts in a sudden step

increase within a small range of Reynolds number ($\Delta Re < 200$). For abrupt-to-smooth transition, the transition occurs at Reynolds number between 2000 and 2500.

4.4 Mach number and flow compressibility

In tubes having an inner diameter less than 500 μm and with a large length-to-diameter ratio (long tube) high pressure ratio between inflow and outflow produces a significant increase of the Mach number along the tube. The compressibility effects can be monitored by the Mach number defined in Eq. (1.3) for gas flows through circular microtubes.

According to conventional theory [63], if the Mach number is less than 0.3, the flow can be modeled locally as incompressible. In addition, when the pressure drop along a pipe length is lower than 5% of the inlet pressure, the effect of flow acceleration in axial direction can be neglected. In other words, the variation of the gas density along the channel can be neglected. The statements above can be translated in terms of the following two inequalities:

$$\begin{cases} \frac{P_{in} - P_{out}}{P_{in}} > 0.05 \\ Ma > 0.3 \end{cases} \quad (4.10)$$

If the first inequality is satisfied, the gas flow can be mathematically described as locally incompressible. However, the density variation along the pipe cannot be ignored. In this case, the effects due to gas acceleration along the pipe become important, even if the Mach number is low. If the Mach number is larger than 0.3 as in the second inequality, the gas flow is not locally incompressible according to conventional theory. In this case the momentum and energy equations are coupled.

The experimental values of average Mach number from the inlet to the outlet are plotted in Figure 4-13 for Reynolds number from 100 to 2000 for the three microtubes tested. It can be noted that the Mach number greatly increases as the tube inner diameter is reduced. This indicates that the flow compressibility can be more significant with downscaling of the channel dimensions. In addition, the average Mach number does not exceed 0.3 for all the three microtubes in laminar regime.

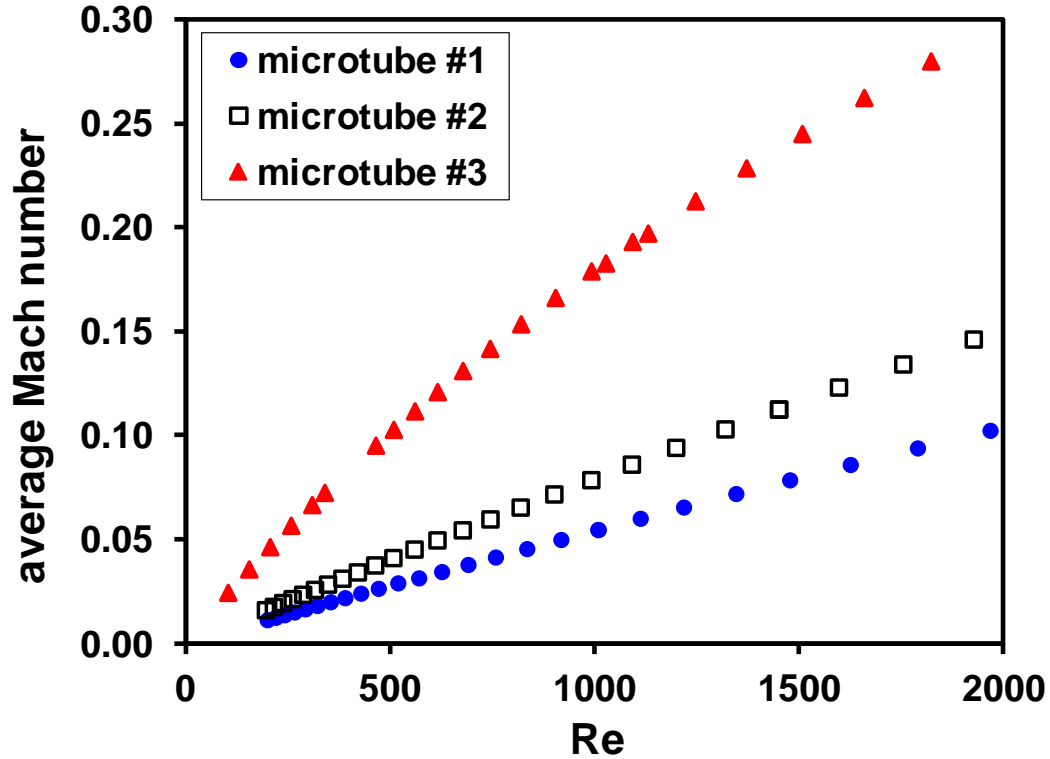


Figure 4-13: Average Mach number as a function of Reynolds number for the three microtubes.

If the Mach number develops linearly along the tube length, its average value obtained from the tube inlet and outlet is representative for the consideration of compressibility effects. However, the axial distribution of Mach number may not be ideally linear, especially in high speed gas flows. In the numerical investigation of Hong *et al.* [137] it was found that the Mach number increases rather mildly along the first part of the tube length, while in the last part the increase in Mach number becomes very sharp. For this reason, the values of the outlet Mach number in the present experiment are checked and shown in Figure 4-14. Comparing Figure 4-13 with Figure 4-14 it is evident that the outlet Mach number is larger than the average value, especially for the smallest microtube. The outlet Mach number is larger than 0.3 in microtube #3 at high mass flow rate. This means that close to the outlet in the case of the microtube #3 the compressibility effects cannot be considered negligible at all. On the contrary, the compressibility can be considered negligible for microtube #1 and #2.

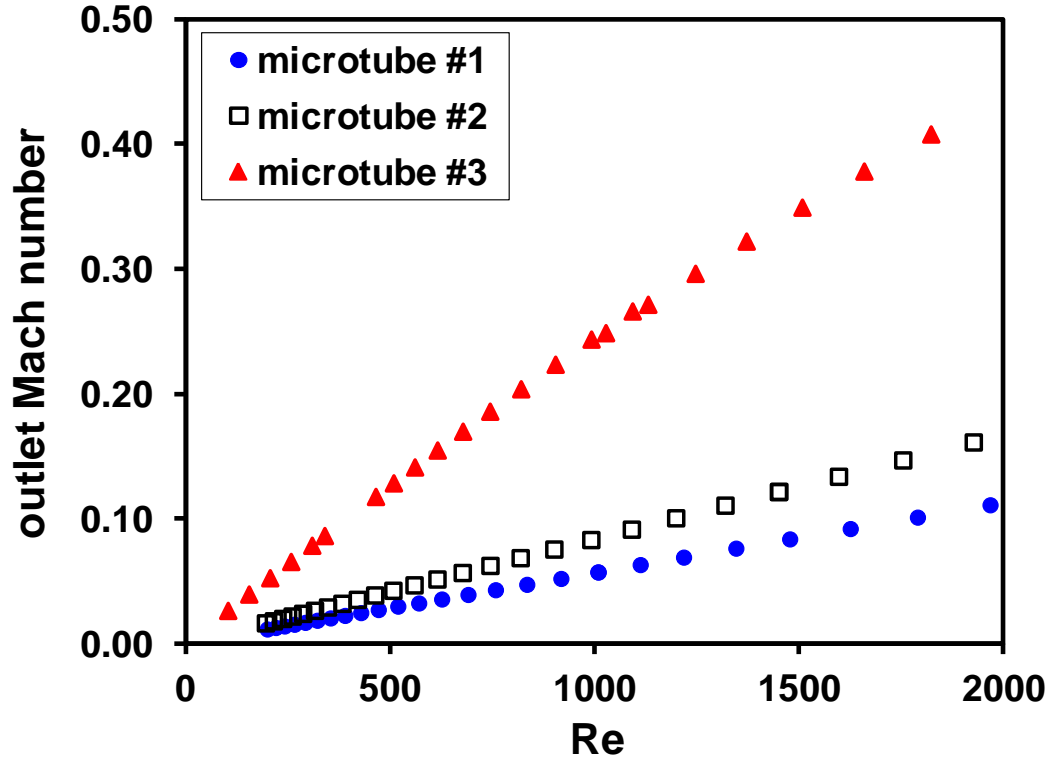


Figure 4-14: Outlet Mach number as a function of Reynolds number for the three microtubes.

In order to check the validity of the second inequality in Eq. (4.10), the value of pressure drop in the experimental tests for all the three microtubes is calculated, as shown in Figure 4-11. It is worth noting that in most cases tested, the pressure drop is larger than 5% of the inlet pressure. Therefore, influence of flow acceleration should be carefully considered in the flow through microtube #1 and #2 for Reynolds number larger than 500 and through microtube #3 for Re larger than 100. In addition, the ratio between the pressure drop and the inlet pressure does not increase linearly with the Reynolds number for microtube #3.

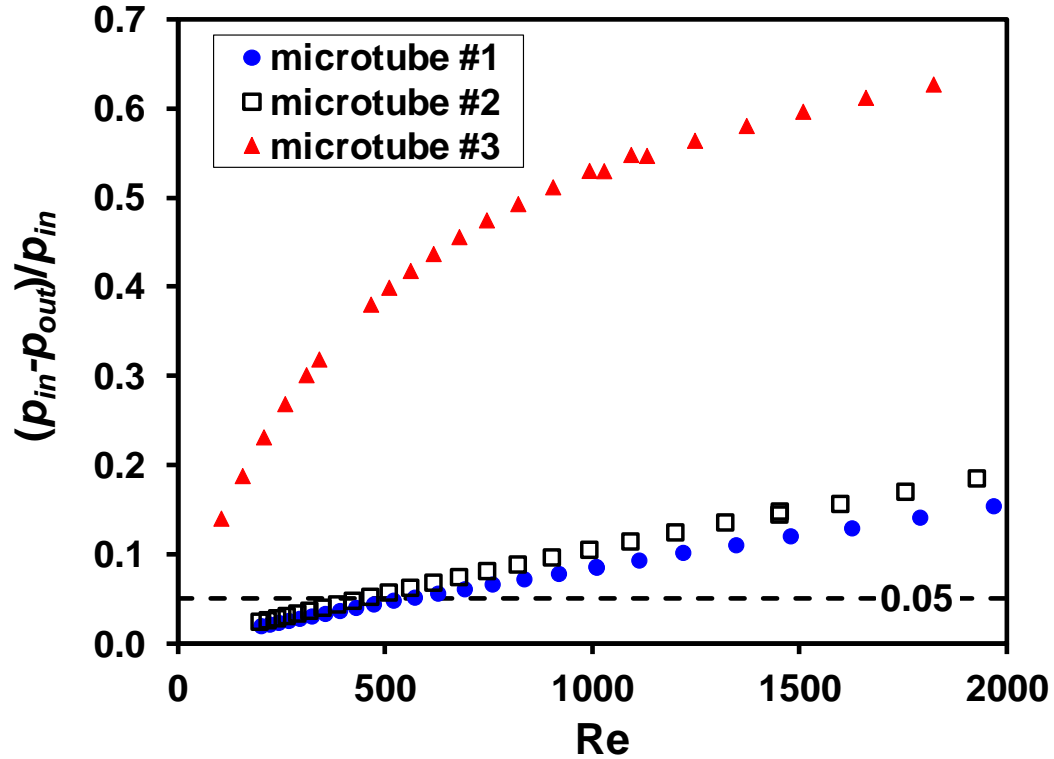


Figure 4-15: Pressure drop of the three microtubes versus Reynolds number.

As mentioned previously, the pressure loss due to gas acceleration is excluded in the evaluation of the friction factor in order to compare with theoretical prediction for incompressible flow. However, it is evident from Figure 4-6 that for adiabatic flow through microtube #3, the experimental friction factor is larger than the predicted values from Poiseuille law ($64/Re$) for Reynolds number greater than 1000. This is because the radial variations of fluid density and pressure results in an extra pressure drop. This extra pressure drop can be theoretically calculated by solving 2-dimensional Navier Stokes equation for compressible flow. Consequently, the value of the friction factor becomes dependent on the flow Mach number for locally compressible flow.

Asako *et al.* [61] have calculated numerically how the friction factor depends on the (average) Mach number in laminar regime and proposed the following correlation:

$$f = \frac{64}{Re} + 2.703 \frac{Ma_{ave}}{Re} + 93.89 \frac{Ma_{ave}^2}{Re} \quad (4.11)$$

An analytical relation between the friction factor for compressible flow and the Mach number has been also proposed by Li *et al.* [62]:

$$f = \frac{64}{Re} \left(1 + \frac{Ma_{ave}^2}{1.5 - 0.66Ma_{ave} - 1.14Ma_{ave}^2} \right) \quad (4.12)$$

Figure 4-16 compares the experimental friction factor with the correlations proposed by Asako *et al.* [61] and Li *et al.* [62] which quantitatively take into account the influence of Mach number. It turns out that the correlation provided by Asako *et al.* [61] works better than the one by Li *et al.* [62] in the prediction of the friction factor for compressible laminar flow, although the difference between these two correlations is relatively small. Furthermore, the increase (compared with Poiseuille law) of experimental friction factors is still underestimated to a certain extent by applying Asako's correlation, especially when the Reynolds number is larger than 1600, as in Figure 4-16.

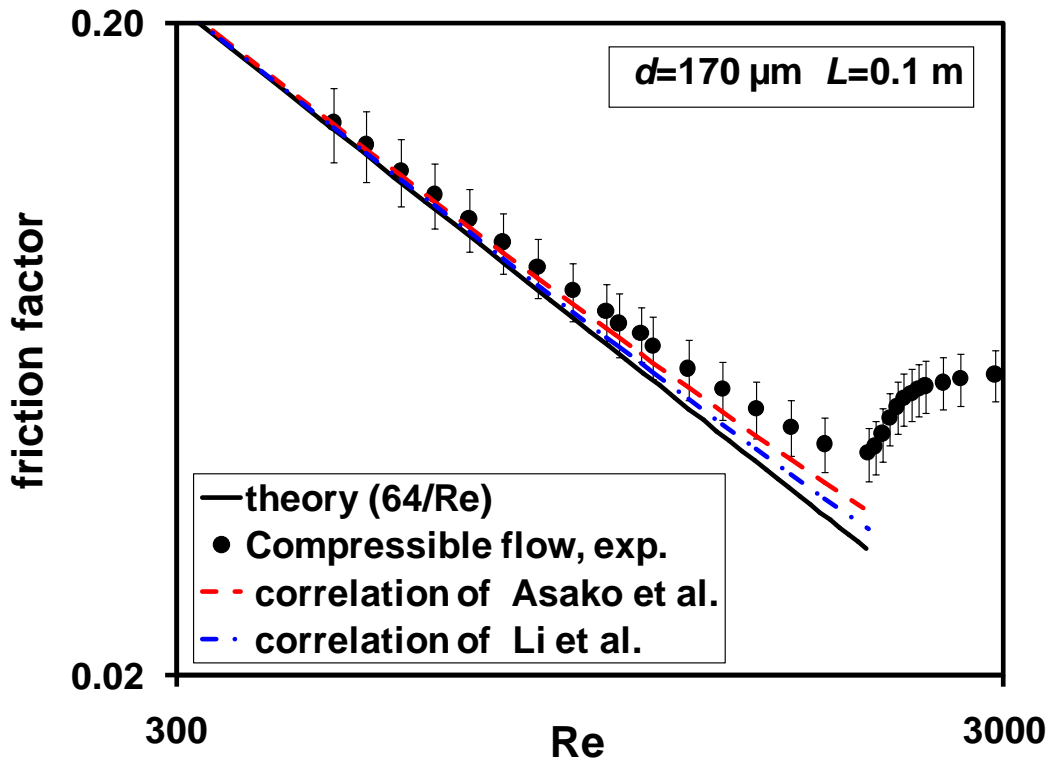


Figure 4-16: Friction factor of compressible flow-comparison between experimental data and theoretical/numerical predictions (by using average Ma as suggested).

By plotting both friction factor and Mach number versus Reynolds number, as shown in Figure 4-17, a distinct deviation from theory can be noted even though the average Reynolds number is smaller than 0.3. Instead, the deviation emerges when the outlet Mach number begins to exceed 0.3. Therefore, the value of friction factor is underestimated if the average Mach

number is used in the correlations by Asako *et al.* [61] and Li *et al.* [62]. The main reason is that the axial distribution of the Mach number is far from being linear if the outlet Mach number is larger than 0.3. Therefore, these data seems to suggest that the outlet Mach must be used instead of its average value in order to check the importance of compressibility effects in microtubes. If the outlet Mach number is larger than 0.3, the flow compressibility cannot be neglected, as well evidenced by the data shown in Figure 4-17.

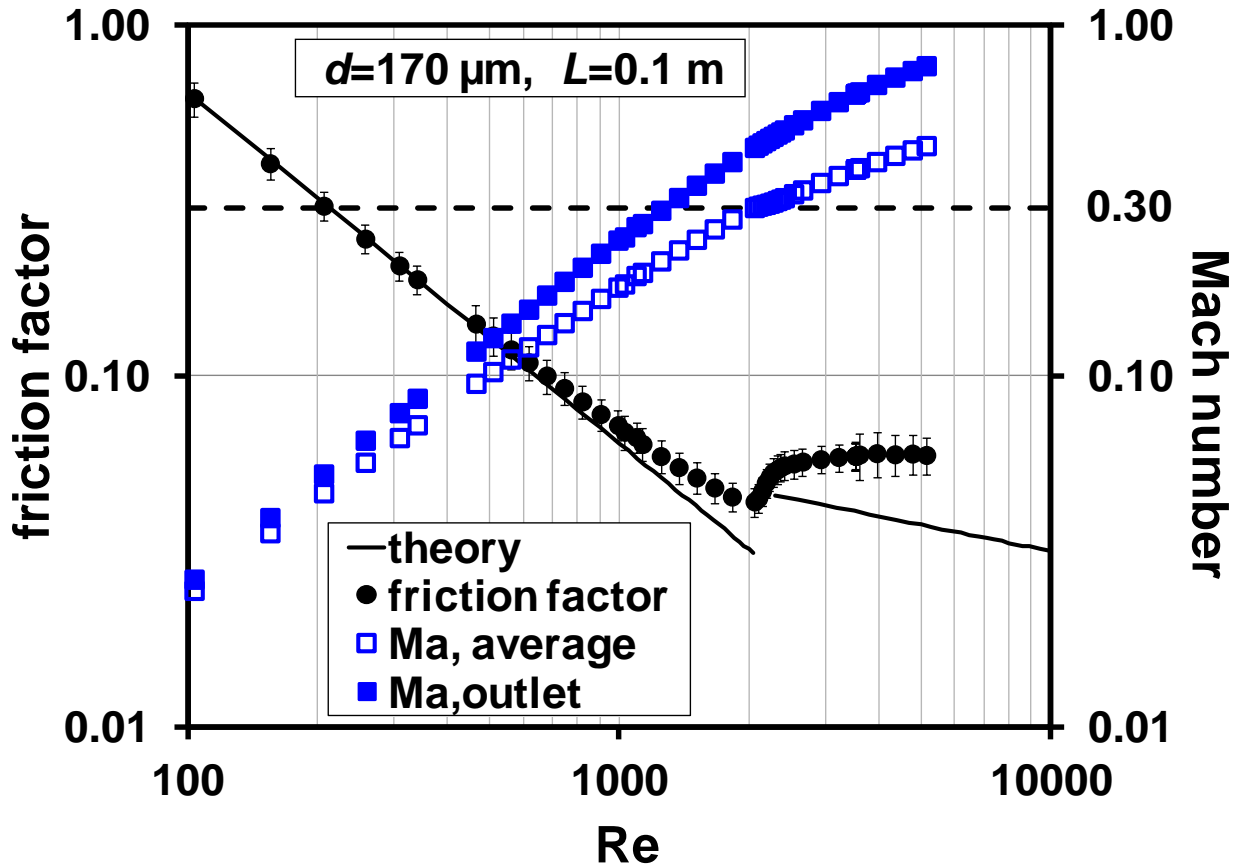


Figure 4-17: Friction factor and Mach number versus Reynolds number through microtube #3.

Figure 4-18 shows the prediction from the correlations in Eq. (4.11) and (4.12) when the outlet Mach number instead of the average one is used for the calculation of friction factor. By using the outlet Mach number, it is noted that the experimental friction factor can be well predicted by both correlations, considering the experimental uncertainties.

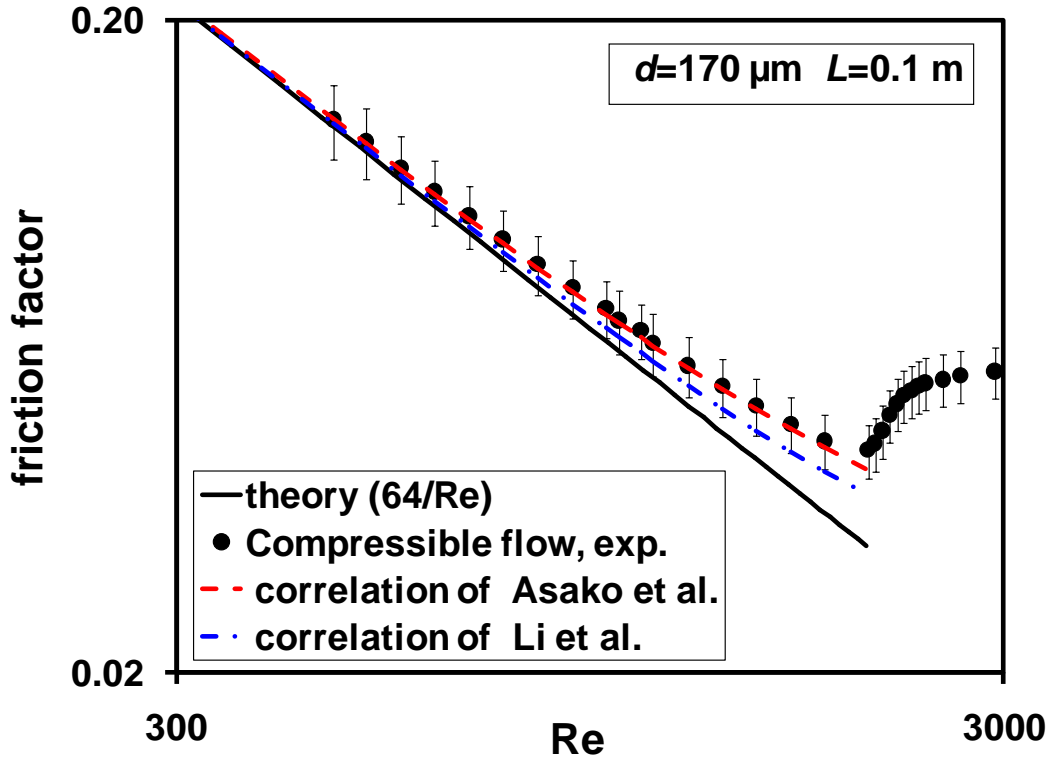


Figure 4-18: Friction factor of compressible flow-comparison between experimental data and theoretical/numerical predictions (by using outlet Mach number).

4.5 Conclusions

In this chapter the characteristics of friction factors of nitrogen flows through commercial stainless steel microtubes with inner diameters of 750 μm , 510 μm and 170 μm have been experimentally investigated in laminar, transitional and turbulent regimes ($\text{Re}=200\text{-}8000$).

For adiabatic gas flow through microtubes, the conventional theory for flow at macro scale is able to predict the friction factor in laminar flow if the effects due to flow compressibility are negligible.

When the gas flow in microtubes is heated, larger values of friction factor have been evidenced and traditional correlation tends to underestimate the effect of temperature-dependent properties. A larger correction factor equal to 2, which is justified by very large temperature gradient at microscale, has been found to take into account this effect accurately for all the three microtubes in tests with different wall temperatures. In addition, the experimental data demonstrate that the values of critical Reynolds number are independent of the magnitude of

wall temperature. However, the heating on the microtube wall can affect the characteristics of laminar-to-turbulent transition.

The flow compressibility effects are evidenced experimentally even in laminar regime ($Re \sim 1200$) for gas flows through the smallest microtube tested. It has been found that the value of the outlet Mach number ($Ma_{out} > 0.3$) is more accurate than that of the average Mach number ($Ma_{ave} > 0.3$) to fully account for the influence of compressibility effects on the friction factor. This has been confirmed by applying the experimental data to the correlations developed by Li *et al.* [62] and Asako *et al.* [61] for the determination of friction factors, which underestimate the friction factors by using average Mach number but predict well if the outlet Mach number is used.

The next chapter will be devoted to the investigation of nitrogen flow forced convection through these three commercial microtubes.

5 Gas Forced Convection through Microtubes

5.1 Theory and data reduction

5.1.1 Thermal entrance region

The *thermal entrance region* of a microchannel is defined as a region where the temperature boundary layer is developing (see Figure 5-1). The thermal entrance region can or cannot correspond to the inlet region of the microchannel; for example, if the heating begins only at some point after the inlet section the thermal entrance region can be uncoupled from the hydrodynamic entrance region. For this reason, in the thermal entrance region the velocity profile could be either developed or developing.

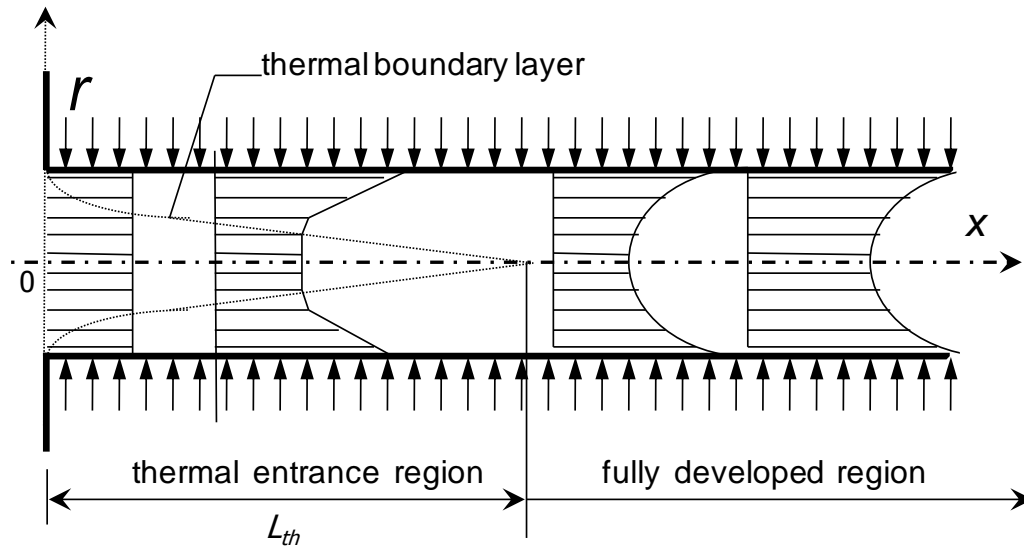


Figure 5-1: Schematic diagram of thermal entrance region.

After the thermal entrance region the local and the bulk temperature continue to change axially but they respect the following equality:

$$\frac{\partial}{\partial x} \left[\frac{T_w(x) - T(r, x)}{T_w(x) - T_b(x)} \right] = 0 \quad (5.1)$$

where x is the axial coordinate, r is the radial coordinate, T_w the wall temperature, T the fluid temperature at the point (r, x) and T_b the bulk temperature defined as:

$$T_b = \frac{1}{\dot{m}c_p} \int_{\Omega} \rho v_z c_p T d\Omega \quad (5.2)$$

in which ρ is the fluid density and d is the inner diameter of the pipe. The region in which Eq. (5.1) is satisfied is called *fully developed region*.

In the thermal entrance region the convective heat transfer coefficient is larger than in the fully developed region. In laminar regime the value assumed by the convective heat transfer coefficient along the fully developed region is constant and depends only on the geometry of the channel cross-section. Therefore, the effect of thermal entrance region cannot be neglected if the length of this region is large compared to the total length of the pipe. The length of this region is called *thermal entry length* and can be calculated as follows [138]:

$$\begin{aligned} L_{thermal} &= 0.034 \text{Re} \text{Pr}_f d, \text{ laminar flow} \\ L_{thermal} &\approx 10d, \text{ turbulent flow} \end{aligned} \quad (5.3)$$

where Pr_f is the Prandtl number of the fluid.

The thermal entry length has been calculated for nitrogen flows through the three microtubes listed in Table 4-1, which have lengths of 500 mm, 200 mm and 100 mm, respectively. The result is shown in Figure 5-2. It can be noted that in turbulent flow regime ($\text{Re} > 4000$) the thermal entry length is small compared with microtube length. Therefore, the influence of thermal development on convective heat transfer can be considered insignificant for all the tested tubes. However, in laminar regime ($\text{Re} < 2300$) the thermal entry region is relatively long at large Reynolds number. Especially for microtube #2 the thermal entry length exceeds 10% of the microtube length when Re approaches 2000. As a result, the effects of thermal development should be considered in the calculation of the average value of the convective heat transfer coefficient. It is important to highlight that the effect due to the entrance region tends to become smaller for microtubes with smaller inner diameter, as microtube #3.

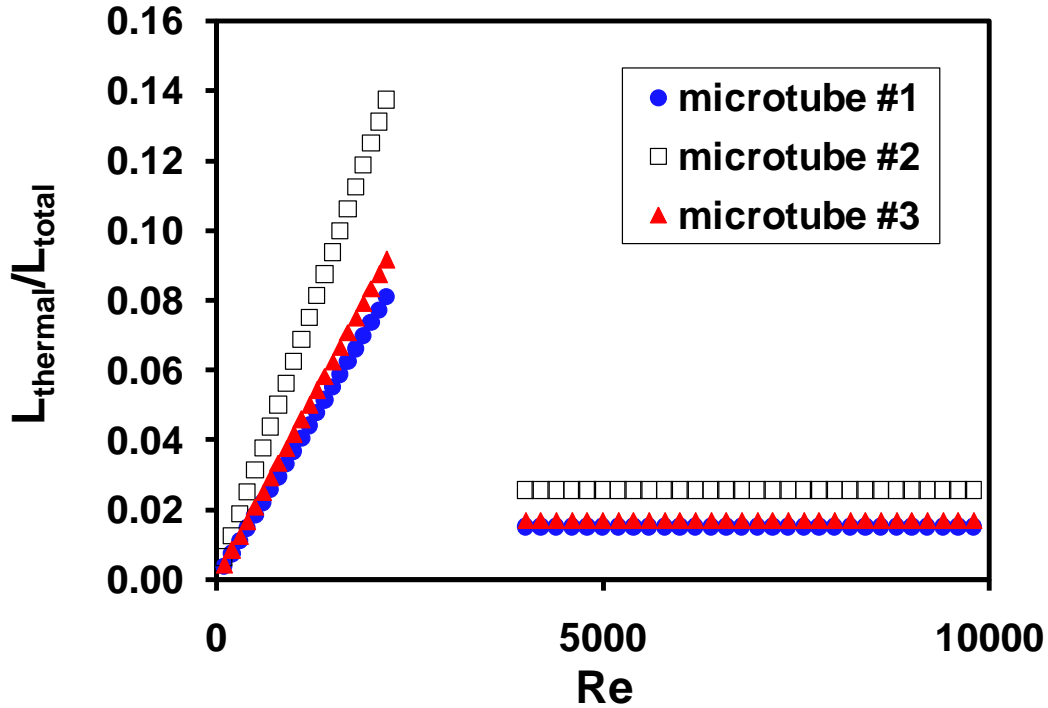


Figure 5-2: Dimensionless thermal entry length of the three microtubes as a function of Reynolds number.

5.1.2 Thermal boundary conditions

In internal forced convection the heat transfer from the wall to the fluid (or inversely, from the fluid to the wall) is characterized by a certain thermal boundary condition specified at the wall-fluid interface. In pure convection the fluid temperature can be determined only in the fluid region without solving the temperature problem for the solid wall. However, in convection through microchannels where the solid wall thickness is comparable to the channel diameter or even larger, the heat conduction solid the solid walls can become crucial in radial and/or circumferential as well as axial directions. In this case the temperature problem for the solid wall should be analyzed simultaneously with that for the fluid in order to obtain the real heat flux distribution on the wall-fluid interface, and this coupled wall-fluid heat transfer is referred to as *conjugate heat transfer*.

The convective heat transfer coefficients are closely linked to the specific thermal boundary conditions applied, especially in the laminar regime where many micro flows are operated. Therefore, for microchannels it is very important know the exact thermal boundary conditions in

order to explain correctly the experimental data and to develop accurate numerical model in the simulation of such problems. The common thermal boundary conditions are described in this section following the classification proposed by Shah and London [67].

In general the thermal boundary conditions can be classified into two categories: T boundary conditions and H boundary conditions. The T boundary conditions can be further divided into the following three types:

1) *T boundary condition*, in which the wall temperature is both axially and peripherally constant. This thermal boundary condition can be described as follows:

$$T|_{\Gamma} = T_w(x) = \text{const.} \quad (5.4)$$

2) *T3 boundary condition*, in which the external wall temperature ($T_{w,ex}$) is constant in the flow direction while the circumferential wall heat flux is proportional to the internal wall temperature ($T|_{\Gamma}$). In this case the thermal boundary condition can be expressed as:

$$k \frac{\partial T}{\partial n} \Big|_{\Gamma} = U_w (T_{w,ex} - T|_{\Gamma}) \quad (5.5)$$

where U_w is the wall thermal transmittance.

This boundary condition can be applied to solid walls with finite thermal resistance. When the wall thermal resistance tends to be infinity (the wall thermal transmittance approaches 0), T3 boundary condition is simplified to T boundary condition.

3) *T4 boundary condition*, in which the temperature of the outer free fluid T_a (ambient temperature) is constant while the wall heat flux is not proportional to the wall temperature but related to thermal radiation. In this case the thermal boundary condition can be written as:

$$k \frac{\partial T}{\partial n} \Big|_{\Gamma} = \varepsilon_w \sigma_0 (T|_{\Gamma}^4 - T_a^4) \quad (5.6)$$

where ε_w is the emissivity of the external wall and σ_0 is the Stefan-Boltzmann constant. It should be underlined that in this case, the wall thermal resistance is considered negligible.

The thermal boundary conditions of approximately constant axial heat transfer rate per unit length are referred to as H boundary conditions, in which there are several difference situations:

1) *H1 boundary condition*, in which the heat transfer rate between the wall and the fluid is constant in flow direction and the wall temperature at any cross section is constant in circumferential direction. This thermal boundary condition can be described as:

$$q' = \dot{m}c_p \frac{dT_b}{dx} = \text{const.}, \quad \text{independent of } x$$

$$T|_{\Gamma} = T_w = \text{const.}, \quad \text{independent of } r \text{ and } \Gamma$$
(5.7)

where \dot{m} is the fluid mass flow rate in the microchannel, q' is the wall heat transfer rate per unit of length of the microchannel and T_b is the bulk temperature. This boundary condition can be commonly encountered in microchannels heated by means of electrical resistance.

2) *H2 boundary condition*, under which the heat transfer rate per unit of heat transfer area (q'') is constant both axially and circumferentially. This boundary condition can be mathematically expressed as:

$$q''\Gamma_h = \dot{m}c_p \frac{dT_b}{dx} = \text{const.} \quad \text{independent of } x$$

$$k \frac{\partial T}{\partial n} \Big|_{\Gamma} = q'' = \text{const.} \quad \text{independent of } x, r \text{ and } \Gamma$$
(5.8)

where Γ_h is the heated perimeter of the microchannel. In this case the wall temperature is not constant along circumferential direction.

3) *H3 boundary condition*, in which the wall heat transfer rate is constant in axial direction while the heat flux is proportional to the wall temperature in circumferential direction. In this case the boundary condition can be written as:

$$q' = \dot{m}c_p \frac{dT_b}{dx} = \text{const.} \quad \text{independent of } x$$

$$k \frac{\partial T}{\partial n} \Big|_{\Gamma} = U_w (T_{w,0} - T|_{\Gamma})$$
(5.9)

Actually H1 and the H2 boundary conditions can be considered as the special cases of H3 boundary condition: with the wall transmittance U_w equal to zero the H3 boundary condition becomes the H2 boundary condition and the H3 boundary condition is the same as the H1 boundary condition at the wall transmittance equal to infinity.

4) *H5 boundary condition*, in which the wall heat flux varies exponentially along the flow direction while the peripheral wall temperature is constant at a particular section x . This boundary condition is described as:

$$q' = q'_0 e^{m'x}$$

$$T|_{\Gamma} = T_w = \text{const.} \quad \text{independent of } (r, \Gamma)$$
(5.10)

where m' is the exponent.

5.1.3 The Nusselt number

For flow through channels of circular cross sections the average value of the Nusselt number can be calculated theoretically for different thermal boundary conditions, as in many textbooks. For fully developed flow in laminar regime under T boundary condition, the average Nusselt number takes the value $\overline{Nu_T}=3.66$ for the case of pressure driven with negligible external volume forces, axial heat conduction, viscous dissipation, flow work and thermal energy sources within the fluid. It is important to highlight that for circular cross section there are no differences between H1, H2 and H3 boundary conditions in terms of Nusselt numbers. In this case, for laminar flows, the Nusselt number can be expressed as:

$$\overline{Nu_H} = \frac{48}{11} \left(\frac{1}{1 + (3/44)S_g^* + (48/11)Br} \right) \quad (5.11)$$

When thermal energy sources within the fluid are absent ($S_g^*=0$) and the viscous dissipation is negligible ($Br=0$) the Nusselt number tends to the value of 48/11.

In this thesis the only thermal boundary condition that has been applied experimentally is the H boundary conditions but the real boundary condition imposed during the experiments will be critically analyzed in the next sections.

There are a lot of correlations for the prediction of the average Nusselt number along a tube in laminar, transitional and turbulent regimes. Among them the ones proposed by Volker Gnielinski are widely used for their good accuracy. Gnielinski accumulated a large number of experimental data in order to investigate the convective heat transfer coefficients of conventional flows in ducts. Combining the experimental data with the theoretical predictions and/or numerical calculations by Shah and London [67], Sieder and Tate [15], Spang [139], Churchill and Zajic [140], etc, he developed a series of equations for calculating the Nusselt number of conventional incompressible flows [23, 133, 141]. Table 5-1 summarizes the expressions of Nu given by Gnielinski for incompressible pipe flows in laminar, transitional and turbulent regimes.

Table 5-1: Calculation of Nusselt number in various flow regimes.

Thermal boundary conditions	Flow regimes	Calculation of Nusselt number	Range of validity
Constant wall temperature (T b.c.)	laminar	$Nu_{T,laminar} = \left[Nu_{T,1}^3 + (Nu_{T,2} - 0.7)^3 + Nu_{T,3}^3 \right]^{1/3}$ where: $Nu_{T,1} = 3.66$ $Nu_{T,2} = 1.615(2300 Pr d / L)^{1/3}$ $Nu_{T,3} = \left(\frac{2}{1 + 22 Pr} \right)^{1/6} (2300 Pr d / L)^{1/2}$	$Re \leq 2300$ $0.1 \leq Pr \leq 10^3$ $d / L \leq 1$
	transitional	$Nu_{T,transitional} = \frac{10^4 - Re}{10^4 - 2300} Nu_{T,laminar} + \frac{Re - 2300}{10^4 - 2300} Nu_{T,turbulent}$	$2300 \leq Re \leq 10^4$ $0.1 \leq Pr \leq 10^3$ $d / L \leq 1$
	turbulent	$Nu_{T,turbulent} = \frac{(0.0308 / 8) 10^4 Pr}{1 + 12.7 \sqrt{0.0308 / 8} (Pr^{2/3} - 1)} \left[1 + (d / L)^{2/3} \right]$	$10^4 \leq Re \leq 10^6$ $0.1 \leq Pr \leq 10^3$ $d / L \leq 1$
Constant heat flux (H b.c.)	laminar	$Nu_{H,lam.} = \left[Nu_{H,1}^3 + (Nu_{H,2} - 0.7)^3 + Nu_{H,3}^3 \right]^{1/3}$ where: $Nu_{H,1} = 4.364$ $Nu_{H,2} = 1.953(2300 Pr d / L)^{1/3}$ $Nu_{H,3} = 0.924(Pr)^{1/3} (2300 Pr d / L)^{1/2}$	$Re \leq 2300$ $0.1 \leq Pr \leq 10^3$ $d / L \leq 1$
	transitional	$Nu_{H,transitional} = \frac{10^4 - Re}{10^4 - 2300} Nu_{H,laminar} + \frac{Re - 2300}{10^4 - 2300} Nu_{H,turbulent}$	$2300 \leq Re \leq 10^4$ $0.1 \leq Pr \leq 10^3$ $d / L \leq 1$
	turbulent	$Nu_{H,turbulent} = \frac{(0.0308 / 8) 10^4 Pr}{1 + 12.7 \sqrt{0.0308 / 8} (Pr^{2/3} - 1)} \left[1 + (d / L)^{2/3} \right]$	$10^4 \leq Re \leq 10^6$ $0.1 \leq Pr \leq 10^3$ $d / L \leq 1$

These expressions consider the effects due to the thermal entrance region and can be also applied to very short pipes ($d/L=1$) with good accuracy. The calculation of Nu in transitional regime, as listed in Table 5-1, is a smooth interpolation of the values indicated for the Nusselt number in laminar and turbulent regime. In addition, at very small values of Prd/L where the developing region can be neglected, the value of Nusselt number is equal to the analytical

prediction under either T boundary condition or H boundary condition. The applicability of these calculations will be examined for gaseous flow convection through microtubes.

5.1.4 Reduction of experimental data

In order to determine the axial trend of the local convective heat transfer coefficient between gas flow and heated wall of the microtube, the bulk fluid temperature at each location along the microtube is needed. This quantity is not easy to measure in a tube having an inner diameter smaller than 1 mm. On the contrary, it is comparatively easier to deduce the mean value of the convective heat transfer coefficient along the whole microtube. The mean value can be expressed as a function of the average fluid bulk temperature and the mean wall temperature.

Under an H boundary condition (constant wall heat flux) the mean Nusselt number can be calculated from the experimental parameters by using the following equation:

$$Nu_m = \frac{hd}{k_f} = \frac{d q_{w,i}}{k_f (\bar{T}_{w,i} - \bar{T}_b)} \quad (5.12)$$

where $\bar{T}_{w,i}$ is the average value of the inner wall temperature along the tube, \bar{T}_b is the gas mean bulk temperature averaged between the inlet and outlet, k_f the fluid thermal conductivity calculated at the fluid average bulk temperature, d the hydraulic diameter of the microtube and $q_{w,i}$ the heat flux on the inner wall of the microtube.

The heat flux can be calculated by means of an energy balance between the inlet and the outlet of the microtube:

$$q_{w,i} = \frac{\dot{m} c_{pf} (T_{b,out} - T_{b,in})}{\pi d L_h} \quad (5.13)$$

where \dot{m} is the mass flow rate, c_{pf} is the gas specific heat at the average bulk temperature, $T_{b,in}$ and $T_{b,out}$ are the values of the gas temperature measured by thermocouples inserted in the inlet and outlet plenums of the test section and L_h is the heated length of the microtube.

By considering the order of magnitude of the wall heat flux imposed by Joule heating on the external surface of the microtubes, the maximum temperature difference between the external and internal surfaces of the microtubes has been estimated to be of the order of 0.15 K for stainless steel ($k_w=15$ W/mK) by using the classical expression of the thermal resistance of an annulus. This temperature difference is smaller than the typical uncertainty of the thermocouples

(± 0.5 K). Therefore, it is possible to replace the wall internal surface temperature by the external surface temperature ($T_{w,e}$) with negligible influence on the Nusselt number. The average temperature of the wall external surface is directly determined by the measurement of a series of K-type thermocouples attached to the microtubes.

Under an ideal H boundary condition, in the fully developed region of a tube a linear axial distribution of bulk temperature is expected ([67]). For this reason, the following definition of the mean bulk temperature is adopted by most researchers for the calculation of the average value of the gas bulk temperature along the microtube under H boundary condition:

$$\bar{T}_b = \frac{T_{b,in} + T_{b,out}}{2} \quad (5.14)$$

5.1.5 Temperature different between fluid and wall: from macroscale to microscale

The temperature difference between the fluid and the wall is a critical point for the accurate determination of the Nusselt number. In this section by means of practical examples the impact of this temperature difference on the Nusselt number when the pipe size is downscaled from macroscale to microscale and the fluid is changed from liquid to gas will be deeply discussed. This analysis is useful in order to provide practical tips in the design of temperature measurement and thermal isolation of the microfluidics devices used for the analysis of forced convection in microtubes.

Under H boundary condition, it is easy to demonstrate that the temperature difference between the wall and the fluid can be expressed as follows:

$$T_w - T_f = \frac{\text{Re}}{4} \cdot d \cdot \frac{\mu C_p}{\lambda} \cdot \frac{\partial T_f}{\partial x} \cdot \frac{1}{\text{Nu}} \quad (5.15)$$

where $\frac{\partial T_f}{\partial x}$ is the gradient of fluid temperature in flow direction which can be expressed as $\Delta T/L$.

It is evident that this difference depends on the dimensions of the tube. In order to have an insight of wall and fluid temperature difference when the tube inner diameter is reduced from macro scale to micro scale, here a convective flow through two different tubes is explored. The geometrical characteristics of the tubes used for this comparison are quoted in Table 5-2. It is assumed that the uniform heat flux imposed at the wall (H boundary condition) is able to heat the

fluid from 20 °C to 80 °C. Two working fluids are considered: water and air. The thermal properties of the two fluids are quoted in

Table 5-3.

Table 5-2: Dimension of the tubes in comparison and assumed boundary conditions.

Parameters	Conventional tube	Microtube
	Tube A	Tube B
Inner diameter (mm)	10	0.1
Length (mm)	1000	100
Fluid inlet temperature (°C)	20	20
Fluid outlet temperature (°C)	80	80
Thermal boundary condition	constant heat flux	constant heat flux

Table 5-3: Thermal properties of water and air [133].

Thermal properties	Water	Air
dynamic viscosity (Pa.s)	0.0004668	0.00001827
thermal capacity (Jkg ⁻¹ K ⁻¹)	4185	1009
thermal conductivity (Wm ⁻¹ K ⁻¹)	0.58	0.024

The convective flow through the circular tubes is assumed fully developed, laminar and incompressible. Therefore, the Nusselt number is theoretically equal to 48/11 under H boundary condition. Using the above data to Eq. (5.15), the temperature difference between fluid and wall is calculated as a function of Reynolds number, as shown in Figure 5-3.

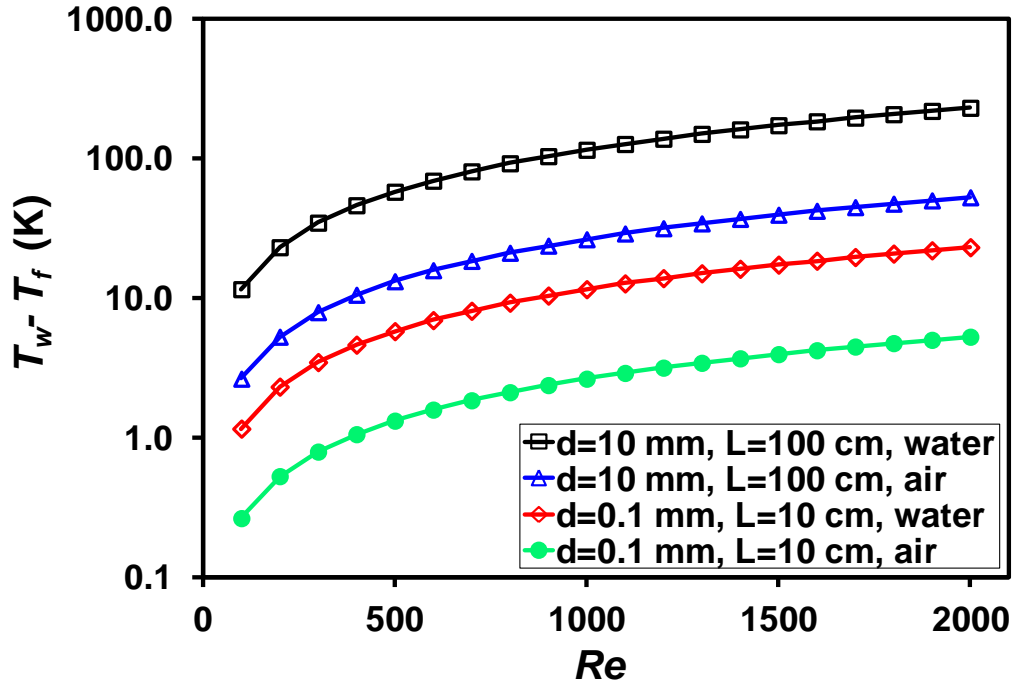


Figure 5-3: Wall and fluid temperature difference as a function of Reynolds number

From Figure 5-3 it is evident that for water flow through a conventional tube (Tube A), the temperature difference between fluid and wall is larger than 10 °C, which is quite favorable for accurate measurement. When the working fluid is changed to air, the temperature difference is greatly reduced by a factor of nearly 10, but is still measurable as its value is generally larger than 10 °C for Re larger than 500. In water flow through microtube the temperature difference is even smaller than that in air flow through macrotube at the same Reynolds number.

Finally, if air is used for flows through microtube, it is evident that this value is surprisingly small. Especially for Re smaller than 400, the temperature difference between wall and fluid is no larger than 1 °C. If typical K thermocouples (accuracy ± 0.5 °C) are used to measure the wall and fluid temperature in this case, the error in the measurement of this temperature difference will be ± 1 °C, which is unfavorably comparable to the experimentally determined temperature difference. As a result, the local Nusselt number evaluated by means of this difference is affected by a very large uncertainty. Therefore, if one wants to investigate experimentally the thermal characteristics of gas flow through microtubes, the lower limit in terms of Re or mass flow rate should be the first concern in the design stage of experiment. This lower limit should be carefully pre-determined based on the size of the tube, the thermal properties of the fluid, as well as estimation on the possible heat loss to the environment.

On the other hand, the lowest curve in Figure 5-3 indicates that if one wants to heat air flow through microtube to a certain temperature, the required temperature difference between fluid and wall, or the thermal driving force, is the smallest compared with liquid fluids or flow through conventional tubes. This to some extent is quite advantageous as the wall temperature does not need to be maintained at a high value. Thus the external heat loss can be effectively reduced. In addition, in this case the measurement of the axial temperature of the external surface of the microtube gives a very good indication of the axial trend of the bulk temperature along the microchannel without using internal sensors due to the limited temperature difference between wall and fluid.

5.1.6 Measurement of fluid outlet temperature

The measurement of the outlet gas bulk temperature can become critical when the mass flow rate is very low (low Reynolds numbers). In the design of the test rig used in this work, the outlet gas temperature is measured by means of a K-type thermocouple inserted into a special section at the end of the tested microtube, as shown in Figure 5-4.

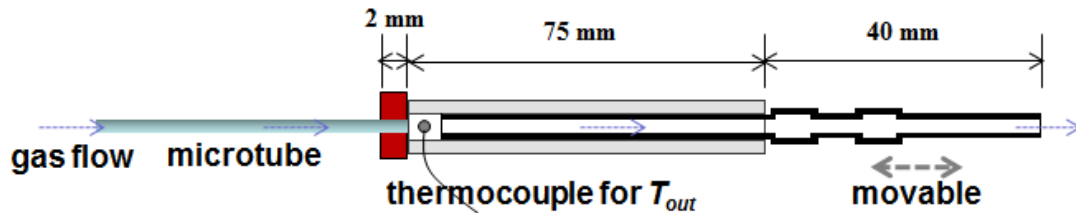


Figure 5-4: Sketch of microtube outlet section designed for the measurement of exit gas temperature.

The thermocouple is held at the center of a small plastic plenum which is directly connected to the microtube and to a movable rubber tube with a non-uniform cross section. The junction of the thermocouple is placed only 1 mm away from the end of the microtube avoiding any contact with it. By changing the position of the rubber tube inside the sheath, the volume of the chamber can be adjusted to limit the thermal losses, as well as to reduce the minor pressure losses at the outlet when the mass flow rate is increased.

In order to investigate the temperature distribution inside the outlet plenum, numerical simulation has been conducted for both microtube #1 and #3 using the commercial CFD code

FLUENT[®] 6.3. The first 5 cm of the length of the plenum which contains the temperature sensor was considered in the numerical model.

The plenum is modeled as a fixed volume supplied with a constant mass flow rate of heated gas which enters in the plenum with a fixed temperature of 353 K. The imposed Reynolds number at the entrance of the plenum is set to 1400 for microtube #1 and 600 for microtube #3.

The results, in terms of two-dimensional temperature distribution inside the plenum, are shown in Figure 5-5. It can be seen that for the larger microtube (#1) (Figure 5-5a) the gas temperature along the plenum centerline remains close to the value of the gas temperature at the entrance of the plenum (outlet section of the microtube) in the first part of the sheath where the temperature sensor is placed. In addition, the gas temperature is quite uniform close to the outlet section of the microtube. On the contrary, for the smaller microtube #3 (Figure 5-5b) it becomes quite challenging to measure accurately the gas exit temperature, because the temperature distribution becomes highly non-uniform in both axial and radial directions. This result highlights that the accurate measurement of the gas outlet temperature can be a problem when low gas flow rates are used through small microtubes.

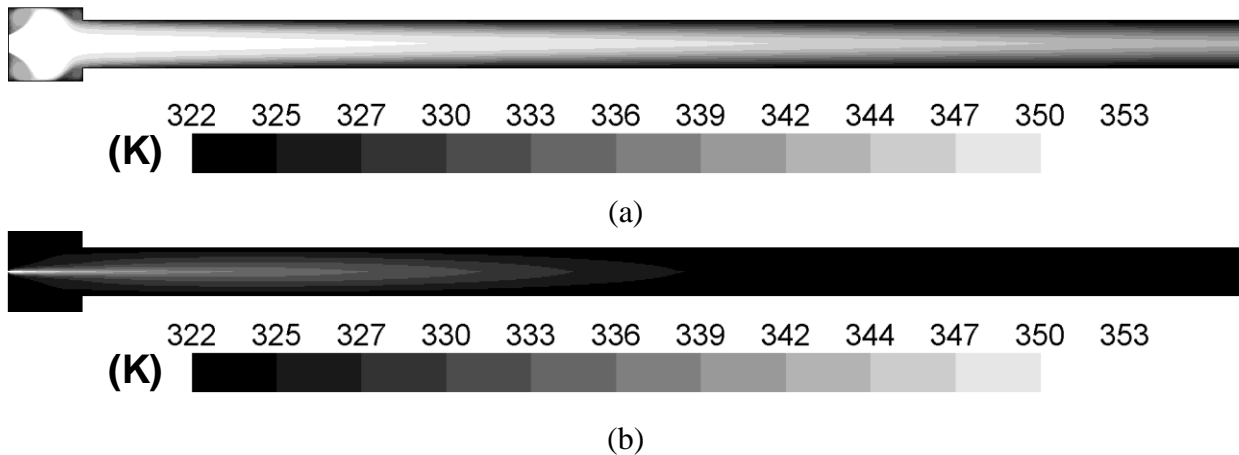


Figure 5-5: Gas temperature contours in the plenum for: (a) microtube #1 at $Re=1400$ at the entrance of the plenum; (b) microtube #3 at $Re=600$ at the entrance of the plenum.

By observing Figure 4-4 it is interesting to note that a reduction of the microtube diameter and of the Reynolds number determines a strong stratification in the plenum. In this case, even if the temperature is measured 1 mm away from the inlet of the plenum, the fluid outlet temperature can be underestimated to some extent. This difference can be larger if the junction of the thermocouple is not placed in the centerline of the plenum due to temperature stratification in

radial direction. The numerical results highlight that great care should be paid to the design of the exit section of the test rig in order to improve the accuracy of the gas exit temperature measurement, especially when the mass flow rate becomes very small and for small microtubes.

Also for large Reynolds numbers, when the compressibility effect becomes significant, the temperature measurement can be problematic at the outlet. It has been demonstrated by Hong *et al.* [142] using CFD simulation, that when the gas compressibility is not negligible the temperature sensor at the exit can be placed within a porous media (i.e. sponge) in order to slow down the gas flow and recover all the gas energy converted in kinetic energy at the exit. This simple trick can prevent mistakes when gas flows with large Ma_{out} (i.e. turbulent regime) are analyzed.

The last two sections have put in evidence that the numerical simulation can be very useful for the optimal design of experiment with microtubes; in fact, great care should be paid to the design of the exit section of the test rig in order to improve the accuracy of the gas exit temperature measurement, especially when the mass flow rate becomes very small and for low inner diameters of the microtubes but, on the other way, the numerical simulation can be also useful in order to analyze the order of magnitude of the expected temperature difference between the wall and the gas.

5.2 Gas micro convection in laminar and transitional regimes

5.2.1 Axial distribution of gas bulk temperature

As discussed before, the experimental determination of the gas local bulk temperature still remains challenging in microtubes. Traditional approaches with temperature sensors are not applicable for the measurement of the bulk temperature inside the microchannels, as the size of the cross section is generally comparable to that of the sensors. In this case, the presence of microsensors within the microtube may modify dramatically the fluid-dynamical and thermal behavior of the system. The non-intrusive techniques for the local measurement of temperature, developed especially for liquid microflows and presented in Chapter 2, are not yet feasible for the analysis of gas flows at micro scale. Their application to the analysis of the gas convection through commercial microtubes has not yet been fully developed.

The main consequence of this fact is that it becomes challenging to measure the axial distribution of gas bulk temperature through a heated microchannel. For this reason, for microtubes under a H thermal boundary condition many researchers estimated the mean bulk temperature along the tube by using Eq. (5.14) for the estimation of Nusselt number, implicitly assuming the axial bulk temperature distribution as linear. Nevertheless, this hypothesis in many cases appeared in literature was not verified by the researchers e.g. by means of a numerical simulation of their specific situation.

Figure 5-6 shows the outer wall temperature (T_w) measured by means of 5 thermocouples attached along microtube #1 at different Reynolds numbers. The gas temperature at the microtube inlet and outlet is also shown in the same figure (empty symbols). It should be noted that there is a distance of 20 mm between the inlet ($x/L=0$) and the position of the first thermocouple on the external surface. This length is taken up by the fittings at the inlet. The relatively long fitting helps to avoid possible gas leakage due to high feeding pressure at inlet (up to 1 MPa). For the outlet fitting of the chamber, this length is reduced to 2 mm.

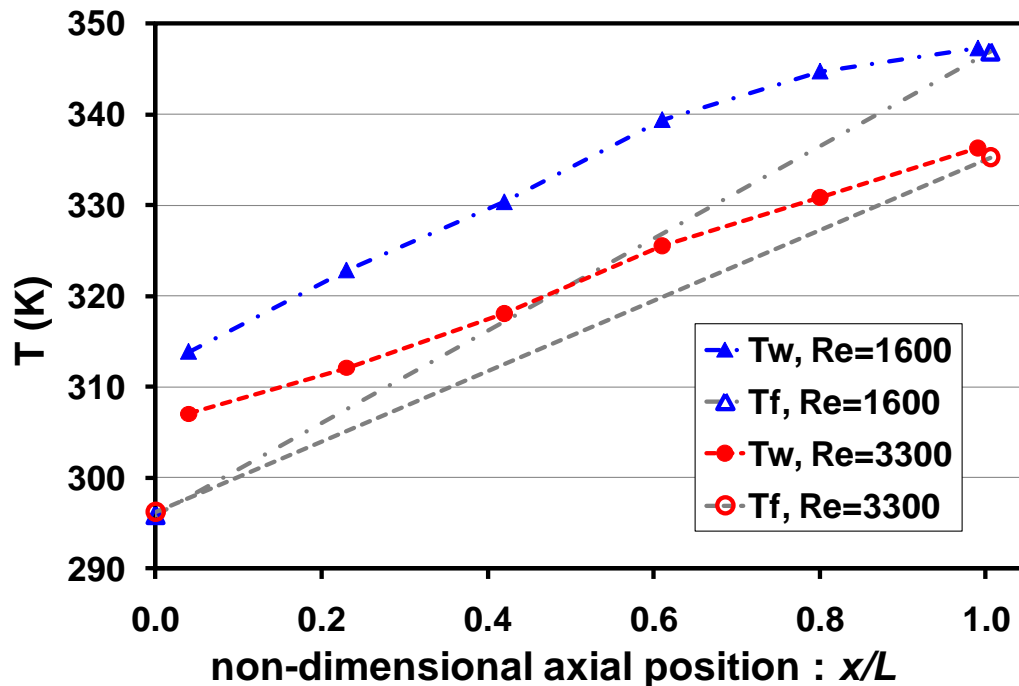


Figure 5-6: Wall and gas temperatures measured at different Re for microtube #1.

The experimental data indicate that very small temperature differences between gas and wall at the outlet for both small and relatively large Reynolds numbers occur. If gas bulk temperature is assumed linearly distributed along the axial direction (grey dotted lines in Figure 5-6), the

mean temperature difference between gas and wall becomes very large especially for small Reynolds numbers and this fact is in disagreement with the conclusions of the previous Section 5.1.5.

In order to verify the real axial distribution of gas bulk temperature, a CFD simulation of the forced convection through the tested microtubes has been conducted by using a finite-volume CFD solver (FLUENT® 6.3). The gas micro flow in the present study is in continuum regime (Knudsen number less than 10^{-3}). Therefore, the Navier-Stokes equations with classical non-slip boundary conditions still hold. On the contrary, the numerical model takes into account the effects of gas compressibility and viscous dissipation. As the bulk temperature gradient along the axis can be relatively large, the temperature dependence of the fluid properties has been taken into account. In Table 5-4 the correlations used in order to estimate the values assumed by the main gas thermophysical properties as a function of the gas temperature are quoted.

Table 5-4: Temperature-dependent thermal properties of nitrogen adopted in numerical simulation.

Properties of nitrogen	Method	Reference values
thermal conductivity	piecewise linear $k = \frac{k_2 - k_1}{T_2 - T_1}(T - T_1) + k_1$	$T_1=273.15$ K, $k_1=0.02386$ W/(m K) $T_2=373.15$ K, $k_2=0.03056$ W/(m K)
heat capacity	weak dependence on temperature	1040 J/(kg K)
density	law of ideal gases	-
viscosity	power law $\mu = \mu_0 (T / T_0)^\alpha$	$\mu_0 = 1.656 \cdot 10^{-5}$ kg/(m s) $T_0=273.15$ K $\alpha = 0.74$

The geometry of the microtube was exactly reproduced in the simulation in terms of inner diameter, external diameter and length. The numerical grid size has been refined for each numerical test until the difference in terms of velocity and temperature between two successive grid refinements becomes one order of magnitude lower than the corresponding experimental uncertainty for the selected variables (temperature and velocity). The calculation was carried out

using the same conditions adopted during the experiment in terms materials, position of fittings and position of the electrodes for the Joule heating of the microtube.

In the numerical model the microtubes are assumed smooth due to their low relative roughness ($\varepsilon/d < 0.02$). In fact, as numerically demonstrated by Croce *et al.* [57], the influence of roughness on the average value of the Nusselt number can be considered negligible for microtubes with a relative roughness up to 2.65%.

In the numerical tests to the microtubes the thermal boundary condition is applied as follows: along the heating length of the microtube an external wall temperature which follows the experimental temperature distribution determined by using the thermocouples has been imposed. For the parts covered by the inlet and outlet fittings a constant heat loss has been imposed, by considering the average value of the heat losses measured in an experimental test in which the microtube was heated without any gas flow. The front and back side surfaces of the microtubes are assumed as adiabatic due to their small areas.

From the numerical simulation, the axial distribution of the gas bulk temperature within two microtubes (#1, #3) has been obtained by applying a heating power equal to 2.8 W for microtube #1 and 0.6 W for microtube #3. In Figure 5-7 the numerical axial distribution of the gas bulk temperature is compared with the bulk temperature measured at inlet and outlet of microtube #1 for $Re=1400$ (red circles). The results shown in Figure 5-7 highlight that the distribution of gas bulk temperature along the microtube is not linear at all.

More specifically, it is possible to note that in the first part of the tube there is a steep increase of gas temperature, which tends to reduce the temperature difference between gas and wall as the flow develops. After this first zone the temperature difference between gas and wall begins to stabilize around a small value, which is of the order of 1 K on average. This axial distribution demonstrates that the use of Eq. (5.14) for calculation of fluid mean temperature must be considered with care in the case of gas flows. In fact, in this case a simple arithmetic average of the measured inlet and outlet temperature for the estimation of the average gas bulk temperature along the tube can be affected by a very large error. For example, in the case shown in Figure 5-7 the gas mean temperature estimated by using Eq. (5.14) is equal to 323.8 K, while the gas mean bulk temperature obtained using the numerical results is 337.6 K. This difference has a strong impact on the evaluation of the Nusselt number by means of Eq. (5.18).

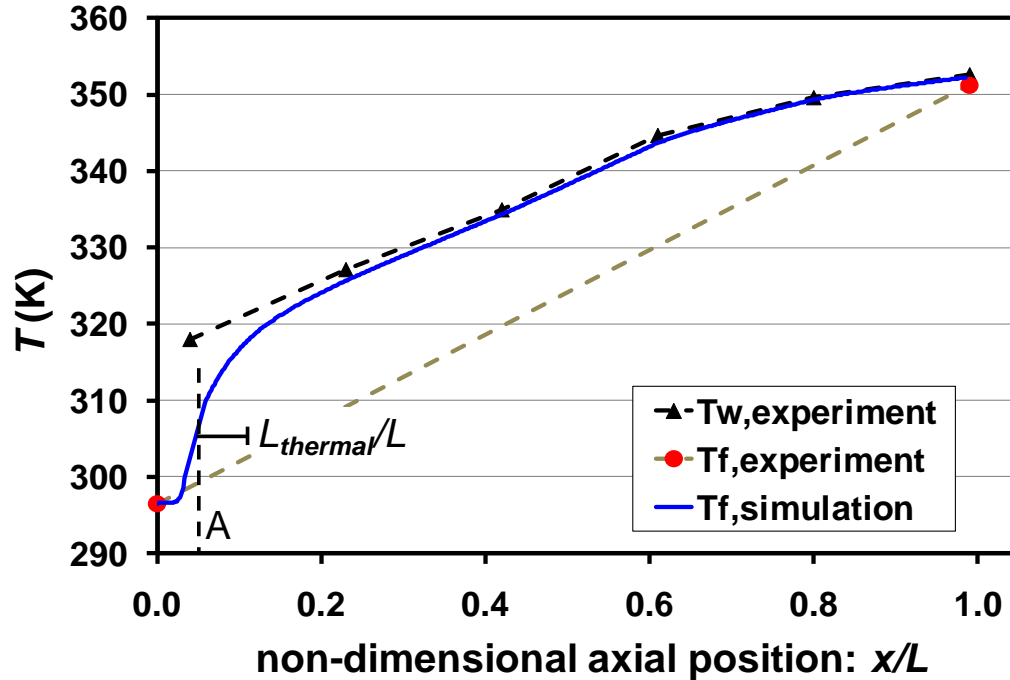


Figure 5-7: Axial gas and wall temperature distribution through microtube #1 at $Re=1400$, under an imposed heating power of 2.8 W.

Similar numerical calculations have been conducted for microtube #3. In Figure 5-8 the results are compared with experimental data obtained at $Re=600$. It can be noted that, in this case, the non-linearity of the bulk temperature axial distribution is more evident.

In addition, in this case there is a significant temperature drop after the end of the heated section due to the presence of the outlet fitting (2 mm in length) which occupies the space between the position of the last thermocouple and the micro-tube end. Since the electrical heating does not cover this length, the direction of heat flux is actually reversed (from the gas to the walls), and the gas bulk temperature decreases rapidly due to small thermal capacity of nitrogen. If the value of the temperature measured within the outlet plenum is used to determine the mean gas bulk temperature along the heated length of the microtube by means of Eq. (5.14), a large inaccuracy will be introduced. As it is evident in Figure 5-8, in this case the linear axial trend between the inlet and the outlet bulk temperature (gray dashed line in Figure 5-8) is far from the axial trend of the gas bulk temperature indicated by the blue line. In this case the value of the experimental average Nusselt number is affected by a large error if the average bulk temperature is estimated by using the measured inlet and the outlet bulk values in combination with Eq. (5.14), even if the outlet gas temperature measurement is very accurate.

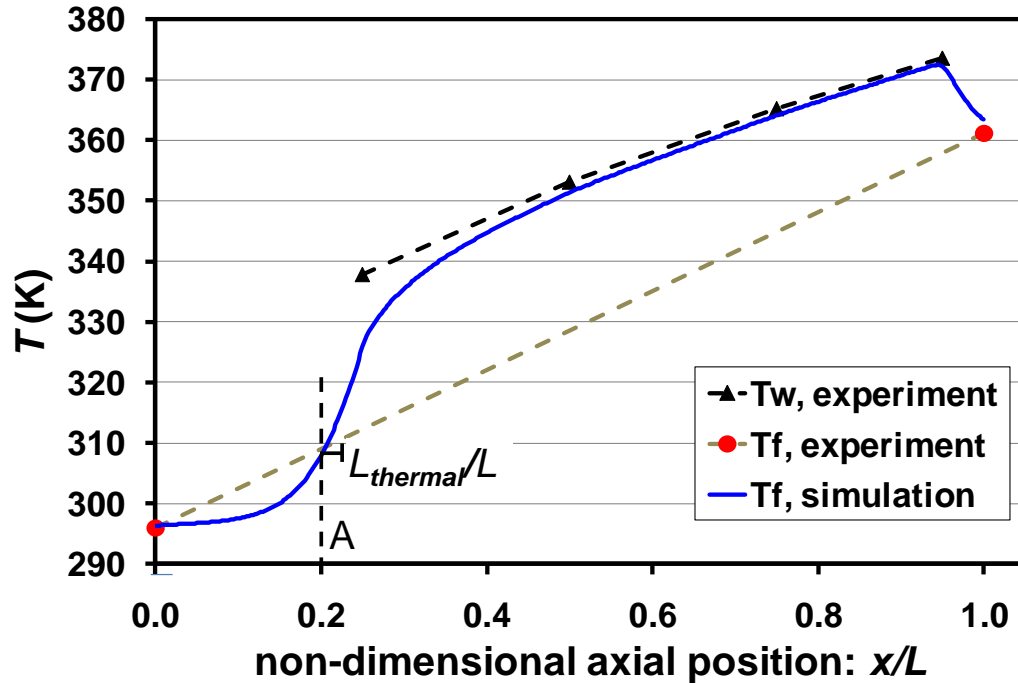


Figure 5-8: Axial gas and wall temperature distribution through microtube #3 at $Re=600$, under an imposed heating power of 0.6 W.

In order to explain the non-linearity of gas bulk temperature in axial direction the effect due to the thermal entrance region can be firstly invoked. The length of the thermal entrance region in a circular tube can be estimated by using Eq. (5.3) which gives a relative length ($L_{thermal}/L$) of the entrance region equal to 0.051 for microtube #1 and 0.025 for microtube #3 in the conditions of Figure 5-7 and Figure 5-8 respectively. In both figures point A indicates the position of the first electrode where Joule heating starts. From this point a segment with a length equal to $L_{thermal}/L$ is shown in order to evidence the extension of the thermal entrance region in microtube #1 and #3. The temperature distribution depicted in Figure 5-7 demonstrates that the extension of the non-linear region remains within the thermal entrance region for microtube #1. This means that in this case the non-linear trend is mainly caused by thermal entrance effects.

On the other hand, Figure 5-8 highlights that for microtube #3 the non-linear region is longer than the thermal entrance region. It is evident that the gas is pre-heated before the position of the first electrode (point A) which means that the heat flux tends to move in the direction opposite to the gas flow due to conduction in the wall (conjugate gas-wall heat transfer). Therefore, in this case the non-linearity of the gas bulk temperature distribution is not merely due to the entrance effects.

In microtubes, the non–linearity of the axial bulk temperature distribution can be due to the presence of specific effects, such as thermal entrance effects, the conjugate heat transfer between the wall and the gas, viscous dissipation and gas compressibility. It is possible to verify whether the main effects can be considered negligible or not in the range of operating conditions adopted during the experimental tests. By recalling the definition of the Graetz number (Gr , thermal entrance effects), the average Mach number (Ma_{avg} , compressibility effects), conduction parameter (λ , conjugate effects) and Brinkman number (Br , viscous effects):

$$\begin{aligned}
 Gr &= Re Pr \frac{d}{L}, \\
 Ma_{out} &= \frac{4\dot{m}}{\pi d^2 p_{out}} \sqrt{\frac{RT_f}{\gamma}}, \\
 \lambda &= \frac{k_w}{k_f} \left(\frac{D^2 - d^2}{dL} \right) \frac{1}{Re Pr}, \\
 Br &= \frac{64\mu}{q_w} \left(\frac{\dot{m}RT_b}{(p_{in} + p_{out})\pi d^2} \right)^2
 \end{aligned} \tag{5.16}$$

The range of variation of these parameters has been calculated and shown in Table 5-5 for all the experimental tests.

The corresponding threshold value for each parameter is also reported in Table 5-5. It is evident that the flow through both microtubes can be considered thermally fully developed since the Graetz number is below 10. The data quoted in Table 5-5 highlight that for microtube #1 compressibility effects can be considered negligible and the conjugate heat transfer becomes important only for very low Reynolds numbers ($Re < 800$). On the contrary, viscous dissipation is important especially for very large Reynolds numbers. The data of Table 5-5 confirm that in the case of the microtube #3 the effects related to conjugate heat transfer cannot be ignored ($\lambda > 0.01$). The same applies to the effect of viscous dissipation ($Br > 5 \cdot 10^{-3}$) for the whole range of Reynolds numbers. On the contrary, the influence of compressibility becomes significant only for large Reynolds numbers ($Re > 1600$). This analysis highlights that the non-linear axial distribution of the bulk temperature evidenced by the microtube #3 for $Re = 600$ can be linked to the conjugate heat transfer effects and viscous dissipation together with thermal entrance effects.

Table 5-5: Typical ranges of the non-dimensional parameters linked to the main effects for the tested microtubes.

Microtube	$d/L*10^3$	Re	Gr (<10)	Ma _{out} (<0.3)	λ (<0.01)	Br* 10^3 (<5)
#1	1.5	500-4000	0.5-4.3	0.03-0.23	0.001-0.02	7-44
#3	1.72	400-3500	0.6-4.1	0.14-0.67	0.04-0.31	26-38

5.2.2 Effect of nonlinear temperature distribution on Nusselt number

It has been demonstrated in the previous sections that a key factor in calculating the value of Nusselt number is the accurate determination of mean temperature difference between wall and bulk fluid. If this difference is very small (~ 1 K), the values of Nusselt number become highly sensitive to the errors introduced not only by the uncertainties of temperature sensors, but also by the averaging method chosen for the local bulk temperature. For microtube #1 at Re equal to 1400, the mean temperature difference between the gas and the wall in the fully developed section of the microtube, obtained by the numerical simulation, is only 0.97 K. This value with an uncertainty of ± 1 K results in an error larger than 100% on the Nusselt number, totally masking its physical essence and making comparison with the classical theory devoid of significance. This can explain some “non-physical” results appeared in literature over the last years.

In order to take into account the non-linear axial distribution of the gas bulk temperature in the evaluation of the Nusselt number, the experimental measurements have been coupled with the numerical results obtained in the simulation of the tests in terms of axial bulk temperature distribution. A curve fitting method is introduced in order to obtain by the numerical results the expression of the average bulk axial temperature in the heated region of microtube.

The axial bulk temperature determined numerically has been approximated by using the following expression:

$$T_f(x) = a \left(\frac{x}{L} \right)^b + c \quad (5.17)$$

in which x is the axial coordinate and a , b , c are parameters to be determined by fitting methods. This method has been applied to the experimental data obtained for microtube #1 heated by imposing an electrical power of 1.2 W with Re in the range 490-4000 and for microtube #3 with

a heating power of 0.6 W and for Reynolds number from 460 to 3350. The values obtained for the fitting parameters a , b , c are given in Table 5-6.

Table 5-6: Value of the fitting parameters obtained for microtube #1 ($P=1.2$ W) and microtube #3 ($P=0.6$ W).

<i>Microtube #1</i>				<i>Microtube #3</i>			
<i>Re</i>	<i>a</i>	<i>b</i>	<i>c</i>	<i>Re</i>	<i>a</i>	<i>b</i>	<i>c</i>
492	-8.887*10 ⁻⁶	-4.624	322.3	461	-26.960	-0.735	399.6
639	-0.013	-2.364	321.7	605	-35.870	-0.616	408.1
830	-0.202	-1.490	321.0	783	-62.240	-0.418	433.4
1079	-1.931	-0.806	322.3	1019	-148.000	-0.205	517.2
1399	-7.851	-0.426	327.4	1325	554.400	0.063	-189.4
1824	-32.390	-0.160	350.5	1722	139.500	0.270	220.7
2366	73.450	0.103	243.5	2238	104.100	0.362	250.6
3082	43.840	0.171	270.9	2907	75.650	0.470	271.5
4001	37.000	0.162	274.0	3349	65.770	0.508	277.1

When the fitting parameters are known, the average gas bulk temperature along the microtube is calculated by integration over the total heated length instead of Eq. (5.14):

$$\bar{T}_b = \frac{1}{L_h} \int_0^{L_h} T_b(x) dx \quad (5.18)$$

and the mean value of the Nusselt number is calculated from Eq. (5.12) and (5.13).

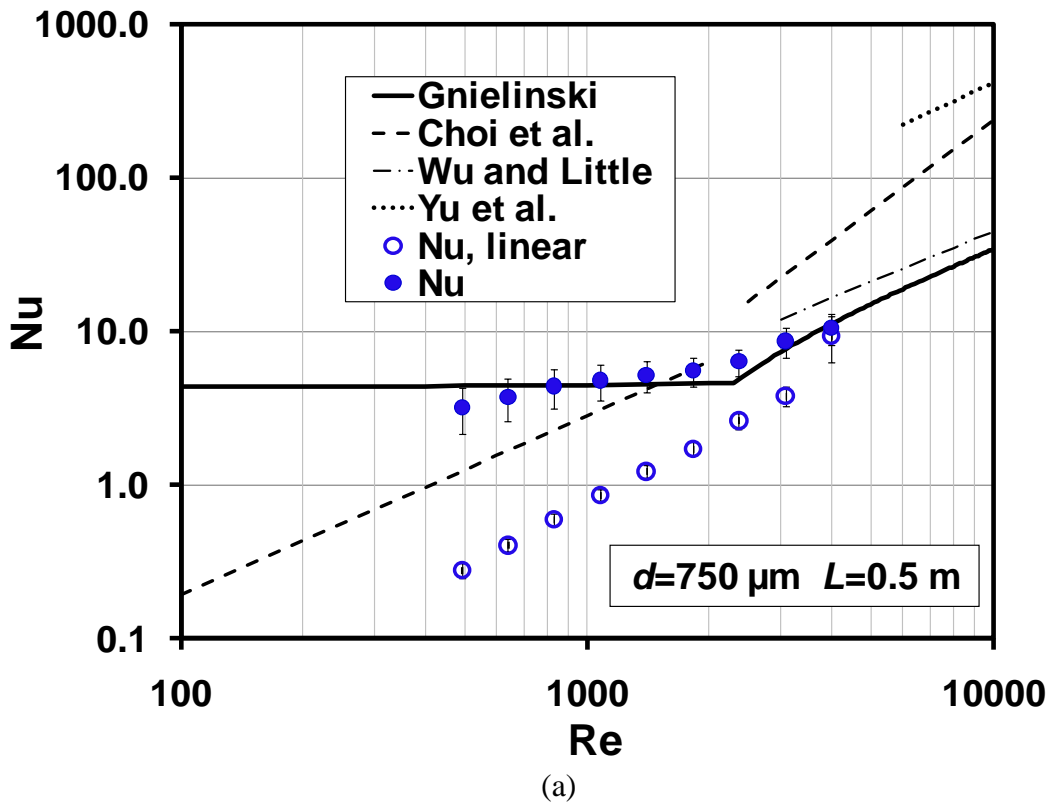
Figure 5-9 shows the trend of the Nusselt number determined by considering the non-linear bulk temperature distribution for microtube #1 (Figure 5-9a) and #3 (Figure 5-9b), respectively. The results are compared with those obtained by calculating the mean bulk temperature using Eq. (5.14) (blank circular symbols).

It is well evident that for low Reynolds numbers the Nusselt number obtained by considering the axial bulk temperature distribution as linear is very low (lower than 1 for $Re < 1000$), while by taking into account the non-linearity, the Nusselt number is always larger than 3 in the laminar regime.

The slight decrease of Nusselt number when the Reynolds number is reduced ($Re < 700$) can be explained by invoking the wall-gas conjugate effects (as indicated in Table 5-5), which tend

to reduce the Nusselt number from 4.364 (H b.c.) to 3.658 (T b.c.) as demonstrated numerically by Mori *et al.* [143]. In addition, the viscous dissipation tends to reduce the Nusselt number but this reduction is small for low Reynolds numbers (which corresponds to low Brinkman numbers).

Figure 5-9(a) also shows the correlations developed by Gnielinski [23] for macro-tubes, and the correlations of Wu and Little [14], Choi *et al.* [18] and Yu *et al.* [19] proposed specifically for microtubes. It is interesting to note that the trend of the Nusselt number based on the non-linear axial distribution of gas bulk temperature is not in agreement with any of the latter, neither in laminar nor in transitional regime. In fact, the trend of experimental data is in a good agreement with the predictions of Gnielinski's correlation.



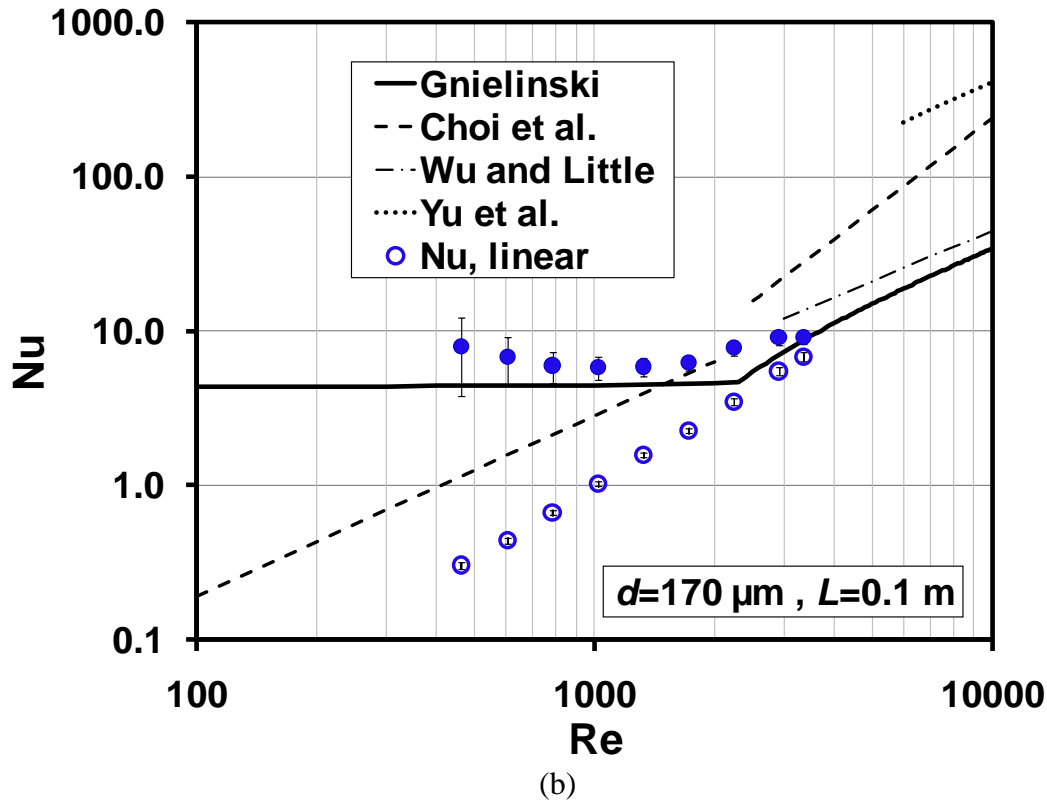


Figure 5-9: Experimental Nusselt numbers as a function of the Reynolds number and comparison with Gnielinski [10], Choi *et al.* [7], Wu and Little [3] and Yu *et al.*[8] correlations for microtube #1 (a) and microtube #3 (b).

Figure 5-9b shows the experimental Nusselt numbers obtained for microtube #3. Similarly in this case, if the non-linear axial bulk temperature distribution is used in order to calculate the average bulk temperature of the gas, the Nusselt number tends to become nearly constant in the laminar regime, in agreement with conventional correlation.

It is important to stress that in the case of the microtube #3 conjugate effects are very strong and viscous dissipation is significant. By considering the combined effect of viscous dissipation and conjugate heat transfer on the Nusselt number, a nearly constant value of Nu is expected in the laminar regime with a value close to 4.364. Anyway, for low Reynolds number, when viscous dissipation can be neglected, the Nusselt number cannot be less than 3.658 even in the case of very large values of λ . The experimental data shown in Figure 5-9 (b) for microtube #3 confirm that Nusselt number is nearly constant in laminar regime.

The experimental uncertainty on Nusselt numbers is also shown in Figure 5-9. The relative uncertainty of Nusselt number can reach 34% for microtube #1 and 53% for microtube #3 at low

Reynolds numbers. The large uncertainty can hide completely the effects of conjugate heat transfer and viscous dissipation. This observation clarifies how the increase of the experimental Nusselt number evidenced by microtube #3 for $Re < 600$ is mainly due to the uncertainty on the experimental data.

In conclusion, if the actual axial distribution of the bulk temperature is accurately taken into account in the evaluation of the Nusselt number, the trend of experimental Nusselt numbers is in satisfying agreement with the conventional theory (classical Gnielinski correlation). On the contrary, Choi's correlation proposed for the prediction of the Nusselt numbers in laminar regime for microtubes strongly underestimates the Nusselt number and, for this reason, it is not recommended.

5.3 Compressible gas micro convection in transitional and turbulent regimes

5.3.1 Compressibility effects in micro convection

Eq. (5.12) and (5.13) can be applied to convective heat transfer when the fluid compressibility effects can be considered negligible. However, for gas flows in microtubes the pressure drop can be very large at large Reynolds numbers. In this case the Mach number increases dramatically from the inlet to the outlet, as reported in the numerical work by Hong *et al.* [144]. Therefore, compressibility becomes significant even at Reynolds numbers less than 2000. The gas compressibility not only will influence the fluid-dynamic behavior of the flow in terms of pressure drop and friction factor, but will have also an impact on the convective heat transfer between wall and the gas.

When the compressibility effects cannot be neglected, the energy balance indicated in Eq. (5.13) is not sufficient to describe the behavior of the system, because part of the heat transferred from wall to fluid (under positive heat flux) will be converted into kinetic energy as the gas accelerates along the microtube. If the fluid temperature measured at the inlet and outlet of microtube is different from the stagnation temperature the total energy transferred from the wall to the gas is underestimated. More in detail, in order to take into account the presence of the conversion between thermal energy and kinetic energy, Eq. (5.13) must be rewritten by substituting the gas bulk temperature at the outlet and at the inlet with the stagnation temperature (*stg*):

$$q_{w,i} = \frac{\dot{m}c_{pf} (T_{f,out,sg} - T_{f,in,sg})}{\pi d L_h} \quad (5.19)$$

Similarly, the temperature difference between gas bulk and wall needs to be re-considered. It is important to recall here that the convective heat transfer between wall and fluid is driven by the local static temperature difference. Therefore, even if the gas stagnation temperature is locally higher than the wall temperature, the heat flux goes from the wall to the fluid as long as the gas static temperature is lower than the local wall temperature. As result, the temperature difference in the calculation of convective heat transfer coefficient h , or Nusselt number, should be the difference between wall temperature and gas static temperature. Combining Eq. (5.12) and (5.19), the expression of mean Nusselt number for compressible flow becomes the following:

$$Nu = \frac{\dot{m}c_{pf}}{\pi k_f L} \frac{T_{out,sg} - T_{in,sg}}{\bar{T}_w - \frac{T_{out,static} + T_{in,static}}{2}} \quad (5.20)$$

It is possible to demonstrate that the gas static temperature and the stagnation temperature can be linked each to other by means of the local Mach number:

$$T_{sg} = T_{static} \left(1 + \frac{\gamma - 1}{2} Ma^2\right) \quad (5.21)$$

where γ is the gas specific heat ratio and the Mach number is defined by:

$$Ma = \frac{4\dot{m}}{\pi d^2 p} \sqrt{\frac{RT}{\gamma}} \quad (5.22)$$

where R is the specific gas constant, and T and p are the gas local bulk temperature and local pressure, respectively.

It is important to underline that the measured fluid temperature is neither exactly the stagnation gas temperature nor the static temperature but, in general, it is in between these two values, due to the incomplete conversion from kinetic energy to thermal energy at the measurement point:

$$\begin{aligned} T_{f,static} < T_{f,measure} < T_{f,sg} \\ T_{f,measure} &= T_{f,static} \left(1 + c_r \frac{\gamma - 1}{2} Ma^2\right) \end{aligned} \quad (5.23)$$

It is possible to take into account the partial conversion which occurs in a real system by introducing the recovery coefficient c_r , which assumes values between 0 and 1, by means of which the measured temperature can be linked to the static value if one knows the value of the

local Mach number, as highlighted by Eq. (5.23). Even if some recommended values for the recovery coefficient can be found in literature, the exact value is extremely sensitive and related to the specific conditions of the test rig, flow conditions, position and placement of thermocouples, etc.

In order to know the specific values of recovery coefficients for temperature measurements of flows through the three microtubes mounted on our test rig, additional experimental tests under adiabatic conditions have been performed. As the value of the recovery coefficient does not depend on the heating conditions of the flow, the results obtained in the adiabatic case can also be used for the heated case. To keep this assumption valid, in practical operations during experiments, greatest caution should be paid for the gas temperature measurement. After the test section is connected to the microtube and the thermal insulation has been placed, the test section should be carefully preserved from any change or modifications, otherwise the value of the recovery coefficient may change from one test to another.

In adiabatic case the difference between wall temperature and fluid static temperature is generally very small. Moreover, at relatively large Reynolds number, when the flow inside the microtube tends to become turbulent, the radial temperature gradient is strongly reduced. Therefore, the wall temperature measured by thermocouple on the external surface of the tube can be considered as a first estimation of the gas bulk fluid static temperature along the tube:

$$\begin{aligned} T_{f,static,adb} &= T_w \\ T_{f,measure,adb} &= T_{f,static,adb} \left(1 + c_r \frac{\gamma - 1}{2} Ma^2\right) \end{aligned} \quad (5.24)$$

where the subscript *adb* indicates the adiabatic condition. Eq. (5.24) can be used in order to determine the value of recovery coefficient at the outlet of microtubes.

5.3.2 Estimation of recovery coefficient under adiabatic conditions

The gas temperature and the wall temperature at the outlet are shown in Figure 5-10 for microtube #1 when Joule heating on the microtube surface is switched off. Nitrogen gas flows through the microtube at ambient temperature. The wall temperature at inlet coincides with the ambient temperature. Due to the large pressure drop, compressibility effects occur along the flow and the fluid accelerates from the inlet to the outlet of the tube. This causes a reduction in the gas internal energy, and the static temperature decreases. As a result, the local temperature of the

wall inner surface, which is in direct contact with the fluid, is reduced by the gas flow. At the outlet plenum where the fluid outlet temperature is measured, the gas thermal energy is partially recovered from kinetic energy as the flow is strongly decelerated. Therefore, the fluid temperature measured at the outlet can be higher than the wall temperature at the outlet, which is measured by the last thermocouple attached to microtube wall. Compressibility effects become more significant at larger Re . Consequently, the microtube wall at outlet is further cooled by the gas flow, and the difference between wall temperature and measured fluid temperature becomes larger. A similar trend has been experimentally evidenced for microtube #2 over a larger range of Reynolds number, as shown in Figure 5-11.

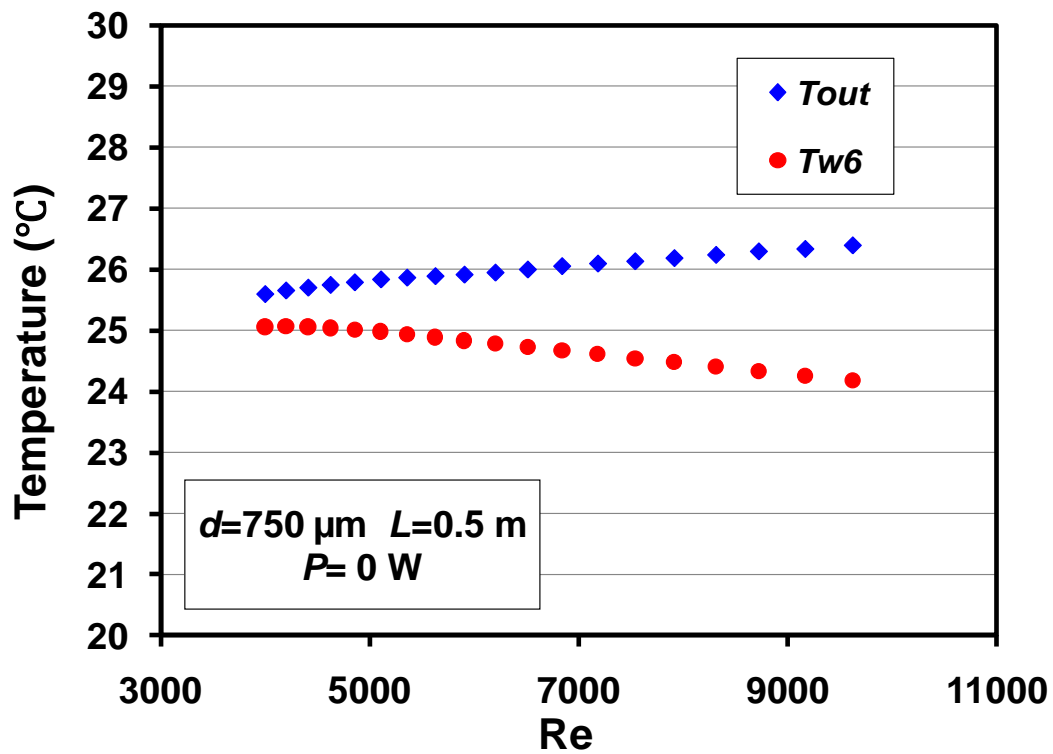


Figure 5-10: Gas and wall temperature at the outlet of microtube #1 under adiabatic condition.

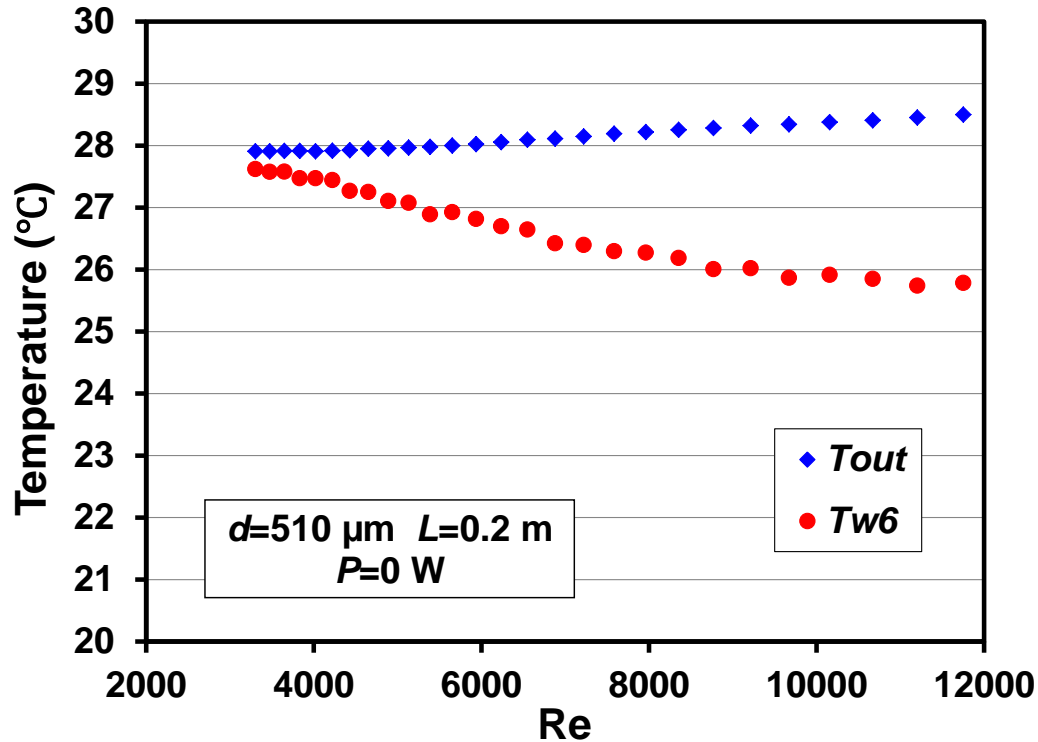


Figure 5-11: Gas and wall temperature at the outlet of microtube #2 under adiabatic condition.

Figure 5-12 shows the wall temperature and fluid temperature at the outlet for microtube #3, which has the smallest inner diameter among the microtubes tested. It can be noted that the fluid temperature measured at the outlet is higher than the local wall temperature under adiabatic conditions. At Reynolds numbers of the order of 4000 the temperature difference between the fluid and wall at the outlet is large, compared to that of the other two microtubes. This indicates that for microtubes of very small inner diameters, the gas compressibility effects are well evident also in transitional regime.

However, with increasing Reynolds number, the difference between the wall temperature and the fluid temperature measured at the outlet decreases for microtube #3 as shown in Figure 5-12. This trend is in disagreement with the trends of the other microtubes, but can be explained by considering that for gas flows through the smallest microtube at high Reynolds number, the fluid velocity can be extremely high at the exit of the microtube. The outlet plenum along with the tip of the thermocouple is not sufficiently large to slow down the high speed gas flow to a certain extent. As a result, only a small amount of thermal energy is recovered from kinetic energy in this case. In this case a use of a porous medium (i.e. sponge) at the outlet in which the

temperature sensor can be accommodated can be very useful in order to slow down the gas flow and to increase the thermal energy recovered.

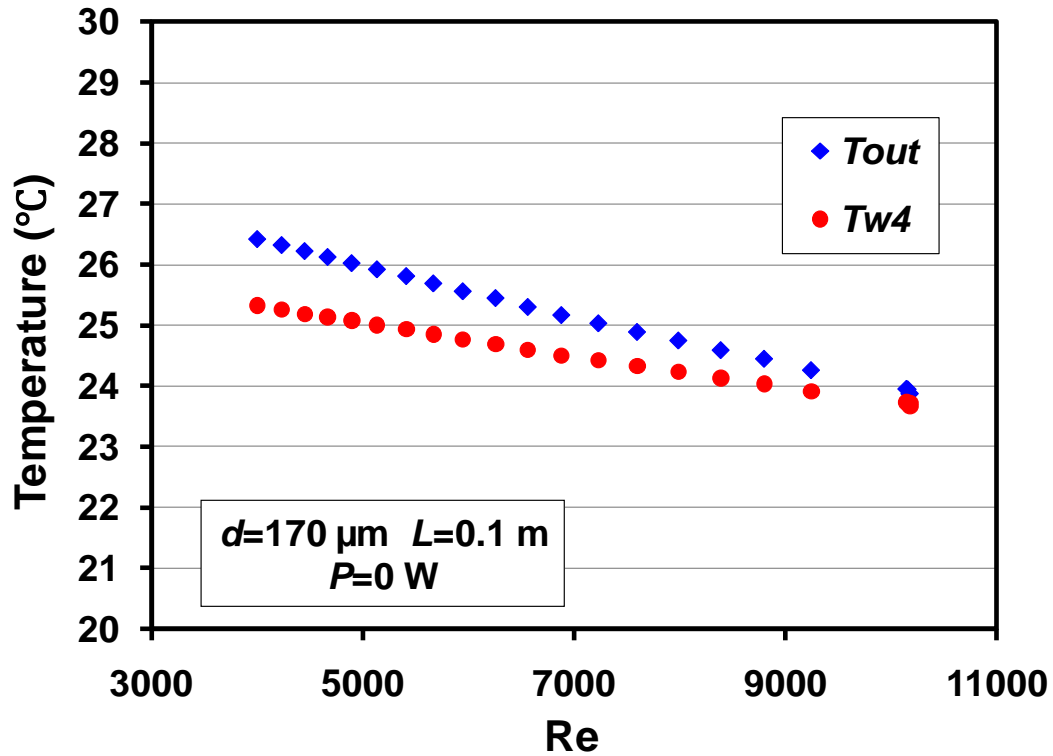


Figure 5-12: Gas and wall temperature at the outlet of microtube #3 under adiabatic condition.

The measured outlet Mach number as a function of Reynolds number for all the three microtubes is plotted in Figure 5-13. It can be noted that, for the same Reynolds number, the outlet Mach number increases with the decrease of microtube inner diameter. Especially for microtube #3, the outlet Mach number approaches unity when the Reynolds number reaches 10000. In addition, the Mach-Re curve tends to flatten as the Reynolds number is increased. At larger Reynolds numbers, the outlet minor losses linked to the abrupt change in the flow area increases greatly due to the larger pressure drop over the full length of the microtube. Due to this fact, the flow outlet pressure is higher than atmospheric pressure and this slows down the increase of Mach number as Re increases.

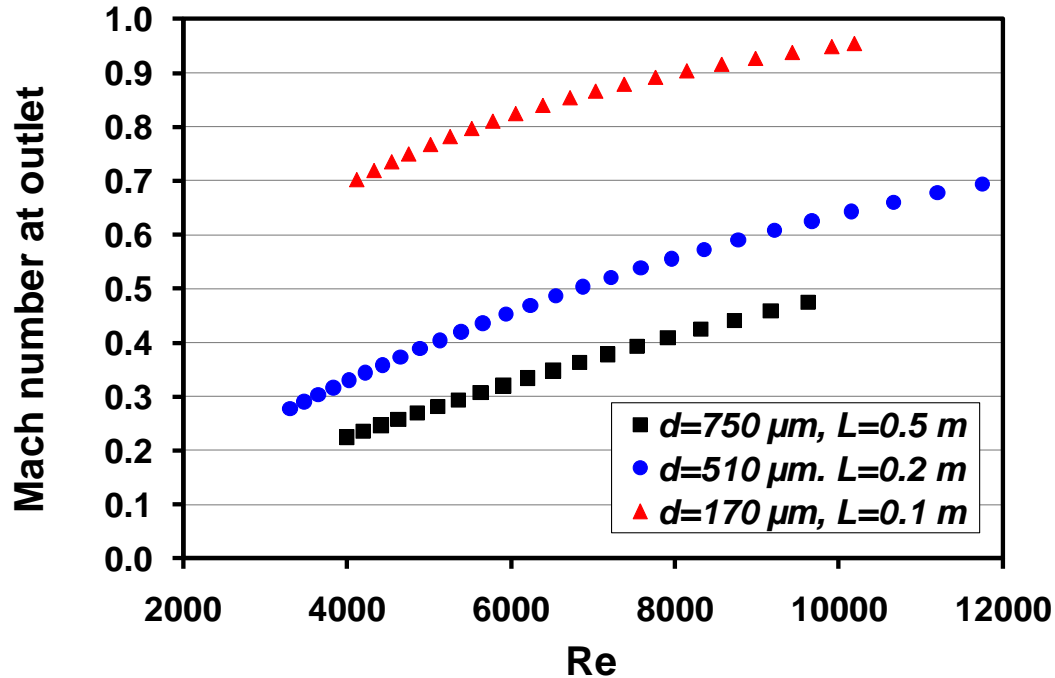


Figure 5-13: Mach number at outlet versus Re for three microtubes.

The recovery coefficients for the flow outlet temperature measurement of the three microtubes can be obtained using Eq. (5.24). Figure 5-14 shows the recovery coefficients versus Reynolds number for the three microtubes. It is possible to note that the value of recovery coefficients decreases considerably with the reduction in microtube inner diameter.

Using smaller microtube and outlet chambers, the conversion from kinetic energy into internal energy is less complete due to the difficulty in the accurate placement of thermocouple tip to the centerline of bulk flow within reduced flow area. In addition, it can be noticed that the recovery coefficients for microtube #1 and #2 are nearly constant over the whole range of Reynolds numbers tested. For the smallest microtube (#3), as expected, the value of the recovery coefficient decreases gradually with the increase of Reynolds number.

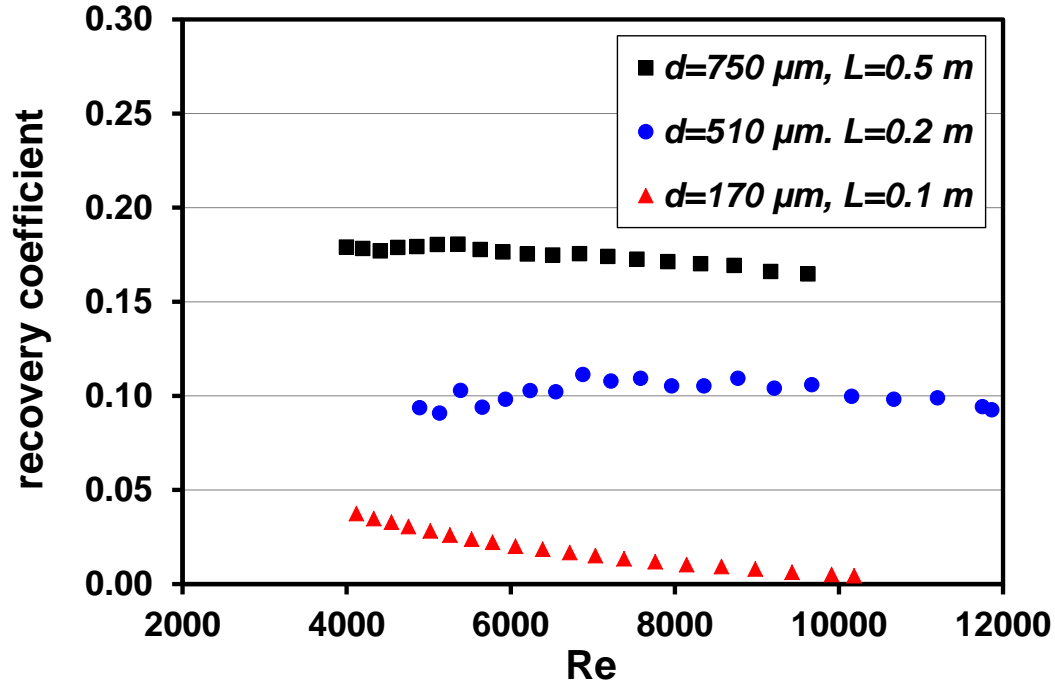


Figure 5-14: Recovery coefficient for gas outlet temperature measurement versus Reynolds number.

For a heated microtube under a constant heating power fixed at 2 W the typical wall temperature and fluid temperature at the outlet are shown in Figure 5-15 for Reynolds numbers from 2780 to 10840. At low and medium Reynolds numbers it can be noted that under heated conditions the measured bulk temperature is lower than local wall temperature, which is normal for an imposed entering heat flux at the wall. However, as the Reynolds number increases, the measured bulk temperature begins to surpass the local wall temperature. This is due to the higher gas velocity obtained at the outlet.

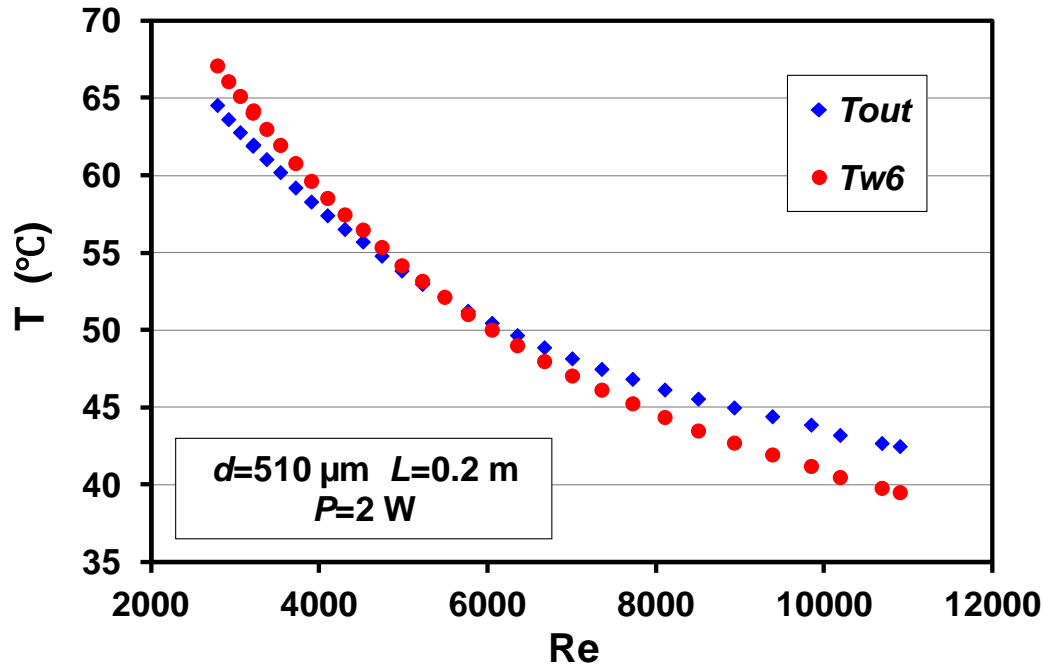


Figure 5-15: Gas and wall temperature at the outlet of microtube #2.

5.3.3 Nusselt number of compressible flows through microtubes

The Nusselt number calculated by using Eq. (5.20) is shown in Figure 5-16 for microtube #1 under a constant heating power fixed 4 W. When the Reynolds number is relatively small and compressibility is of negligible importance ($Re < 7000$), the Nusselt number follows the trend of Gnielinski correlation [23]. On the contrary, as the outlet Mach number increases and the compressibility effects gain in significance, the experimental Nusselt number begins to deviate from Gnielinski correlation. However, also in this case, the experimental data confirm that the trend of Nusselt number does not follow any of the correlations proposed specifically for microtubes by Wu and Little [14], Choi *et al.* [18] and Yu *et al.* [19] even by considering the uncertainties of Nusselt numbers which are between 9.6 % and 19.7%.

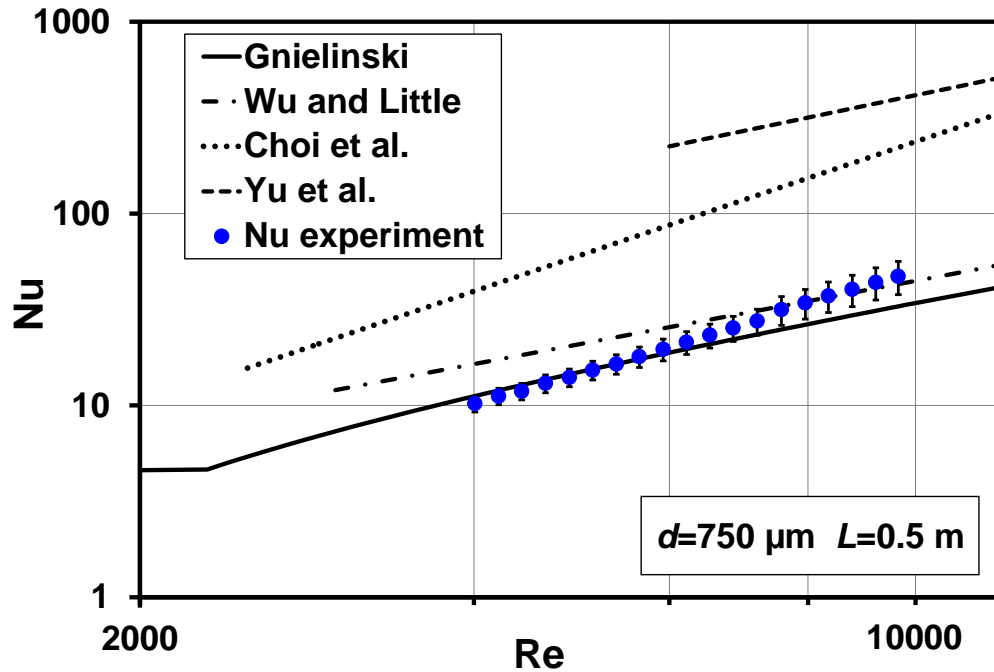


Figure 5-16: Nusselt number as a function of Reynolds number for microtube #1.

A similar trend is evidenced in Figure 5-17 by the Nusselt numbers determined by using the microtube #2 under a constant heating power of 2 W. At Reynolds number smaller than 4000, the experimental results can be well predicted by Gnielinski correlation [23]. When the Reynolds number continues to increase, the enhancement of the convective heat transfer becomes more evident due the compressibility. Therefore the heat transfer coefficient rises. This helps to explain the disagreement between conventional theory and experimental data obtained in the past at micro scale, which is often simply interpreted as “scaling effects” without a detailed physical explanation. It should be underlined that sometimes this disagreement in the open literature may also be partly due to very large uncertainties of Nusselt numbers obtained at high Reynolds number. In the present test for microtube #2 the uncertainties rise from 7.0% up to 18.3% at the highest Reynolds number tested.

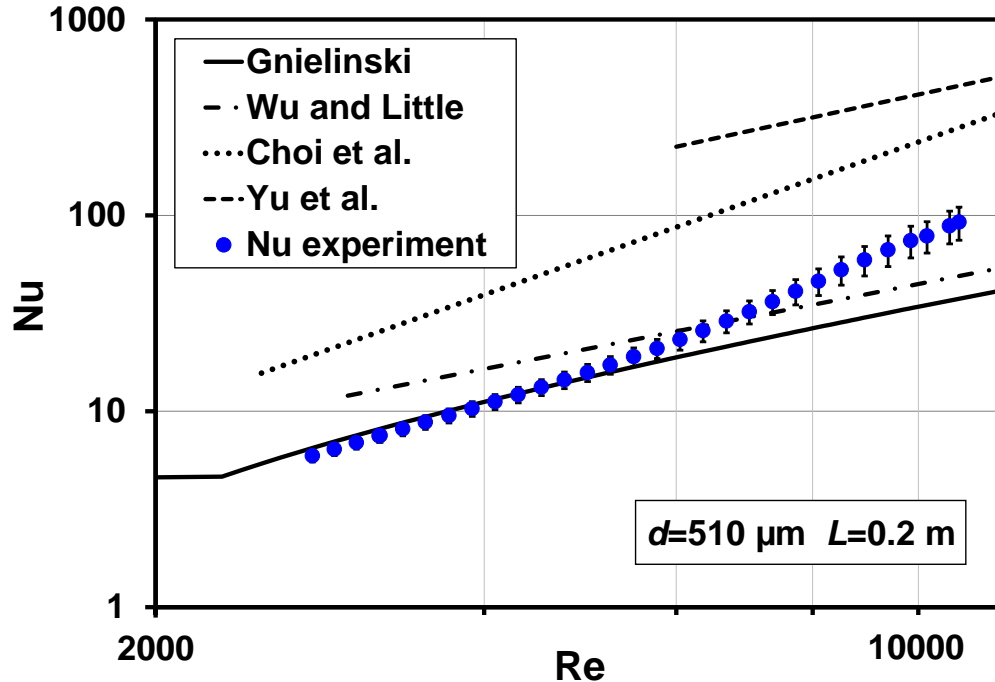


Figure 5-17: Nusselt number as a function of Reynolds number for microtube #2.

Figure 5-18 shows the Nusselt number as a function of Reynolds number through microtube #3 under a constant heating power fixed 0.4 W. The Nusselt number is surprisingly high compared with the other two microtubes. This corresponds to the larger outlet Mach numbers obtained in this tube even at low and medium Reynolds numbers. In fact, at Reynolds number equal to 3894 the outlet Mach number reaches 0.69 for microtube #3. At the same Reynolds number, the outlet Mach numbers are smaller than 0.35 for both microtubes #1 and #2. This means that, for this tube the compressibility effects becomes important even in laminar regime, as confirmed by the data presented in Chapter 4 on the friction factors.

The large Nusselt numbers compared to the predictions of the conventional correlations where the compressibility effects are not accounted for, are qualitatively in agreement with the numerical prediction obtained by Croce and D'Agaro [145], who evidenced higher values of Nusselt number at high Mach numbers in heated gas flows at microscale.

In this case, it is interesting to note that the experimental data are in good agreement with the correlation proposed by Choi *et al.* [18]. However, the Choi's correlation does not link the value assumed by the Nusselt number to the Mach number, as this increase is mainly caused by the compressibility effects, and the agreement is only due to the similarity of the conditions adopted for microtube #3 with respect to the conditions investigated by Choi *et al.* [18]. The limited

predictive power of the Choi's correlation is highlighted by the disagreement evidenced when the Choi correlation has been compared with the results obtained with microtube #1 and #2.

This fact confirms that the correlations proposed by Wu and Little [14], Choi *et al.* [18] and Yu *et al.* [19] are not physically based and for this reason cannot be recommended for the prediction of the Nusselt number in microtubes.

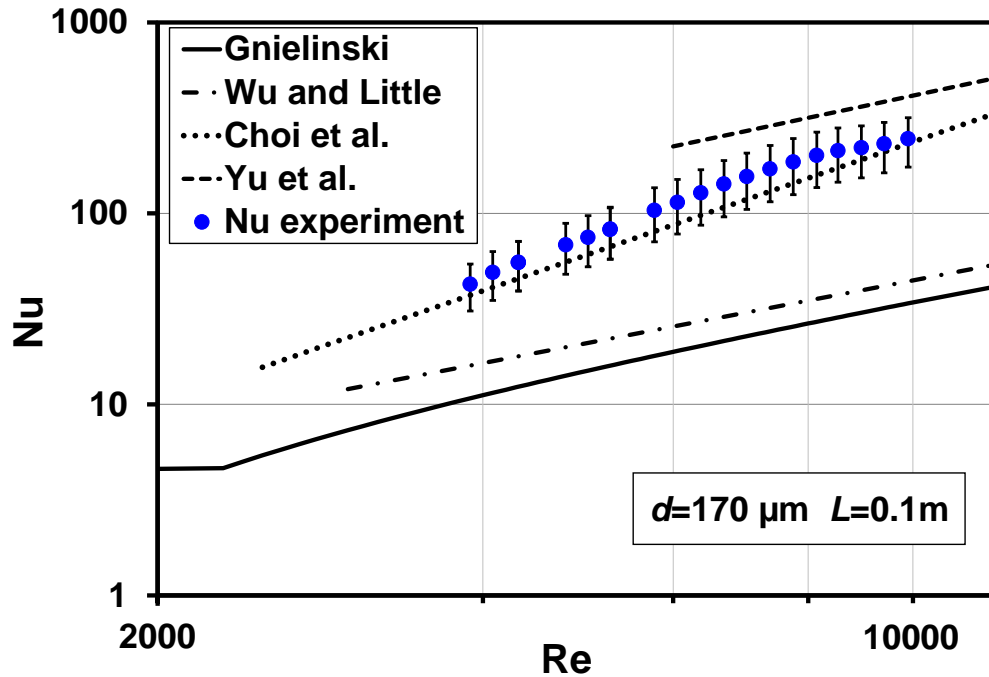


Figure 5-18: Nusselt number as a function of Reynolds number for microtube #3.

The experimental results in terms of Nusselt numbers have evidenced that the convective heat transfer coefficient in microtubes for nitrogen flows is strongly affected by the Mach number. The gas compressibility plays an important role especially for smaller microtubes ($d < 200 \mu\text{m}$). Since for compressible flows the flow velocity is developing from inlet to outlet of the microtube, the flow is actually never hydrodynamically nor thermally fully developed throughout the full length. This leads to a varying local Nusselt number along the axis, instead of a constant value like for incompressible flows under both H (constant heat flux) and T (constant wall temperature) boundary conditions. In addition, in turbulent regime ($\text{Re} > 2300$) the role of the thermal boundary conditions imposed on the microtube becomes negligible. As pointed out by Guo and Wu [146], a fully developed flow does not exist inside a microtube when the compressibility is not negligible, and the temperature profile becomes strongly coupled to the velocity profile in this case. Under these conditions it becomes more difficult to predict the value

of Nusselt number, for example, by means of a specific correlation. In this case the mean Nusselt number is influenced not only by the Reynolds and the Prandlt number (as stated by the correlations proposed by Wu and Little [14], Choi *et al.* [18] and Yu *et al.* [19]), but also by the ratio between the length of the microtube and its inner diameter, the outlet Mach number and the average wall temperature. In other words, if a correlation has to be suggested for the prediction of Nusselt number for gas flows in microtubes, it is expected to have the following functional expression:

$$Nu = Nu\left(\text{Re}, \text{Pr}, Ma_{out}, \frac{L}{d}, \frac{\bar{T}_w}{\bar{T}_b}\right) \quad (5.25)$$

which takes into account more parameters than the correlations proposed by Wu and Little [14], Choi *et al.* [18] and Yu *et al.* [19].

In summary, the conventional correlation for the Nusselt number given by Gnielinski, rather than those proposed specifically for micro convection, still holds for the analysis of forced convection through microtubes but only in the case in which the compressibility effect can be considered negligible. When compressibility is no longer negligible, the convective heat transfer at microscale outperforms that at conventional scale due to additional heat transfer linked to fluid internal energy conversion. This enhancement of heat transfer is very strong when the dimensions of microtubes decrease ($d < 200 \mu\text{m}$).

5.4 Main conclusions of Chapter 5

In this chapter the main features of gas convective heat transfer in commercial stainless steel microtubes have been investigated by combining experimental data and numerical prediction. The experimental tests have been performed in laminar, transitional and turbulent regimes ($\text{Re}=400-12000$). It has been demonstrated that the effects related to the measurement of gas exit temperature, the non-linear axial gas bulk temperature distribution and flow compressibility have strong impacts on the determination of the Nusselt number.

As the total uncertainty of the Nusselt number is highly sensitive to the uncertainty of the gas exit temperature measurement, great care must be taken in the design of microtube exit section in order to have an accurate estimation of gas exit temperature, especially for gas flows at low Reynolds numbers and through microtubes of small inner diameters.

The axial bulk temperature distribution along the heating length of a microtube under H boundary conditions can be strongly non-linear for gas flows. By means of numerical simulations it has been demonstrated that a steep increase of temperature in the first part of the heating length takes place due to both the thermal entrance region and the conjugate heat transfer between the gas and the solid walls, as well as other scaling effects such as viscous dissipation. After this zone, the bulk temperature follows the wall temperature with a small difference.

It has been demonstrated that the assumption of a linear distribution of the bulk temperature results in Nusselt numbers in dependence on the Reynolds number in the laminar regime. This assumption generates very small values of the Nusselt number at low Reynolds numbers. On the contrary, if the real axial distribution of the bulk temperature is accurately taken into account in the evaluation of the Nusselt number, the trend of the experimental Nusselt numbers is in satisfying agreement with the conventional theory.

The experimental data have evidenced that Choi's correlation proposed for the prediction of the Nusselt numbers in laminar regime for microtubes strongly underestimates the Nusselt number and, for this reason, it is not recommended. On the contrary, the classical Gnielinski correlation seems to be able to predict the Nusselt numbers in laminar and transitional regime. Even if the influences due to conjugate effects, viscous dissipation and compressibility, are not taken into account, this correlation overestimates the Nusselt numbers very slightly in the laminar regime.

The conventional calculation of the convective heat flux should be modified for compressible gas flows in order to take into account the conversion between kinetic and internal energy. To predict the level of conversion of the internal energy in kinetic energy the knowledge of the value of the recovery coefficient is needed. A method to measure the value assumed by the recovery coefficient as a function of the Reynolds number is proposed. Attention should be paid to both the measurement of this parameter in the adiabatic case and its application to heated conditions, because the value might be dependent on the specific test rig, flow conditions, positions and placement of thermocouples, and so on.

The conventional correlations by Gnielinski for the prediction of the Nusselt numbers validated for incompressible flows are not able to work correctly in microtubes having an inner diameter less than 200 μm because the compressibility effects tend to become significant. When the flow compressibility is no longer negligible, the value of the Nusselt number surpasses the

conventional predictions due to the extra heat transfer from the wall linked to the internal energy conversion. This enhancement of heat transfer is very strong when the dimensions of the microtubes decrease.

5.5 From microtubes to micro heat exchangers: from fundamentals to application

The investigation of nitrogen flow and heat transfer through the three microtubes (#1, #2 and #3) has been important in order to improve the knowledge on the fluid-dynamic and thermal behavior of gas flows in various flow regimes (laminar, transitional and turbulent) through miniaturized tubes. This analysis has allowed to verify the boundaries of the applicability of the conventional theory to microtubes, and to understand the main scaling effects which can be important for the analysis of internal gas flows as the characteristic dimensions of the channels are decreased.

However, most microfluidic devices and systems are composed by a massive amount of micro-sized elements such as microchannels, micro pores, micro cavities, etc. These microelements are carefully organized in certain ways in order to accommodate flows for controlled mixing, separation, heat transfer and/or chemical reaction. The experience accumulated on the behavior of gas flows through a single microtube can be very useful in order to optimize the performances of the microdevices obtained by collecting many microtubes as in the case of the micro heat exchangers. Motivated by this, the present investigation continues with the analysis of gaseous flows in micro heat exchangers, which are very diffuse microfluidic devices employed in many practical thermal controlled systems. The critical analysis of the optimal design and fabrication of micro heat exchangers for gas flows by means of experimental tests and numerical simulations will be the main goal of the following chapters.

6 Design of Micro Heat Exchangers for Gas Flows

6.1 Fundamental theory and design pre-calculation

In this thesis the frictional and thermal performances of micro heat exchangers (microHEX) in which two gas currents with different temperature flow through a series of rectangular microchannels made by microfabrication on a plastic or metallic substrate is studied. The core of the microHEX is obtained by means of a stack of layers in which the microchannels are made.

Figure 6-1 shows the typical structure of the stacked core of a double-layered microHEX (Figure 6-1(a)) and of a multi-layered one (Figure 6-1(b)). The core is stacked in such a way that the layers in which the hot and the cold gas flow are alternated. The core is housed in a shell made of polymer. The low heat conductivity of polymer (compared with metal) ensures low heat losses with the ambience.

Some important features have been pursued in the realization of the core of the microHEXs tested in this work. For the double-layered micro heat exchanger the thin plate between the hot and cold flow has been designed in order to be easily removed. In this way, the material and thickness of the partition foil can be chosen more or less freely based on various purposes.

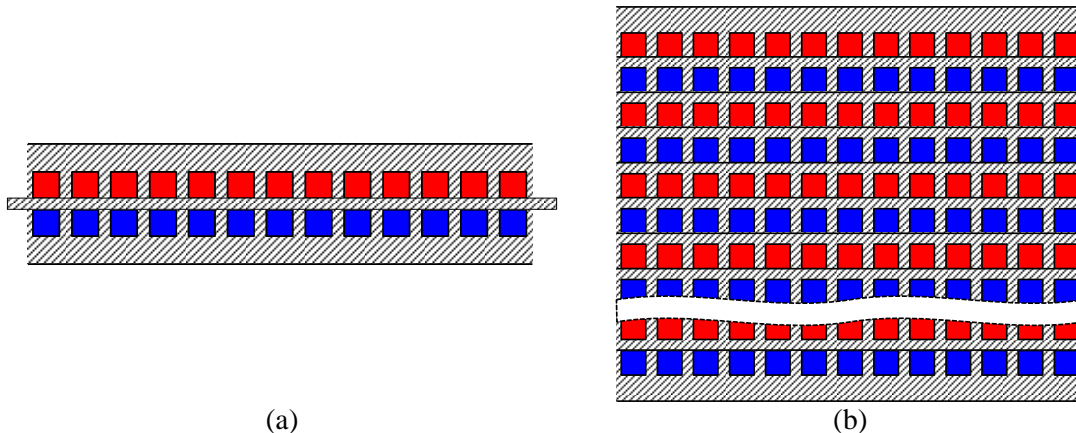


Figure 6-1: Schematic of the micro heat exchanger core. (a) double-layered; (b) multi-layered.

In addition, the core of the double-layered microHEX has been designed with a square shape, which enables the rotation of one layer in the double-layered design to generate various flow

arrangements (countercurrent, cocurrent and cross flow) while the hot and cold layers remain in perfect thermal contact, as shown in Figure 6-2. With this design the most common flow arrangements can be achieved in only one micro device.

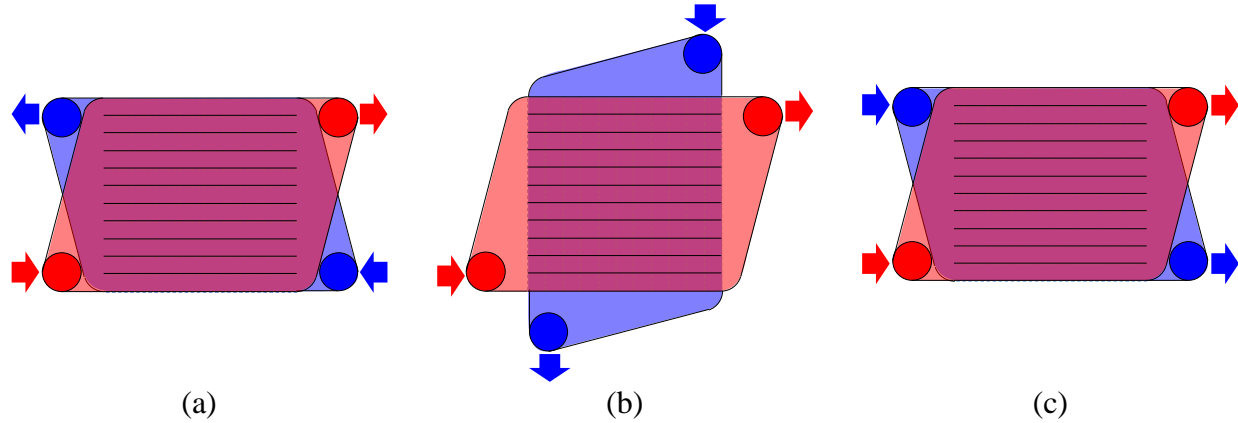


Figure 6-2: Three flow arrangements achievable in one device.

The analysis of the frictional performances of the gas-gas double-layered microHEX starts from the evaluation of the hydraulic diameter of the microchannels by using the classical definition of hydraulic diameter for a non-circular channel:

$$d_h = \frac{4WH}{2(W + H)} \quad (6.1)$$

where W is the width of microchannels and H is the height of microchannels.

In the design of the core of the double-layered microHEX square, microchannels have been considered with a hydraulic diameter equal to 200 μm . In fact, the width and height of the microchannels have been chosen to be equal to 200 μm , considering the microfabrication techniques available at Institute for Micro Process Engineering (IMVT), KIT, where the micro heat exchangers tested in this work have been made. The typical core of the micro HEX is designed to be 39.8 mm long and made by 133 parallel microchannels on each layer.

The maximum temperature of the hot gas flow is limited to 370 K (starting from room temperature) by considering the temperature resistance of the mass flow controllers used in the test rig and temperature regulating systems.

The Reynolds number of the gas flow through a single microchannel can be expressed as:

$$Re = \frac{\rho \bar{u} d_h}{\mu} = \frac{2\dot{m}_0}{\mu(W + H)} \quad (6.2)$$

where \dot{m}_0 is the mass flow rate through one microchannel, \bar{u} is the mean flow velocity, μ and ρ are the dynamic viscosity and density of the fluid, respectively.

In order to estimate the pressure drop through the microchannel, the value of theoretical friction factor is needed. It is assumed that the Hagen–Poiseuille law can be considered still valid for laminar flow through microchannels with a hydraulic diameter equal to 200 μm and the Blasius equation has been used for turbulent flow in agreement with the results evidenced in Chapter 3 of this thesis. Therefore, the friction factor can be calculated as:

$$\begin{aligned} f &= \frac{57}{Re} \quad (\text{laminar}) \\ f &= 0.3164Re^{-0.25} \quad (\text{turbulent}) \end{aligned} \quad (6.3)$$

When the value of friction factor is known, the net pressure drop through the microchannel can be calculated from the following equation valid for incompressible flows:

$$\Delta p_{net} = f \frac{L}{d_h} \frac{\rho \bar{u}^2}{2} = f \frac{L}{d_h^3 (W + H)^2} 2\dot{m}_0^2 \quad (6.4)$$

where L is the length of the microchannel.

The total pressure drop is estimated by:

$$\Delta p_{total} = \Delta p_{in} + \Delta p_{net} + \Delta p_{out} \quad (6.5)$$

where Δp_{in} and Δp_{out} are the local pressure losses at the microchannels inlet and outlet. These minor losses can be calculated by Eq. (4.8).

From these parameters the general range of pressure drops and mass flow rates can be estimated by using Eq. (6.1) to (6.5). The ranges of these physical parameters are listed in Table 6-1. From the values of parameters to be measured, the measurement instruments are carefully selected with specific full scales.

Table 6-1: Prediction of operating conditions and selection of sensors.

Operating parameters	Range	Selection of measurement devices	Accuracy of the devices
Pressure	0-40 bar	WIKA 0-2.5 bar, 0-10 bar, 0-40 bar	± 0.51 % of F.S.
Mass flow rate (double-layered microHEX)	0-20 kg/h	BROOKS 0-6 kg/h, 0-30 kg/h	± 1 % of the measured value if $20\%F.S. < \dot{m} < F.S.$
Mass flow rate (20-layered microHEX)	0-350 kg/h	BROOKS 0-700 kg/h	± 0.2 % of F.S. if $\dot{m} < 20\%F.S.$
Temperature	290-370 K	CONATEX K-type thermocouple	± 0.5 K

6.2 Heat conduction in the solid wall

As demonstrated in Chapter 1 by means of a critical review of the existing literature, all the available experimental works on gas flow micro heat exchangers concluded that conventional theory on heat exchangers failed to explain the experimental data due to heat conduction in the solid wall. Another unusual result evidenced in literature is that the flow arrangements (cross flow, cocurrent flow and countercurrent flow) makes no difference in microHEX on the thermal performances of these devices when highly conductive material (copper, stainless steel and ceramic) are used as partition foils among the hot and the cold fluids, as evidenced by the work of Bier *et al.* [32], Meschke *et al.* [33] and Koyama and Asako [34]. However, in these works the authors did not consider the problem related to the optimal choice of the solid materials and of the thickness of the partition foils in the design phase of their microHEXs. Moreover, after their experimental tests no statement was made on how the thermal conductivity of the partition foils affects the performance of the gas microHEX.

Heat exchanger effectiveness is strongly influenced by the thermal conductivity of the solid material used as separation wall between the hot and cold fluid due to the axial conduction within the wall. The impact of the thermal conductivity of the partition wall on the heat

exchanger effectiveness has been numerically investigated by Stief *et al.* [147] in 1999. Figure 6-3 shows the effectiveness of a countercurrent micro heat exchanger as a function of the partition wall thermal conductivity. If the thermal conductivity approaches to 0, the solid wall tends to insulate the hot and cold flows and the effectiveness tends to 0. On the contrary, when the wall is made with a highly thermally conductive material, the heat conduction at the wall becomes the prominent way to transfer heat inside the core of the micro heat exchanger and, as a result, the fluid flows out of the device with a smaller temperature difference with regard to the inlet temperature, and heat exchanger effectiveness is reduced accordingly.

It is evident that the numerical calculation made by Stief *et al.* [147] indicates an optimal value for the wall thermal conductivity of the order of 1 W/mK in order to obtain the best efficiency for a gas-to-gas heat exchanger. The influence of axial conduction on the thermal performance of the present microHEX is discussed in more detail in Section 7.4 by analyzing the experimental data from present design and comparison with the results in publications.

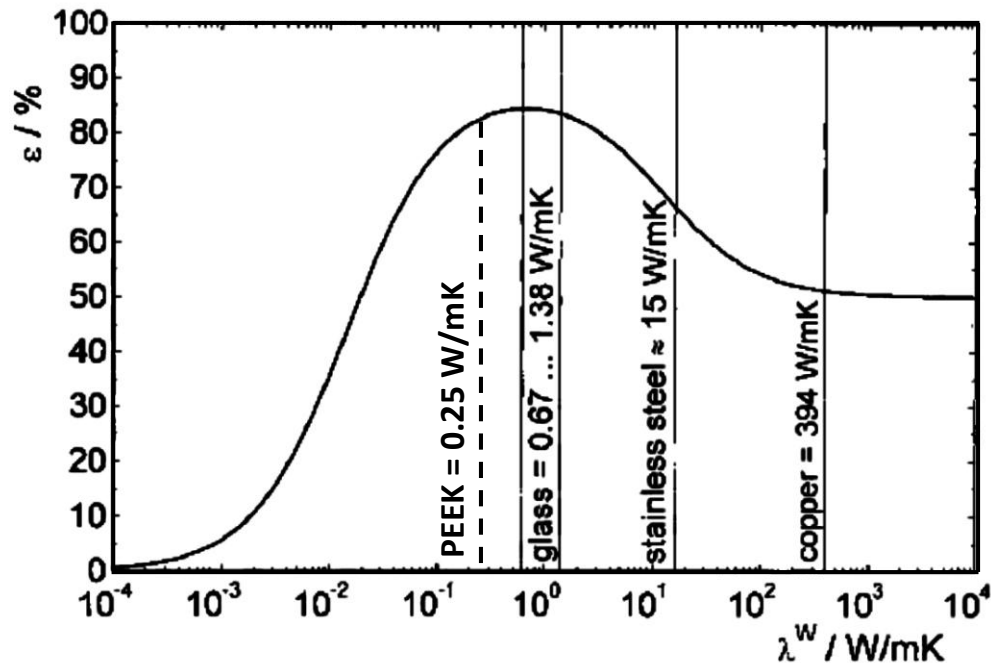


Figure 6-3: Heat exchanger effectiveness in dependence on the wall thermal conductivity (adapted from Stief *et al.* [147]).

For PEEK with thermal conductivity of 0.25 W/mK, the double-layered microHEX presented in this work is expected to have relatively high effectiveness if the numerical results of Stief *et al.* [147] are correct (see Figure 6-3).

For this reason, in the design of the microHEX used in the tests described in this thesis the external shell of the heat exchanger has been made by using a polymer material in order to minimize the possible heat losses to the environment. The partition foil between the hot and cold gas flows has been made in PEEK (polyether ether ketone) in order to reduce the influence of wall axial conduction and to verify the Stief's numerical predictions in terms of effectiveness. By using PEEK as the solid material, the axial heat flux in the wall becomes small compared with convective heat flux from wall surface to fluid. In addition, it is expected that with the present design the dependence of microHEX thermal performance on flow arrangements can be distinguished experimentally.

Other kinds of partition foils have been used (copper, stainless steel, aluminum) in order to verify experimentally the role of the heat conduction at the partition wall on the thermal performances of a microHEX and hence to obtain an experimental validation of the Stief's curve shown in Figure 6-3; these results are presented in Chapter 7.

6.3 Influence of manifold configuration on flow distribution

The core of a gas-to-gas microHEX needs to be connected to feeding and venting pipes in order to have gaseous flows in and out of the device at a controlled mass flow rate. In general the inlets of the parallel microchannels are fed by using a distributing manifold. A collecting manifold is similarly added to collect the gas at the outlet of each microchannel. The configuration and the shape of these manifolds may influence the uniformity of flow distribution among the microchannel in particular when the number of microchannels per layer is large. In order to optimize the frictional and the thermal performances of the microHEX it is mandatory to obtain a flow distribution among the parallel microchannel as uniform as possible; this can be obtained by optimizing the configuration and the shape of the distributing/collecting manifolds of the device.

To meet this goal, five different configurations of manifolds have been numerically studied in connection of a single layer in order to check the possible influence of the manifold shape and configuration on the gas flow distribution among the channels of the layer.

As an example, two of the most common configurations for such kind of manifold are shown in Figure 6-4. Type A generates flow paths of an S type, while Type B gives a U type flow path. A qualitative comparison on the features of these two different flow paths is described in [148].

As the micro heat exchangers are designed to work with a large pressure range (up to 40 bar), a group of small pillars with diameter of 0.8 mm have been added to the distribution/collecting manifold in order to maintain mechanical stability and to avoid possible deformation of the device under high pressure. This is especially useful for microHEXs with countercurrent arrangement, which generates highly asymmetric pressure on both surfaces of the partition foil. These small pillars are applied to all the tested manifolds in order to support the thin partition foil between the hot and cold flows and to prevent any possible deformations or breaks of the foil. Actually such supporting pillars or similar supporting structures are quite common in microdevices (such as micro evaporators), if the dimension and thickness of microstructures are greatly reduced in order to guarantee the mechanical stability of the device. However, due to the presence of these supporting pillars, the models available in literature and cited before for the analysis of the impact of the manifold configuration on the flow distribution among the parallel microchannels are not able to predict the flow distribution in the double layered microHEX made at KIT and used in the experimental tests described in this thesis.

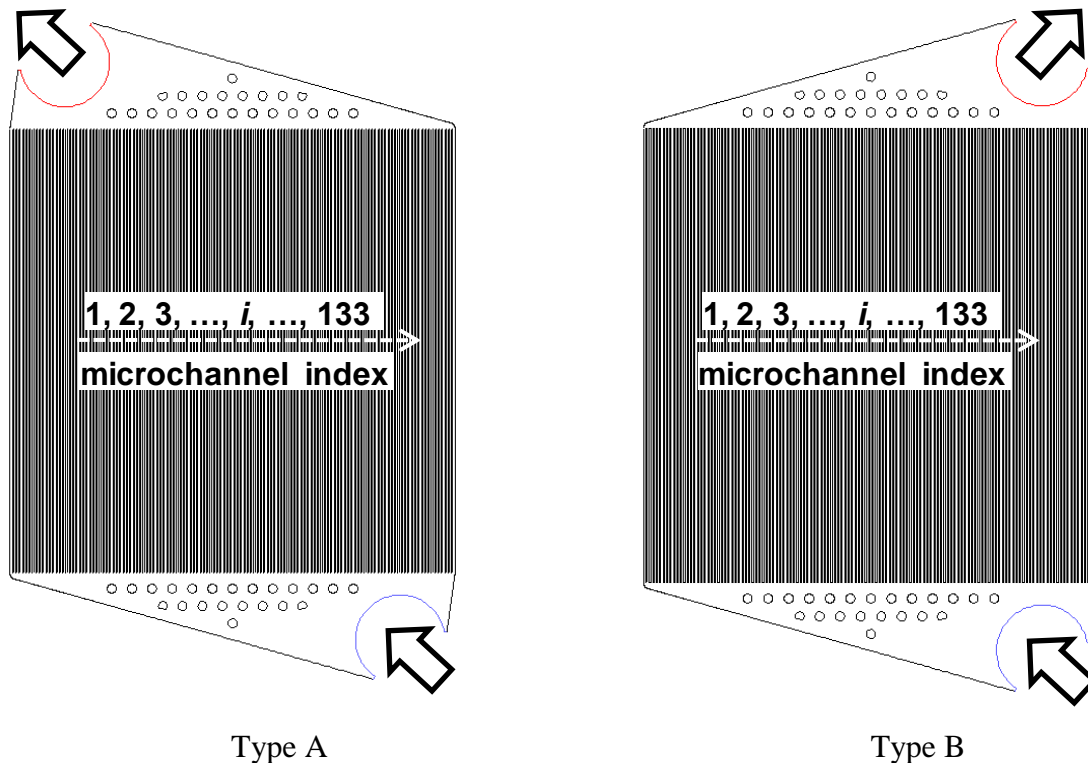


Figure 6-4: Configurations of a typical layer to generate an S-type flow (Type A) and a U-type flow (Type B).

The position of the feeding port in Type C and Type D are relatively far from the inlets of the microchannels, as shown in Figure 6-5. The large area of the manifold and the large number of small pillars may help to distribute the flow uniformly in the manifold before to enter into the parallel microchannels. Unlike the designs of Type A and Type B, the Type C and D configurations do not change too much the flow direction from the feeding port through the microchannels down to the venting port. In addition, Type D has enlarged feeding/exhaust ports in order to have smaller flow velocity at the same mass flow rate in the distributing/collecting chambers. However, it needs to be verified whether these configurations are able to generate a satisfying uniform flow distribution among the 133 parallel channels of the double-layered microHEX.

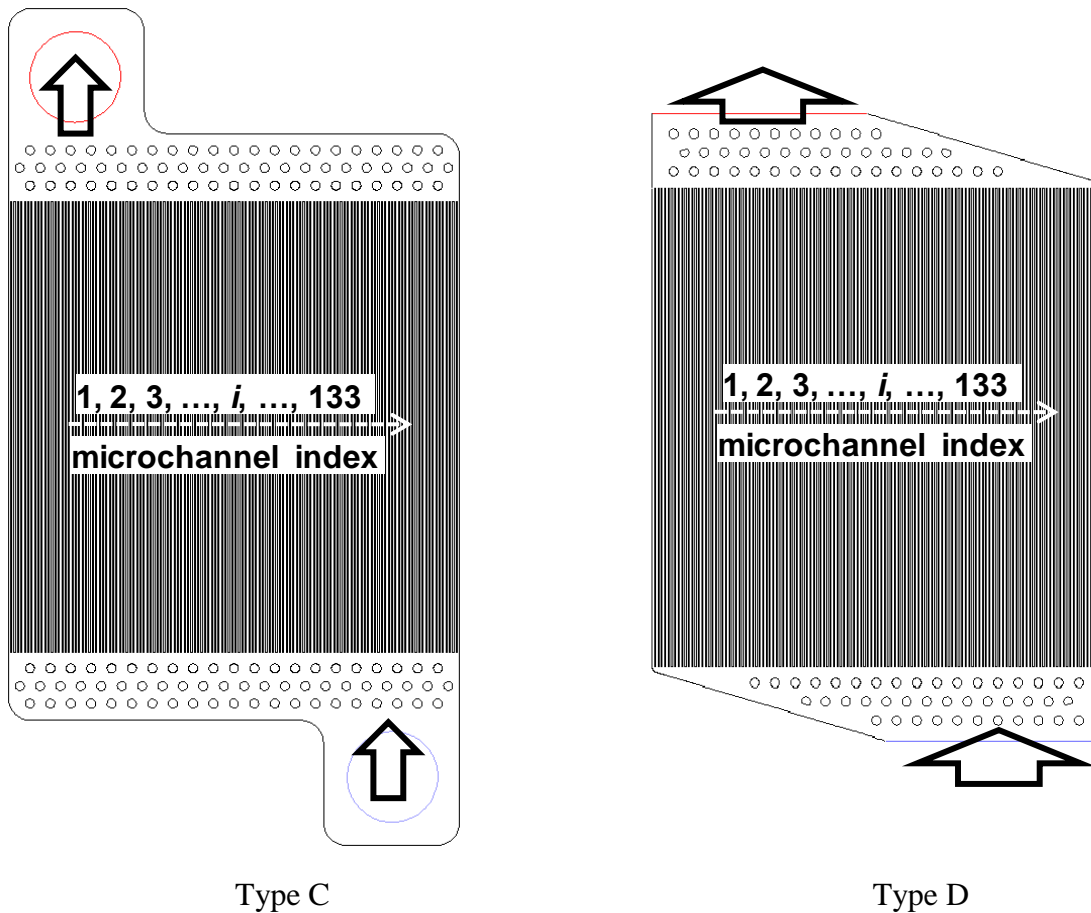


Figure 6-5: Configurations of a typical layer in the design of Type C and Type D.

The Type E configuration (see Figure 6-6) is based on some classical models (i.e., as in [40]) in which the directions of inflow and outflow are normal to the axis of microchannel. According to Renault *et al.* [40], the optimal angle θ (see Figure 6-6) for the Type E manifold of the

inclined external wall facing the inlets/outlets of microchannels can be related to the aspect ratio of microchannels and to the total number of parallel microchannels by using the following correlation:

$$\theta = An^{-B} \quad (6.6)$$

where n is the total number of parallel microchannels.

The coefficients A and B are calculated by:

$$\begin{aligned} A &= 6.4309 + 575.55r^{*} - 258.71r^{*2} \\ B &= 0.9801 - 0.0425r^{*} - 0.0888r^{*2} \end{aligned} \quad (6.7)$$

in which r^* is the aspect ratio of the rectangular microchannel.

The correlations above have been obtained by considering 20 parallel microchannels connected with two manifolds of Type E; an angle for the manifolds calculated by using Eq. (6.6) and Eq. (6.7) guarantees a uniform flow distribution among the 20 channels with a maximum difference in terms of flow rate among the channels less than 3.5% (Renault *et al.* [40]). However, the prediction of these correlations has never been checked for a larger number of parallel microchannels (i.e. $n > 100$) like in this case. Therefore, the last design in the present work is based on the Renault correlation in order to check its validity when a large number of parallel microchannels are considered. In the microHEX core, the microchannels have an aspect ratio of $r^* = 1.0$ and their total number n is equal to 133 per layer. Applying these values to Eq. (6.6) and (6.7), the angle θ is calculated to be 5.1° , which is applied to the configuration of Type E, as shown in Figure 6-6.

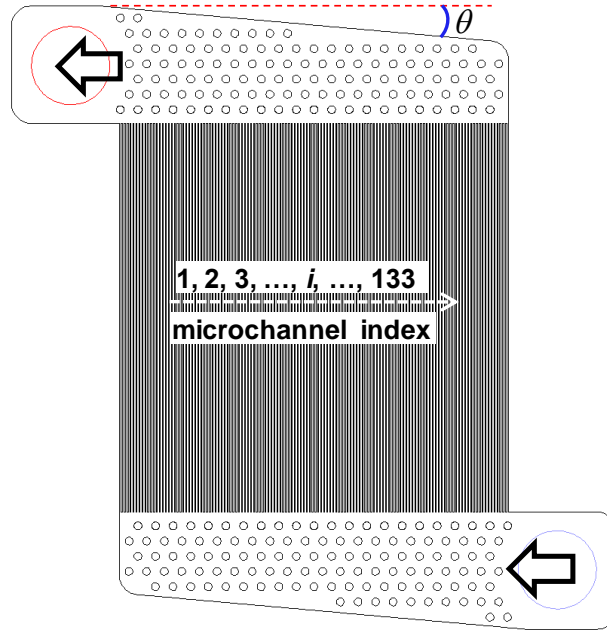
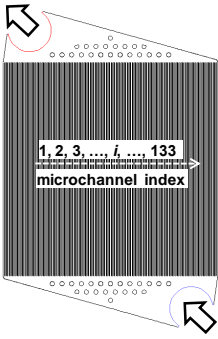
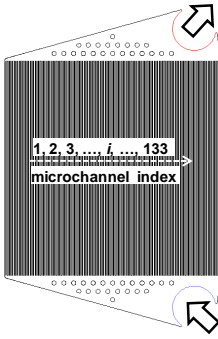
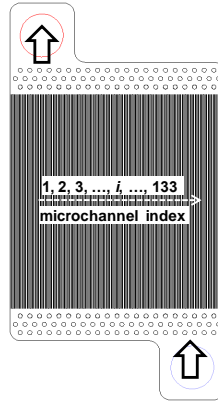
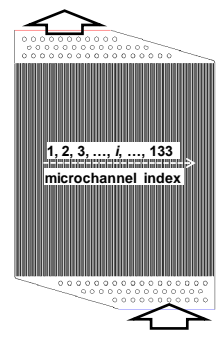
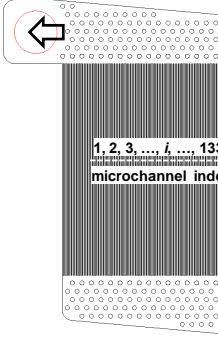


Figure 6-6: Configurations of a typical layer in the design of Type E.

The main characteristics of the 5 configurations tested numerically are summarized in Table 6-2, where different designs for the configuration of manifolds connected to the inlet and outlet of 133 parallel microchannels are displayed.

Table 6-2: The main characteristics of the 5 types of configurations.

Type A	Type B	Type C	Type D	Type E
				
Symmetric flow path in S shape	Asymmetric Flow path in N shape	Enlarged distributing and collecting areas	Enlarged feeding and discharging areas	Configuration based on the Renault-model, $\theta = 5.1^\circ$ [40]

Since the existing models available in literature for the analysis of the effect of the manifolds shape and configuration on the flow distribution among the parallel microchannels cannot be applied to the microHEX made for these tests due to the presence of the pillars in the manifolds and due to the different location and direction of inflow and outflow ports, in order to know exactly how the different configurations of the manifold affect the flow distribution and to select the best one from the five configurations described before, all the 5 configurations have been numerically investigated using the finite volume solver ANSYS FLUENT[®] 6.3.

The following assumptions have been applied to the CFD models:

- 1) A two-dimensional model of the manifold and layer is considered;
- 2) The flow is modeled as incompressible and isothermal;
- 3) The walls have been considered as smooth surfaces;
- 4) No heat transfer is activated;
- 5) The pressure at the venting port is fixed equal to 100 kPa.

The mass flow distribution through every channel is shown in the following figures. The flow distribution is numerically examined for two different feeding pressures: 160 kPa and 500 kPa, which correspond to the lower and larger mass flow rates that will be experimentally tested. To have an insight into the mass flow distribution through each microchannel, the mass flow rate

through every microchannel (q_i) under different feeding pressure was calculated. The average mass flow rate q_{ave} is calculated by:

$$q_{ave} = \frac{1}{n} \sum_{i=1}^n q_i, \quad n = 133 \quad (6.8)$$

where q_i is the mass flow rate of microchannel i .

Figure 6-7 shows the deviation of the mass flow rate through each microchannel from the average mass flow rate for a Type A configuration of the manifolds. It is evident that for microchannels in a broad middle section of the layer, the mass flow is relatively uniform and close to the average value. However, for microchannels close to the boundary of the layer, the mass flow rate becomes larger or smaller than the average value. In addition, at larger mass flow rate or higher feeding pressure the flow distribution is less uniform through microchannels near the boundary. However, in the middle part the flow distribution is much less influenced by the feeding pressure. This stable distribution is quite favorable for the performances of the microHEX.

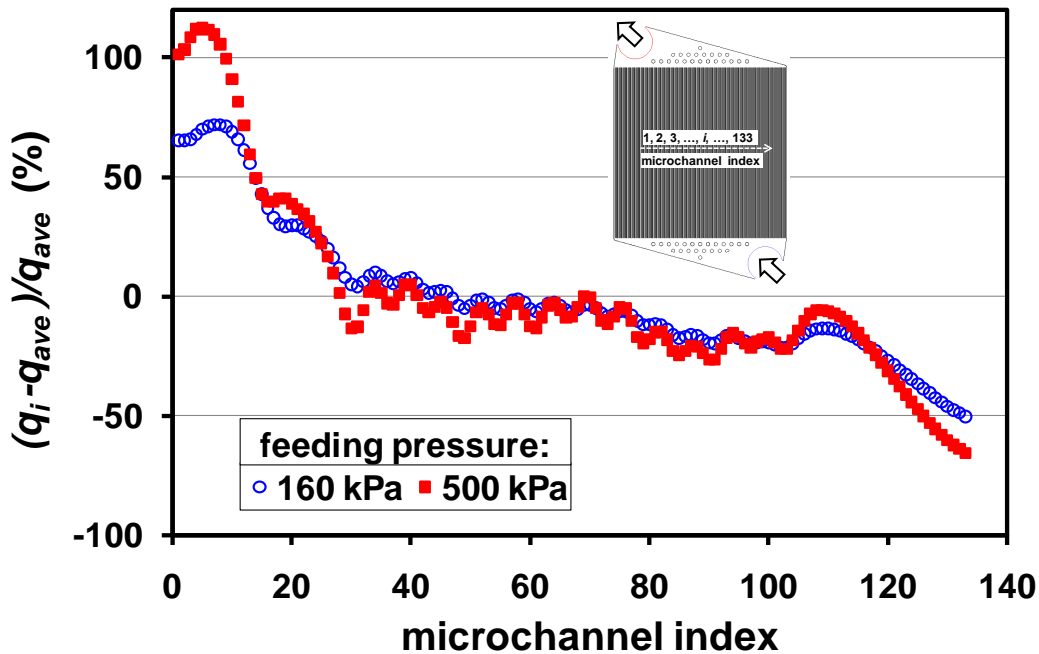


Figure 6-7: Mass flow distribution in the Type A configuration of the manifolds.

As shown in Figure 6-8, the U-shape flow generated by the Type B configuration of the manifolds does not perform well in terms of uniform flow distribution among the parallel

microchannels of the layer. From one side to the other of the layer, the mass flow rate through each microchannel increases almost linearly. Consequently, a uniform flow distribution can never be obtained by applying such kind of configuration. The simulation results suggest that a U-shape flow should always be avoided in the design of manifold configuration for microHEX. Otherwise, one may obtain laminar flow in some microchannels and transitional or even turbulent flow in the others with unstable results.

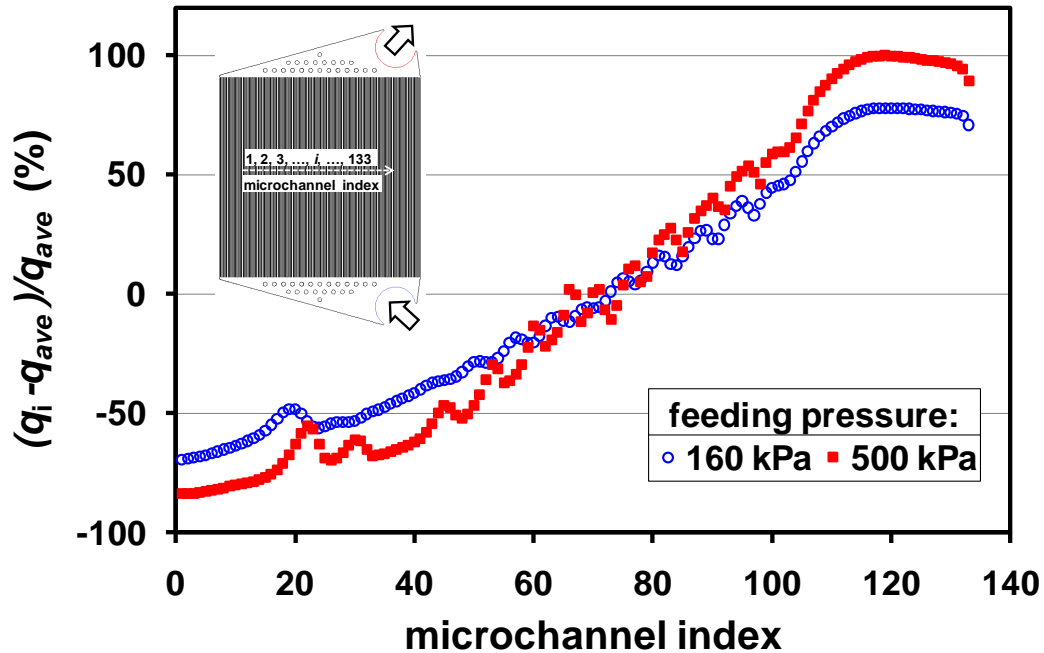


Figure 6-8: Mass flow distribution in the Type B configuration of the manifolds.

Figure 6-9 shows that the flow in the Type C configuration of the manifolds exhibits an asymmetric distribution having a parabolic shape, with lower flow rates in the middle section of layer and larger at the boundaries.

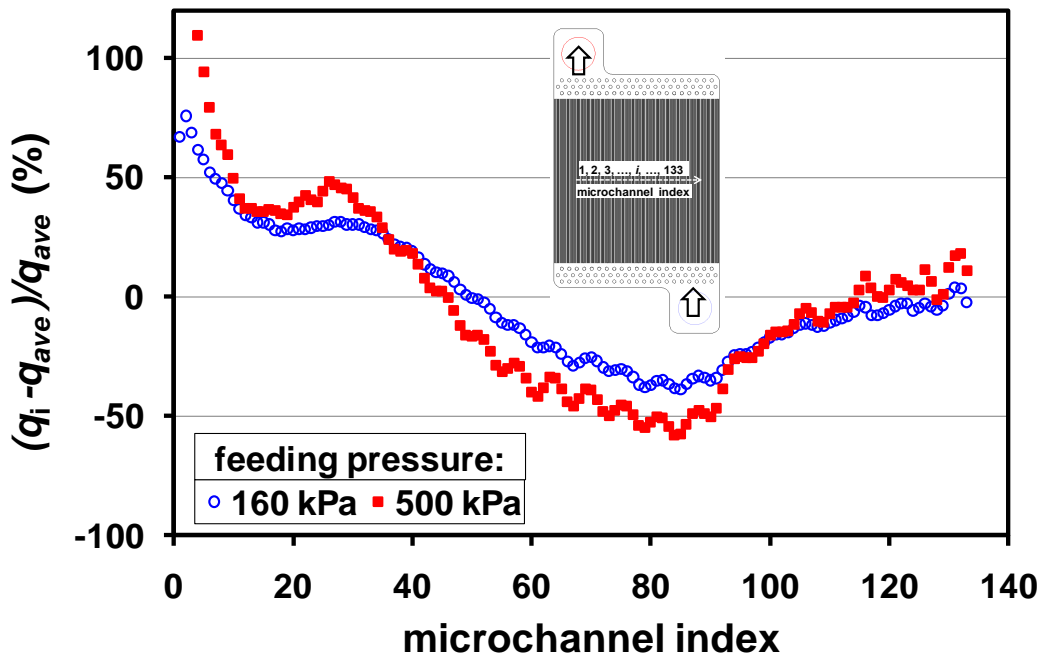


Figure 6-9: Mass flow distribution in the Type C configuration of the manifolds.

Type D configuration of the manifolds generates non-uniform flow rate distribution throughout the whole layer, as highlighted by the data shown in Figure 6-10. The mass flow rate decreases and increases sharply through neighboring microchannels from one side to the other of the layer. By comparison between Type A and Type D, it seems that the enlargement of feeding/venting port determines a negative effect on the flow distribution among the parallel channels.

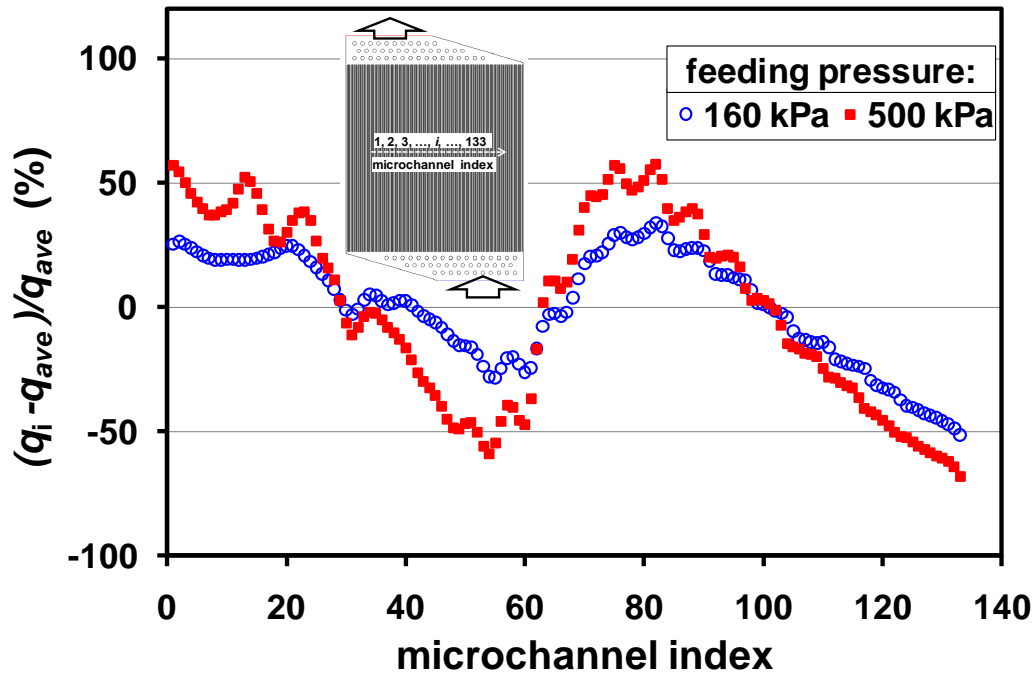


Figure 6-10: Mass flow distribution in the Type D configuration of the manifolds.

The flow distribution obtained by considering the Type E configuration optimized by considering the correlation proposed by Renault *et al.* [40] is plotted in Figure 6-11 for the two feeding pressures. It can be noted that the flow distribution mildly changes from the first microchannel to the last one. However, the deviation from the average mass flow rate remains considerably large through the majority of the parallel microchannels. This means that the correlation proposed by Renault is less suitable in the case of supporting pillars and for a large number of microchannels.

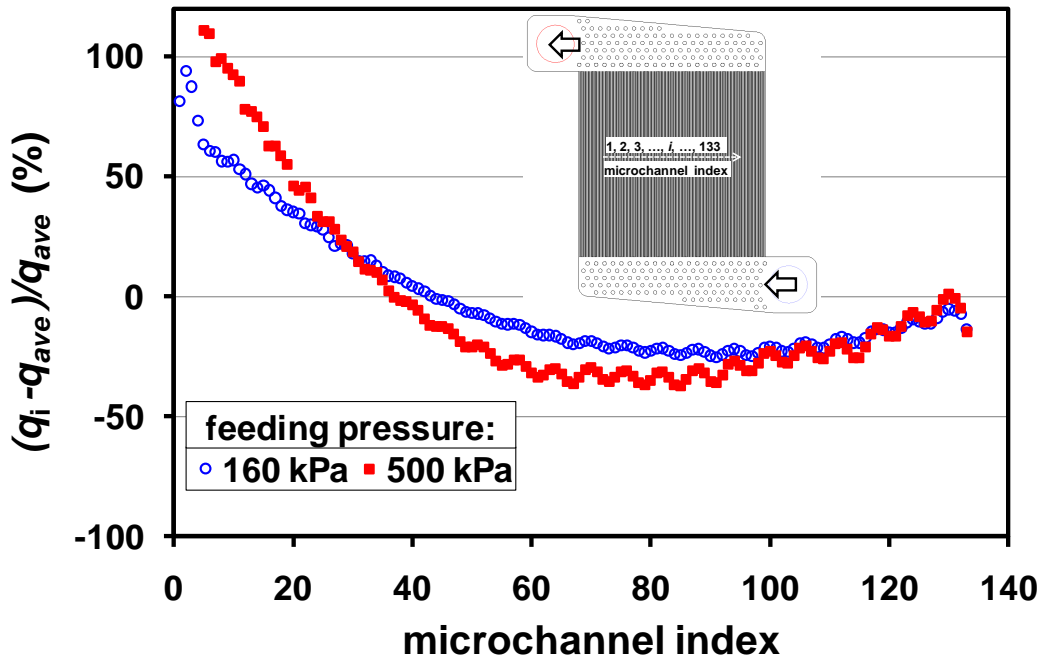


Figure 6-11: Mass flow distribution in the Type E configuration of the manifolds.

In summary, five different designs for the configuration of manifold have been numerically tested in order to verify the level of uniformity of the mass flow rate reachable among the parallel 133 microchannels which are present in the single layer of the microHEX tested in this thesis. A common conclusion from all the computational results is that low pressure tends to improve the uniformity of flow distribution. By comparing the results of these five configurations of the manifolds it is possible to conclude that Type A performs best in terms of uniform distribution, followed by Type E and C. The other two configurations (B, D) are not able to generate uniformly distributed flow through the 133 parallel microchannels. Therefore, the Type A configuration has been selected for the realization of the manifolds and for the position of the ports of the microHEX made at KIT.

6.4 2D simulation of flow distribution and pressure drop

Now the configuration of the single layer in terms of manifold shape and position of the ports is fixed. In this section, the exact mass flow rate and pressure distribution inside the device and their dependence on the absolute feeding pressure is numerically investigated. These numerical

results offer interesting insights for the optimization of the measurement strategies to better characterize experimentally the performance of such micro device.

6.4.1 Numerical model and Validation of the grid dependence of the results

A new two dimensional model has been built with FLUENT and the influence of the grid size on the results has been carefully examined. Three sets of meshes with different coarseness were developed, as listed in Table 6-3. The grid dependence of the numerical results has been checked for four different pressure drops under which the total mass flow rate was monitored. The finest mesh was taken as a reference. From Table 6-3 it can be noted that with the fine mesh (213 335 cells) the relative difference in the mass flow rate is less than 1% for all the pressure drops imposed during the computation. Therefore, the model of the layer has been built with a fine mesh.

Table 6-3: Validation of grid dependence.

p_{in} (kPa)	p_{out} (kPa)	Total mass flow rate (kg/s) and relative diff. (%)		
		Coarse mesh (95 970 cells)	Fine mesh (213 335 cells)	Very fine mesh (280 734 cells)
110	100	1.63 (1.37%)	1.60 (-0.41%)	1.60 (ref.)
120	100	2.32 (2.42%)	2.26 (-0.29%)	2.27 (ref.)
130	100	2.87 (2.82%)	2.77 (-0.86%)	2.79 (ref.)
150	100	3.70 (3.17%)	3.58 (-0.08%)	3.59 (ref.)

Numerical simulation may provide useful information on the local distribution of flow in the manifolds and in the microchannels and this information can be useful for the optimization of the measurement system (i.e. selection of the best position for the pressure and temperature sensors within the manifolds).

In this thesis a full layer of the microHEX, including the distributing manifold, the full length of the 133 parallel microchannels and the collecting manifold, has been simulated in order to check the pressure drop and flow distribution in different sections of the full layer. The numerical results obtained by using these two models are compared in the following paragraphs.

6.4.2 Flow distribution and pressure drop of a full layer

The numerical results from the simulation of a complete layer of the device are discussed in this section for feeding pressure set at 110 kPa, 160 kPa, 250 kPa and 500 kPa. The flow is vented from the exhaust port at atmospheric pressure, namely 100 kPa. With this model the mass flow rate and pressure drop through all the microchannels are self-balanced.

The velocity field in the distribution manifold and the microchannels is given in Figure 6-12 for a feeding pressure of 160 kPa. As the velocity profile in the microchannels does not change after the hydraulic entry length, only a part of the microchannel length is shown in Figure 6-12. The same will be applied thereafter for the downstream part of the layer. From Figure 6-12 it can be noted that the velocity in the distribution manifold is generally higher than that in the microchannels. This is because the total flow area normal to the streamline upstream in the distribution manifold is smaller than the total flow area downstream across all the parallel microchannels. For steady flow the mass flow rate is conserved at any cross section, which leads to larger flow speed at smaller cross section, and vice versa. This is a common feature of most microchannel devices using distribution connections between macro piping lines and microchannels.

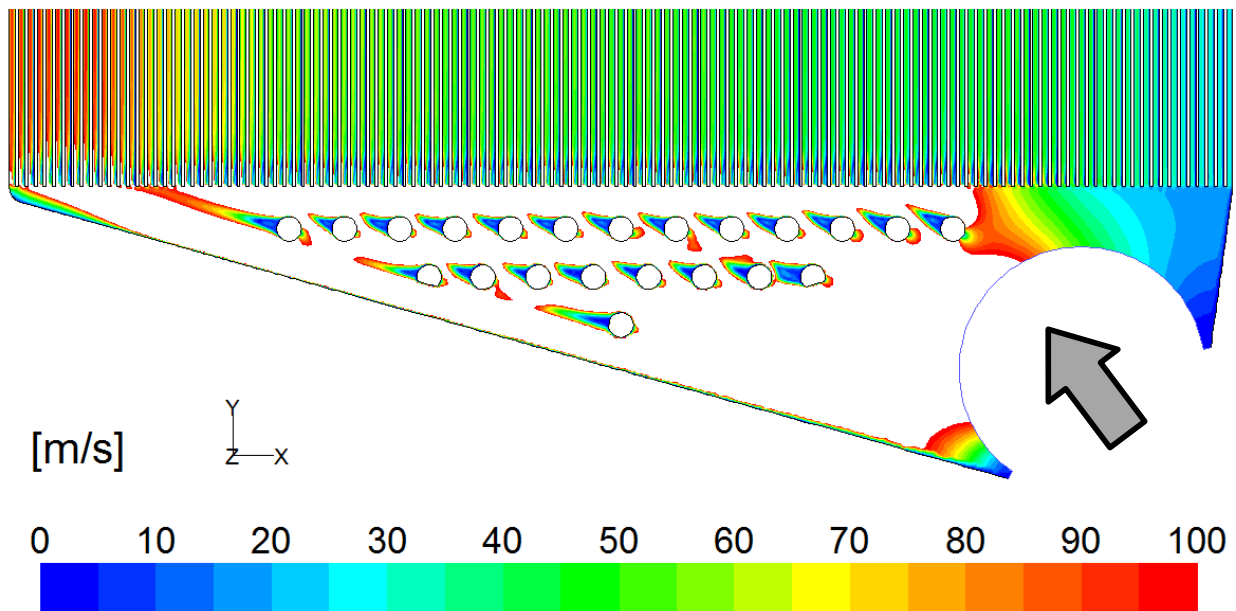


Figure 6-12: Flow velocity field in the distribution manifold and microchannels at feeding pressure of 160 kPa (length of microchannel partly displayed, velocity > 100 m/s in white region).

The velocity contour of the downstream part of the layer is shown in Figure 6-13. By observing the velocity distribution, it can be noticed that the flow velocity through the microchannels closest to the feeding port (or with short flow path) is unexpectedly the lowest. This is related to the pressure distribution throughout the whole layer.

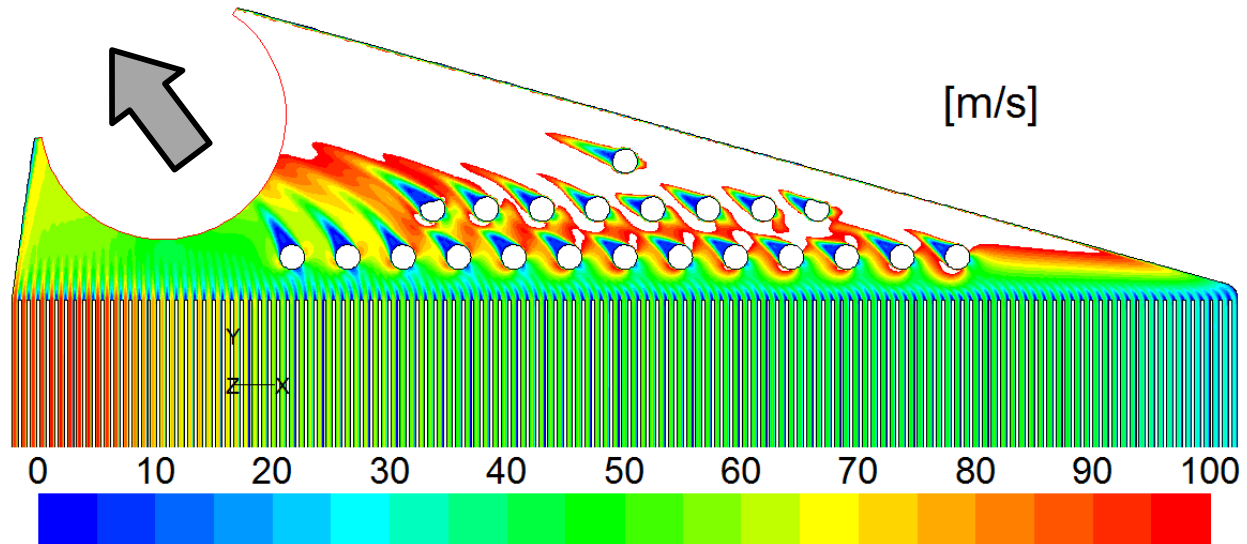


Figure 6-13: Flow velocity field in the collecting manifold and microchannels at feeding pressure of 160 kPa (length of microchannel partly displayed, velocity > 100 m/s in white region).

The pressure contour for the upstream part of the layer is shown in Figure 6-14, for the downstream part in Figure 6-15. The pressure at the inlets of the microchannels close to the feeding port is very high. This is caused by the high pressure at the outlets of these microchannels, as it is shown in Figure 6-15. The pressure drop from the microchannel outlets to the venting port is larger for microchannels further away from the venting port. This affects the pressure development inside the microchannels all the way from inlet to outlet. Accordingly the pressure distribution at the inlet region of the microchannels is influenced.

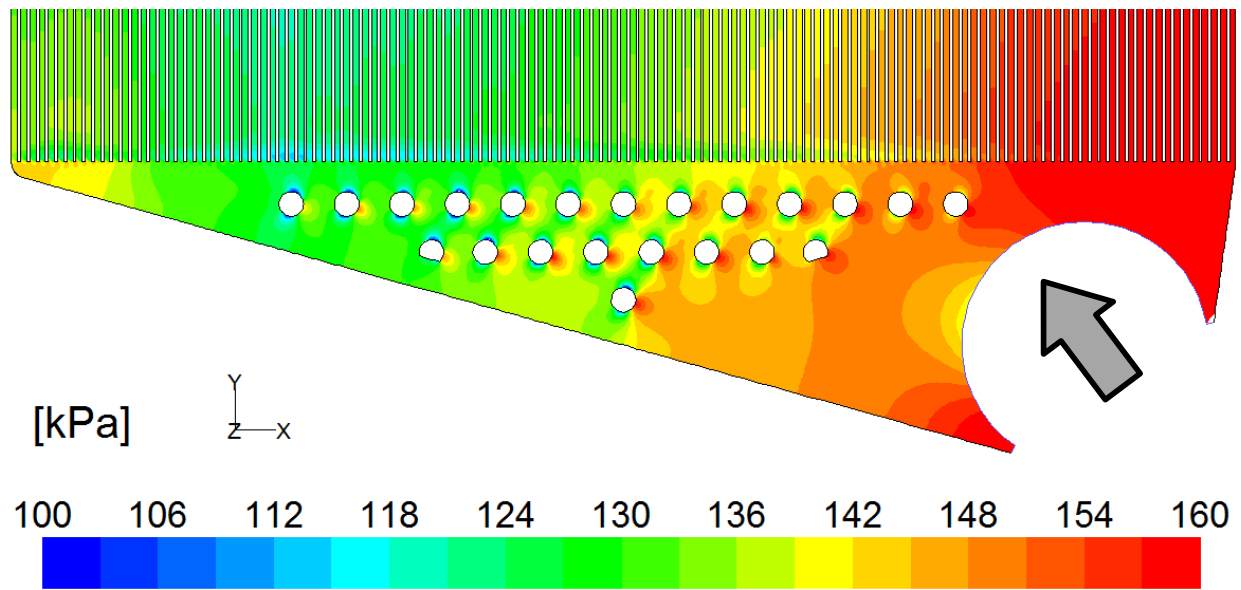


Figure 6-14: Static pressure in the distributing manifold and microchannels at feeding pressure of 160 kPa (length of microchannel partly displayed).

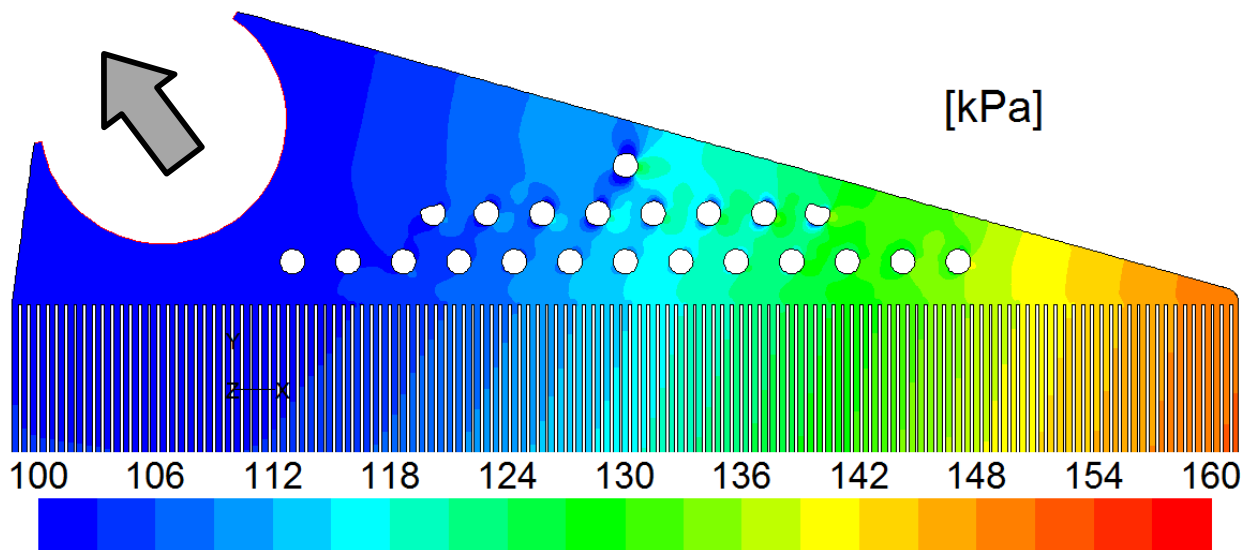


Figure 6-15: Static pressure in the collecting manifold and partial length of microchannels at feeding pressure of 160 kPa (length of microchannel partly displayed).

Figure 6-16 compares the distribution of mass flow rate through all the parallel microchannels for different feeding pressure values. The microchannels furthest from the feeding port show the highest mass flow rate. The mass flow rate decreases in the microchannels approaching the feeding port, with small fluctuations in between due to disturbances created by the pillars. Actually from Figure 6-16 it can be seen that the existence of the pillars seems to even the mass

flow distribution by creating an average flow velocity. In the region far from the pillars, the mass flow rate gradient is steeper. In addition, by increasing the feeding pressure, the uniformity of the mass flow rate distribution worsens and the presence of the pillars becomes more evident.

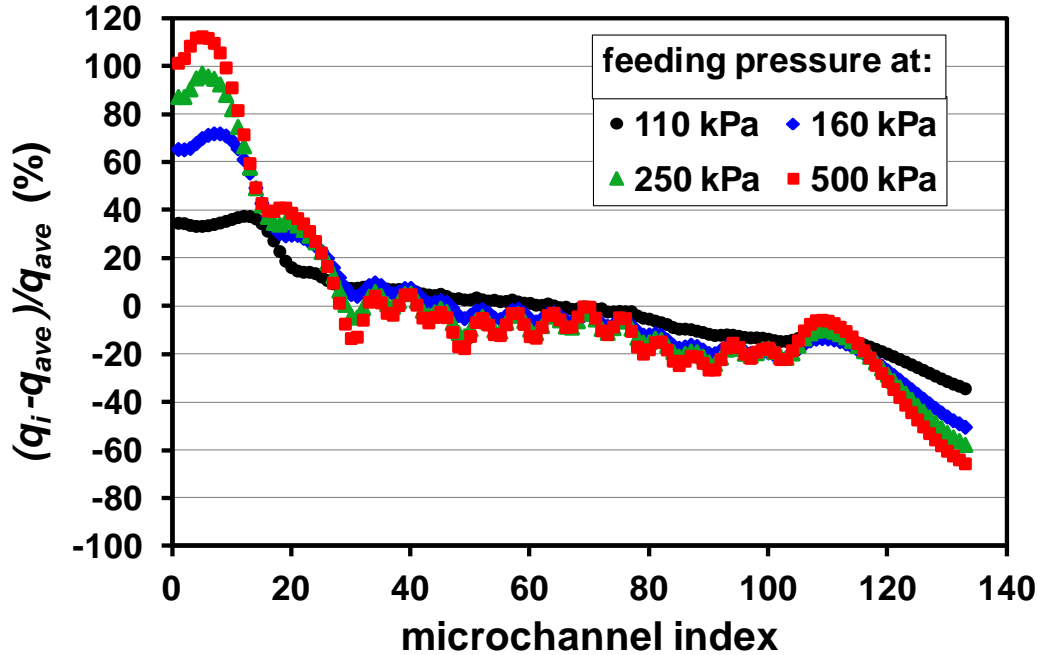


Figure 6-16: Mass flow rate of each microchannel under different feeding pressure.

The pressure at the inlet and outlet of each microchannel is compared for all the parallel microchannels in a dimensionless way. Similarly to the average mass flow rate, the mean pressure averaged over all the 133 microchannels is calculated by

$$p_{ave} = \frac{1}{n} \sum_{i=1}^n p_i, \quad n = 133 \quad (6.9)$$

where p_i is the pressure in microchannel i .

In Figure 6-17 the pressure difference between the feeding port and the inlet of each microchannel is shown as a function of the imposed feeding pressure. Generally, by imposing higher pressure at feeding port a higher fraction of pressure is lost in the manifold before the inlet of the channel. For an imposed feeding pressure of 500 kPa the feeding pressure is 50% higher than the inlet pressure of a large number of microchannels (microchannels with an index number from 10 to 60). Therefore, if the pressure measured at the feeding port or piping line (which is easy to be measured) is considered as the inlet pressure of the microchannels, a large measurement error may be introduced especially when the feeding pressure is large. For all the

values of the feeding pressure investigated, a negligible pressure loss in the manifold was found for microchannels very close to the feeding port, indexed from around 110 to 133. For these microchannels, the flow path from the feeding port is very short and free of obstructing pillars. For several microchannels furthest away from the feeding port, the pressure loss is also relatively small due to the fact that there are no obstacles in form of pillars within the flow path.

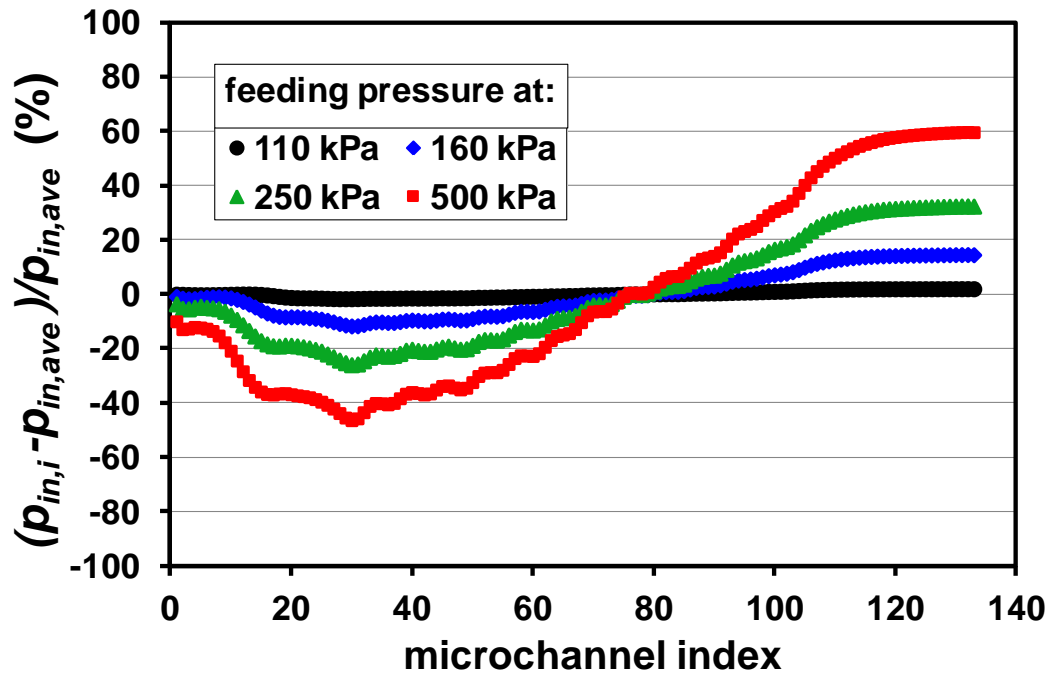


Figure 6-17: Pressure distribution at inlet of each microchannel.

Besides pressure distribution, the pressure loss at the distribution manifold is calculated for all the microchannels subjected to different feeding pressure values, as shown in Figure 6-18. Generally, with higher pressure at feeding port a higher fraction of pressure is lost due to the flow distribution and the supporting pillars. Therefore, if the pressure measured at the feeding port or piping line (which is the easiest way to perform) is considered as the inlet pressure of the microchannels, a large uncertainty may be introduced especially at high pressure values or larger mass flow rates.

For a fixed feeding pressure, a negligible pressure loss was found for microchannels very close to the feeding port, indexed from around 110 to 133 for the present microHEX. For these microchannels, the flow path from the feeding port is very short and free of obstructing pillars. For several microchannels furthest away from the feeding port, the pressure loss is also relatively small due to the fact that there are no obstacles in form of pillars within the flow path.

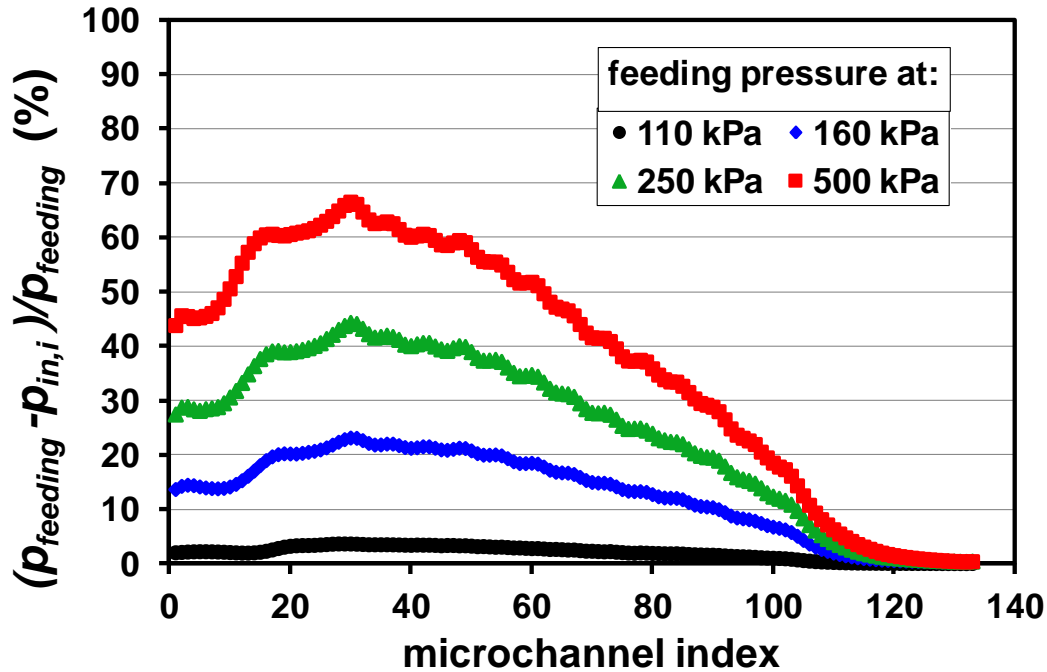


Figure 6-18: Pressure drop in the distribution manifold (from feeding port to inlet of microchannel).

The pressure distribution at the outlets of the parallel microchannels is shown in Figure 6-19 for different feeding pressure values. Compared with that at the microchannel inlets, the pressure distribution at the outlets is relatively linear. The further the microchannel is away from the exhaust port, the larger the outlet pressure becomes. Similarly, higher feeding pressure values increase the maldistribution of outlet pressure. The outlet pressure of the microchannel located at the middle of the whole panel is most representative of the average pressure.

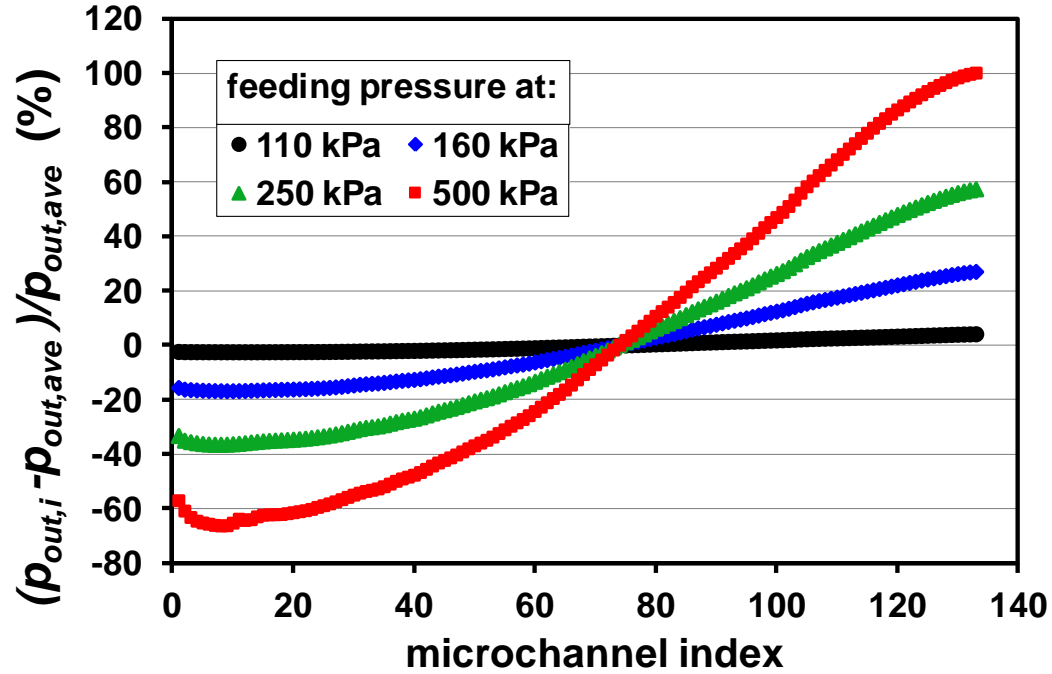


Figure 6-19: Pressure distribution at outlet of each microchannel.

Figure 6-20 shows the pressure loss from microchannel outlet to the exhaust port. In the pillar-free region with the shortest flow path, the pressure loss is very small. An exception is the feeding pressure of 500 kPa. At feeding pressure higher than 250 kPa, the microchannel outlet pressure becomes larger than 1.5 times of atmospheric pressure.

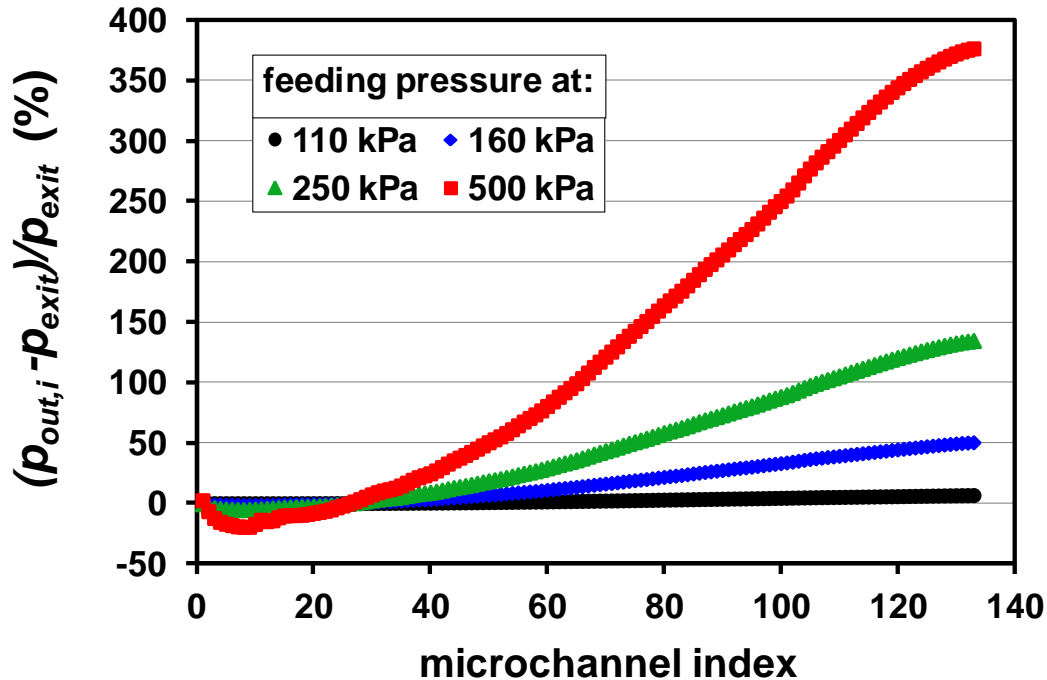


Figure 6-20: Percentage of pressure drop in the collecting manifold (from outlet to exhaust port).

The statistical data of numerical simulation of the whole layer are listed in Table 6-4, in terms of mass flow distribution, microchannel inlet pressure distribution and outlet pressure distribution. The number of microchannels showing a mass flow rate within a band of $\pm 20\%$ of the average value is counted. The same has been performed for the pressure at inlet and outlet. It can be noted that at low feeding pressure the distribution of these parameters is very uniform. Uniformity tends to deteriorate with increasing the inlet pressure. For a feeding pressure up to 500 kPa and above, more than half of all the microchannels show magnitudes for these parameters falling outside the range of $\pm 20\%$. Therefore, for the present micro heat exchanger, it is suggested that the feeding pressure should be kept lower than 250 kPa in order to maintain uniform flow distribution in a large part of the 133 parallel microchannel of the layer.

Table 6-4: Uniformity of mass flow rate and pressure distribution in terms of microchannel number from 2D simulation.

p_{in} (kPa)	p_{out} (kPa)	Mass flow rate	Pressure at inlet	Pressure at outlet
		Num. of channels with $q_i < (1 \pm 20\%) q_{ave}$	Num. of channels with $p_{in,i} < (1 \pm 20\%) p_{in,ave}$	Num. of channels with $p_{out,i} < (1 \pm 20\%) p_{out,ave}$
110	100	102/133	133/133	133/133
160	100	87/133	133/133	115/133
250	100	83/133	81/133	43/133
500	100	79/133	40/133	23/133

6.5 3D simulation of flow distribution and pressure drop

The numerical models applied in the previous sections are two dimensional; which means that the real thickness of the manifolds, pillars and microchannels were not taken into account in the numerical simulation. The use of 2D models is very diffuse in the literature related to the optimization of the manifolds such as the work of Balaji and Lakshminarayanan [39], Commenge *et al.* [36], Tonomura *et al.* [38] and Renault *et al.* [40]. In this section the numerical model will be improved in order to take into account of the finite height of the layer and the numerical results obtained with this 3D model will be compared with the results obtained with the 2D model presented before.

The sidewalls between the microchannels are 100 μm thick and 200 μm high. The small pillars have the same height as the microchannels. Figure 6-21 shows the geometrical construction used in the 3D numerical model of one layer. As the flow is symmetric in the third dimension, only half of the microchannel height is simulated in order to limit the computational efforts.

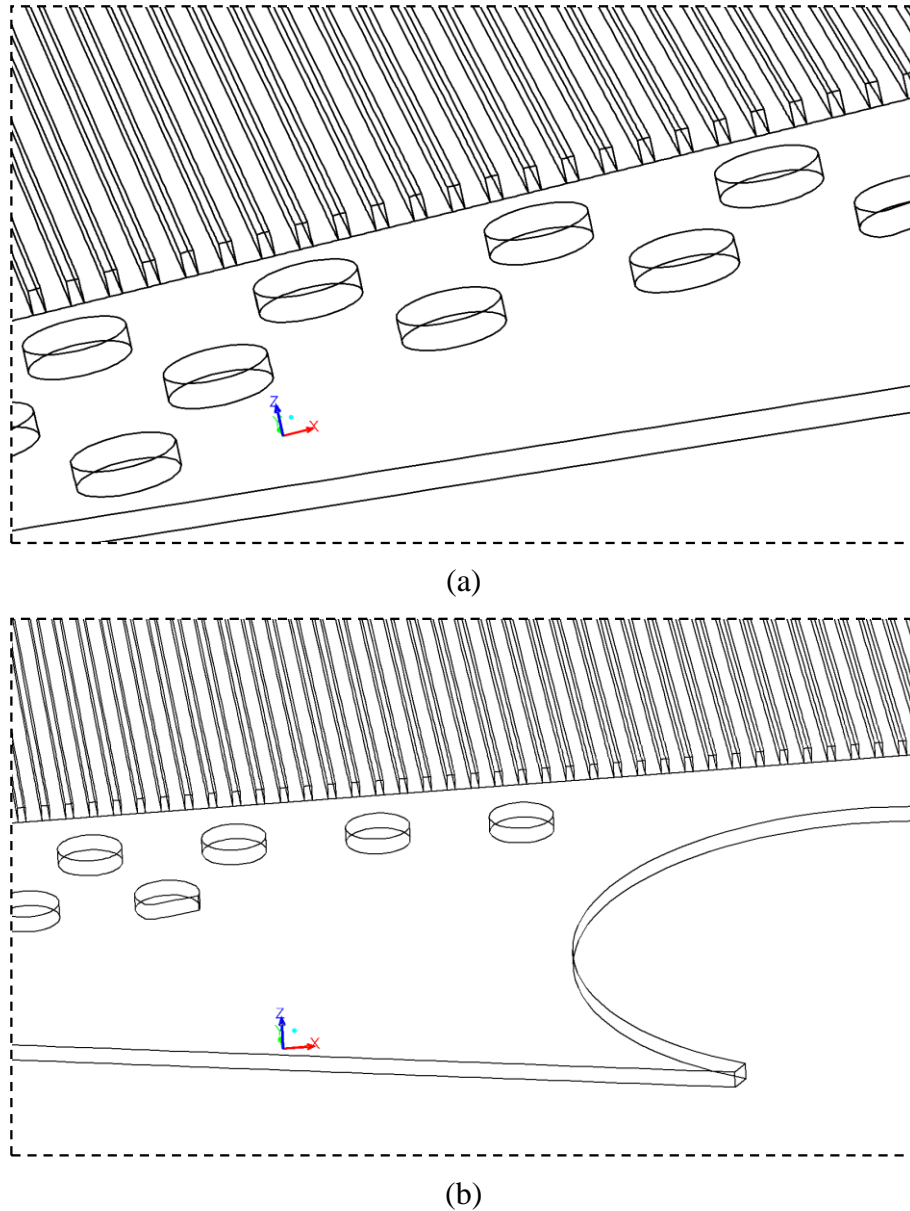


Figure 6-21: Partial views of 3D geometry of one layer. Microchannels with sidewalls (a); small pillars and feeding port (b).

The flow distribution obtained from 2D and 3D numerical simulation is compared in Figure 6-22 for the same feeding pressure, which is fixed at 500 kPa. It is evident that the flow distribution obtained by using the 3D model becomes more uniform than that obtained with the 2D model. This is probably due to the additional frictional drag on the bottom and top of the microchannels which is considered in the 3D model. Especially for flow distribution along the side microchannels, the deviation is greatly reduced by using 3D model. This means that the 2D

model tends generally to overestimate the flow maldistribution. The maximum deviation from the average mass flow rate is no larger than 50% for all the 133 parallel microchannels.

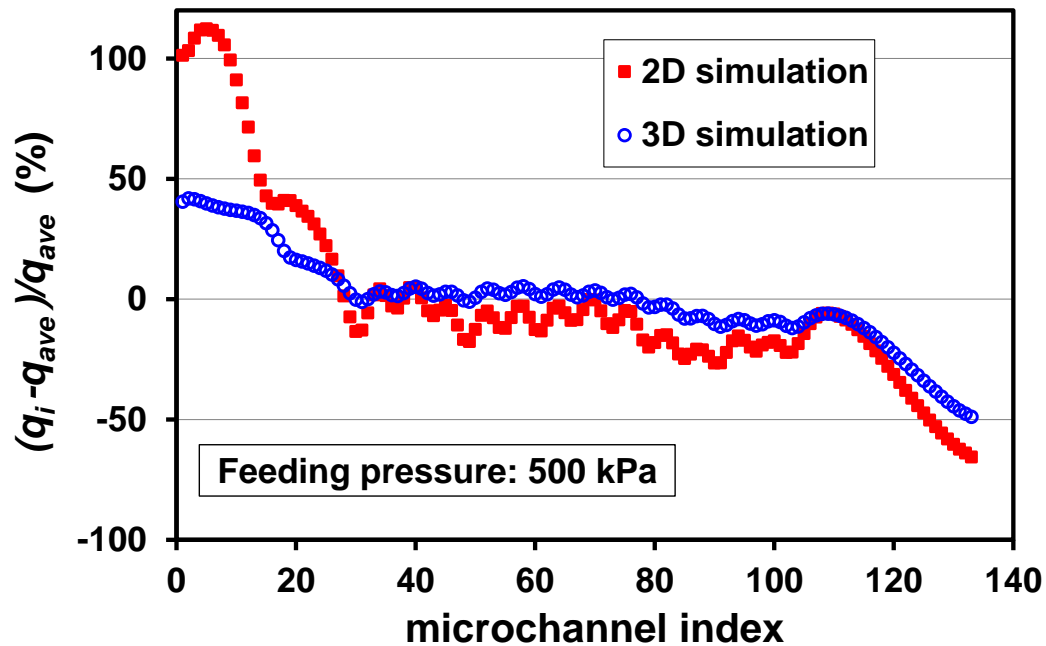


Figure 6-22: Comparison of flow distribution obtained from 2D and 3D models.

It would be also interesting to analyze the dependence of flow distribution on the feeding pressure by using the 3D model. However, due to huge amount of computational resource required in 3D full simulation, the flows at only two feeding pressures are simulated in the present work, namely, 500 kPa and 160 kPa. The mass flow distribution is plotted in Figure 6-23 for these two feeding pressures. It can be noted that the results obtained with the 3D model highlight that the flow distribution is less dependent on the feeding pressure. By observing the data points in Figure 6-23, the relative deviation of flow rate is almost the same through more than 100 microchannels for two completely different feeding pressures. The performance of the manufactured device will benefit from this conclusion because the experimental results obtained at different mass flow rates or pressures can be considered comparable if the change in flow distribution can be considered negligible.

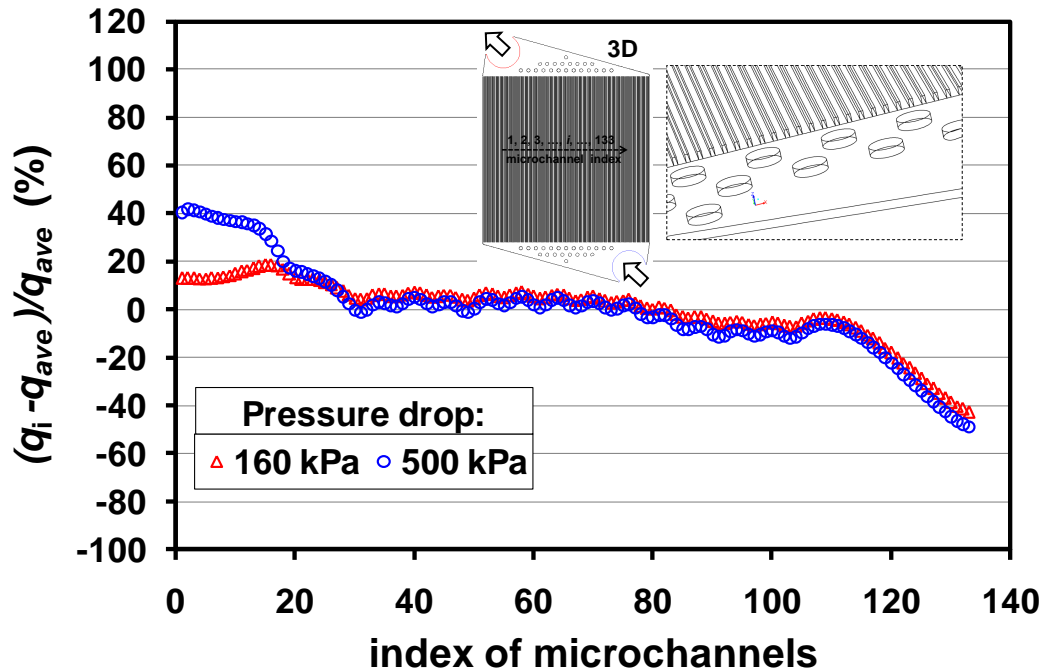


Figure 6-23: Mass flow distribution obtained from 3D simulation at two different feeding pressures.

Similar to Table 6-4, the uniformity of flow rate and pressure distribution is statistically analyzed in Table 6-5 by using numerical results obtained from the 3D simulation for feeding pressure equal to 160 and 500 kPa. It should be highlighted that the flow distribution is greatly improved by applying 3D simulation. More specifically, at feeding pressure equal to 160 kPa, 120 out of the total 133 microchannels have mass flow rate within $\pm 20\%$ of the average mass flow rate as evidenced by the 3D simulation, this number is only 87/133 in the results obtained from 2D simulation. When the feeding pressure is increased to 500 kPa, there are 22 more microchannels in the 3D model having mass flow rate within this range than those in the 2D model.

Table 6-5: Uniformity of mass flow rate and pressure distribution in terms of microchannel number from 3D simulation.

p_{in} (kPa)	p_{out} (kPa)	Mass flow rate	Pressure at inlet	Pressure at outlet
		Num. of channels with $q_i < (1 \pm 20\%) q_{ave}$	Num. of channels with $p_{in,i} < (1 \pm 20\%) p_{in,ave}$	Num. of channels with $p_{out,i} < (1 \pm 20\%) p_{out,ave}$
160	100	120/133	133/133	117/133
500	100	101/133	40/133	24/133

6.6 Conclusions

The design of a microHEX for gas flow has been discussed in this chapter in terms of prediction of the range of main parameters in the test, thermal conduction in the solid wall of microHEX, influence of manifold configuration on flow distribution and the dependence of flow distribution on the operating pressure of the microdevice.

By using the conventional theory, the pressure and mass flow rate under which the double-layered microHEX operates is pre-calculated. This prediction enables the correct selection of measurement devices with appropriate full scales, such as pressure transducers, mass flow controllers and thermocouples.

By analyzing the influence of heat conduction in the solid wall on the effectiveness of the microHEX, polymer has been selected for the housing shell of the microHEX in order to minimize the heat losses and to optimize the thermal performance of the device. Different materials (PEEK, stainless steel, aluminum and copper) have been chosen for the partition wall in order to experimentally examine the influence wall axial conduction on the thermal performance of microHEX and to check the prediction of Stief.

The impact of the configuration of the distributing/collecting manifolds on the flow distribution through all the parallel microchannel of a single layer has been numerically checked by using five different types of manifolds. The numerical results evidenced that low operation pressure is beneficial for uniform flow distribution. By comparison of the data on the five configurations, Type A which generates symmetric flow in the layer performs best in terms of flow distribution and is accordingly applied to the design and manufacture of the microHEX.

A full layer using Type A for the manifolds has been further studied by applying a complete 2D numerical model, from which the distribution of mass flow rate, flow velocity and pressure throughout the layer have been obtained for different values of feeding pressure. The analysis of the numerical results facilitates the experimental test in which the positions of pressure measurement at both inlet and outlet of the parallel microchannels are carefully determined so that the values of the measured pressure are sufficiently representative of the average inlet and outlet pressure of the 133 microchannels.

The numerical study on flow distribution has been extended to 3D simulation, which considers the test device with a finite depth of the microchannels and manifolds. The results determined by the 3D simulation show a remarkable 30% improvement in terms of uniform mass flow distribution compared with the results obtained from the 2D simulation, which is quite favorable to accurately estimate the performance of the microHEX during experiment.

7 Experimental Investigation on Gas Flow Micro Heat Exchangers

7.1 Description of the experimental apparatus

In this section the main results obtained by means of experimental tests on a double-layered microHEX made at KIT are described. The detailed geometrical and thermophysical parameters of the double-layered microHEX tested in this work are listed in Table 7-1. On both hot side and cold side the gas flows through 133 parallel microchannels. The hot side is separated from the cold side by an interchangeable partition foil. The microchannels are made on a PEEK substrate by mechanical microfabrication; each microchannel has a square cross section with a size of 200 μm and a length of 39.8 mm. The thickness of the PEEK cover under the channels is 5000 μm . The parallel microchannels are separated by side walls having a thickness of 100 μm . The double-layered microHEX has a surface-to-volume ratio of 2500 $\text{m}^2 \cdot \text{m}^{-3}$. It should be highlighted that this value is much larger than the typical values of conventional compact heat exchangers ($<1000 \text{ m}^2 \text{ m}^{-3}$).

Table 7-1: Parameters of the micro heat exchangers for fabrication.

Micro heat exchanger	Value of parameters
Channel width W : (μm)	200
Channel height H : (μm)	200
Hydraulic diameter d_h : (μm)	200
Channel length L : (mm)	39.8
Surface roughness of microchannel: (μm)	0.15
Thickness of channel side wall s_1 : (μm)	100
Thickness of partition wall s_2 : (μm)	100, 500
Material of housing shell	PEEK
Thermal conductivity of housing shell: ($\text{WK}^{-1}\text{m}^{-1}$)	0.25
Number of channels per layer	133
Number of layers per fluid	1 and 10
Ratio of (heat transfer) surface to (flow) volume: (m^2m^{-3})	2500 and 4750

The typical PEEK layer with 133 parallel microchannels, distributing/collecting manifolds and feeding/venting ports is shown in Figure 7-1(a). The microchannels have been manufactured into polished PEEK platelets using mechanical precision machining [2, 149]. CNC-controlled tooling systems and miniaturized tools made from natural diamond have been used. The accurate control of the design allows manufacturing of microchannels with an absolute dimension uncertainty of about $\pm 1\ \mu\text{m}$ in all three dimensions (width, depth and length of the microchannels). The average surface roughness inside the microchannels was not measured but estimated to be in the range of 150 nm. This was based on experiences with the manufacturing of microstructure devices made of PEEK at KIT, as well as on measurements undertaken by Hecht *et al.* [150] and Vittoriosi *et al.* [151]. The ratio between the average roughness and the hydraulic diameter of the microchannels is about $7 \cdot 10^{-4}$. Due to this low value the estimated relative roughness is most likely small enough to be neglected in the estimation of the frictional losses and of the thermal performance of the device.

The PEEK layer has a width of 39.8 mm, which is identical to the length of the microchannels. In order to obtain a cross flow arrangement the layers can be rotated by 90 degree. Figure 7-1(b) shows a magnified area of the distributing manifold. It is important to underline that in the previous experimental works dealing with the analysis of the thermal performance of gas micro heat exchangers appeared in literature [32, 33, 34], the fluid temperature and pressure were measured only before the feeding ports, and/or after the venting ports: no additional information about the value of these parameters within the microdevice (in particular within the manifolds) was in general known. As demonstrated in Chapter 6, the presence of the manifolds is significant in microHEX and if one neglects the role of the manifolds in terms of frictional behavior and heat losses can obtain results which are strongly underestimated in terms of real pressure temperature losses. This can explain the large disagreements between the experimental data and the theory evidenced in some paper published in the past [34]. In the present study pressure and temperature sensors have been placed within the manifolds in order to obtain more accurate measurements very close to the ends of the microchannels. Two K-type thermocouples and one pressure sensor are delicately placed on the top surface of the manifold in order to monitor the local values. The position of the sensors have been carefully selected on the basis of the numerical results presented in Chapter 6, obtained with a 3D simulation of the full device; the position of the sensors has been selected in order to

obtain measured parameters which can be considered as sufficiently representative of their average values within the inlet and outlet manifolds.

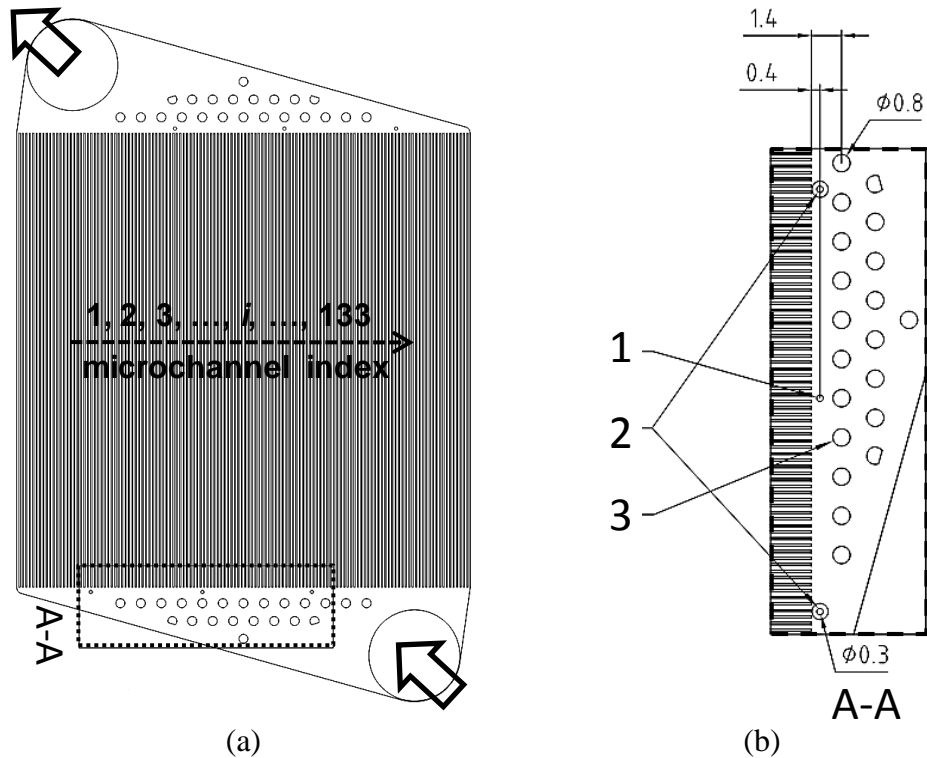


Figure 7-1: Typical layer (with 133 microchannels) of the micro heat-exchanger (a); in-situ measurement in distribution/collecting manifolds (b) (1- pressure sensor; 2- temperature sensor; 3- pillars. unit: mm).

Figure 7-2 shows the photograph of the cover PEEK layer manufactured with 133 parallel microchannels as well as distributing and collecting manifolds. The cylindrical pillars inserted into the manifolds are well evident in Figure 7-2. It is shown how pressure ports and customized thermocouples are carefully integrated very close to the inlets and outlets of microchannels.

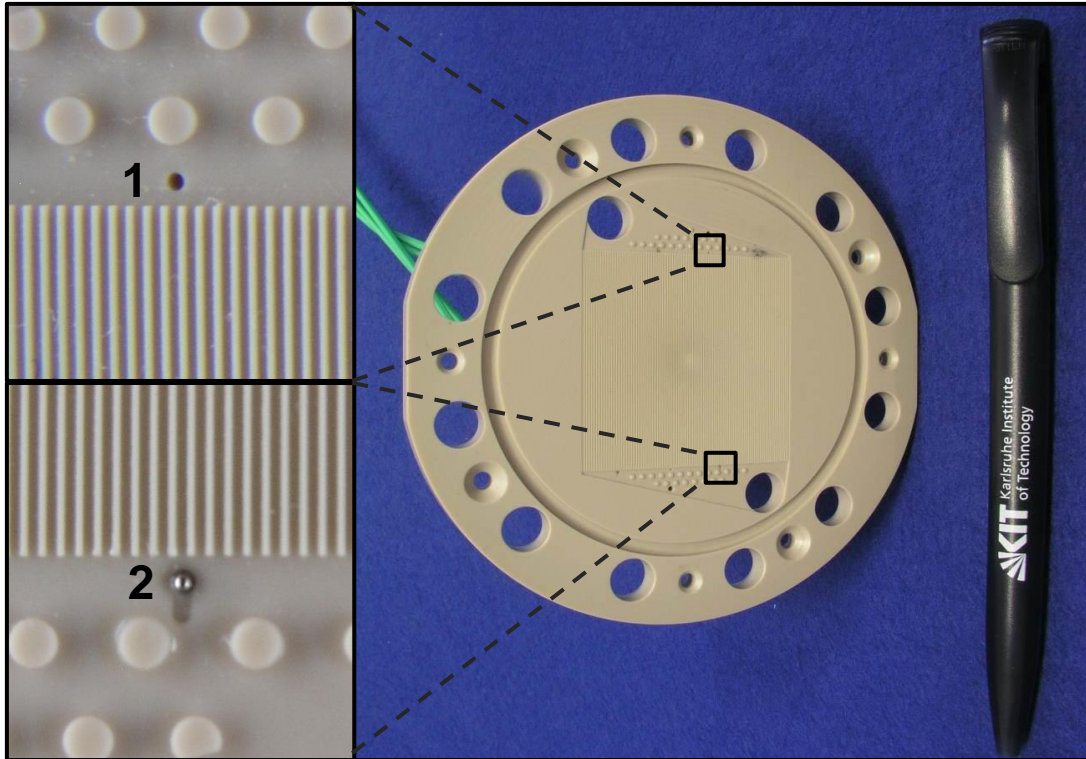


Figure 7-2: A typical layer manufactured in PEEK material with integrated pressure (1) and temperature (2) sensors.

An exploded CAD (Computer-aided design) drawing of the micro heat exchanger ready for packaging is shown in Figure 7-3(a). The temperature (1) and pressure (2) are measured at the distributing and collecting manifolds for both hot and cold fluids. The core of the micro heat exchanger is housed in a shell made of PEEK (5). The low thermal conductivity of polymer helps to prevent heat loss from the core to the environment. For the double-layered micro heat exchanger the thin plate (6) between the hot and cold flow can be exchanged using different materials. The material and thickness of the plate (6) can be selected according to various purposes. The thick metallic covers (4) compress all the layers together by a group of screws to ensure the leak tightness of the whole device. Figure 7-3(b) shows the photograph of the device ready for assembling.

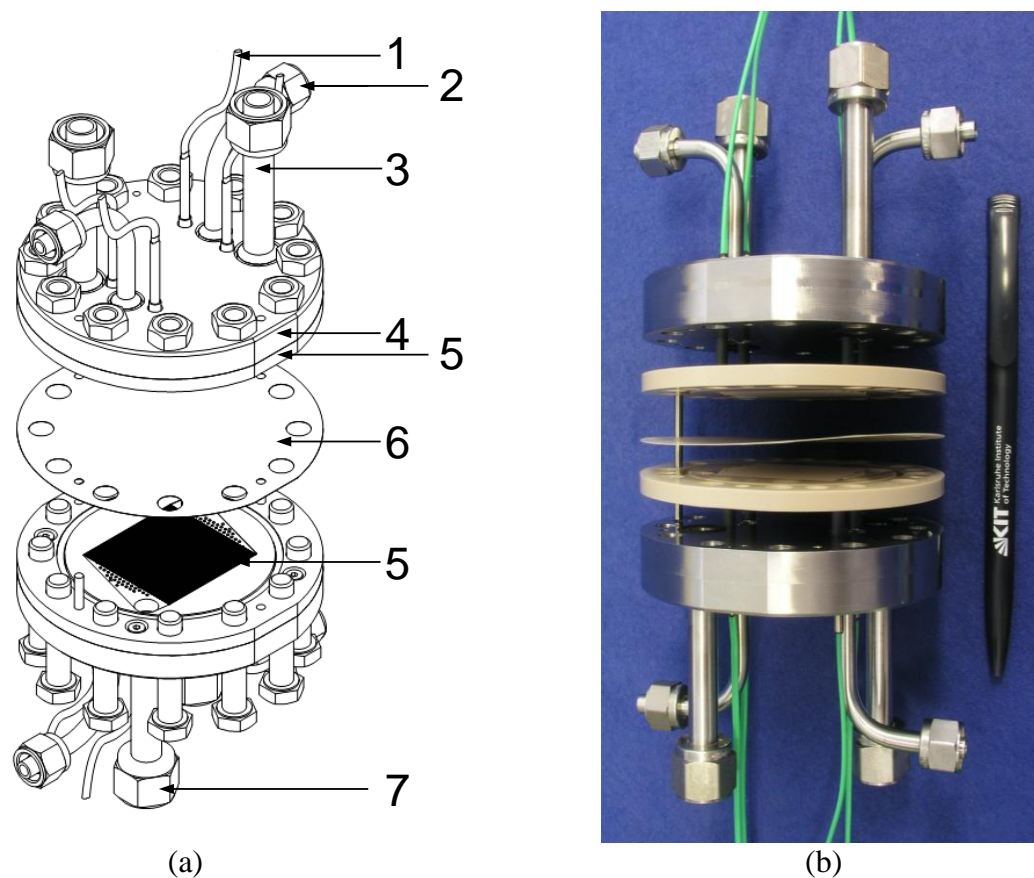


Figure 7-3: Exploded schematic of the double-layered microHEX (a: 1- connection of thermocouple; 2- connection of pressure transducer; 3- feeding/venting port of the first fluid; 4- metallic cover; 5- PEEK cover with 133 microchannels; 6- partition foil between two fluids; 7- feeding/venting port of the second fluid) and photograph of the manufactured device (b).

As explained previously, the experimental apparatus provides flexible change among cocurrent, countercurrent and cross flow arrangements. Figure 7-4 shows the schematic layout of the test rig. High pressure air flow at room temperature is supplied by the gas source (at 10 bar by a compressor and up to 40 bar by the gas flask). The gas flow is firstly filtered by a 60-micrometer filter (Swagelok) to get rid of possible impurities. The gas pressure is adjusted by a pressure regulator in order to reach the optimum pressure requirements by the mass flow controllers (MFCs) for different mass flow rates. After the pressure regulator, the flow is split into two branches which are proposed to supply the hot and cold branches of the microHEX. The flow rate of each branch is controlled by a MFC (Brooks SLA5851 or SLA5853). A buffer vessel with a volume of 10 liter is installed between the pressure regulator and the MFCs to avoid disturbances. After the MFCs, the gas temperature is regulated by the temperature unit of

7.1 Description of the experimental apparatus

the experimental system to provide both hot and cold flows at fixed temperature. With an imposed temperature and flow rate, both hot and cold flows enter the gas micro heat exchanger with a certain flow arrangement (countercurrent, cocurrent or cross flow). The exiting gas flow is vented to the atmosphere.

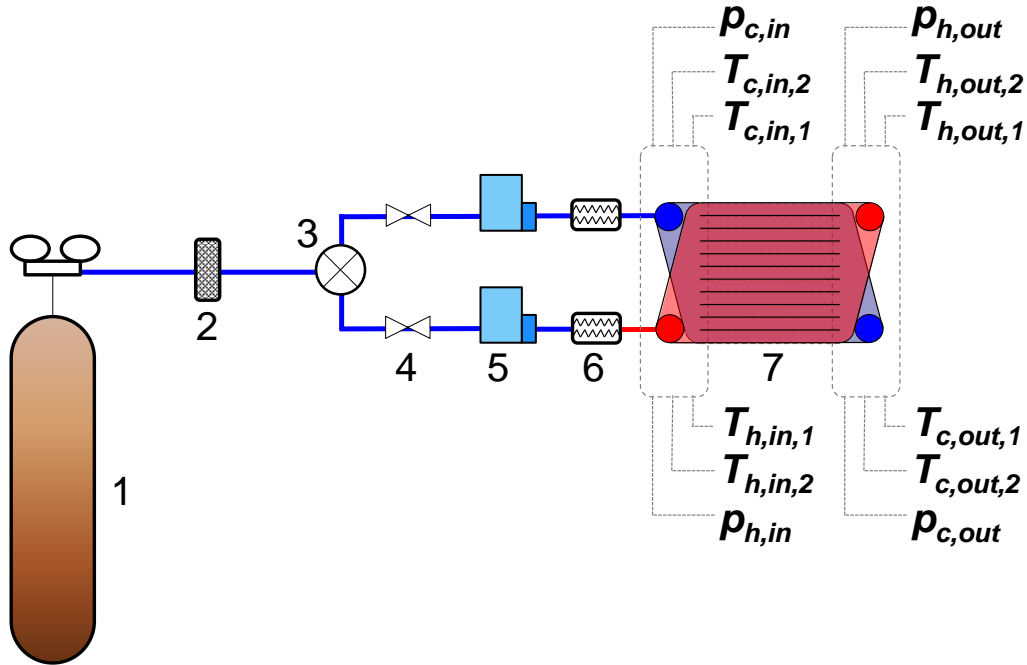


Figure 7-4: Schematic layout of the test rig. (1- gas source, 2- filter, 3- flow splitter, 4- valves, 5- mass flow controller, 6- temperature regulator, 7- micro heat exchanger).

The test rig is shown in Figure 7-5, where the main devices are evidenced by following the same numerical notation used in Figure 6-4; it is possible to note the pressure regulator (1), the mass flow controllers (5), the micro heat exchanger (7) and the temperature regulators (6).

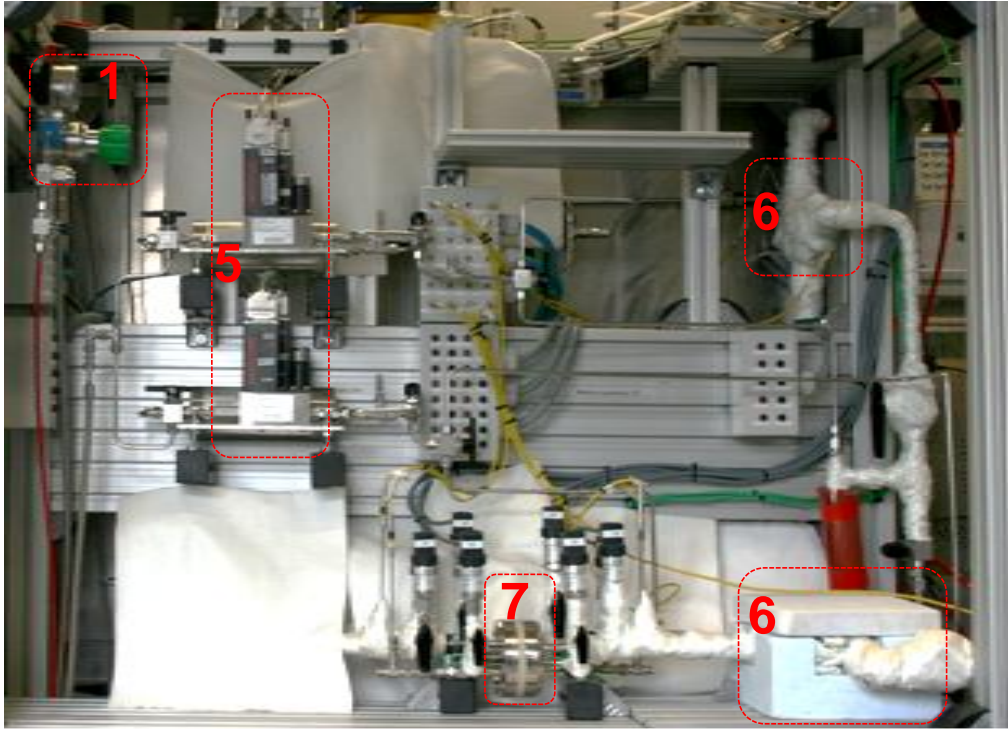


Figure 7-5: Photograph of the test system (1- pressure regulator of gas source; 5- mass flow controllers; 6- temperature regulators; 7- micro heat exchanger).

Figure 7-6 shows the micro device connected to the experimental loop; the external connections of pressure sensors and thermocouples are indicated. During the tests, the micro heat exchanger is wrapped with a thick thermal insulation material in order to minimize the heat losses.

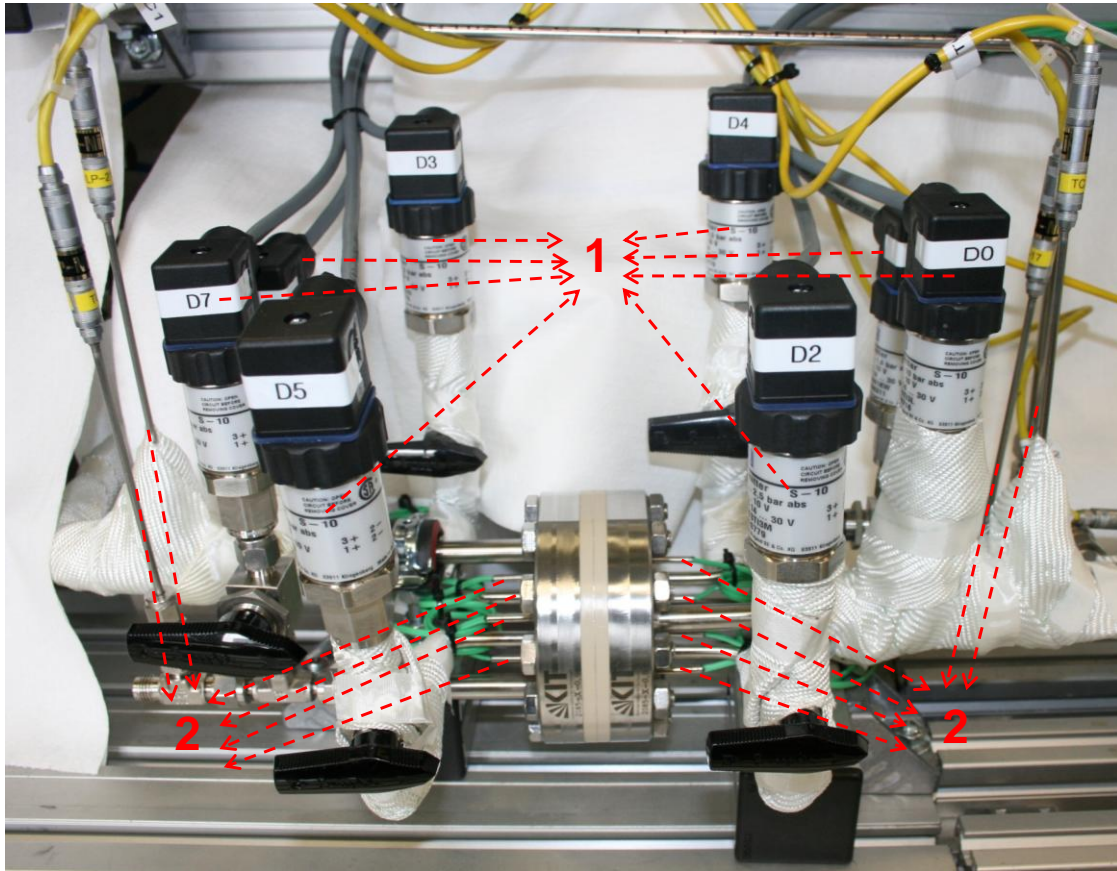


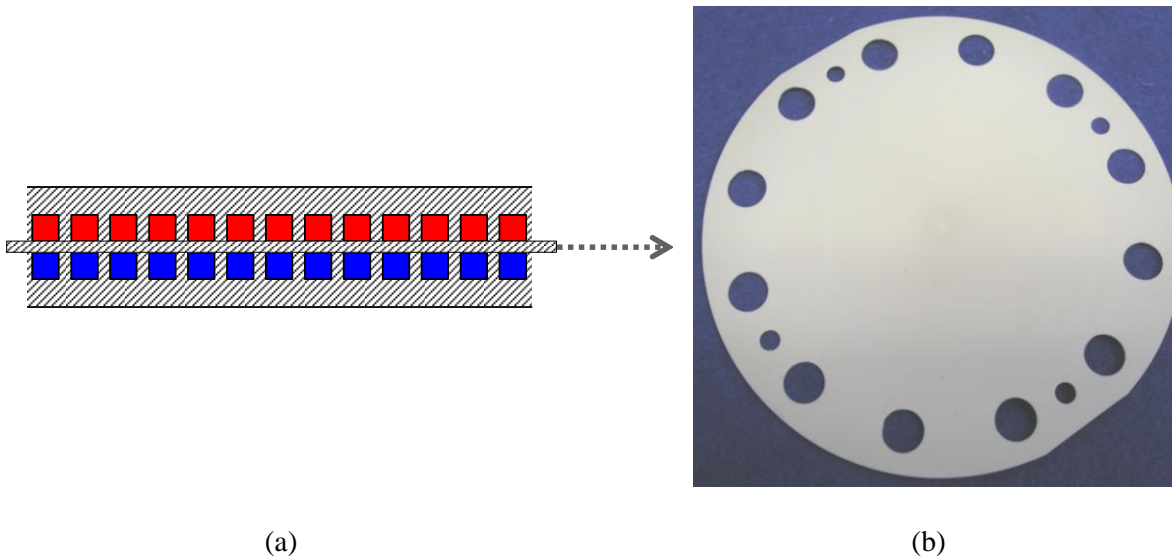
Figure 7-6: Photograph of the micro heat exchanger in test (1- pressure sensors; 2- thermocouples).

The typical accuracy of the sensors used in the test rig is listed in Table 7-2. Based on these values, the total uncertainty linked to the heat exchanger effectiveness is estimated to be between 2.8% and 5.0%. The total uncertainty on the overall heat transfer coefficient and on the volumetric heat exchange rate is estimated to be equal to 4.3% and 2.0%, respectively.

Table 7-2: Uncertainties in the measurements

Measurement	Uncertainty
Pressure (Wika)	± 0.51 % of F.S.
Temperature (Conatex)	± 0.5 K
Mass flow rate (Brooks)	± 1 % of the measured value if $20\% \text{F.S.} < \dot{m} < \text{F.S.}$ ± 0.2 % of F.S. if $\dot{m} < 20\% \text{F.S.}$

Figure 7-7(a) schematically shows the double-layered micro heat exchanger with the upper cover (in PEEK), parallel microchannels for hot fluid, partition foil, parallel microchannels for cold fluid and the lower cover (in PEEK). A photo of a PEEK foil is given in Figure 7-7(b).

**Figure 7-7:** The double-layered micro heat exchanger (a) and the partition foil (b)

The double-layered micro heat exchanger has been tested with five partition foils made with four materials having a quite different thermal conductivity. The detailed parameters of the tested foils are listed in Table 7-3, where each partition foil has been indicated by means of a code which will be recalled in the result discussion.

Table 7-3: List of partition foils in the present tests.

Partition foils	Code	Thickness (μm)	Thermal conductivity ($\text{WK}^{-1}\text{m}^{-1}$)
Thick PEEK foil	P500	500	0.25
Thin stainless steel foil	SS100	100	15
Thin aluminum foil	AL100	100	150
Thin copper foil	C100	100	400
Thick copper foil	C500	500	400

7.2 Data reduction

Classical theory developed for conventional heat exchangers is applied to the reduction of the present experimental data. The heat transfer rate can be calculated by measuring the temperature difference between the inlet and the outlet and the mass flow rate on the hot side:

$$Q_h = \dot{m}_h c_{p,h} (T_{h,in} - T_{h,out}) \quad (7.1)$$

where the subscript h refers to the hot side, and c_p is the specific heat capacity of air.

It is also possible to know the value of this parameter from similar data measured on the cold side:

$$Q_c = \dot{m}_c c_{p,c} (T_{c,in} - T_{c,out}) \quad (7.2)$$

where the subscript c refers to the cold side.

Ideally the heat transfer rate obtained from both sides should be the equal. However, in practice due to different amount of heat loss on both sides, the two parameters may slightly differ from each other. Therefore, in the present data reduction the heat transfer rate is averaged from both sides:

$$Q_{ave} = \frac{Q_h + Q_c}{2} \quad (7.3)$$

The logarithmic mean temperature difference (LMTD) of the counter flow micro heat exchanger is defined by:

$$\Delta T_{LMTD} = \frac{(T_{h,out} - T_{c,in}) - (T_{h,in} - T_{c,out})}{\ln \frac{T_{h,out} - T_{c,in}}{T_{h,in} - T_{c,out}}} \quad (7.4)$$

The overall heat transfer coefficient is calculated by:

$$U = \frac{Q_{ave}}{A \Delta T_{LMTD}} \quad (7.5)$$

where A is the heat transfer area.

The volumetric heat exchange power can be determined by the following equation:

$$q_v = \frac{Q_{ave}}{133WHL} \quad (7.6)$$

where W , H and L are the width, height and length of the microchannel, respectively.

The heat exchanger effectiveness, defined by the ratio of the actual heat transfer rate to the maximum capacity of heat transfer rate, can be calculated by:

$$\varepsilon = \frac{Q_{ave}}{(\dot{m}c_p)_{\min} (T_{h,in} - T_{c,in})} \quad (7.7)$$

Finally, the number of transfer unit (NTU) is calculated by using the following equation:

$$NTU = UA / (\dot{m}c_p)_{\min} \quad (7.8)$$

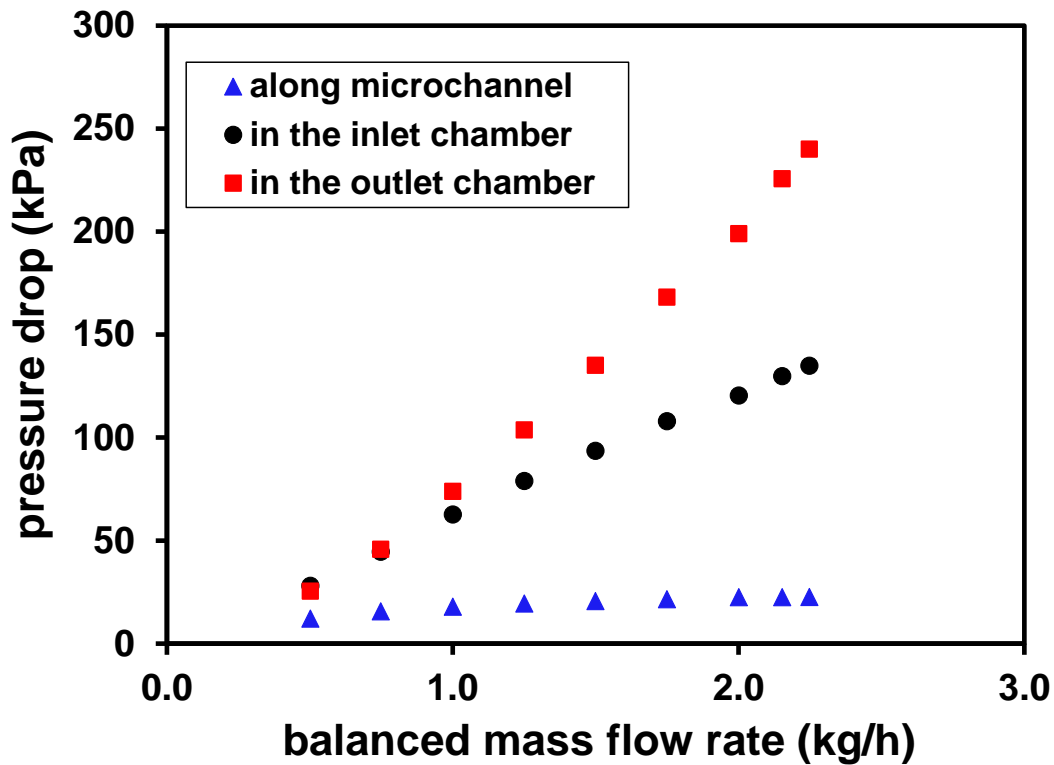
7.3 Pressure losses

Pressure drop along the micro heat exchanger is examined for different mass flow rates for a micro heat exchanger having the same mass flow rate in the hot and cold branches (balanced mass flow rate $(\dot{m}c_p)_{hot} = (\dot{m}c_p)_{cold}$). As mentioned before, in the experiment the pressure is not only measured at the inlet and outlet of the parallel microchannels, but also at the feed port and exhaust port. Therefore, the pressure drop from the feed port to the inlets of microchannels can be directly measured. The same holds for the pressure drop from the outlets of microchannels to the exhaust port.

$$\Delta p_{tot} = \Delta p_{in} + \Delta p_n + \Delta p_{out} \quad (7.9)$$

These pressure losses, together with the pressure drop along the microchannel (Δp_n in Eq. (7.9)), are plotted in Figure 7-8(a) as a function of the gas mass flow rate. It can be noted that the outlet manifold has dominating pressure drop, especially at large mass flow rate, while the

pressure drop along the microchannels is generally small, compared to that either in the outlet manifold or in the inlet manifold. In Figure 7-8(b) the percentage of the pressure drop in each section out of the total pressure drop (pressure drops along the microchannel, in the inlet manifold and in the outlet manifold) is plotted as a function of mass flow rate. It can be noted from Figure 7-8(b) that as the mass flow rate increases, larger percentage of the total pressure drop is concentrated in the outlet manifold. More in detail, for a mass flow rate equal to 2 kg/h, the pressure drop due to the outlet manifold is equal to 65% of the total pressure drop, the pressure drop due to the inlet manifold is 30% of the total pressure drop and the frictional resistance due to the microchannels is responsible of a 5% of the total pressure drop. These pressure data are measured for one single layer. Therefore, the conclusions are independent on the flow arrangement.



(a)

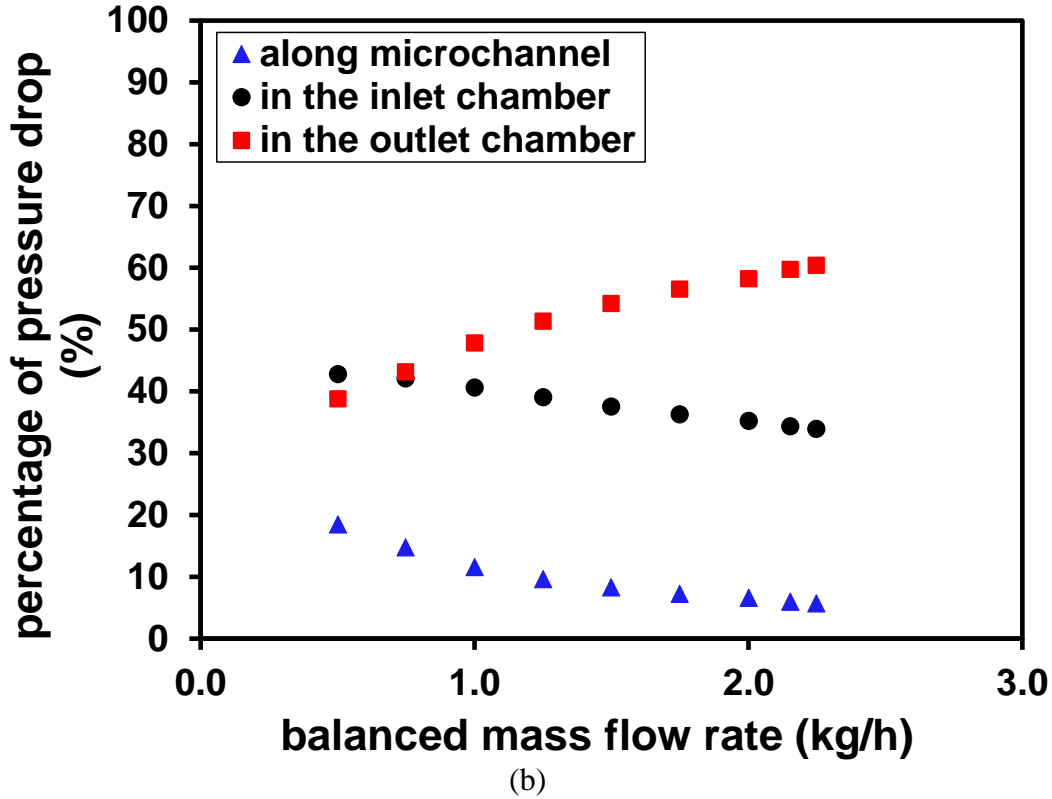


Figure 7-8: Pressure drops in different sections of the micro heat exchanger.

In order to explain the large pressure drops linked to the manifolds it is important to highlight that within the manifolds a series of cylindrical pillars are present in order to guarantee the mechanical stability of the device operating under a very large feeding pressure. The small pillar array in the inlet and outlet manifolds tends to disturb the flow and it is responsible of the increase of the pressure drop. These results underline as the deep fluid-dynamic analysis of the characteristics of the inlet and outlet manifolds has to be considered of primary importance during the design of a micro heat exchanger.

7.4 Axial heat conduction in solid walls

7.4.1 A novel method to account for wall axial conduction

The heat exchanger effectiveness is calculated by using Eq. (7.7) from experimental data. Meanwhile, the theoretical value of effectiveness can be calculated analytically by using the ε – NTU theory for conventional heat exchangers. For balanced flow ($(\dot{m}c_p)_{hot} = (\dot{m}c_p)_{cold}$) and

countercurrent arrangement, the effectiveness can be theoretically calculated by using the following expression [134]:

$$\varepsilon = 1 - \frac{1}{1 + NTU} \quad (7.10)$$

It is important to emphasize that the effect of axial conduction in the wall is not taken into account in the above theoretical calculation developed for conventional heat exchangers. However, it has been demonstrated by the previous works appeared in the available literature that the effect of the wall conduction can be significant for micro channel heat exchangers where the wall thickness in many cases can be comparable to the hydraulic diameter of the microchannels.

It is possible to modify Eq. (7.10) by taking into account the axial wall heat conduction in a countercurrent heat exchanger as proposed by Shah and Sekulic in [152]:

$$\varepsilon' = 1 - \frac{1}{1 + NTU \frac{1 + \lambda\Phi}{1 + \lambda NTU}} \quad (7.11)$$

in which the longitudinal conduction parameter λ appears, defined as the ratio of axial conductive heat flux in wall (q_w) and convective heat flux of the fluid (q_f):

$$\lambda = \frac{q_w}{q_f} = \frac{k_w A_w / L}{\dot{m} c_p} \quad (7.12)$$

where k_w is the thermal conductivity of the solid wall, A_w the cross sectional area of the wall, \dot{m} the mass flow rate and c_p the thermal capacity of the fluid.

The parameter Φ is defined by:

$$\Phi = \sqrt{\frac{\lambda NTU}{1 + \lambda NTU}} \quad (7.13)$$

In Eq. (7.11) to (7.13), NTU is the number of transfer unit obtained by neglecting the wall axial conduction. However, this method for the determination of the effectiveness is generally not practical from an experimental point of view because the values of NTU calculated by using the measurement of temperature and mass flow already include the influence of axial conduction and if these values are applied to Eq. (7.11) incorrect results in terms of effectiveness are generated.

In the present work, a novel method is developed in order to accurately take into account the effect of axial conduction. In this method, it is assumed that the effectiveness with axial conduction can be calculated by using Eq. (7.10) (valid for negligible wall axial conduction) but by using the NTU values obtained experimentally:

$$\varepsilon' = 1 - \frac{1}{1 + NTU'} \quad (7.14)$$

In order to highlight that the value of NTU is the value of the number of transfer unit obtained from the experimental data the notation NTU' is used in Eq. (7.14).

The value of NTU evaluated without taking into account the role of the wall axial conduction can be calculated by combining Equation (7.11), (7.13) and (7.14). The equation by means of which NTU can be calculated is the following:

$$\left(\sqrt{\frac{\lambda NTU}{1 + \lambda NTU}} \right)^3 + \frac{1}{\lambda} \left(\sqrt{\frac{\lambda NTU}{1 + \lambda NTU}} \right)^2 - NTU' = 0 \quad (7.15)$$

The value of NTU can be obtained by solving this algebraic equation (i.e., by using MATLAB), in which the experimental values of λ and NTU' are introduced. When the NTU value is known, the theoretical effectiveness in the case of no axial conduction can be calculated by using Eq. (7.10).

In order to check the accuracy of this method, Figure 7-9 compares the values of the effectiveness obtained experimentally for a counter-current double-layered microHEX with balanced flow rates when an aluminum partition foil (AL100) is used with the data obtained by using Eq. (7.10) (without to consider wall axial conduction) and Eq. (7.11) (wall axial conduction accounted for). It is worthy to note that the experimental data are in very good agreement with Eq. (7.11). On the contrary, the prediction of the heat exchanger effectiveness obtained by using Eq. (7.10) ignoring wall axial conduction overestimates the thermal performance of the microHEX. This result underlines that in such a case the effect of the wall axial conduction along the core of the heat exchanger cannot be considered as negligible. As the mass flow rate increases, the effect of wall axial conduction on the heat exchanger effectiveness becomes weaker and the prediction given by the two models tend to coincide and to be in agreement with the experimental data.

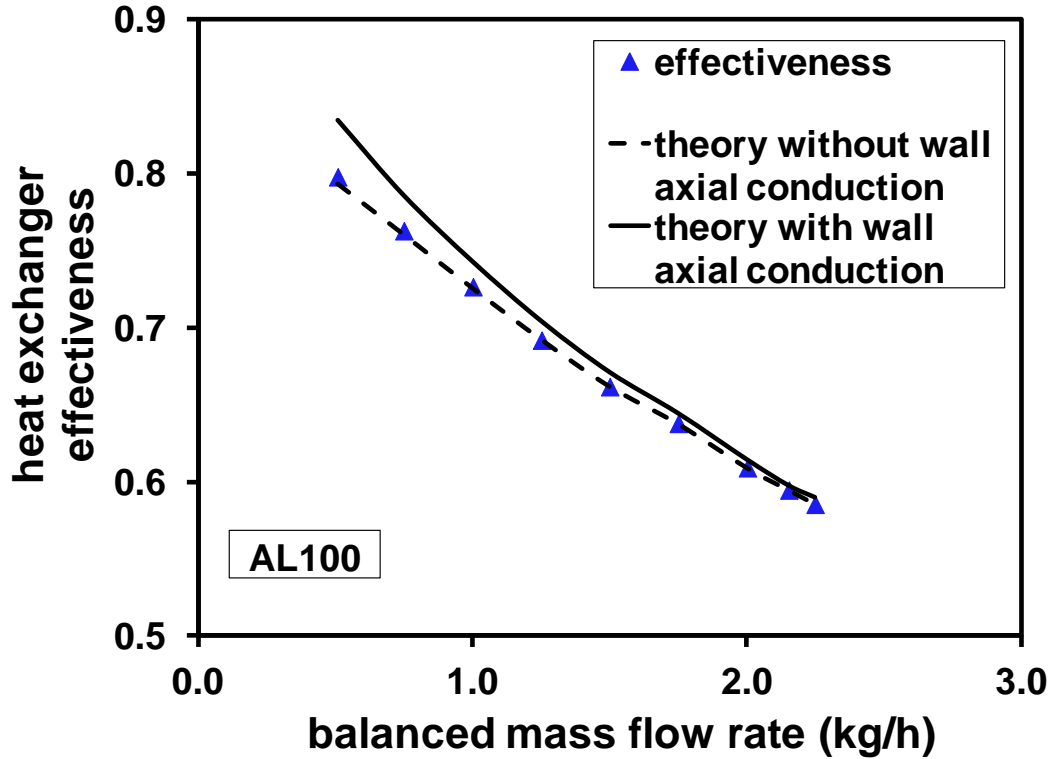


Figure 7-9: Effectiveness of a countercurrent double-layered micro heat exchanger with a thick aluminum partition foil (AL100) in comparison with theoretical predictions of Eq. (7.10) (continuous line) and Eq. (7.11) (dashed line).

7.4.2 Influence of wall axial conduction on the performance of microHEX

The method presented in the previous paragraph is used here to study the influence of the wall axial conduction on the thermal performance of a microHEX. In order to identify when the wall axial conduction can be considered negligible or not in a heat exchanger the wall axial conduction parameter defined by Eq.(7.12) can be used for a micro heat exchanger made of homogenous solid material and composed of rectangular microchannels, as in the works of Bier *et al.* [32], Meschke *et al.* [33] and Koyama and Asako [34]:

$$\lambda = \frac{k_w}{k_f} \frac{(W + s_2)(H + s_1)}{L \frac{W + H}{2}} \frac{1}{RePr} \quad (7.16)$$

where k_w is the thermal conductivity of the solid wall (in this case PEEK), k_f the fluid thermal conductivity, Re the Reynolds number, Pr the Prandtl number of the fluid, s_1 the thickness of sidewall between parallel microchannels, s_2 the thickness of the partition wall separating the cold

flow and the adjacent hot flow, and W , H and L the microchannel width, height and length, respectively.

For the double-layered microHEX used in this thesis, the option for the material and thickness of the partition wall is made flexible while the side wall and the cover remain unchanged. The value of the wall axial conduction parameter for such composition of difference solid materials can be computed as follows by using its definition in Eq.(7.12):

$$\lambda = \frac{k_{partition} (W + s_2) \frac{s_1}{2} + k_{PEEK} [Hs_2 + (W + s_2)s_{cover}]}{k_f L \frac{W + H}{2}} \frac{1}{RePr} \quad (7.17)$$

where s_{cover} is the thickness of the PEEK covers of the microHEX, which is 5 mm in the present design. All the geometrical parameters used in Eq. (7.17) are schematically indicated in Figure 7-10, except for the variable L which is the length of the microchannels. The contribution of axial conduction in the microchannel side walls and the covers, which is presented by the second term on the right side of Eq. (7.17), is insignificantly slight if the partition wall is made of highly conductive material, such as aluminum and copper. However, if the partition foil is made of less conductive material, such as PEEK and silicon, this term may become significant.

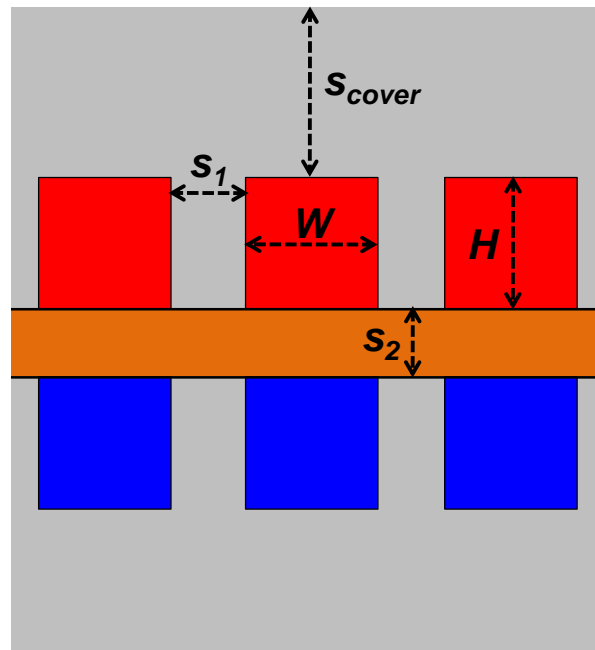


Figure 7-10: Geometrical parameters of the double-layered microHEX (red color – microchannels for hot flow; blue color – microchannels for cold flow).

In order to have an insight into the influence of wall axial conduction for this kind of microHEX, by using the data of the gas-to-gas microHEX tested in the works of Bier *et al.* [32], Meschke *et al.* [33] and Koyama and Asako [34], the value of the axial conduction parameter which characterizes these experimental tests has been derived and depicted in Figure 7-11, as a function of Reynolds number. The value of the axial conduction parameter was calculated for each experimental test by considering the declared dimensions of the tested microchannels, thicknesses of the walls, thermal conductivity of the materials, thermal properties of the fluids as well by considering the range of the specific operating conditions declared by the authors in their papers. Figure 7-11 also includes the data points obtained from the current experiment for the five different partition foils.

By observing these data points, it can be noted that the axial conduction parameter has a decreasing trend with the increase of Reynolds number. Therefore, for micro heat exchangers having a core made with conductive materials, larger Reynolds numbers or higher mass flow rates are suggested in order to avoid large axial heat conduction in the wall. It can be noted that, for the micro heat exchangers tested by Meschke *et al.* [33] and Koyama and Asako [34] as well as the copper device tested by Bier *et al.* [32], the conductive heat flux in solid wall is larger than 10% of the convective heat flux ($\lambda > 0.1$). This is also the case of the double-layered microHEX tested in the present work when a thick copper partition foil is used (C500), which has been deliberately considered in order to obtain operative conditions very close to the conditions investigated by Meschke *et al.* [33] and Koyama and Asako [34], who used thick partitions walls (2000 μm and 300 μm , respectively) for their gas-to-gas microHEXs.

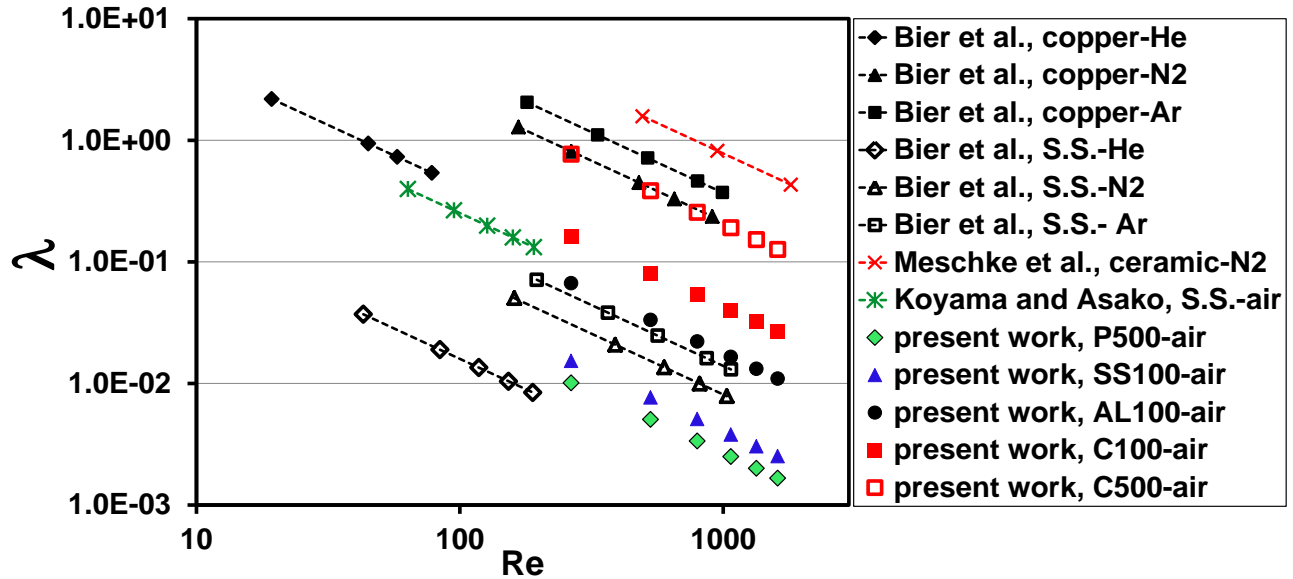


Figure 7-11: Longitudinal conduction parameter in the previous and present work for gas-to-gas micro heat exchanger (S.S. refers to stainless steel).

In some cases the axial conductive heat flux at the wall is comparable to or even larger than the convective heat flux ($\lambda > 1$) especially for very low gas flow rates ($Re < 100$). In this case the temperature profile tends to flatten out throughout the micro heat exchangers and the heat transfer deteriorates. The large values of the axial conduction parameter associated to the tests conducted by Bier *et al.* [32], Meschke *et al.* [33] and Koyama and Asako [34] can explain why these authors have found that an isothermal model (uniform wall temperature) can be appropriate to explain their experimental trends. If comparison is made among the tests carried out by Bier *et al.* [32] for micro heat exchangers made of two different materials, it can be found that for the same gas species (e.g. helium) the axial heat conduction in copper micro heat exchangers is approximately one order of magnitude higher than that in stainless steel micro heat exchangers. For the same material (stainless steel), the axial conduction parameter is larger in the test of Koyama and Asako [34] than that in the investigation by Bier *et al.* [32] with nitrogen. This is because a thicker wall was used by Koyama and Asako [34] for the micro heat exchanger with respect to the wall used by Bier *et al.* [32].

The five partition foils used in the present work guarantee values of the axial conduction parameter in the range between 1 and 0.001 which means that by using these foils it becomes possible to investigate the effect of the wall axial conduction in the microHEX core for a large range of values of λ .

The wall axial conduction parameter is greatly reduced by using partition foils of smaller thickness (i.e. C100) and/or materials with a low thermal conductivity (i.e. P500).

It is evident that the thick PEEK partition foil (P500) is able to guarantee the lowest values of the axial conduction parameter due to its very low thermal conductivity. However, this does not necessarily mean high heat exchanger effectiveness because the transverse heat transfer from one fluid to the other may also be greatly suppressed by low values of thermal conductivity. This aspect will be investigated by comparing the results obtained for a thick copper partition foil (C500) with the results obtained with the thick PEEK foil (P500).

By using Eq. (7.11) it is possible to estimate the theoretical effect of λ on the heat exchanger effectiveness of a counter-current heat exchanger. In Figure 7-12 the theoretical value of the effectiveness is shown as a function of Reynolds number and of the wall axial conduction parameter. The curve obtained for $\lambda=0$ underlines the trend expected when the effect of the wall axial conduction is absent. . It is evident by the data of Figure 7-12 that, for $\lambda<0.01$, the decrease of the effectiveness due to the effect of the axial conduction can be considered negligible. On the contrary, if $\lambda>0.1$, the thermal performance of the microHEX dramatically worsens. These results enable to consider as a threshold value for an a-priori investigation of the effect due to the wall axial conduction in a microHEX the value of λ equal to 0.01: in fact, when λ is lower than 0.01 the effect of wall axial conduction on the thermal performance of a microHEX can be considered as negligible; on the contrary, for λ larger than 0.01 the effect of the wall axial conduction must be accounted for.

Finally, it should be emphasized that this theoretical calculation only considers the effect of the wall axial conduction by ignoring the effect on the microHEX thermal performance of the transverse heat transfer among the microchannels. However, in practice, if axial conduction is reduced by using less conductive solid material, the transverse heat transfer may be reduced as well.

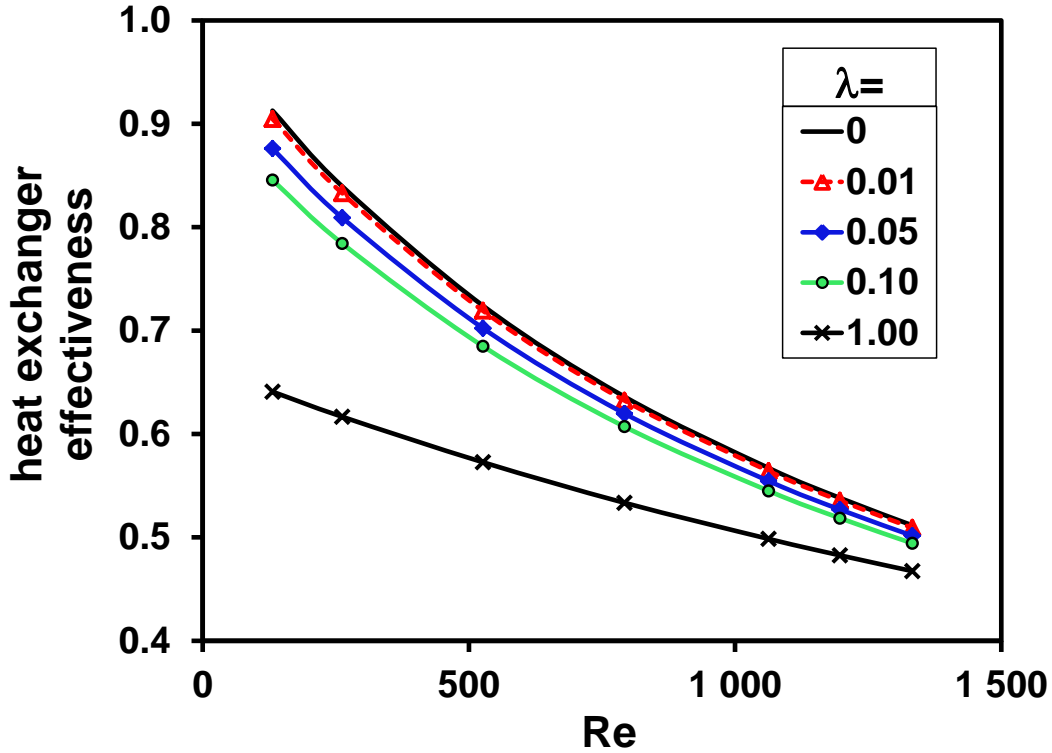


Figure 7-12: Heat exchanger effectiveness as a function of Reynolds number for different magnitudes of axial conduction parameter.

Although all the experimental research on gas flow micro heat exchangers reported strong axial conduction effects at the wall, similar problem seems to be not important in the analysis of the thermal behavior of microHEX when liquid flows are considered as working fluids as in [25] and [31]. By considering the expression of the axial conduction parameter (Eq. (7.17)) it is evident that the value of λ is influenced by the thermophysical properties of the fluid by means of the Prandtl number and the fluid thermal conductivity.

In fact, if the ratio between the wall axial conduction parameter calculated for a gas (i.e. air) and the wall axial conduction parameter calculated for a liquid (i.e. water) in the same device is calculated, one obtains, for a fixed Reynolds number:

$$\frac{\lambda_{air}}{\lambda_{water}} = \frac{k_{water} Pr_{water}}{k_{air} Pr_{air}} \quad (7.18)$$

By introducing in Eq. (7.17) the values of the typical properties of water and air at the temperature of 25 °C this ratio is equal to about 220, which means that λ for water is generally 220 times lower than λ obtained for air through the same microHEX. This highlights that great

attention must be paid to wall axial conduction when the working fluid in a microHEX is changed from liquid to gas.

In order to highlight the influence of the fluid nature on the wall axial conduction parameter, the value assumed by λ for the microHEX tested by Bier *et al.* [32], Meschke *et al.* [33] and Koyama and Asako [34] has been calculated by changing their working gases into water. By observing the values of λ shown in Figure 7-13 it is evident that, when water is used as working fluid in the microHEXs tested by Bier *et al.* [32] and Koyama and Asako [34], most of the data points fall below the threshold values of λ equal to 0.01, which means that the effect due to the wall axial conduction can be considered as negligible in these cases except for the copper micro heat exchanger working under very low Reynolds numbers ($Re < 100$) for which λ becomes larger than 0.01. Therefore, in liquid microHEX the influence of wall axial conduction on the thermal performance of these devices is greatly reduced compared to gas microHEX.

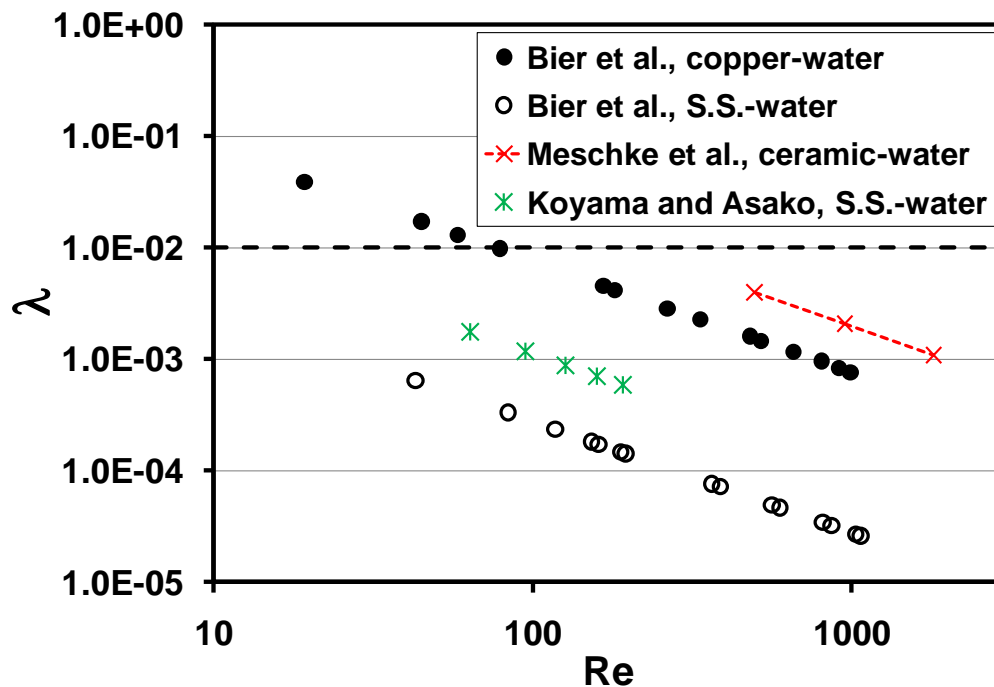


Figure 7-13: Wall conduction parameter by changing the working gases in previous work into water.

7.5 Thermal performance of microHEX with balanced flows

The experimental results obtained for the double-layered microHEX are discussed in this section as function of the flow arrangement (countercurrent, cocurrent and cross flow arrangement). In

all the tests, the mass flow rate of air on the hot side is regulated to be equal to the mass flow rate on the cold side, which generates balanced flows. The experimental results obtained for unbalanced flows are discussed in Section 7.6.

7.5.1 MicroHEX with countercurrent arrangement

7.5.1.1 Overall heat transfer coefficient and volumetric heat exchange rate

The overall heat transfer coefficient calculated by Eq.(7.5) is plotted in Figure 7-14 as a function of the mass flow rate in a counter-current microHEX with balanced mass flow rates for the five partition foils quoted in Table 7-3. It can be noted that the thermal performance of the countercurrent microHEX, in terms of overall heat transfer coefficient, is strongly influenced by the thermal conductivity and thickness of the partition foil, as well as the mass flow rate. In general, better thermal performance is achieved at larger mass flow rate and for thin partition foils.

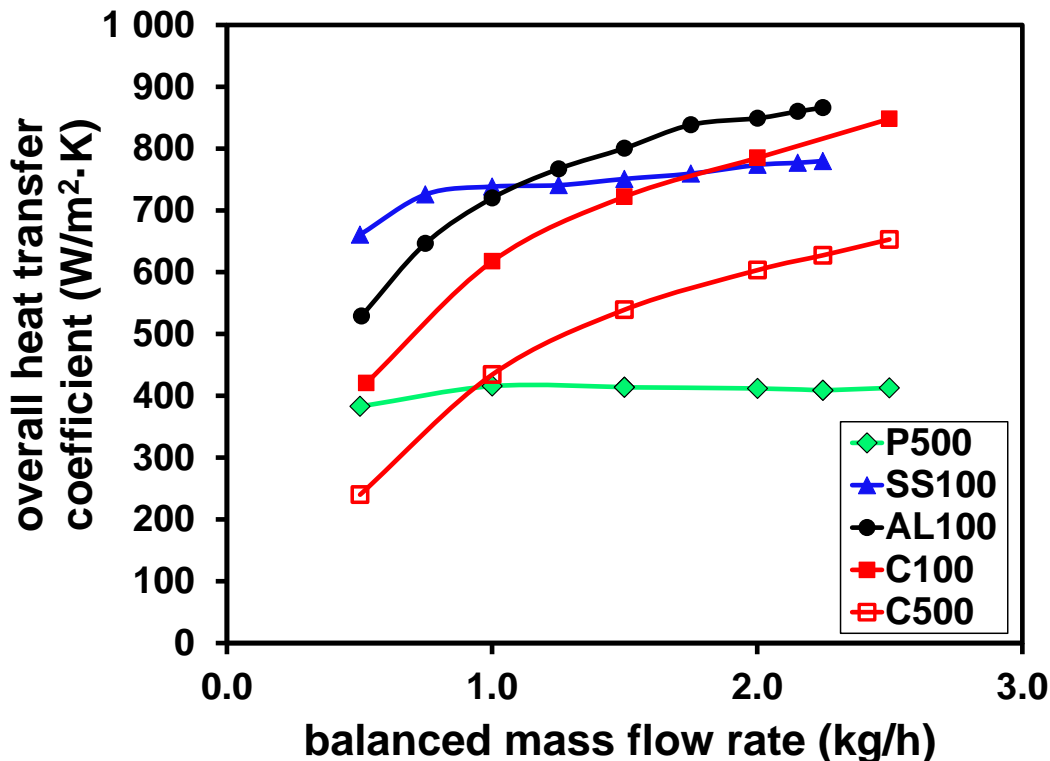


Figure 7-14: Heat transfer coefficient of the microHEX as a function of mass flow rate.

Specifically, the dependence of the heat transfer coefficient on the mass flow rate decreases for partition walls with lower thermal conductivity. This is quite evident for the experimental

results obtained using the PEEK foil (P500), followed by stainless steel foil (SS100), although it experiences slight growth in heat transfer coefficient as the mass flow rate increases. The slopes are steeper for partition foils with larger thermal conductivity, especially for aluminum and copper. In addition, it is indicated in Figure 7-14 that by reducing the thickness of the partition foil, the overall heat transfer of the device can be greatly improved; this means that the role of the thermal resistance due to heat conduction across the foil cannot be neglected on the determination of the total thermal resistance even in the case of materials with large thermal conductivity. This is well evidenced by the experimental results from copper foils C100 and C500 having two different thicknesses (100 μm and 500 μm). However, it is worthy to note that for partition foils made of the same material, the increase of overall heat transfer coefficient versus mass flow rate is nearly the same for different thicknesses.

The volumetric heat exchange rate, which indicates the heat exchange capacity of the device within a certain flow volume, is shown in Figure 7-15 for the countercurrent microHEX using different partition foils. It is evident that, compared with conventional heat exchangers, their micro-scaled counterparts have extremely promising potential to deliver heat from one fluid to another by reaching values of volumetric heat exchange rate up to 100 MW/m^3 for the gas mass flow rate tested. As it is evident, the volumetric heat exchange rate increases monotonically with the increase of gas mass flow rate. Moreover, the microHEXs with thin stainless steel foil (SS100) and aluminum foil (AL100) performed nearly equally best among all the five partition foils in terms of heat exchange power per volume, although the former has quite different overall heat transfer coefficient from the latter. At large mass flow rate, i.e. $\dot{m} > 2 \text{ kg/h}$, the volumetric heat exchange rate obtained from the microHEX with thick PEEK (P500) tends to worsen with respect to the other partition foils.

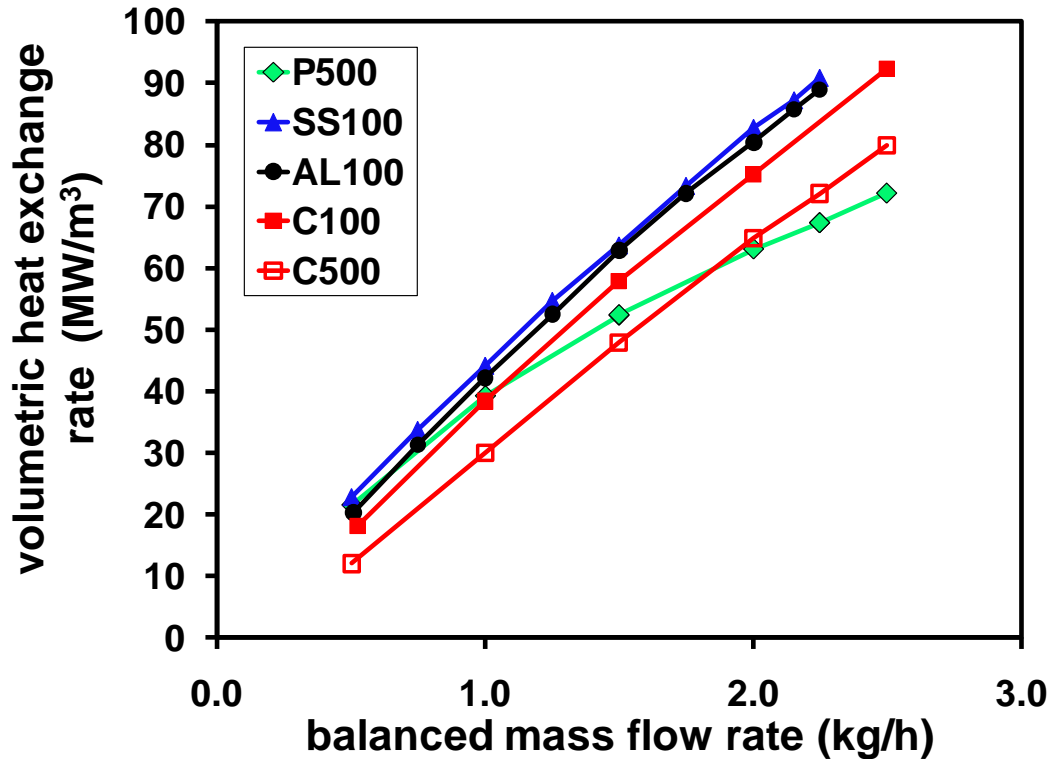


Figure 7-15: Volumetric heat exchange rate as a function of mass flow rate.

7.5.1.2 Heat exchanger effectiveness

Figure 7-16 shows the experimental effectiveness of the countercurrent microHEX with a thin stainless steel foil (SS100) in comparison to theoretical predictions with Eq. (7.10) and without Eq. (7.11) wall axial conduction. In this case, no difference can be observed between the two theoretical predictions, which means that in this case the effects due to wall axial conduction can be considered negligible. The experimental data are found in good agreement with theoretical predictions. In addition, the heat exchanger effectiveness decreases quickly as the mass flow rate increases.

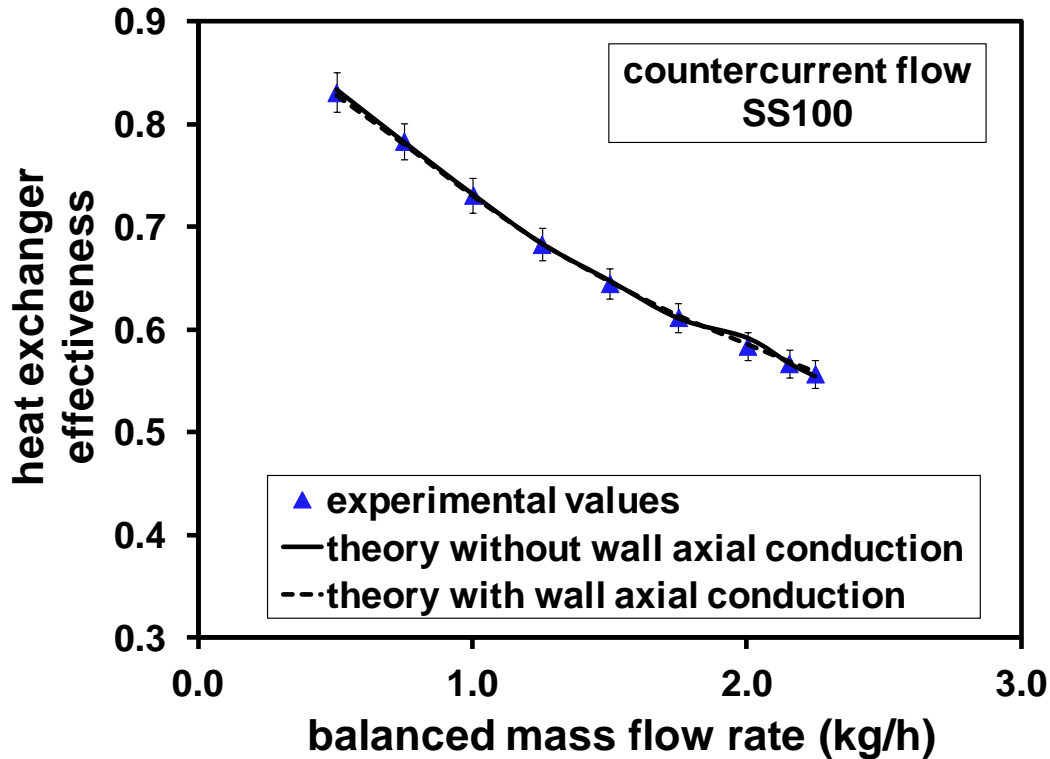


Figure 7-16: Effectiveness of microHEX with thin stainless steel foil (SS100) in comparison with theoretical prediction.

In comparison to Figure 7-16, the experimental results obtained from the counter-current microHEX with a partition foil of the same thickness but made in copper (C100) are plotted in Figure 7-17. In this case, it can be noted that the results are well predicted by theory only if wall axial conduction is accurately taken into account by using Eq. (7.11). By increasing the thermal conductivity of partition foil, the influence of wall axial conduction on heat exchanger effectiveness gains in significance. More specifically, the effectiveness of the micro device is reduced by axial conduction in the wall, which is clearly evidenced at low mass flow rate. Figure 7-16 also suggests that the negative influence of axial conduction on heat exchanger effectiveness can be suppressed by increasing the mass flow rate of working fluid.

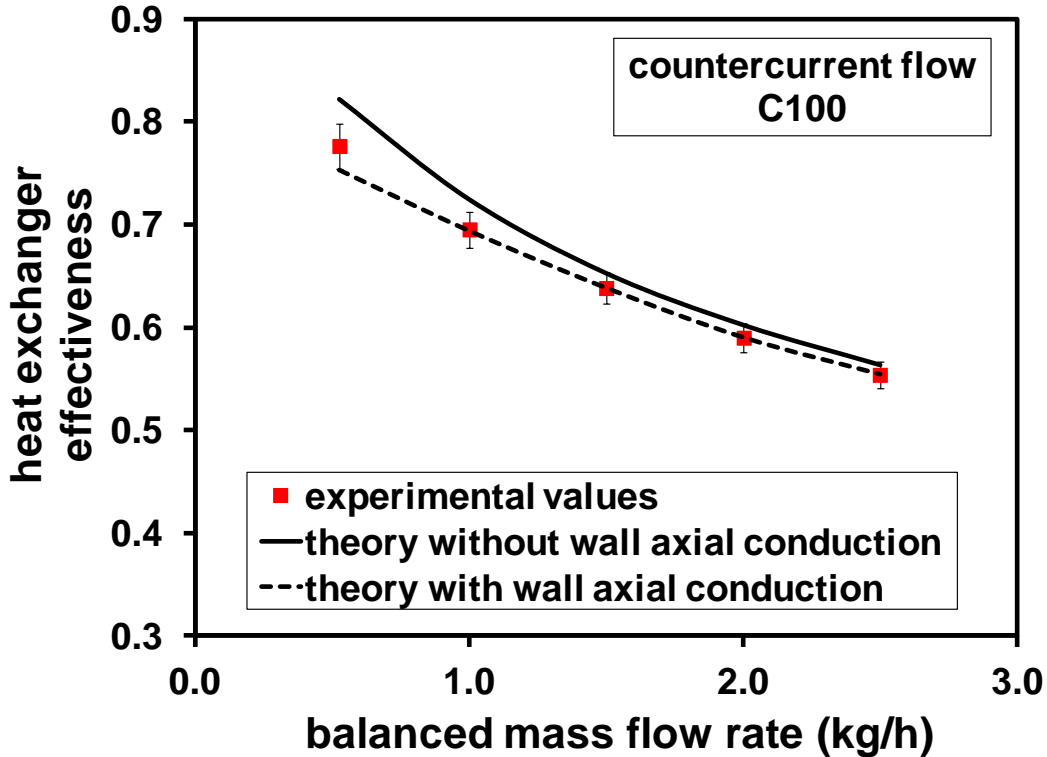


Figure 7-17: Effectiveness of microHEX with thin copper foil (C100) in comparison with theoretical prediction.

Figure 7-18 shows the results obtained for a countercurrent microHEX with the partition foil C500 (copper, 500 μm). It is evident that by increasing the thickness of the copper wall from 100 μm to 500 μm the influence of the axial wall conduction is greatly magnified. Therefore, this result suggests to reduce the thickness of highly conductive foils in order to achieve better thermal performance of microHEX for gas flows. In addition, by comparing Figure 7-18 with Figure 7-16 and Figure 7-17, it can be noted that when the axial conduction becomes stronger, the effectiveness exhibits a weaker dependence on gas mass flow rate.

The results on thin aluminum foil (AL100) have been shown in Figure 7-9. In this case the effect of the wall axial conduction on the effectiveness is evident especially for low mass flow rates.

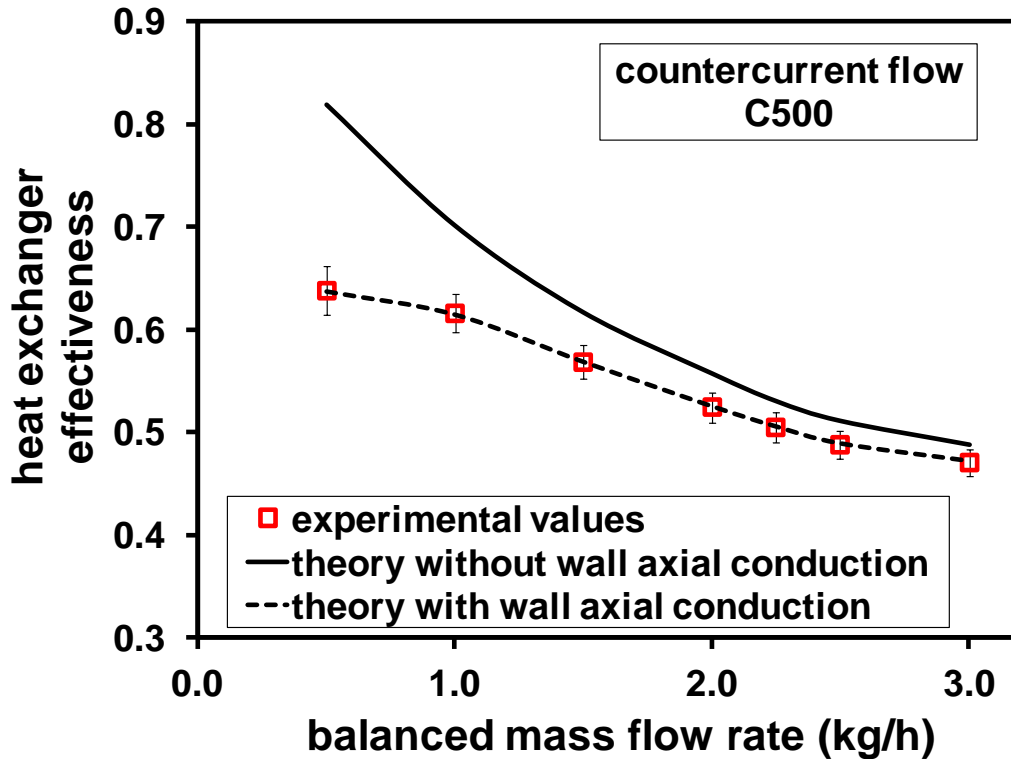


Figure 7-18: Effectiveness of microHEX with thick copper foil (C500) in comparison with theoretical prediction.

The experimental results obtained for a countercurrent microHEX with a thick PEEK foil (P500) are given in Figure 7-19. The effect of the axial thermal conduction in this case is completely negligible for the whole range of mass flow rate investigated. This result confirms the conclusions made by means of the data depicted in Figure 7-11 for which in the case of the partition foil P500 the wall conduction parameter λ is lower than its threshold value (0.01). In this case the dependence of the effectiveness on the gas mass flow rate is stronger with respect to the other partition foils and the values assumed by the effectiveness are very low, down to 30%.

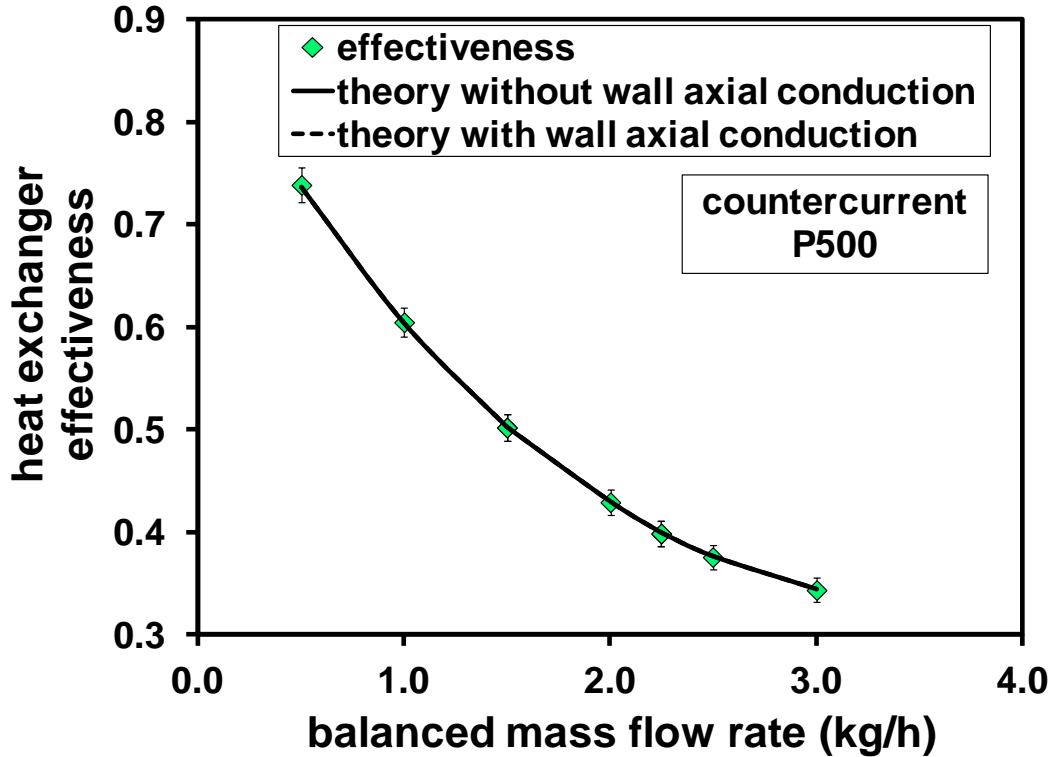


Figure 7-19: Effectiveness of countercurrent microHEX with thick PEEK foil (P500).

The experimental results obtained for the countercurrent microHEX in terms of effectiveness are compared in Figure 7-20 for all the five partition foils listed in Table 7-3. It is interesting to note that the best thermal performance is neither from the micro HEX with the least conductive partition foil (P500), nor from the one with the most conductive foil (C500). Instead, the devices with foil of medium thermal conductivity, such as stainless steel (SS100) and aluminum (AL100), show higher effectiveness. This conclusion, to the best of the authors' knowledge, for the first time experimentally validates the reliability of the numerical work by Stief *et al.* [147] on the optimal thermal conductivity of micro heat exchangers.

However, the numerical work of Stief *et al.* [147] did not investigate how the influences of axial conduction changes as a function of mass flow rate. At the lowest mass flow rate in the present experiment (0.5 kg/h, corresponding to a Reynolds number of 260), the effectiveness of the microHEX with a thick copper foil (C500) is more than 10% lower than that of the device with thick PEEK foil (P500), as shown in Figure 7-20. When the mass flow rate is doubled, the devices with the two foils perform equally well in terms of effectiveness. If the mass flow rate is tripled, the performance of the microHEX with copper foil surpasses that of the one with PEEK

foil, and this trend becomes more evident for larger mass flow rate. Therefore, it can be concluded that for the same thickness of the foil, at lower mass flow rate the microHEX in which the core is made with a solid material having low thermal conductivity tends to perform better. At large mass flow rate more conductive solid materials lead to better performance. This conclusion can be further validated by comparing the experimental data obtained from the microHEX with thin stainless steel foil (SS100) and thin aluminum foil (AL100).

In addition, by comparing the results obtained by using two copper foils with different thicknesses, (i.e. C100 and C500) it can be noted that the reduction in the foil thickness helps to improve the performance of the micro heat exchanger. However, the minimum thickness of the foil is in many cases bounded by mechanical constraints linked to the maximum operating pressures under which the device is expected to work. For instance, in the present study a thin PEEK foil with a thickness of 100 μm was broken during the leak tightness tests.

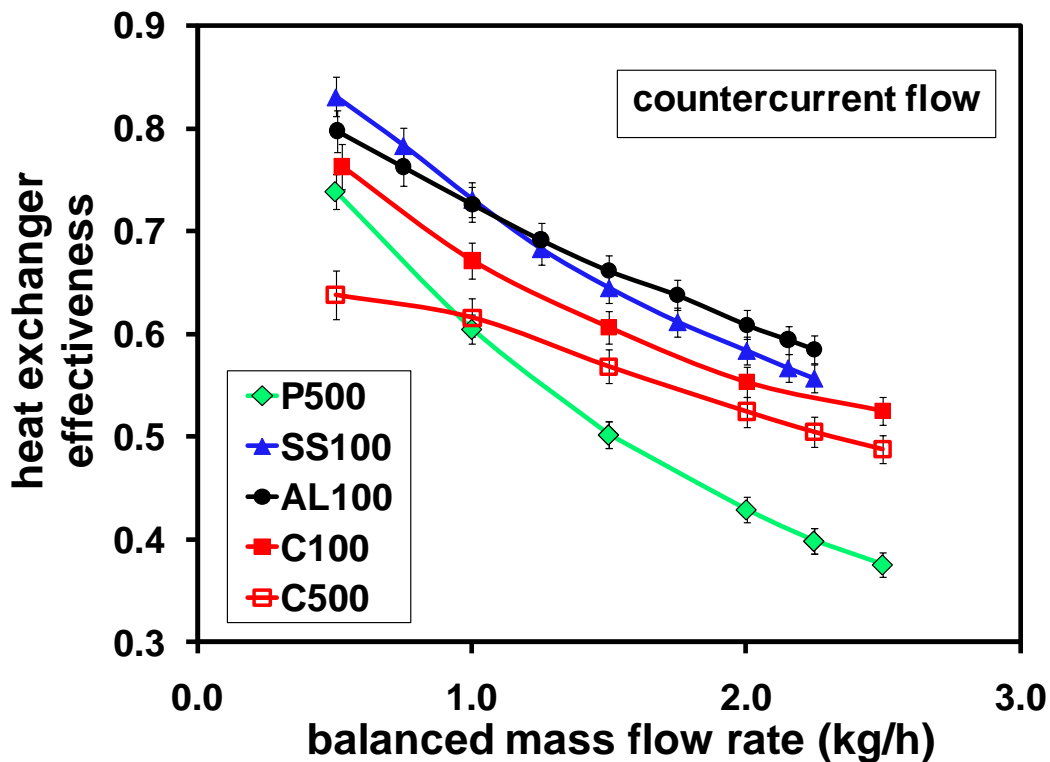


Figure 7-20: Effectiveness of microHEX as a function of mass flow rate for various partition foils.

7.5.2 MicroHEX with cross flow arrangement

7.5.2.1 Calculation of theoretical heat exchanger effectiveness for cross flow

The experimental values of heat exchanger effectiveness for cross flow can be directly calculated from the data reduction procedures described in Section 6.2. However, the theoretical prediction of the effectiveness value for cross flow is more complicated than the cases of countercurrent or cocurrent flow.

The logarithmic mean temperature difference of a general heat exchange device is defined by:

$$\Delta T_{LMTD} = \frac{\Delta T_1 - \Delta T_2}{\ln \frac{\Delta T_1}{\Delta T_2}} \quad (7.19)$$

where ΔT_1 and ΔT_2 are temperature difference between the fluids at both ends of the device.

The expression of the ΔT_{LMTD} for a countercurrent or cocurrent flow arrangement takes the following form:

$$\Delta T_{LMTD} = \frac{(T_{h,out} - T_{c,in}) - (T_{h,in} - T_{c,out})}{\ln \frac{T_{h,out} - T_{c,in}}{T_{h,in} - T_{c,out}}}, \text{ countercurrent} \quad (7.20)$$

$$\Delta T_{LMTD} = \frac{(T_{h,in} - T_{c,in}) - (T_{h,out} - T_{c,out})}{\ln \frac{T_{h,in} - T_{c,in}}{T_{h,out} - T_{c,out}}}, \text{ cocurrent}$$

On the contrary, for asymmetric flow arrangements, as in the case of a cross flow arrangement, the definition of the logarithmic temperature difference is not easy to be linked to the inlet and outlet values of temperature. In general, a correction factor F is introduced in order to calculate the mean temperature difference in asymmetric flow arrangements [133, 152] and [153]:

$$\Delta T_m = F \Delta T_{LMTD,c} \quad (7.21)$$

in which $\Delta T_{LMTD,c}$ is the log-mean temperature difference of a pure countercurrent flow. The correction factor F takes on the value between 0 and 1.

Based on Eq. (7.21), the NTU value of an asymmetric flow can be calculated by [133]:

$$NTU = \frac{NTU_c}{F} \quad (7.22)$$

where NTU_c indicates the number of transfer unit in an equivalent countercurrent flow heat exchanger having the same inlet and outlet temperature of the hot and cold fluids of the asymmetric device. It is possible to introduce the dimensionless temperature changes P in both hot and cold flows defined by:

$$P_h = \frac{T_{h,in} - T_{h,out}}{T_{h,in} - T_{c,in}}, \text{ hot flow}$$

$$P_c = \frac{T_{c,out} - T_{c,in}}{T_{h,in} - T_{c,in}}, \text{ cold flow}$$
(7.23)

The number of transfer unit of an equivalent countercurrent heat exchanger can be therefore calculated as:

$$NTU_c = \frac{P}{1-P}$$
(7.24)

in which P is the average dimensionless temperature change calculated as follows [133]:

$$P = \frac{P_h + P_c}{2}$$
(7.25)

In order to obtain the NTU value in Eq. (7.22), the value of correction factor should also be known besides NTU_c . The evaluation of F can be done by using specific graphs or empirical approximations as a function of the flow arrangements indicated in [133]. For example, for balanced flows, the expression of the correction factor is the following:

$$F = \frac{1}{(1 + aNTU^b)^c}$$
(7.26)

where the coefficients a , b and c depend on many parameters, such as flow arrangement, tube arrangement, number of flow pass, tube or plate, mixed or unmixed flows, etc. For balanced unmixed flows with cross flow arrangement, the suggested values for these coefficients are $a=0.433$, $b=1.60$, and $c=0.267$ as reported in [133].

When the NTU value of HEX with cross flow arrangement is obtained, the theoretical value of effectiveness can be calculated using the following expressions [133, 152]:

$$\varepsilon = 1 - \exp(-NTU) - \exp(-2NTU) \sum_{n=1}^{\infty} S_n(NTU)$$

$$S_n(x) = \frac{1}{(n+1)!} \sum_{j=1}^n \frac{(n+1-j)}{j!} x^{n+j}$$
(7.27)

As an example, in Table 7-4 the values of the correction factor and of the theoretical effectiveness, calculated by using Eq. (7.26) and (7.27), are quoted for a cross flow microHEX in which the thin PEEK foil (P500) is used as partition foil as a function of the imposed mass flow rate in the case of balanced flows. It is interesting to note, by observing the values reported in Table 7-4, that the correction factor F gradually approaches to 1 as the mass flow rate increases. This fact indicates that when the mass flow rate increases, the cross flow microHEX tends to have the same effectiveness of a countercurrent microHEX having the same inlet and outlet temperature for the cold and hot flows. The same conclusion can be drawn by considering different partition foils.

Table 7-4: Calculation of heat exchanger effectiveness for cross flow (P500 foil).

Mass flow rate	P_{ave}	NTU _C (equivalent countercurrent flow)	NTU (cross flow)	F	ϵ_{theory}
0.50	0.655	1.895	2.517	0.753	0.590
1.00	0.573	1.341	1.595	0.841	0.505
1.50	0.480	0.924	1.020	0.906	0.426
2.00	0.415	0.709	0.757	0.937	0.373
2.25	0.385	0.627	0.662	0.947	0.349
2.50	0.363	0.571	0.598	0.955	0.331
3.00	0.332	0.498	0.517	0.963	0.306

7.5.2.2 Overall heat transfer coefficient and volumetric heat exchange rate

Experimental tests have been performed on cross flow microHEXs with four different partition foils, namely, P500, SS100, AL100 and C100. Figure 7-21 shows the overall heat transfer coefficient of the cross flow microHEXs determined experimentally as a function of the imposed mass flow rate in a microHEX with balanced flows. For a cross flow microHEX with thick PEEK foil, the overall heat transfer coefficient never exceeds 400 W/(m²K), making it the last choice among all the partition foils in design of such devices. The difference in terms of overall heat transfer coefficients for the other partition foils is very small. The experimental data highlight that the stainless steel foil gives slightly better results in terms of overall heat transfer

coefficients with respect to the other partition foils especially at low and moderate mass flow rates.

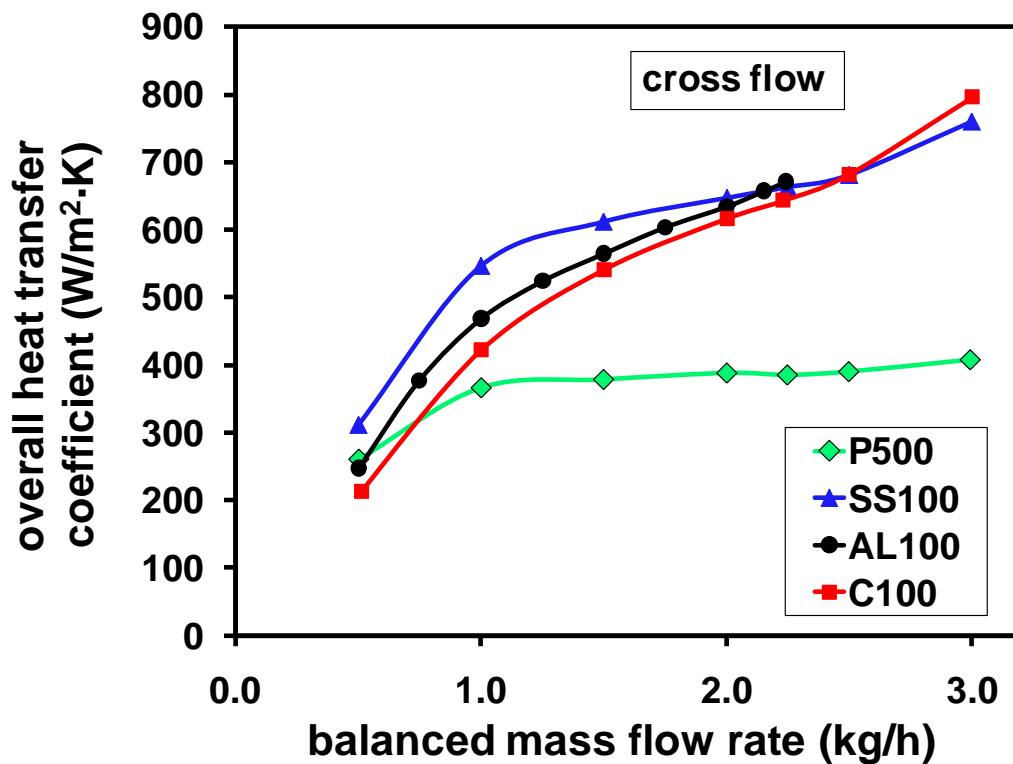


Figure 7-21: Heat transfer coefficient of cross flow microHEX as a function of mass flow rate.

The volumetric heat exchange rate is shown in Figure 7-22 for the four partition foils. Similarly, stainless steel foil determines slightly larger value of the volumetric heat exchange rate than the other foils at the same mass flow rate. The increase of volumetric heat exchange rate versus mass flow rate exhibits quite linear trend for partition foils made of stainless steel, aluminum and copper. On the contrary, for the cross flow microHEX with the thick PEEK foil, this increase becomes slower at larger mass flow rate.

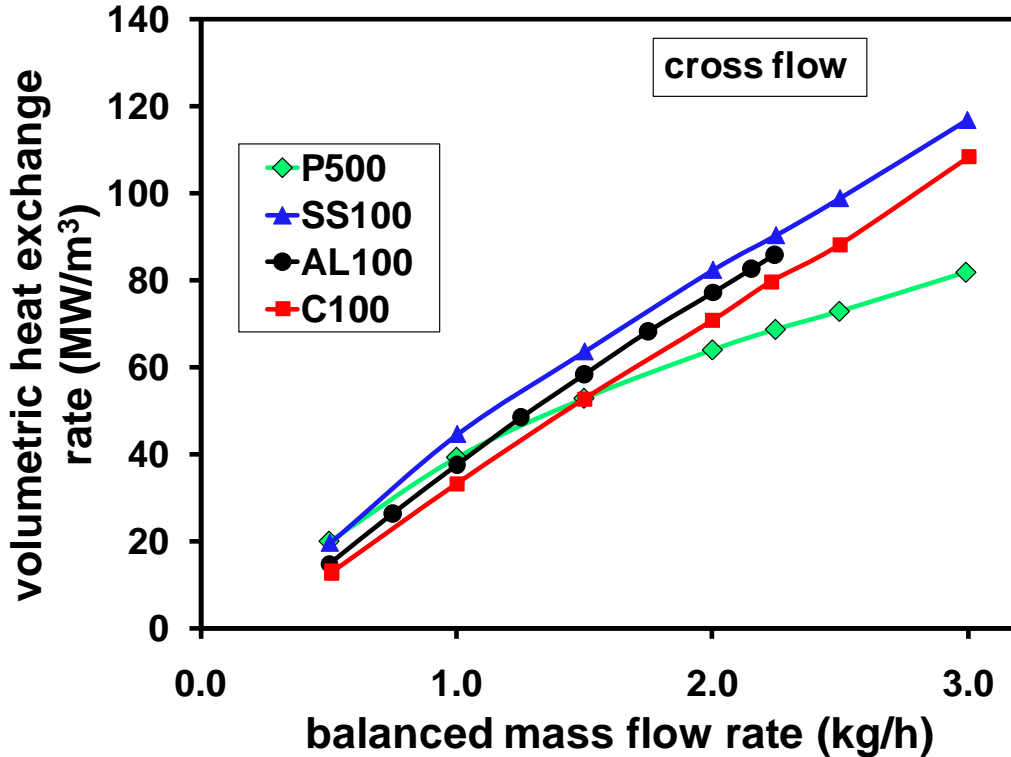


Figure 7-22: Volumetric heat exchange rate of cross flow as a function of mass flow rate.

7.5.2.3 Heat exchanger effectiveness

The heat exchanger effectiveness as a function of mass flow rate for a cross flow microHEX with balanced flows is plotted in Figure 7-23 for a thick PEEK partition foil (P500). It is possible to observe how, as the mass flow rate increases, the experimental value of effectiveness drops sharply. This steep trend suggests that in this microdevice the mass flow rate should be maintained sufficiently low in order to guarantee a large value of effectiveness. In addition, it is evident from Figure 7-23 that theoretical prediction steadily underestimates the value of heat exchanger effectiveness for all the mass flow rates tested. As demonstrated for countercurrent microHEX, in the case of PEEK foil, axial conduction in the solid walls should be extremely small. Therefore, this deviation is not likely to be explained by invoking the effect due to wall axial conduction.

In this case a possible explanation of the difference between the experimental and the theoretical results can be linked to the approximation of the theoretical approach available for the treatment of cross flow heat exchangers. In fact, this approach is based on a series of empirical correlations (see Eq. (7.26)) which have been obtained on the basis of tests conducted on macro

heat exchangers in which, usually, only metallic partition foils are used. The use of these correlations when partition foils with low thermal conductivity are used (as in the case of P500) can determine incorrect results. It is interesting to note that the difference between the theoretical values and the experimental ones tends to decrease when the mass flow rate increases.

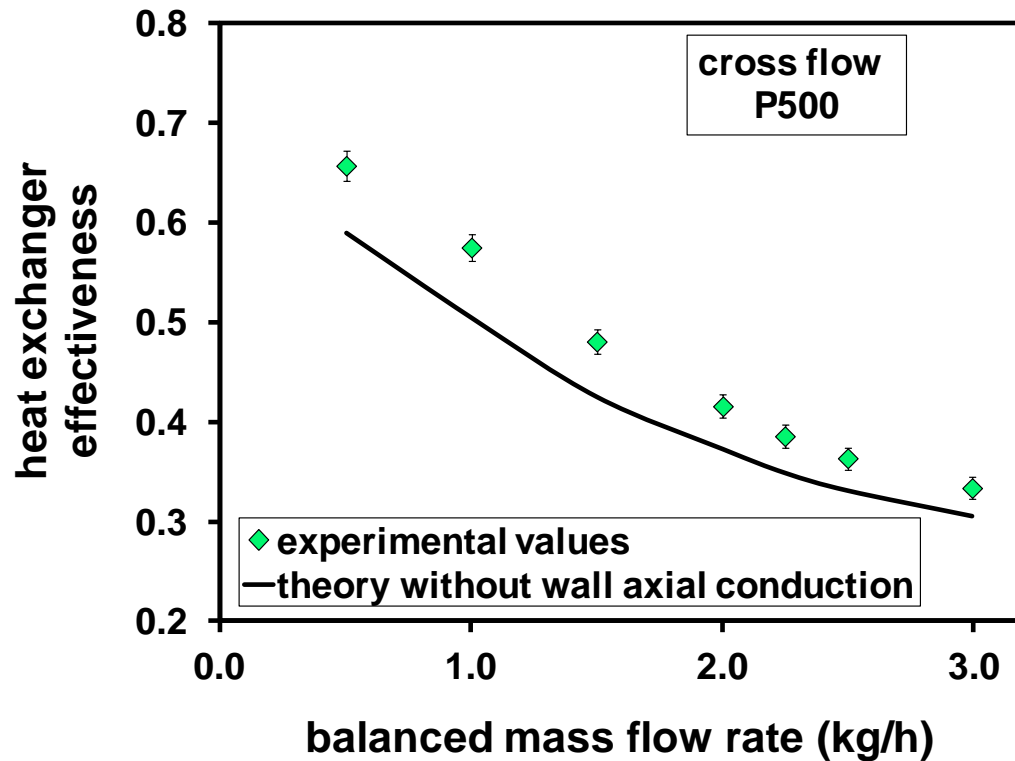


Figure 7-23: Effectiveness of microHEX with thick PEEK foil (P500) in comparison with theoretical prediction.

The experimental results obtained in terms of effectiveness for a cross flow microHEX with thin aluminum foil (AL100) are shown in Figure 7-24. It can be noted that unlike the case of P500, the values of effectiveness tends to decrease rather gradually with the increase of the mass flow rate in a balanced flow microHEX. Again, it is evident that the theory is able to predict the experimental trend but a certain underestimation of the effectiveness is confirmed also by the data obtained with AL100. As evidenced in the case of countercurrent flow arrangement, in this case the axial conduction may play a role and can justify the deviation between theory and experiment.

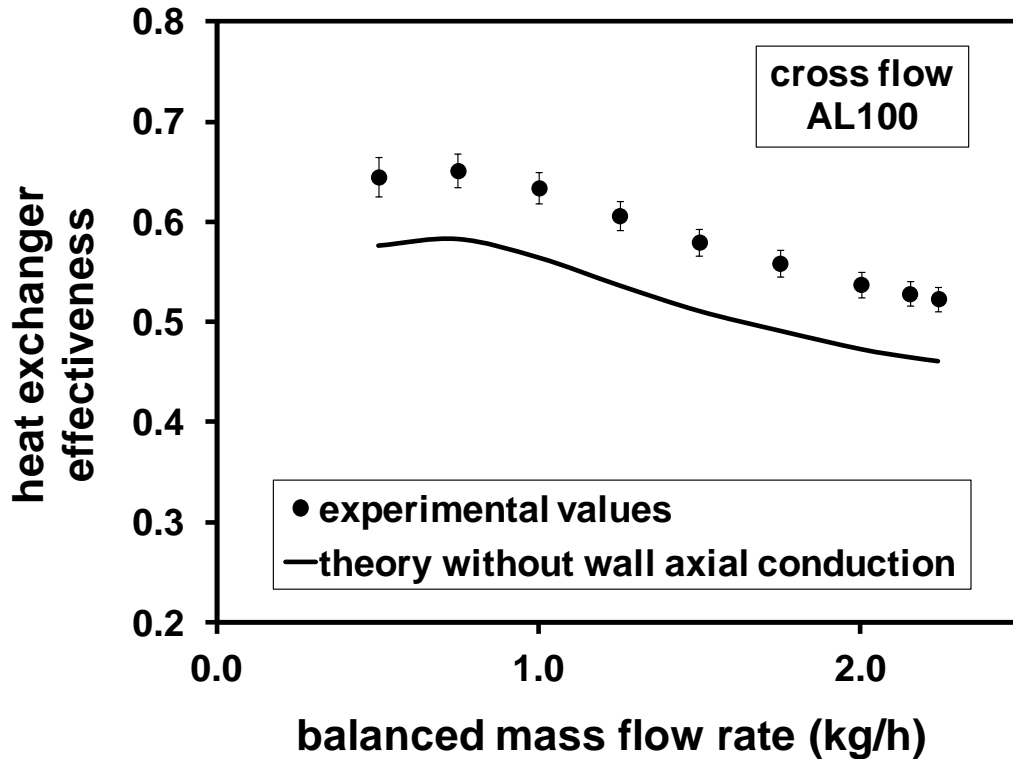


Figure 7-24: Effectiveness of microHEX with thin aluminum foil (AL100) in comparison with theoretical prediction.

The same difference between the experimental results and the theoretical predictions have been evidenced by using the partition foils in copper (C100) and stainless steel (SS100) as evidenced by Figure 7-25 and Figure 7-26.

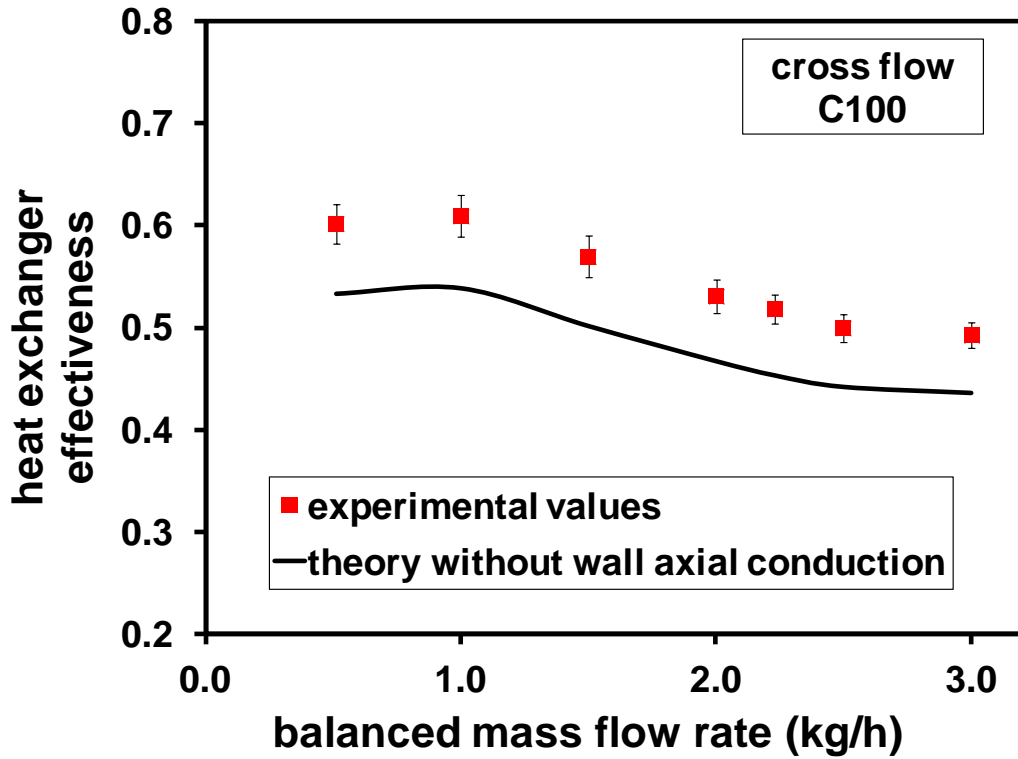


Figure 7-25: Effectiveness of cross flow microHEX with thin copper foil (C100).

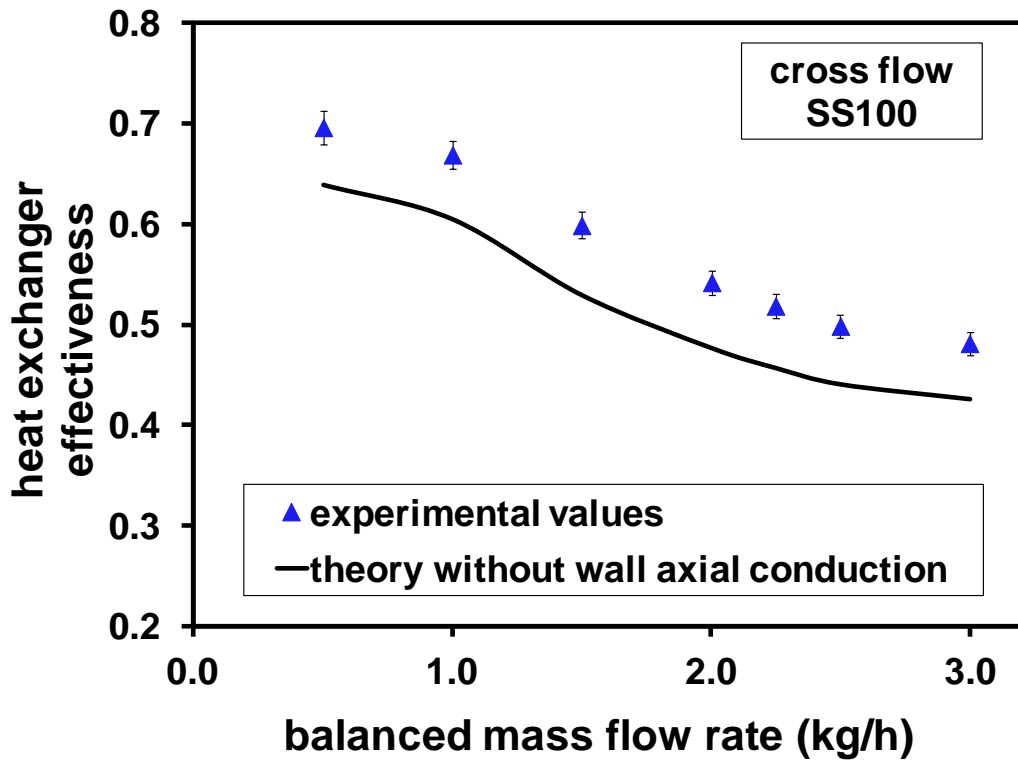


Figure 7-26: Effectiveness of cross flow microHEX with thin stainless steel foil (SS100).

The effectiveness of cross flow microHEXs is compared in Figure 7-27 for all the partition foils tested. It is evident that the microHEX with thick PEEK foil exhibits a behavior completely different from the other microHEXs due to the large thickness and low thermal conductivity of the partition wall.

The other three partition foils have similar performance especially at large mass flow rate, where the axial conduction plays a less significant role. At mass flow rate smaller than 1.5 kg/h, the effectiveness of the microHEX with a stainless steel foil is the largest among all the three metallic foils which have the same thickness, while the data from microHEX with copper foil is the smallest. By considering the different thermal conductivities of these three materials, one can expect that the microHEX with copper foil should ideally perform best due to the lowest thermal resistance between the flows. However, this is opposite to the practical case. Although the thermal resistance is greatly reduced by using highly conductive material, the wall axial heat conduction in partition wall is enhanced as well. By comparison it can be validated that axial conduction tends to reduce the effectiveness of cross flow microHEX.

Furthermore, it can be concluded that by increasing the thermal conductivity of partition foil, both thermal conduction across hot and cold flows and wall axial conduction are improved. The former imposes a positive effect on effectiveness while the latter has a negative impact. In the real case, these two effects are competing with each other in terms of effectiveness. In the case of 100 μm thick foil for cross flow, it can be experimentally confirmed that the heat conduction across the foil is less important than the wall axial conduction. If the dimension in the direction of foil thickness is further reduced, i.e., to tens of or even several microns, it could be expected that the gain in effectiveness due to the heat conduction across the foil can be larger than the losses due to the wall axial conduction. However, such thin foil can become mechanically weak and could not sustain the high pressure needed by the flows.

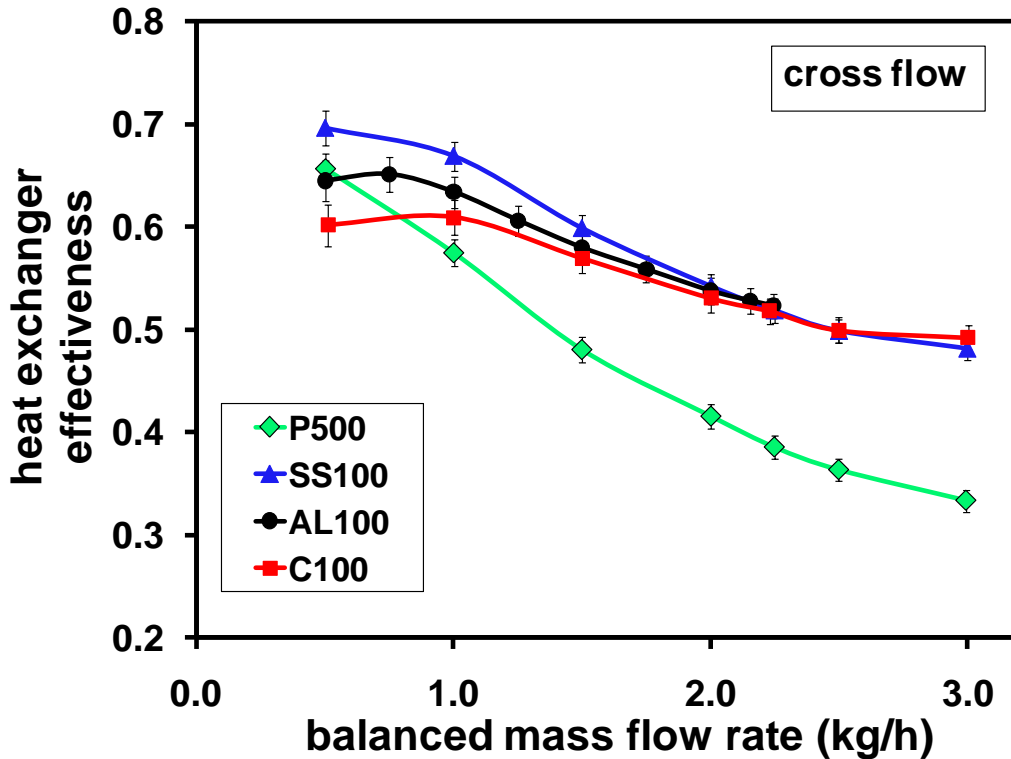


Figure 7-27: Effectiveness of cross flow microHEX with various partition foils.

7.5.3 MicroHEX with cocurrent arrangement

By exchanging the inlet and the outlet ports of the layers with parallel microchannels manufactured in it, the device can be changed from a countercurrent into a double-layered cocurrent microHEX. Experimental tests have been conducted for this flow arrangement by testing four partition foils, namely, P500, SS100, AL100 and C100.

7.5.3.1 Overall heat transfer coefficient and volumetric heat exchange rate

The experimental values of overall heat transfer coefficient for a cocurrent micro HEX with balanced flows are plotted as a function of the mass flow rate in Figure 7-28. Compared with countercurrent flow arrangement, cocurrent flow shows lower overall heat transfer coefficients at the same mass flow rate. Similarly to the case of countercurrent and cross flow arrangement, the overall heat transfer coefficient of microHEX with thick PEEK foil tends to flatten out at large mass flow rate. The cocurrent microHEX with copper foil exhibits slightly larger heat transfer coefficients than the devices with the other metallic foils, while in the cases of counter-current

and cross flow, this value is lower. This could be a hint that wall axial conduction plays a less significant role in the case of cocurrent flow arrangement.

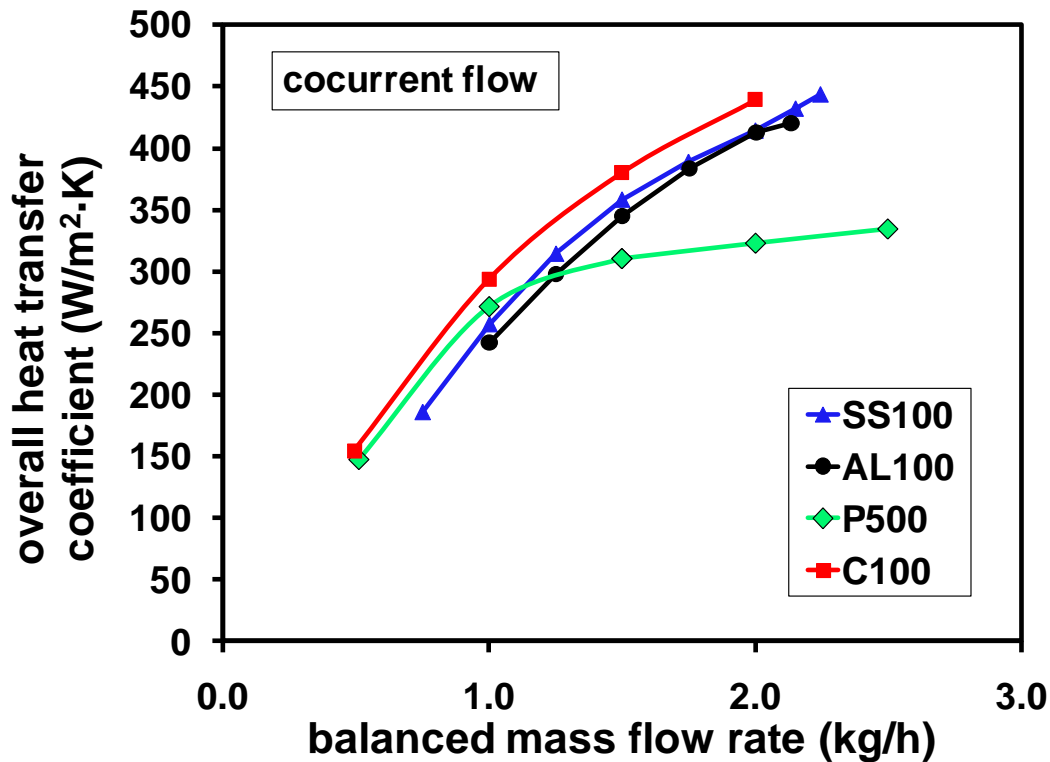


Figure 7-28: Overall heat transfer coefficient of the cocurrent microHEX as a function of mass flow rate.

Figure 7-29 presents the experimental results in terms of heat exchange rate per unit volume. Although the microHEX with thick foils has the lowest overall heat transfer coefficient, its heat exchange rate is the largest. This is because the low axial conduction helps to maintain large temperature difference between the inlet and outlet of flow along the heat exchanger core. The values of volumetric heat exchange rate in cocurrent microHEXs with metallic foils are quite close to each other for the same mass flow rate.

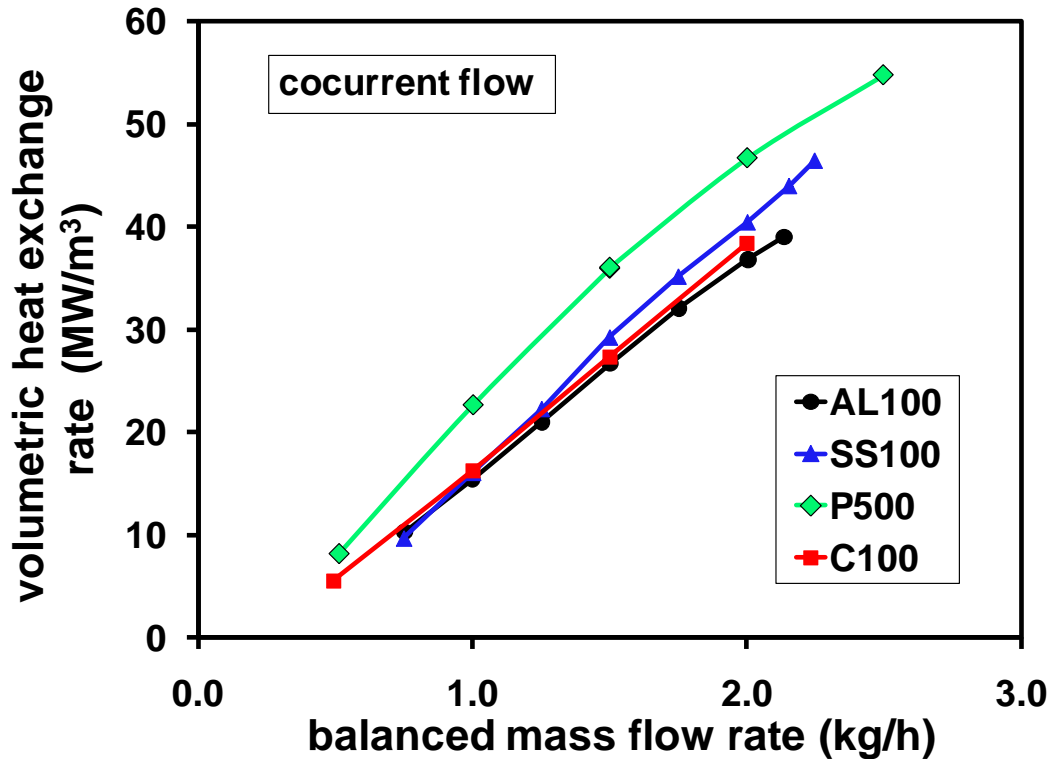


Figure 7-29: Volumetric heat exchange rate versus mass flow rate for cocurrent flow.

7.5.3.2 Heat exchanger effectiveness

In this section the experimental results on cocurrent microHEX effectiveness are discussed. The experimental data are compared with the theoretical calculation made by using the conventional theory for heat exchangers. It is well known that the theoretical value of effectiveness for a balanced cocurrent flow heat exchanger can be calculated by [152]:

$$\varepsilon = \frac{1 - \exp(-2NTU)}{2} \quad (7.28)$$

It should be noted that this calculation was developed from conventional heat exchangers where generally wall axial conduction is negligible.

The results from microHEX with thick PEEK foil are shown in Figure 7-30 together with theoretical predictions of Eq. (7.28) by neglecting the effect due to the wall axial conduction. It is evident that all the experimental values are below the theoretical up limit, which is 50% for all co-current heat exchangers with balanced flows. More specifically, the effectiveness goes down as the mass flow rate increases, and this trend is similar to the trend evidenced before for

countercurrent and cross flow arrangements. More importantly, the experimental data are in very good agreement with theoretical calculation in which wall axial conduction is not considered.

In the case of balanced cocurrent flows, local temperature rise in cold flow is ideally equal to the local temperature decrease in hot flow. The partition foil between the two flows works at a value of temperature equal to the average value between hot and cold flows, as schematically shown in Figure 7-31. As a result, the temperature of the partition foil tends to be uniform along the microHEX and it remains “neutral” and almost constant in axial direction. The constant axial temperature in partition wall generates an axial conduction flux equal to zero in the solid wall, no matter how large the thermal conductivity of the solid wall is. Therefore, it can be concluded that there is no axial conduction in the partition wall in the case of co-current flow arrangement. This explains why the conventional theory without wall axial conduction is able to well predict the experimental data. This result is completely different from the results obtained for countercurrent and cross flow arrangements where the partition foil is characterized by a non-uniform temperature distribution along the axial direction.

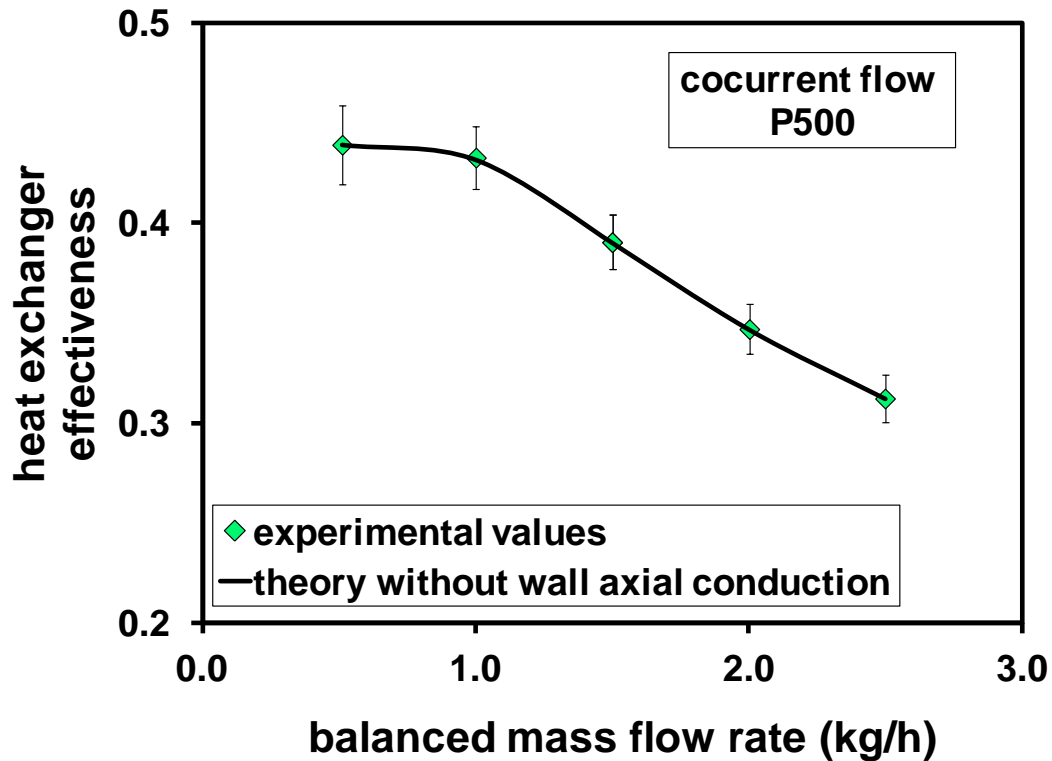


Figure 7-30: Effectiveness of microHEX with thick PEEK foil (P500) in comparison with theoretical prediction.

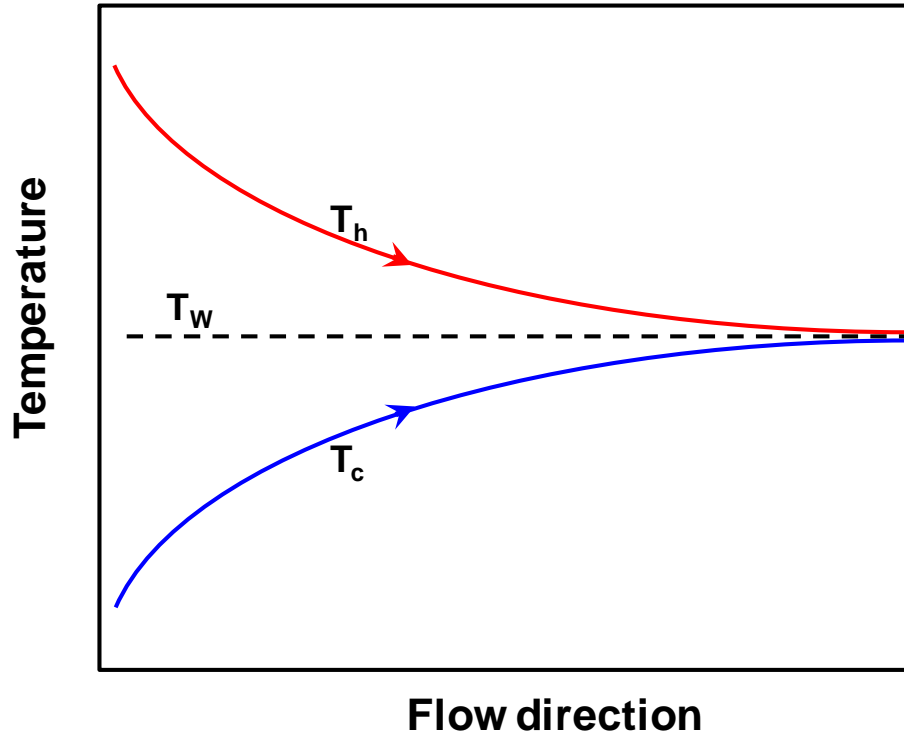


Figure 7-31: Schematic diagram of local fluid and wall temperature development in cocurrent flow heat exchanger.

This conclusion can be further verified by considering the experimental data obtained with the microHEX with thin aluminum (AL100), stainless steel (SS100) and copper (C100) foils. The experimental results are compared with the theoretical prediction of Eq. (7.28) in Figure 7-32, Figure 7-33 and Figure 7-34. It is evident that the agreement between the experimental data and theory in terms of effectiveness is very good for all the metallic partition foils investigated. In addition, in the case of metallic foils the decrease of effectiveness when the mass flow rate is increased is very low if compared with the trend obtained for P500 foil. This indicates that although there is no effect of wall axial conduction in the case of cross flow arrangement, the thermal conductivity of solid material still influences heat exchanger effectiveness in terms of thermal resistance across the partition foils.

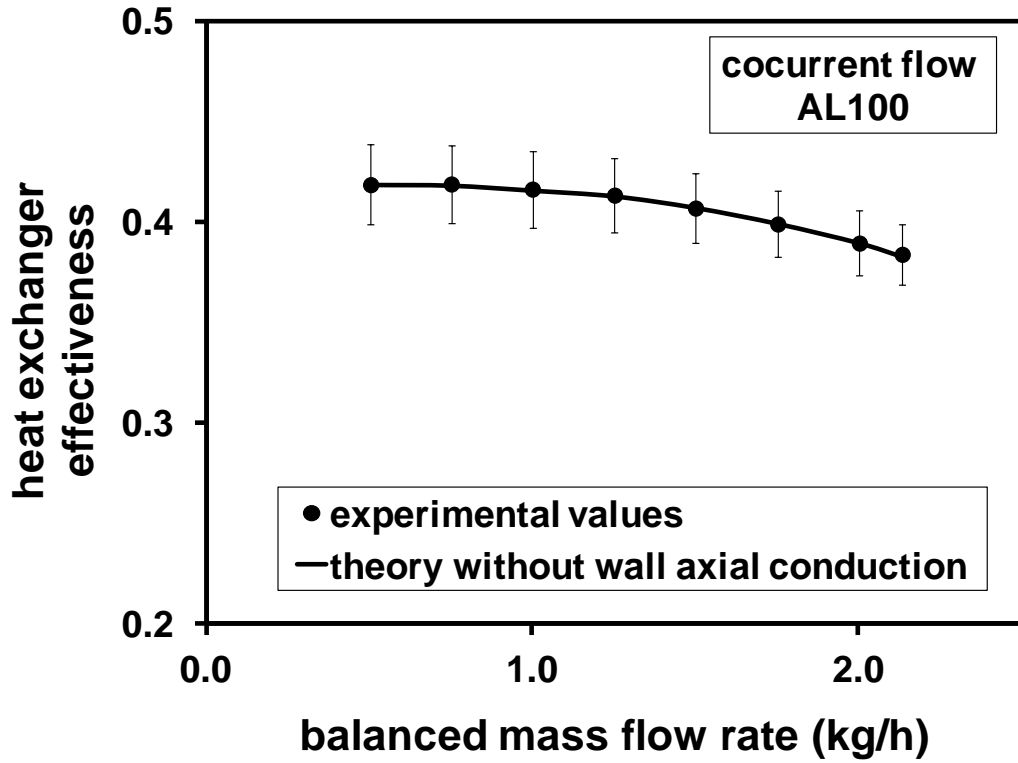


Figure 7-32: Effectiveness of microHEX with thin aluminum foil (AL100) in comparison with theoretical prediction.

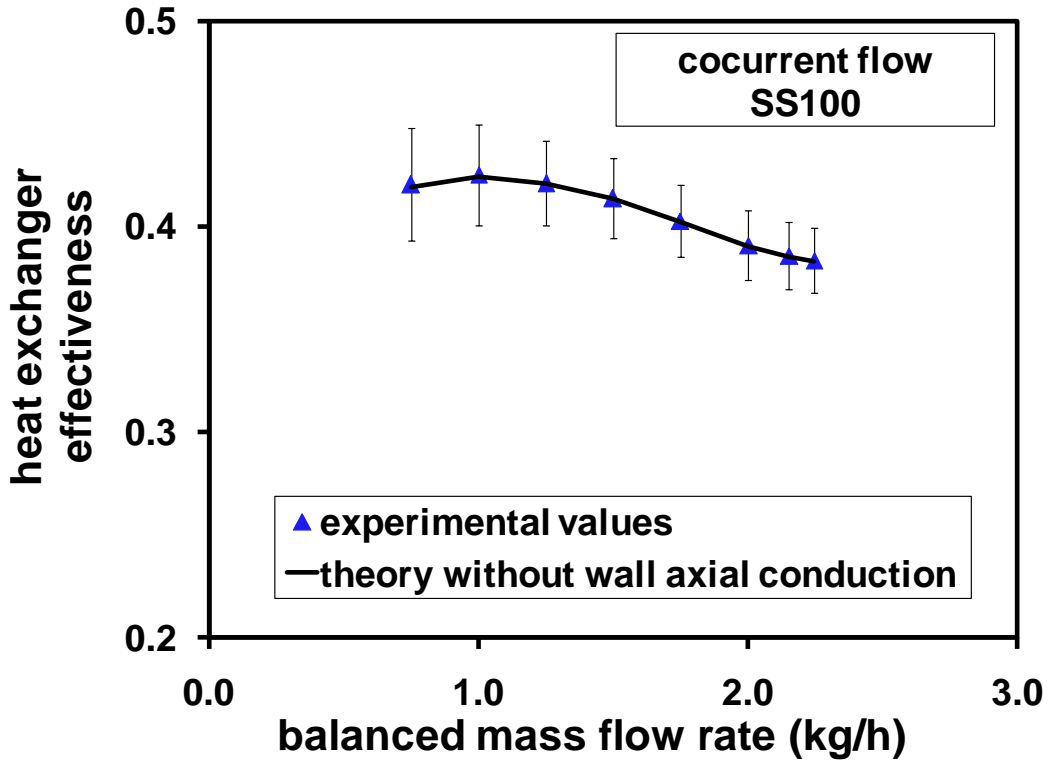


Figure 7-33: Effectiveness of cocurrent microHEX with thin stainless steel foil (SS100).

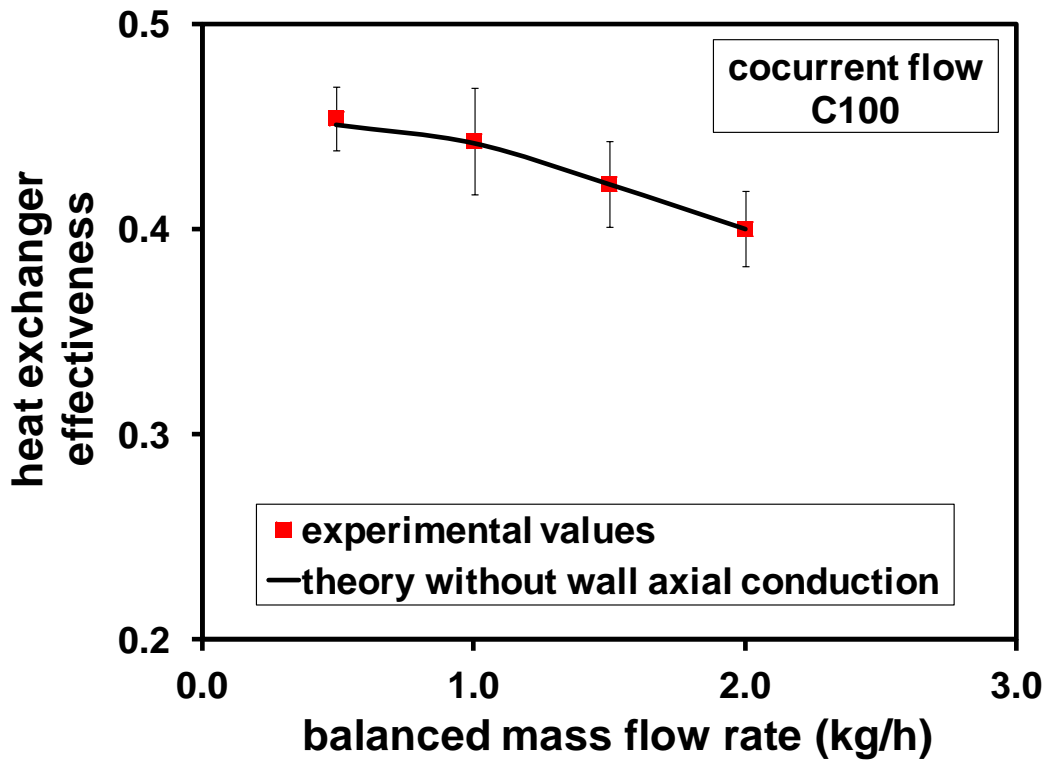


Figure 7-34: Effectiveness of cocurrent microHEX with thin copper foil (C100).

Figure 7-35 compares the experimental results in terms of effectiveness obtained by testing the four partition foils. It is evident how in the case of co-current flow, the influence of wall axial conduction on effectiveness can be completely neglected. In Figure 7-35 the differences between the three metallic foils (SS100, AL100 and C100) are masked by the error bars. However, it is well distinguishable that metallic foils perform better than the thick PEEK foil does, as the large thermal resistance across the partition foil in the latter generates a large temperature barrier between the two flows.

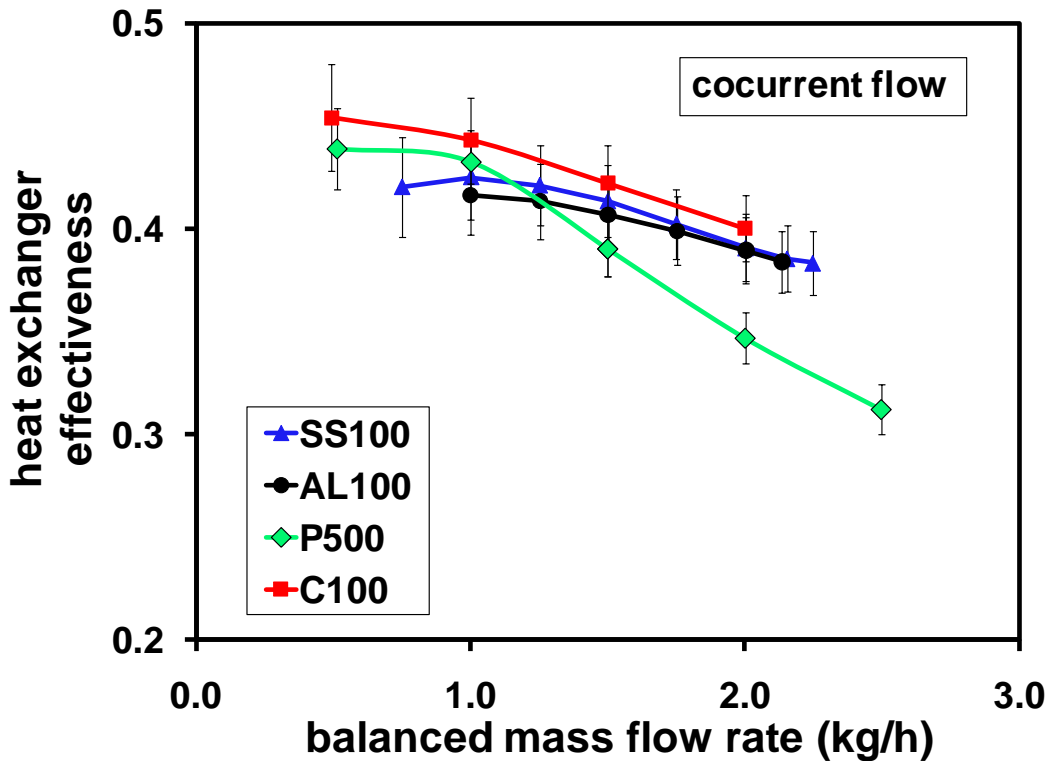


Figure 7-35: Effectiveness of cocurrent flow microHEX with various partition foils.

7.5.4 Comparison among different flow arrangements

In the previous three sections the thermal performance of microHEX has been investigated by using different partition foils (P500, SS100, AL100, C100 and C500) under the same flow arrangement (countercurrent, cross flow or cocurrent). It would also be interesting to compare the experimental results among different flow arrangements for a fixed partition foil in order to emphasize the role of the flow arrangement on the performance of a microHEX.

The values of effectiveness obtained for a double-layered microHEX in which a thick PEEK foil is used as partition foil are plotted in Figure 7-36 for countercurrent, cross flow and cocurrent arrangements. As demonstrated before, the effectiveness of all the flow arrangements decreases with the increase of mass flow rate. It is well evident that, at the same mass flow rate, countercurrent flow is able to guarantee the largest effectiveness, followed by cross flow, while the effectiveness of cocurrent flow is the lowest. This result was expected by considering the convectional theory validated for compact heat exchangers. Typical values of effectiveness for a double-layered microHEX with a PEEK partition foil is of the order of 75%-60% for countercurrent flow at mass flow rates lower than 1 kg/h and decreases down to 40% at large mass flow rates. On the contrary, for cocurrent flow the effectiveness is lower than 50% and less sensitive to the mass flow rate.

Moreover, the values of effectiveness of these three flow arrangements tend to converge as the mass flow rate increases. This indicates that the effectiveness of microHEX is less dependent on flow arrangements at larger mass flow rate. In addition, it can be noted that for microHEX with thick PEEK foil, the difference between countercurrent and cross flow arrangements is very small.

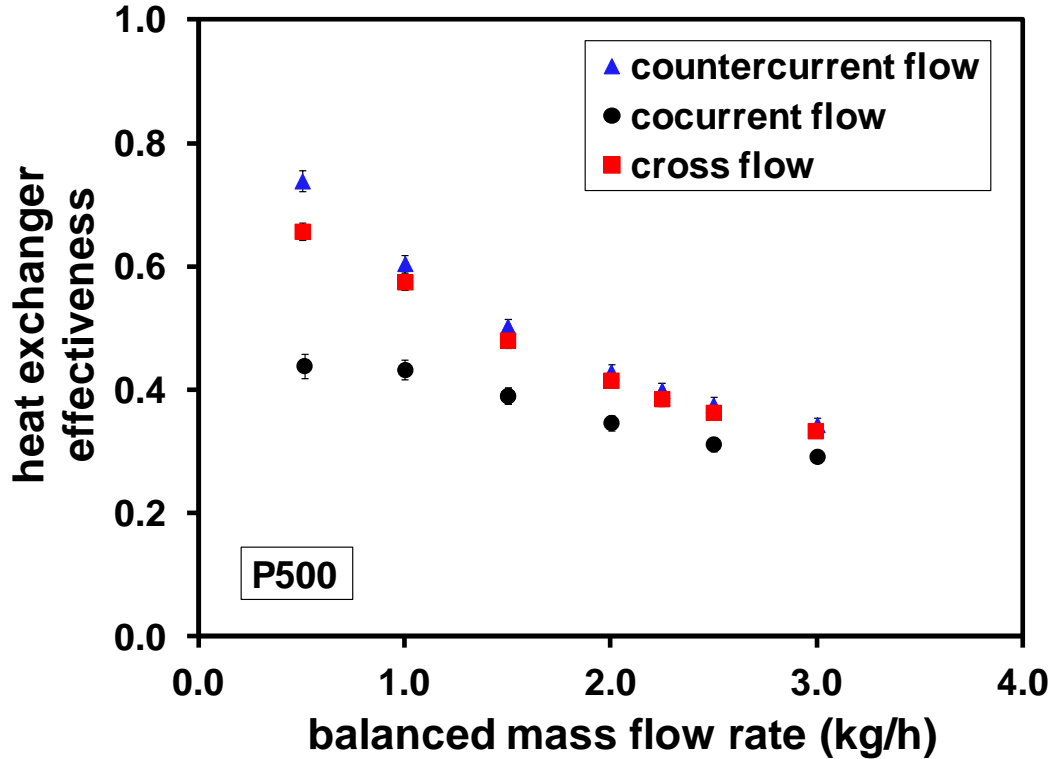


Figure 7-36: Comparison of effectiveness among three flow arrangements with thick PEEK partition foil (P500).

Figure 7-37 compares the experimental results in terms of effectiveness for a microHEX with a more conductive partition foil (AL100) as a function of the mass flow rate for the three flow arrangements. The difference between countercurrent and cross flow arrangements is larger in this case. The maximum value of effectiveness obtained for countercurrent flow configuration is of the order of 80% and never less than 60% at large mass flow rates. By comparing these values with those obtained with a PEEK partition foil it is evident that the aluminum partition foil is able to guarantee larger effectiveness.

Compared with PEEK foil, the thermal performance of a microHEX with aluminum foil is less influenced by the operating mass flow rate. It can also be noticed that the experimental uncertainty in tests with cocurrent flow arrangement is larger than the tests with countercurrent arrangement. This may provide some useful suggestions in the design of such microfluidic devices in order to ensure satisfying measurement accuracy.

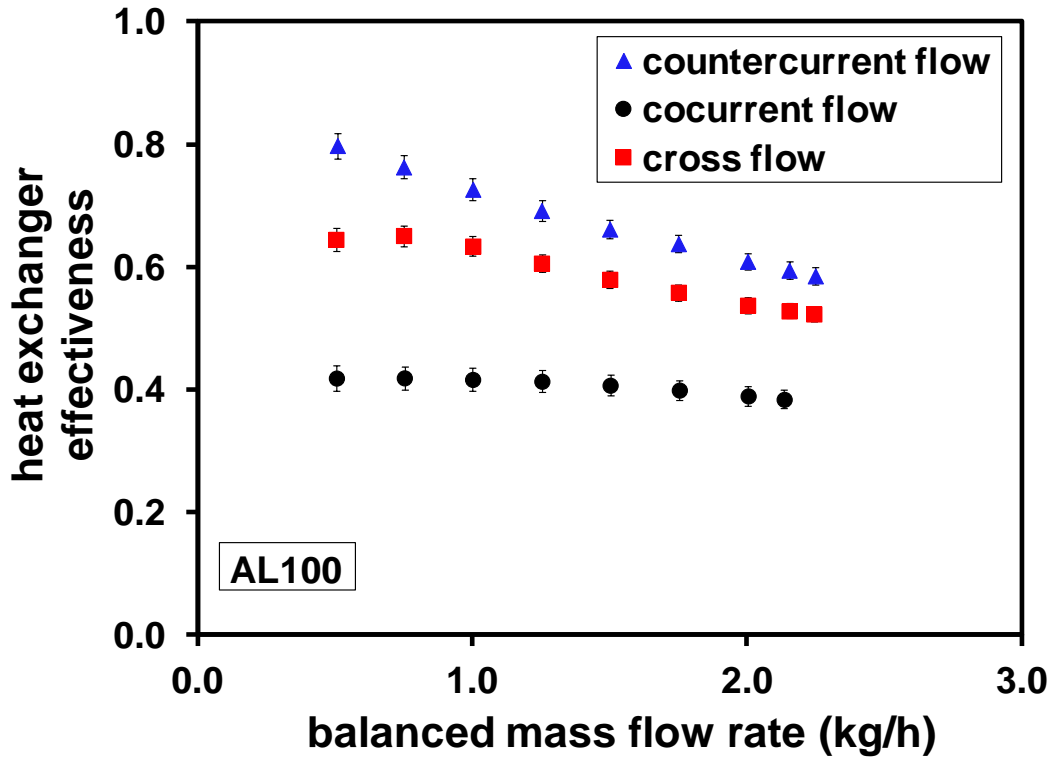


Figure 7-37: Comparison of effectiveness among three flow arrangements with thin aluminum partition foil (AL100).

For sake of completeness, the comparison between the performance in terms of effectiveness obtained for the three flow arrangements with a stainless steel (SS100) and copper (C100) partition foil is shown in Figure 7-38 and Figure 7-39 respectively.

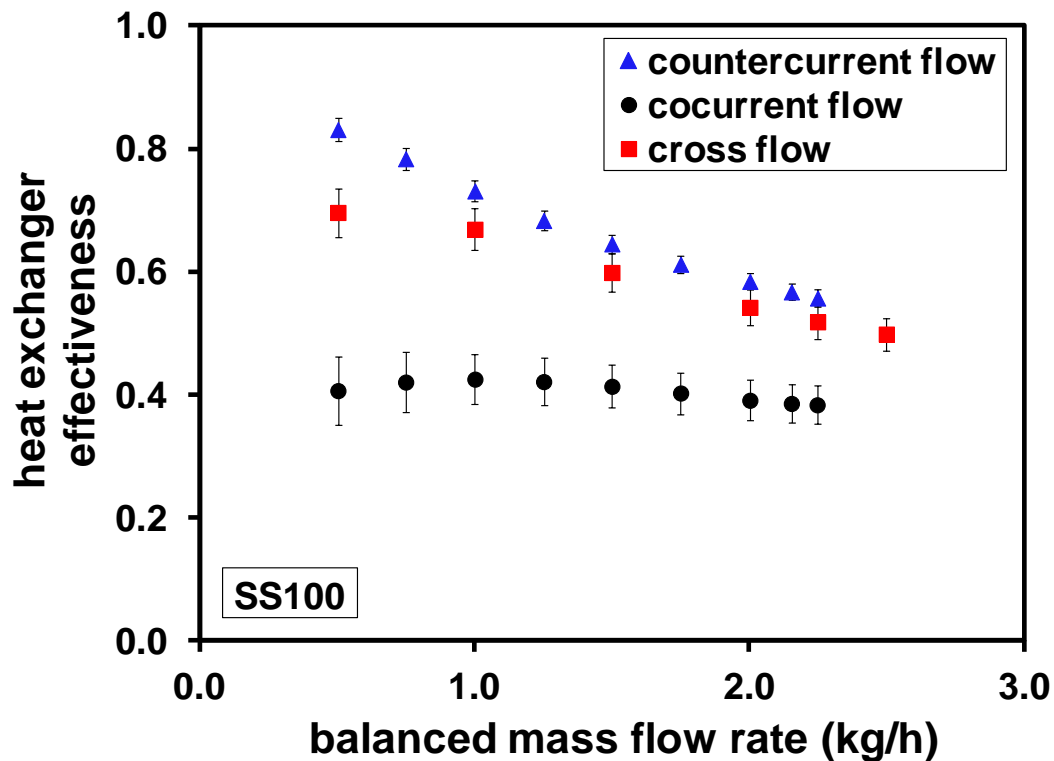


Figure 7-38: Comparison of effectiveness among three flow arrangements with SS100 foil.

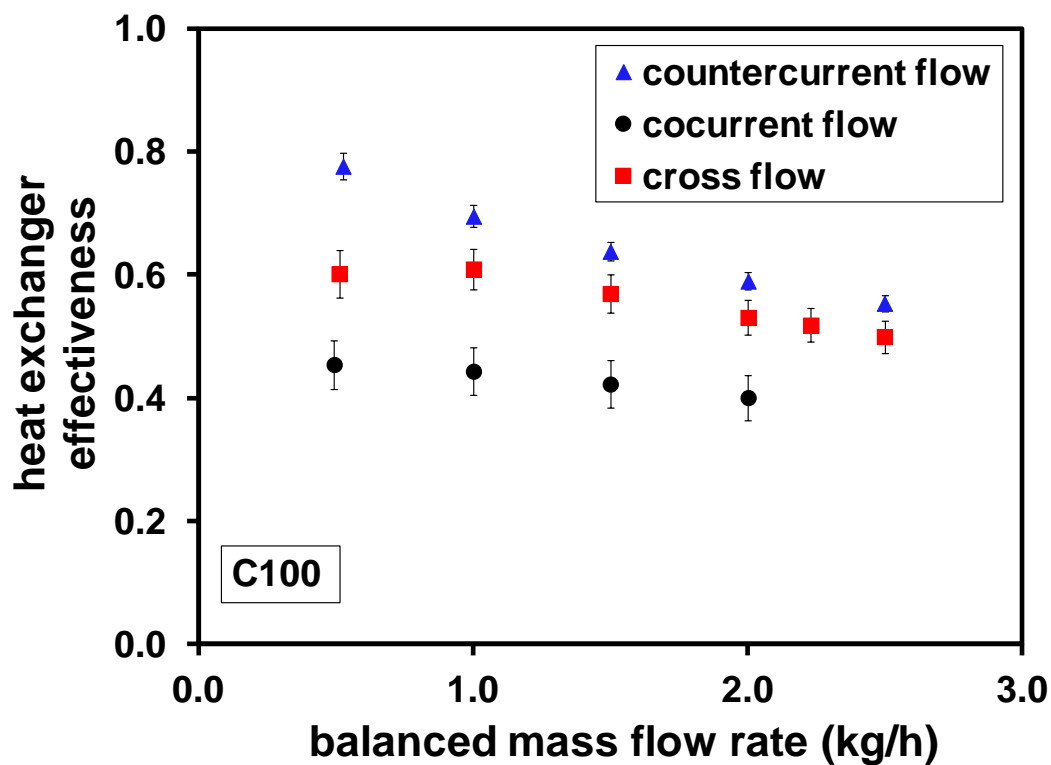


Figure 7-39: Comparison of effectiveness among three flow arrangements with C100 foil.

Figure 7-38 and Figure 7-39 confirm that the countercurrent flow arrangement is able to give the largest values of effectiveness and the cocurrent flow arrangement is the worse configuration for this kind of device. These data highlight that the value of the effectiveness is around 40% for a cocurrent microHEX independently by the material used as partition foil.

7.6 Thermal performance of microHEX with unbalanced flows

The experimental investigation presented in Section 7.5 has been focused on microHEX having balanced flows; in this case the heat capacity rate ($\dot{m}c_p$) of hot flow is equal to that of cold flow. In practical applications, the heat capacity rates of both flow may not be the same as in the case in which equal mass flow rate of different fluids (such as gas and liquid) or the same fluid at different mass flow rates for hot and cold flows are used.

However, for gas flow micro heat exchangers, there are almost no data available on thermal performances of microHEX with unbalanced flows. The only data for this kind of operative conditions appeared in literature can be found is in the work by Kee *et al.* [35] on mixed gas flow in heat exchanger with gapped microchannels. The authors found deviation from classic theory and attributed this to temperature-dependent properties of the gaseous fluid without an accurate analysis of their data.

These reasons motivated the extension of the present study to the analysis of microHEX with unbalanced flows. Experimental tests were carried on countercurrent flow microHEX with a thin aluminum foil (AL100). Both hot and cold flows are fed with dried air as the working fluid. As the temperature range of both flows is limited (from 300 K to 340 K) and they experience similar temperature change in countercurrent flow arrangement, the effect of temperature-dependent property can be considered negligible (i.e. $c_p = \text{const.}$) in this case. The test rig presented in Section 7.1 is used for these tests where the mass flow rates of both hot and cold currents are adjusted in order to obtain unbalanced flows. In the experimental tests of unbalanced flows, the mass flow rate on cold side is carefully tuned to different values while the flow rate on hot side is kept constant.

7.6.1 Conventional theory on unbalanced flow heat exchanger

For a conventional countercurrent heat exchanger with unbalanced flows, the effectiveness cannot be calculated by Eq. (7.10) any more. Instead, it should be calculated by [152]:

$$\varepsilon = \frac{1 - \exp[-NTU(1 - C^*)]}{1 - C^* \exp[-NTU(1 - C^*)]} \quad (7.29)$$

where C^* is the ratio of heat capacity rate of the two flows and takes the form of

$$C^* = \frac{\min(\dot{m}c_p)}{\max(\dot{m}c_p)} \quad (7.30)$$

Figure 7-40 shows the curves of effectiveness as a function of NTU for four different values of heat capacity rate ratio. It is evident that the condition of balanced flow, where C^* is equal to 1, guarantees lower values of the heat exchanger effectiveness. At $NTU=4$, the heat exchanger loses 18% in effectiveness under balanced case if compared with the most unbalanced case ($C^*=0$). However, at the best of the knowledge of the author the curves shown in Figure 7-40 have not yet been compared with experimental data on gas flow microHEX.

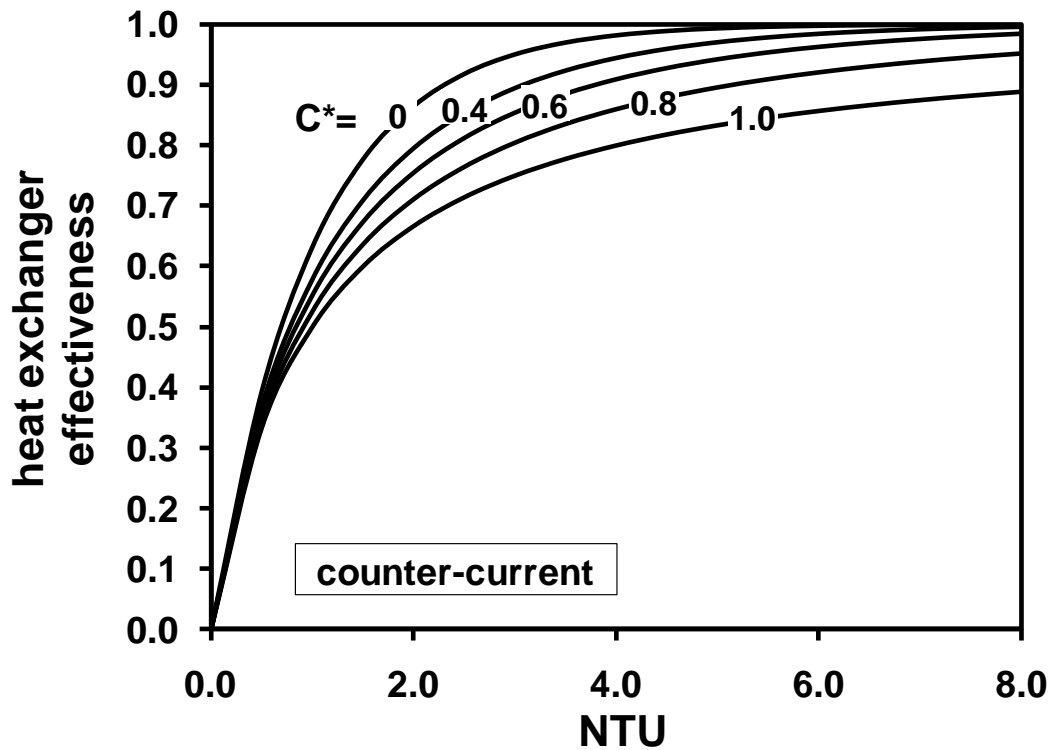


Figure 7-40: Countercurrent flow heat exchanger effectiveness as a function of NTU for various ratios of heat capacity rate.

7.6.2 Countercurrent microHEX with unbalanced gas flow

The experimental values of effectiveness for a countercurrent microHEX with an aluminum partition foil are plotted in Figure 7-41 as a function of mass flow rate ratio (which coincides in this case to the ratio of heat capacity rate). As expected, it can be noted that the effectiveness is the lowest when the mass flow rates are balanced. This is in agreement with conventional theory on heat exchangers [152] and on the results plotted in Figure 7-40. When the mass flow rate of cold flow is not equal to that of hot flow, either larger or smaller than the latter, the effectiveness is dramatically increased. Especially at the ratio of mass flow rate equal to 1.53, the microHEX performs almost at its maximum thermal capacity with ε close to 1. The theoretical prediction from Eq. (7.29) is also included in Figure 7-41. It is worthy to note that the conventional theory is able to precisely predict the experimental data obtained with the gas-to-gas microHEX if one takes into account the typical values of the experimental uncertainty (error bars in Figure 7-41).

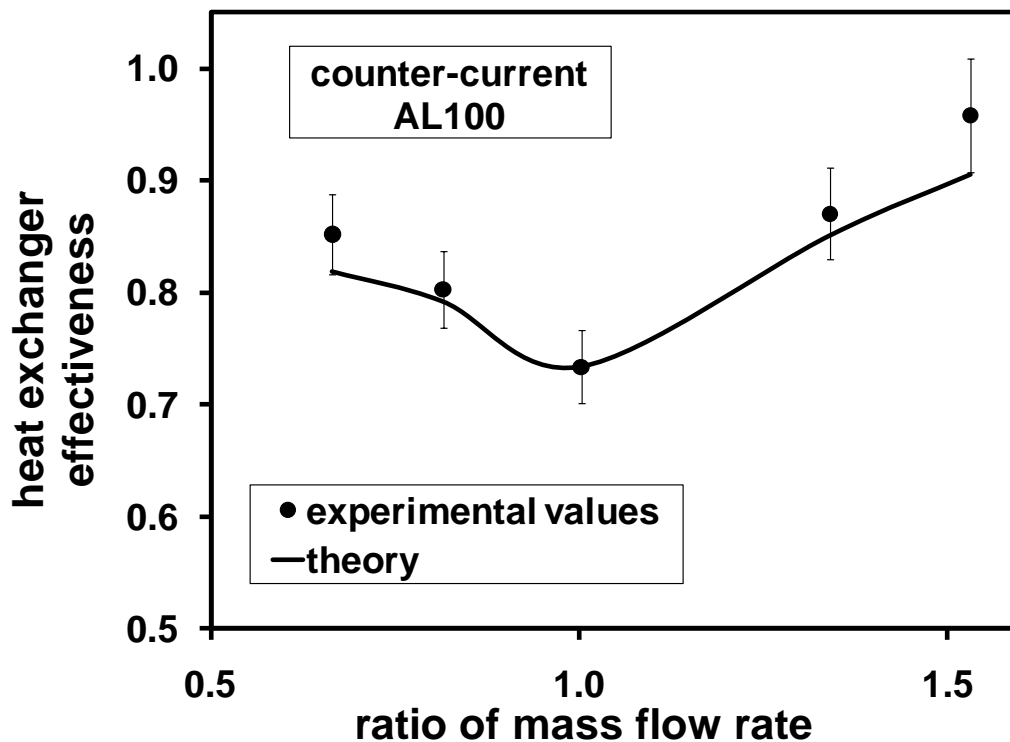


Figure 7-41: Comparison between experimental effectiveness and theoretical prediction for unbalanced flows.

Figure 7-42 plots the theoretical effectiveness- NTU curves for three values of heat capacity rate ratio, namely, 1.0, 0.8 and 0.6. By inserting experimental data points at different values of

C^* into the graph, it can be found that the data strictly obey the trends of the theoretical curves. The highest effectiveness is achieved at large value of number of transfer unit and low ratio of heat capacity rate C^* . In addition, it is important to observe that the typical values of the experimental uncertainty ($\sim 5\%$) associated to the tests make it impossible to obtain a more accurate check of the validity of conventional theory by means of the experimental data since the experimental uncertainty is comparable with the difference of effectiveness obtainable with C^* ranging between 0.6 and 0.8 or from 0.8 to 1.

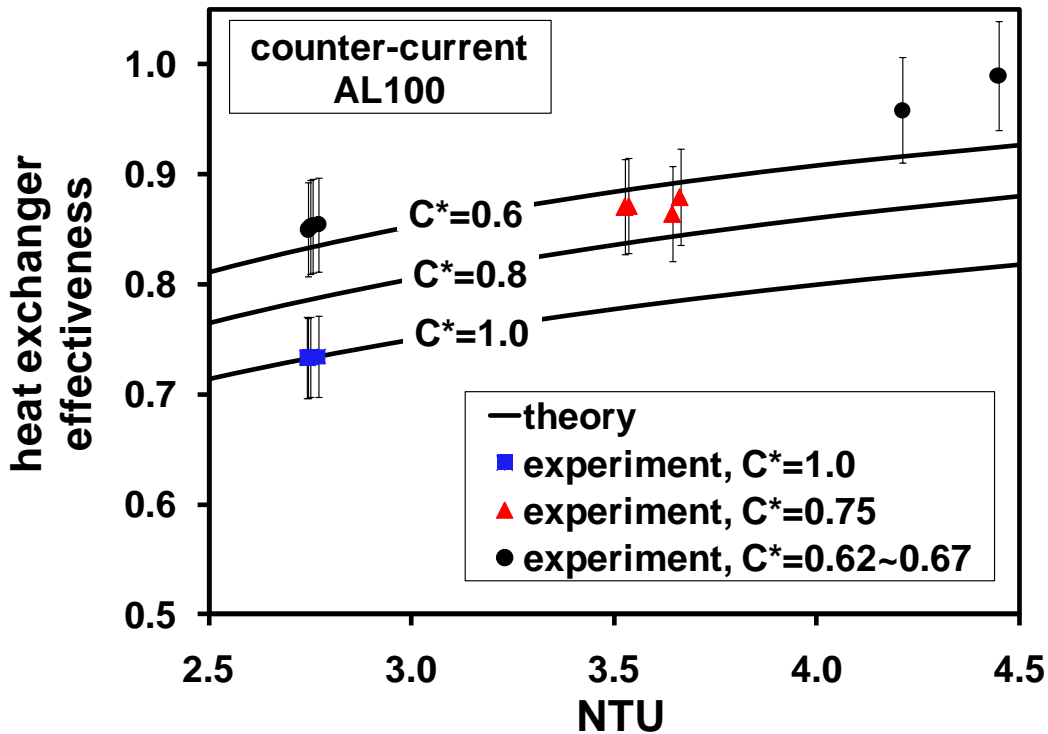


Figure 7-42: Experimental values of effectiveness as a function of NTU.

7.7 Conclusions

This chapter focuses on the experimental investigation on the characteristics of a double-layered microHEX by analyzing the influences of wall axial conduction, flow arrangement (countercurrent flow, cocurrent flow and cross flow), mass flow rate, thickness and thermal conductivity of the partition foil on the thermal performance of the microdevice.

A detailed introduction to the experimental apparatus has been presented in order to evidence how the design and optimization in Chapter 6 of the microHEX have been realized

experimentally and to highlight that accurate fabrication and experimentation are essential to the test systems of microdevice for gas flows.

The experimental results show that the distributing and collecting manifolds have much larger pressure losses than the typical pressure drop along the microchannels, most likely due to the integrated micro pillars. This conclusion underlines how the fluid-dynamic design of the micro heat exchanger manifolds is of primary importance for the optimization of the performance of this kind of micro device.

A novel method to account for the wall axial conduction in countercurrent microHEX has been proposed, and this method has been tested to be able to accurately estimate the influence of axial conduction on the effectiveness of the microHEX. By introducing the wall axial conduction parameter (Eq. (7.17)), the significance of axial conduction in the work of Bier *et al.* [32], Meschke *et al.* [33] and Koyama and Asako [34] have been evaluated quantitatively and compared to those of the present microHEX with five different partition foils (made of PEEK, stainless steel, aluminum and copper, and of different thickness). The results explain how the thermal performance of microHEXs in terms of effectiveness is influenced by the wall axial conduction and by the thermophysical properties of the working fluid.

The overall heat transfer coefficient depends on the thermal conductivity of the partition foil, especially for microHEXs with countercurrent and cross flow arrangements. Larger mass flow rate favorably strengthens the overall heat transfer coefficient and increases the volumetric heat exchange rate, but results in lower heat exchanger effectiveness for all the three flow arrangements tested.

The experimental results confirm that the effectiveness of microHEX with countercurrent and cross flow arrangements is highly dependent on the thermal conductivity of the partition wall, where the axial conduction has negative impact on the effectiveness of the device. The prediction of the values of countercurrent microHEX effectiveness is in good agreement with experimental data by considering the effect due to the axial conduction in the partition foil.

In the case of cocurrent flow arrangement, axial conduction has quite limited impact on the thermal performance of a microHEX but the effectiveness has been found slightly influenced by the thermal resistance across the partition foil. Due to the absence of axial heat flux in partition foil, the conventional theory without considering wall axial conduction is able to predict the performance of cocurrent flow microHEX.

By comparing the performance of micro heat exchangers having different flow arrangements, it is confirmed that the highest effectiveness has been achieved in countercurrent flow arrangement while cocurrent flow arrangement exhibits lowest performance. Moreover, it has also been evidenced that the effectiveness of microHEX becomes less dependent on flow arrangements at larger mass flow rate, as the values of effectiveness of these three flow arrangements tend to converge to the same value as the mass flow rate increases.

The experimental results on unbalanced gas flow microHEX with countercurrent flow arrangement confirm the validity of conventional theory in the prediction of microHEX effectiveness under various values of ratio of heat capacity rate.

8 Numerical Simulation on Micro Heat Exchangers

8.1 Numerical model

In the experimental tests on microHEX, pressure and temperature values are obtained by sensors placed very close to the inlets/outlets of microchannels. In order to know how the temperature and pressure develop along the channels, a numerical simulation of the whole heat exchanger core has been performed both for a double-layered and a multi-layered micro heat exchangers. In addition, in the numerical simulation more options on thermal conductivities of partition foils have been investigated.

8.1.1 Geometrical construction of numerical model

The simulation was based on the exact geometry of microHEXs designed and manufactured as stated in the previous chapters. The arrangement of hot and cold flows in the core of the microchannel heat exchanger is shown in Figure 8-1(a). The flow patterns modeled numerically are limited to cocurrent and countercurrent flow arrangements. The hot layers and cold layers are stacked alternatively in the direction of height. The full simulation of such a device with thousands of layers and microchannels requires unbelievably intensive computation. To save computational time, only a typical symmetrical element of the heat exchanger core is simulated in all three dimensions, including the hot flow, the cold flow, the partition wall and the side wall, as shown in Figure 8-1(b).

The three-dimensional geometry of the numerical model is shown in Figure 8-2(a). Besides the hot flow, cold flow and the partition wall between them, the side wall is also simulated because it may also play a role to deliver heat from the hot layer to the cold layer. Figure 8-2(b) schematically shows the expected directions of the heat flux in the solid wall. In addition, this model allows the simulation of both cocurrent and countercurrent flows within the same geometry by modifying the boundary condition at the inlet and outlet.

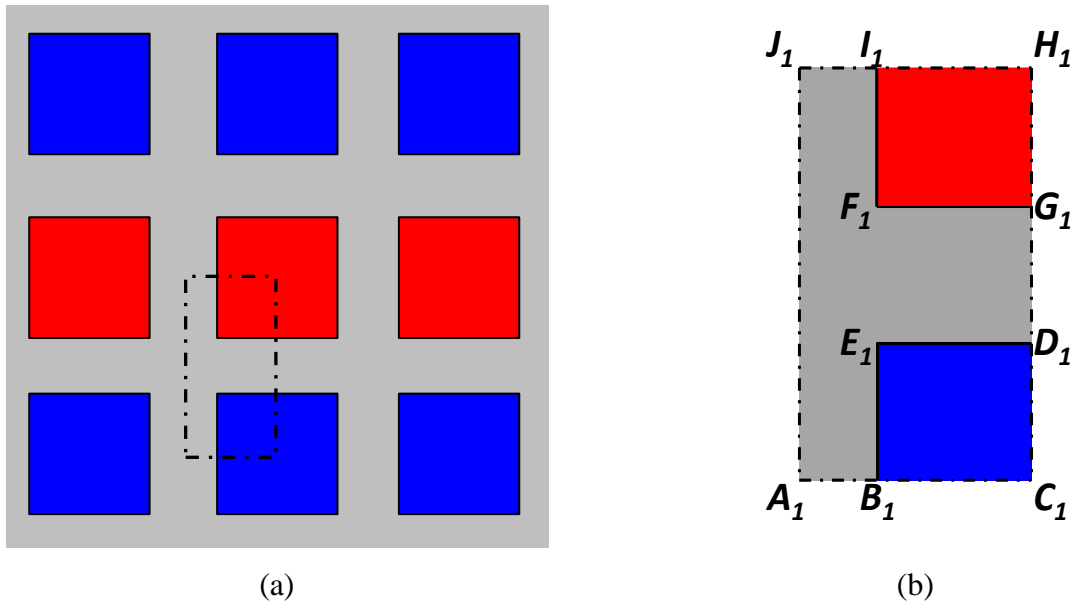


Figure 8-1: A multi-layered micro heat exchanger with hot and cold flows (a) and a typical element from it (b). ($C_1D_1=D_1G_1=G_1H_1=0.1$ mm, $A_1B_1=0.05$ mm, microchannel length $A_1A_2=39.8$ mm)

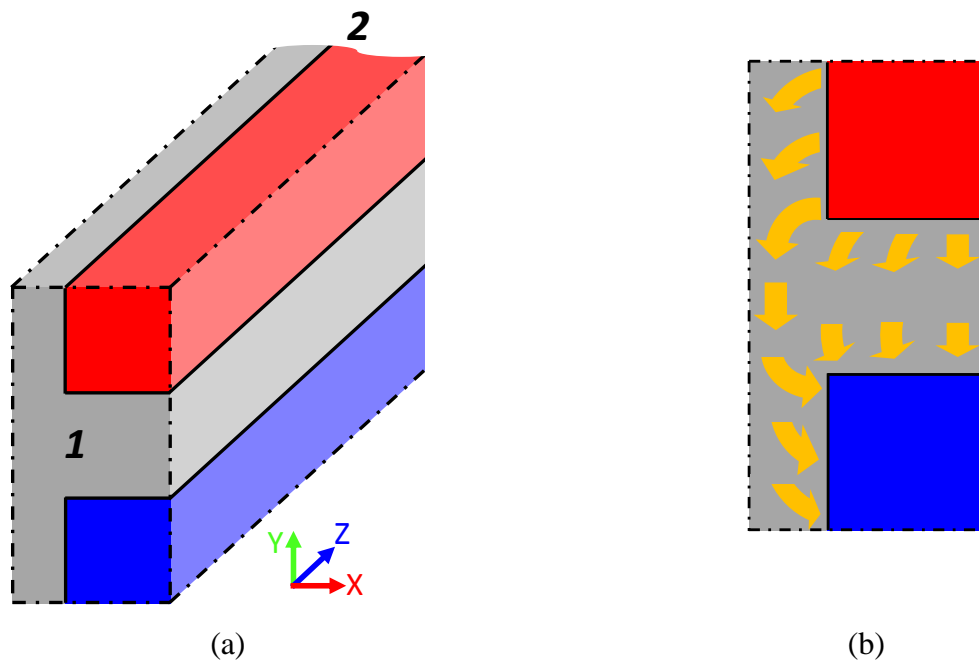


Figure 8-2: 3D model of two microchannels with partition and side walls (a) and schematic display of heat flux (b).

8.1.2 Conditions applied to numerical model and computational method

In the simulation the hot flow is set to have the same mass flow rate as that of the cold flow (balanced flows). The inlet temperature of the hot flow and cold flow is fixed at 350 K and 300 K, respectively. These values are very close to the parameters used during the experimental tests but not exactly the same, because during the experiment the inlet temperature had different values around 350 K in each specific steady case. The boundary condition imposed at the inlet of the microchannels is set as the mass flow inlet, while at the outlet a value of pressure corresponding to the values of outlet pressure measured experimentally at the same mass flow rates are imposed. The front and back surfaces of the side wall and partition foil are assumed to be adiabatic due to their small surfaces compared with axial heat transfer area and the low thermal conductivity of gas around them. All the other surrounding walls or planes in the multi-layered model are imposed with symmetric boundary conditions (see Figure 8-2). In the double-layered model, the boundary conditions on some surrounding walls or planes are not symmetric and they will be explained in detail in Section 8.2.

In most simulation cases, the mass flow rate through a single microchannel is set to be $5.223 \cdot 10^{-7}$ kg/s, which corresponds to a Reynolds number of 550 and an equivalent mass flow rate of 1 kg/h through one layer (with 133 microchannels) of the microHEX. In addition, in some cases the mass flow rate is doubled or tripled in order to investigate the influence of flow velocity on the performance of microHEX and to have more data for a comparison with experiment.

The air flow is assumed as locally incompressible because in all the experimental tests the outlet Mach number is always smaller than 0.2 (below the threshold value of 0.3). However, this does not mean that the fluid is set to a constant density throughout all the simulation cases. The specific values of pressure and temperature in each case may influence the fluid density. Therefore, in the numerical model the fluid density is calculated from ideal gas equation.

As demonstrated before, unlike experimental test, the simulation is able to decouple the influence of thermal conductivity from mechanical stability of different solid materials. In the numerical model, the solid walls are set invulnerable to any pressure difference. A very extensive range of thermal conductivity is applied to the partition foils, which changes from 10^{-4} up to 10^4 W/(mK).

The finite volume solver of ANSYS Fluent 6.3[®] is used to solve the governing equations, in which fluid pressure is set coupled with flow velocity. Second order upwind or higher scheme [154] is applied to special discretization of the numerical model. The residuals of physical parameters are monitored after each iterative calculation. Converged computational results are obtained when the absolute value of residual is smaller than 10^{-6} in continuity, velocity and energy.

8.1.3 Validation of result dependence on grid density of numerical model

Before running the final simulation, the dependence of results on mesh density is carefully examined by constructing three different sets of mesh for the same geometry, as shown in Table 8-1. The computation was done for a balanced countercurrent flow at various Reynolds numbers. The outlet temperature of both hot and cold flows is monitored in the simulation. The numerical results are compared between each other by using the results from the finest mesh as the reference. It is evident that the relevant differences in the results are never larger than 0.02%, which is at least two orders of magnitude smaller than the uncertainty in experiment. Therefore, it can be concluded that the coarse mesh is sufficient for simulation without introducing any significant error.

Table 8-1: Validation of result dependence on grid density.

Re		Temperature (K) and relative diff. (%)		
		Coarse mesh (450 000 cells)	Fine mesh (1 843 200 cells)	Very fine mesh (3 600 000 cells)
500	$T_{h,out}$	326.96 (0.02%)	326.99 (0.02%)	326.91 (ref.)
	$T_{c,out}$	323.04 (-0.02%)	323.09 (0.00%)	323.09 (ref.)
700	$T_{h,out}$	329.03 (0.00%)	329.03 (0.00%)	329.03 (ref.)
	$T_{c,out}$	320.98 (0.00%)	320.97 (0.00%)	320.97 (ref.)
1200	$T_{h,out}$	333.44 (-0.01%)	333.44 (-0.01%)	333.46 (ref.)
	$T_{c,out}$	316.56 (0.01%)	316.54 (0.00%)	316.54 (ref.)

8.2 Simulation of the double-layered microHEX

8.2.1 Numerical model

The model of double-layered microHEX shares many common features with the multi-layered model presented in Section 8.1. However, there are also some distinct differences. The microchannels of double-layered microHEX are manufactured on a PEEK plate with a thickness of 8 mm. In addition, in the double-layered microHEX, the material and thickness for the partition foil are changeable. Therefore, the selection of a typical element from the double-layered one is different from the multi-layered one. Figure 8-3(a) schematically shows a part of the double-layered microHEX. A typical element is taken from it and shown in Figure 8-3(b). It is evident that the boundary conditions are not symmetric on the top of hot flow and bottom of cold flow. Due to the large thickness of the PEEK plates, the low thermal conduction of PEEK material, as well as the good thermal insulation of the double-layered device during tests, the top wall ($J_1H_1J_2H_2$) of hot flow and the bottom wall ($A_1C_1A_2C_2$) of cold flow are assumed as adiabatic in the numerical model.

Figure 8-4 depicts the geometric model of the double-layered microHEX in three dimensions. In the simulation, the thickness of the partition wall and its thermal conductivity can be changed, while the dimension and thermal properties of the side wall are kept fixed.

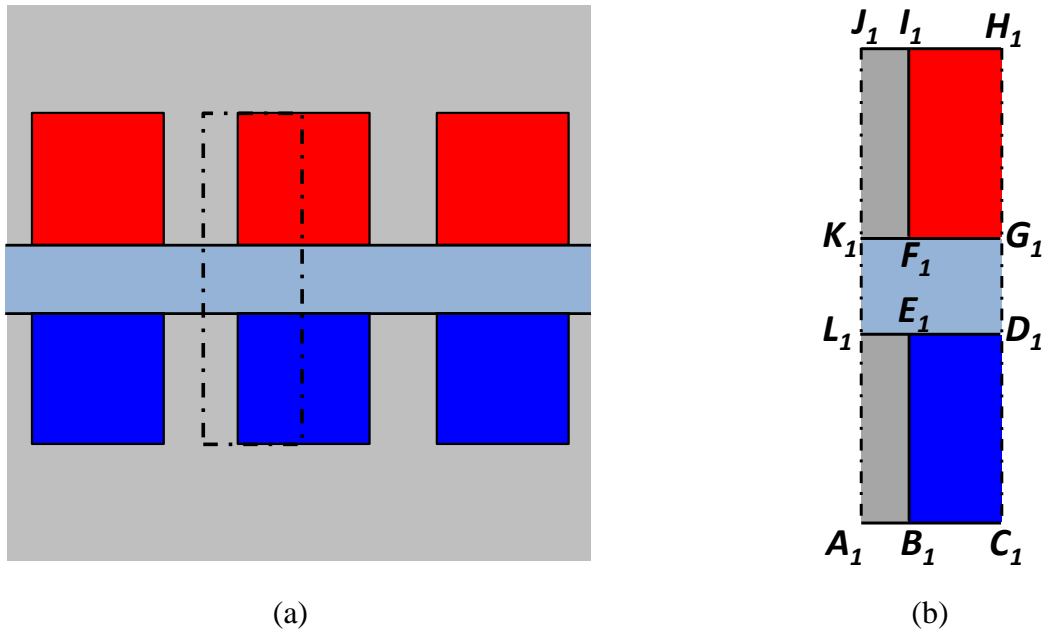


Figure 8-3: A double-layered micro heat exchanger with hot and cold flows (a) and a typical element from it (b). ($D_1G_1=0.1$ mm, $C_1D_1=G_1H_1=0.2$ mm, $A_1B_1=0.05$ mm, channel length $A_1A_2=39.8$ mm)

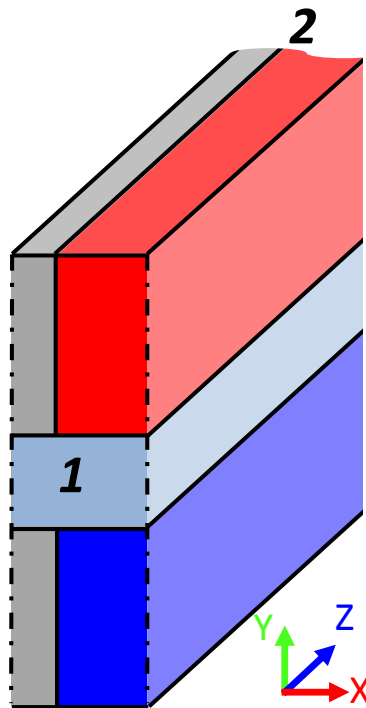


Figure 8-4: 3D model of two microchannels with partition and side walls in the double-layered microHEX.

8.2.2 Temperature distribution

Figure 8-5 displays the temperature distribution on the right symmetric plane ($C_1H_1C_2H_2$) at different thermal conductivities of partition wall. It can be noted that, if the partition wall is not thermally conductive ($k=0.01$ W/(mK)) there is very slight temperature difference between the two surfaces of the partition wall at the same axial position. The partition foil serves as a thermal barrier between the two flows. As a result, the temperature change in the bulk flow is very small in flow direction, and the heat exchange between hot flow and cold flow is very poor.

This situation is greatly improved by increasing the foil conductivity to 1 W/(mK), as shown in Figure 8-5(b). The lower thermal barrier across the hot and cold flows leads to a decreasing temperature difference on both surfaces of the partition wall. In addition, the fluid exits the microchannels at a large temperature difference from the entrance.

By applying highly conductive partition foil ($k=1000$ W/(mK)) between the two flows, the temperature difference across the foil is not significantly reduced compared with Figure 8-5(b), because this value is already very small at thermal conductivity of 1 W/(mK). Instead, the axial temperature gradient is strongly reduced in this case. Due to this reason, no improvement on the flow outlet temperature can be observed by changing the partition foil conductivity from 1 W/(mK) to 1000 W/(mK). It can be expected that if the foil conductivity continues to increase, the axial temperature difference in the foil is further reduced. This hampers the temperature increase in the cold flow as well as temperature decrease in the hot flow.

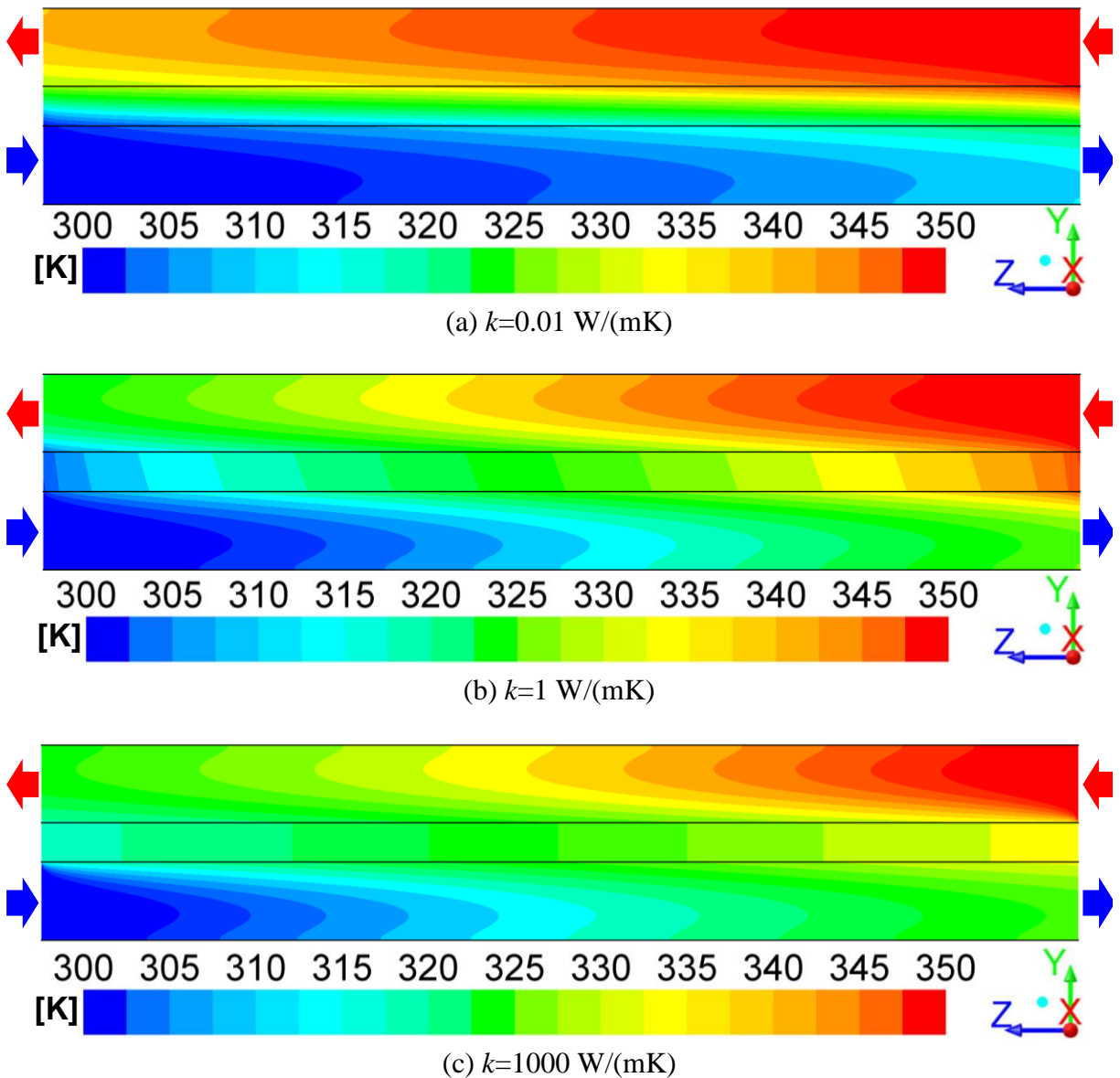


Figure 8-5: Temperature contour on the right vertical symmetric plane ($C_1H_1C_2H_2$) for three different thermal conductivities of partition foil (Black lines indicate the surfaces of solid walls).

In the work of Koyama [69] on a gas flow microchannel heat exchanger, the influence of axial conduction in the partition wall was numerically examined by two-dimensional simulation which only considers hot flow, cold flow and partition wall. Actually, the side walls between the parallel microchannels on one layer can also conduct heat from the hot side to the cold side through the partition foil. In 2D simulation it is not possible to include the side wall in the

numerical model. However, the present 3D model is quite advantageous in full consideration of side wall effects on the thermal performance of microHEX.

The temperature field on the left vertical symmetric wall ($A_1J_1A_2J_2$) is shown in Figure 8-6 for the same three values of partition foil thermal conductivity. In all the three cases, the side wall is made of PEEK and has a constant thermal conductivity of 0.25 W/(mK), while the conductivity of the partition wall changes enormously. At very low thermal conductivity of the partition foil, the temperature difference between the upper side wall and the lower side wall is very different. When the thermal conductivity of the partition foil is increased to 1 W/(mK), the lateral temperature gradient in the partition foil is smaller than that in the side wall. This means that in this case, the side walls become thermal barriers stronger than the partition wall. With a thermal conductivity of the partition wall going up to 1000 W/(mK), the temperature difference on both sides of partition foil totally vanishes.

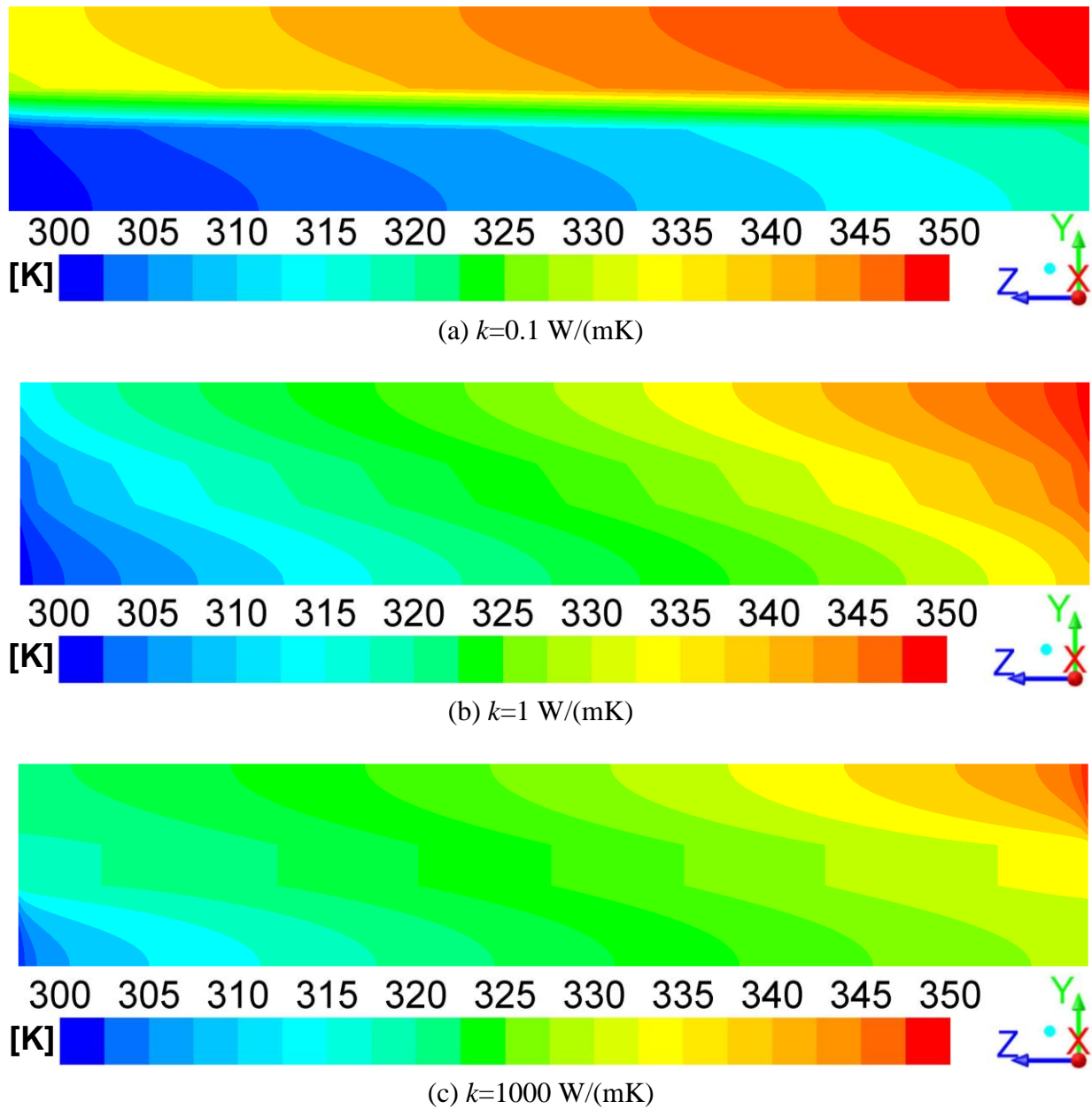
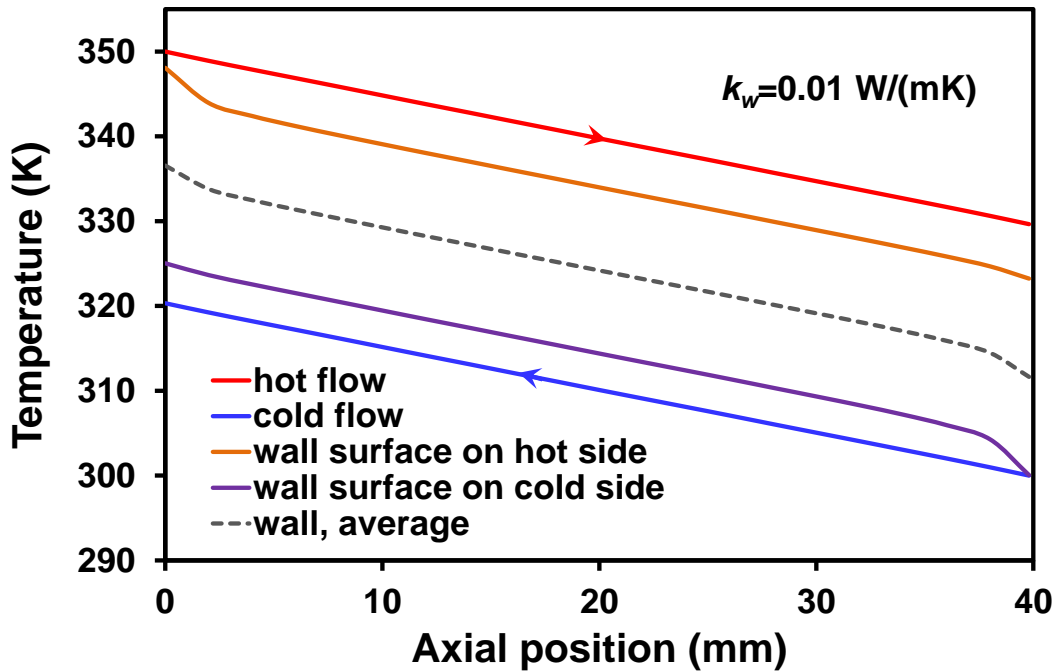


Figure 8-6: Temperature contour on the left vertical symmetric wall ($A_1J_1A_2J_2$) for three different thermal conductivities of partition wall.

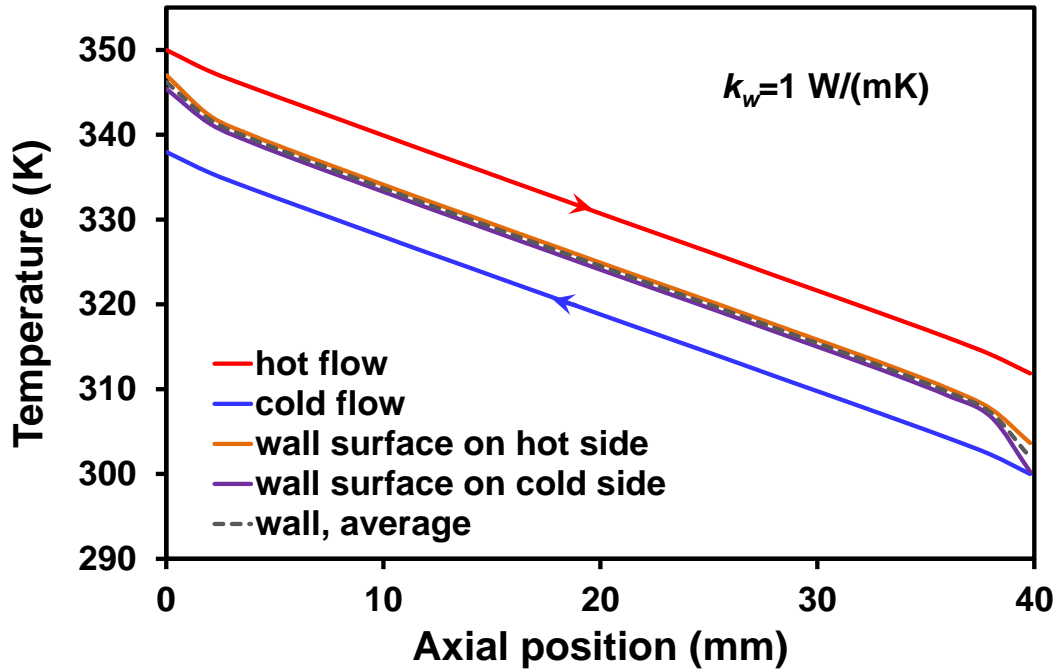
Figure 8-7 compares the axial temperature distribution in the double-layered microHEX with partition foils of quite different values of thermal conductivity. The fluid temperature is the mean local bulk temperature and the wall temperature is averaged on the local cross sections. It can be noticed that with foil of very low thermal conductivity (0.01 W/(mK)), the heat transfer from the hot fluid to the cold fluid tends to be “blocked” by the partition wall. The temperature difference

between the upper and lower surfaces of the partition wall is significantly large across a mere thickness of 100 μm . Figure 8-7(b) shows a more favorable case in which both flows experience a large temperature change from inlet to outlet. With moderate thermal conductivity the partition foil does not act as a thermal barrier between hot and cold fluids any more.

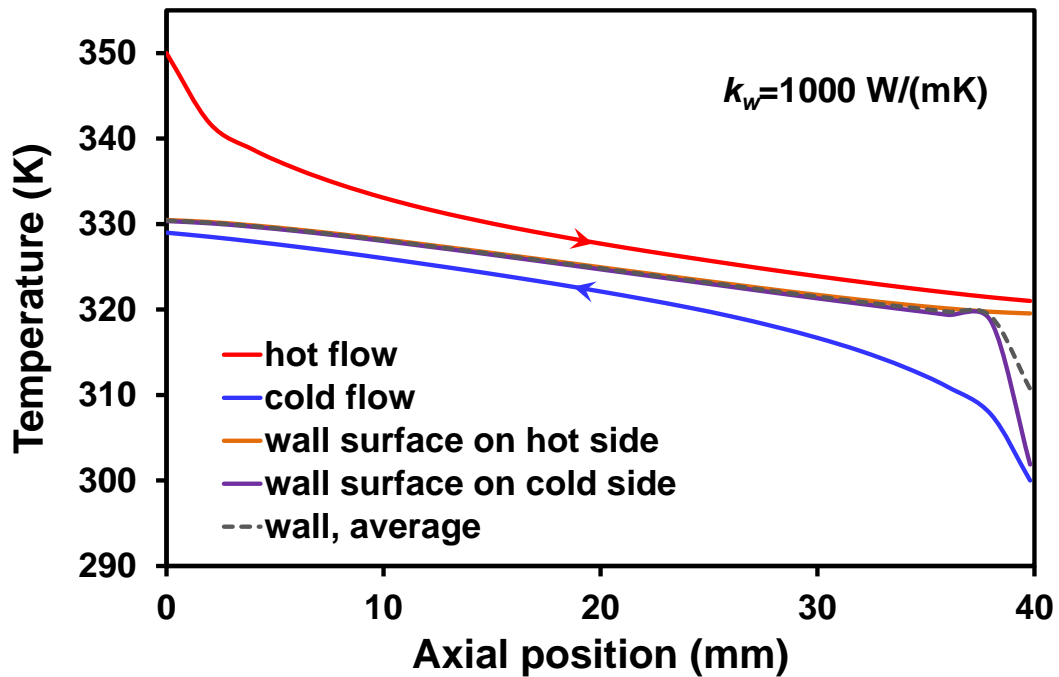
However, this does not necessarily mean that the larger the thermal conductivity of the partition wall, the better the heat exchanger performance. Numerical simulation has been done for thermal conductivity at the magnitude of 1000 W/(mK). Such highly conductive material may also be found in laboratory and industry, such as diamond or diamond-like carbon, graphene and carbon nanotubes. If such material would be used to manufacture a micro heat exchanger, the axial temperature distribution would be similar to that plotted in Figure 8-7(c). Specifically, the axial temperature gradient in the partition wall is greatly reduced due to very strong axial heat conduction in the solid wall. Moreover, the bulk temperature of the fluids is far from being linear due to the axial variation of the heat flux exchanged.



(a)



(b)



(c)

Figure 8-7: Axial temperature distribution for the countercurrent double-layered microHEX with partition foil made of different solid materials (different thermal conductivity).

Figure 8-8 shows the axial trend of local overall heat transfer coefficient for a countercurrent double-layered microHEX with a partition foil with three different values of thermal conductivity corresponding to the three cases in Figure 8-7. It is evident that for microHEX with a foil made of material with very low thermal conductivity ($k=0.01$ W/(mK)), the value of the overall heat transfer coefficient is constant in the axial direction. When the thermal conductivity of the partition foil is increased to 1 W/(mK), the distribution of overall heat transfer coefficient becomes not constant at the microchannel inlet region and outlet region, and the value of overall heat transfer coefficient in this case is almost four times larger than that in the case of the partition foil conductivity equal to 0.01 W/(mK). On the contrary, if the foil is made of material with the value of thermal conductivity equal to 1000 W/(mK), the value of the overall heat transfer coefficient decreases noticeably from the inlet all the way to the outlet of the microchannel due to very strong wall axial conduction in this case. More significantly, an increase of partition foil thermal conductivity from 1 to 1000 W/(mK) does not improve the average value of the overall heat transfer coefficient at all.

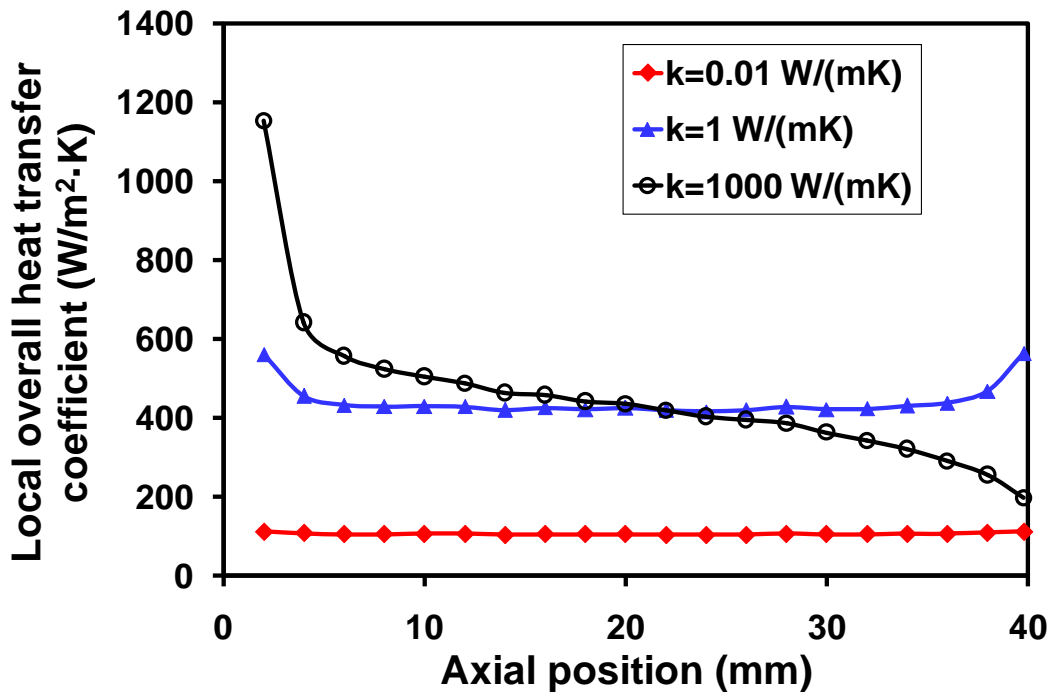


Figure 8-8: Axial distribution of overall heat transfer coefficient for a countercurrent double-layered microHEX with partition foil made of different materials.

8.2.3 Effectiveness of the double-layered microHEX

Based on the temperature obtained from numerical simulation, the values of heat exchanger effectiveness can be calculated. The effectiveness of the double-layered microHEX is plotted in Figure 8-9 over a very wide range of thermal conductivity of partition wall. It can be found that at extremely low wall thermal conductivity the effectiveness tends to be zero, because the heat flux across the partition wall is almost zero under this condition. As the thermal conductivity increases, the thermal barrier between the hot and cold flows becomes lower and more heat can be exchanged. However, after a certain value of thermal conductivity, the heat exchanger effectiveness begins to decline if the thermal conductivity continues to increase. This is due to the strong axial conduction activated along the partition wall, which tends to reduce the temperature gradient in flow direction.

In addition, it is interesting to notice that the slope of the curve obtained for very large values of the wall thermal conductivity is steeper than that obtained for low values of thermal conductivity. This is because at very low thermal conductivity, the heat flux across the partition foil is mainly blocked by the large wall thermal resistance, which is inversely proportional to the thermal conductivity. When the conductivity increases, the thermal barrier across the wall is reduced. However, after a certain large value of thermal conductivity, the thermal resistance becomes so small that further increase of conductivity almost does not influence the effect due to this thermal barrier. Meanwhile, the axial heat conduction gradually becomes significant as the thermal conductivity continues to increase. Axial conduction tends to reduce the temperature difference in the wall. Thus, the temperature difference in the flow is gradually reduced as thermal conductivity increases.

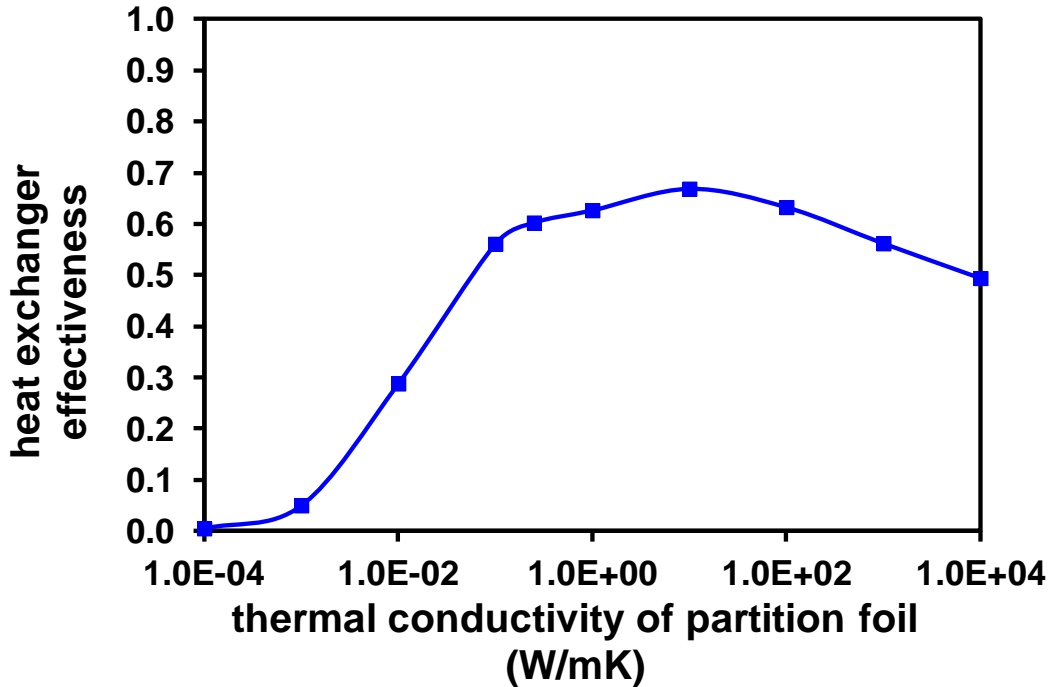


Figure 8-9: Heat exchanger effectiveness for a double-layered microHEX as a function of partition wall thermal conductivity at $Re=550$ (countercurrent flow arrangement).

The influence of operating mass flow rate on heat exchanger effectiveness is also studied by using the numerical simulation. The results obtained for a countercurrent double-layered microHEX are compared in Figure 8-10 for Re equal to 550, 1100 and 1600, which respectively correspond to balanced mass flow rates of 1.0, 2.0 and 3.0 kg/h. It is evident that as the mass flow rate increases, the microHEX effectiveness is reduced, which confirms the trend observed in the experimental data reported in the previous chapter. This reduction is more gradual at larger mass flow rate by comparing the three curves for the same thermal conductivity.

More importantly, at large wall thermal conductivity the curves tend to flatten out for large mass flow rate. This fact can be explained by recalling the discussion presented in Section 7.4.2. The axial conduction parameter is inversely proportional to the Reynolds number (and to mass flow rate). As a result, at large mass flow rates the influence of axial conduction is lower even if the thermal conductivity of partition foil is large. Therefore, the heat exchanger effectiveness is less dependent on foil conductivity at larger mass flow rate.

In addition, it should be mentioned that at $Re=1600$, the convergence of the computational results obtained by imposing a wall thermal conductivity of 10^4 W/(mK) was problematic. Converged results could not be obtained regardless of what solution methods used or the number

of iteration and values of under-relaxation factors applied in the computation. For this reason, the effectiveness for $Re=1600$ with a wall thermal conductivity equal to 10^4 W/(mK) is missing in Figure 8-10.

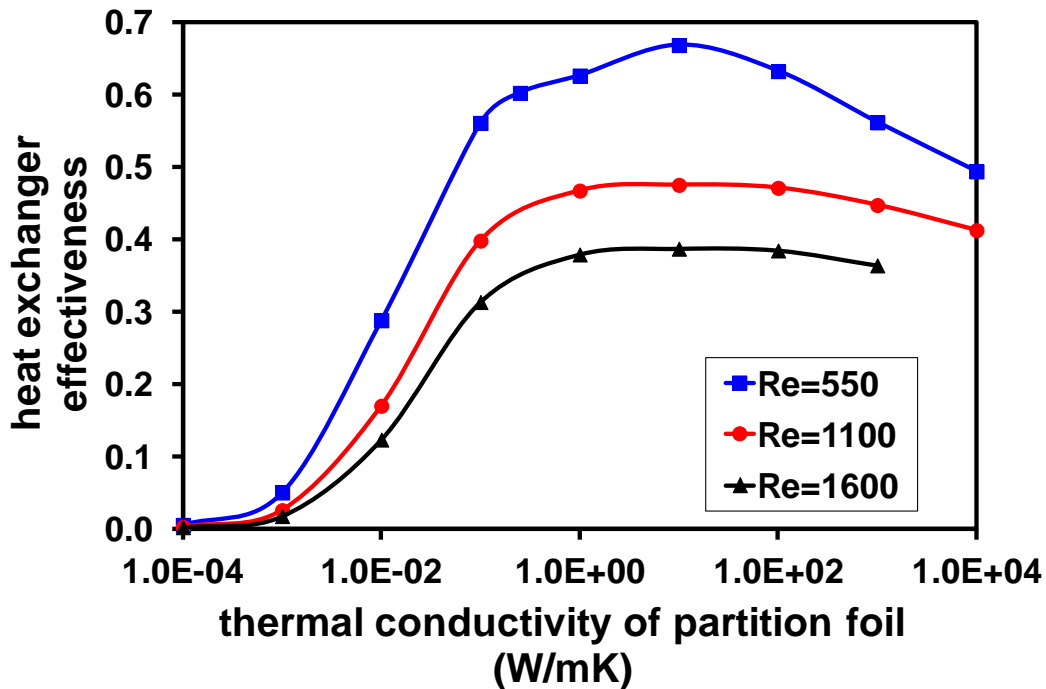


Figure 8-10: Heat exchanger effectiveness as a function of partition wall thermal conductivity at different Reynolds numbers (countercurrent flow arrangement).

The thickness of the partition foil also influences the thermal performance of the microHEX, as already evidenced by the large amount of experimental data presented in the previous chapter. In order to check this point numerically, the geometry of the numerical model was carefully modified in order to impose a thickness of the partition foil equal to 100, 150 and 500 μm . The simulation results are shown in Figure 8-11. It can be noted that an increase in the partition foil thickness generally reduces the heat exchanger effectiveness throughout the whole range of partition foil thermal conductivity.

However, the mechanism in the reduction of effectiveness at low thermal conductivity (increasing arm of the curve, $k < 10$ W/(mK)) is completely different from that at high thermal conductivity (decreasing arm of the curve, $k > 10$ W/(mK)) for various partition foil thickness. At low values of thermal conductivity, the axial conduction does not play a role and the reduction in effectiveness is caused by the increased value of thermal resistance across the foil. At large thermal conductivity, the thermal barriers due to the partition foil becomes negligible but, axial

conduction, which has a negative effect on effectiveness, becomes predominant. An increase of the foil thickness raises the value of wall axial conduction parameter (see Eq. (7.17)) and consequently reduces the heat exchanger effectiveness.

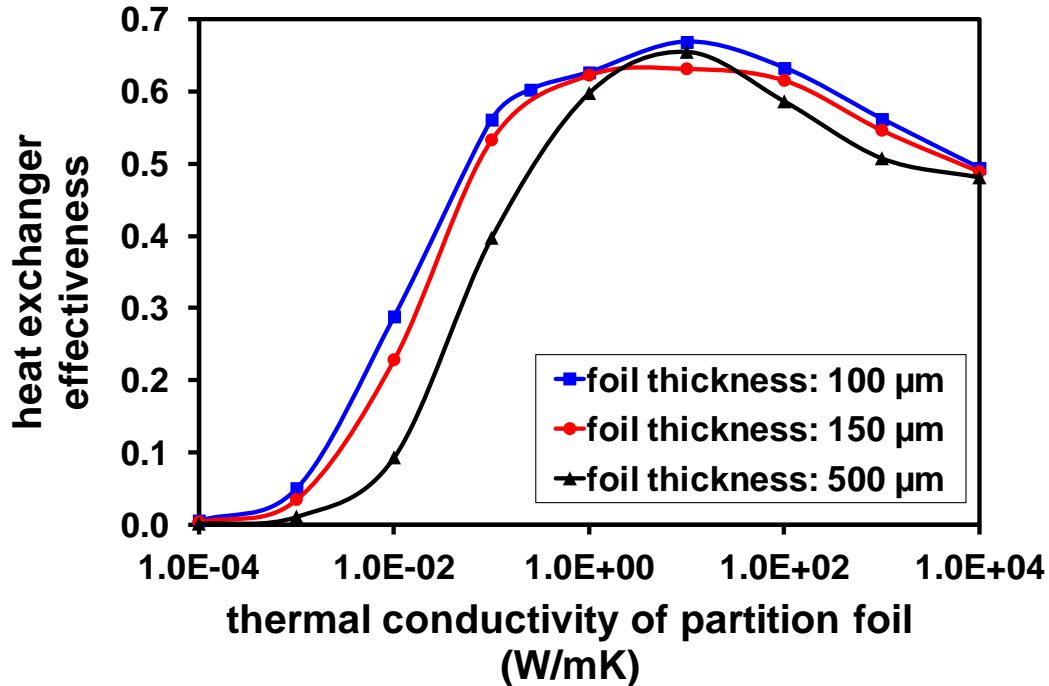


Figure 8-11: Heat exchanger effectiveness as a function of partition foil thermal conductivity with different foil thicknesses (countercurrent flow arrangement).

Besides countercurrent flow, the influence of partition foil thermal conductivity on heat exchanger effectiveness for a cocurrent double-layered microHEX was also numerically investigated for an imposed balanced mass flow rate of 1.0 kg/h. The numerical results are shown in Figure 8-12. When the thermal conductivity of the partition foil is low, the heat exchange between hot and cold flows is mainly blocked by the large thermal resistance of the partition foil and, as a consequence, the microHEX effectiveness is very low. By increasing the thermal conductivity of the partition foil, the heat exchange between the hot and cold gas can be improved. However, the improvement of the heat transfer disappears when the foil thermal conductivity becomes larger than 1 W/(mK). As explained in the previous chapter during the discussion of the experimental data obtained for a co-current microHEX, when the thermal conductivity is sufficiently large, the conjugate effects due to the axial conduction along the partition foil are completely negligible because the partition wall tends to have an uniform temperature along the micro heat exchanger core. Therefore, in this case an increase of the

thermal conductivity of the partition foil does not lead to a decrease of the microHEX effectiveness as in the case of the counter-current arrangement.

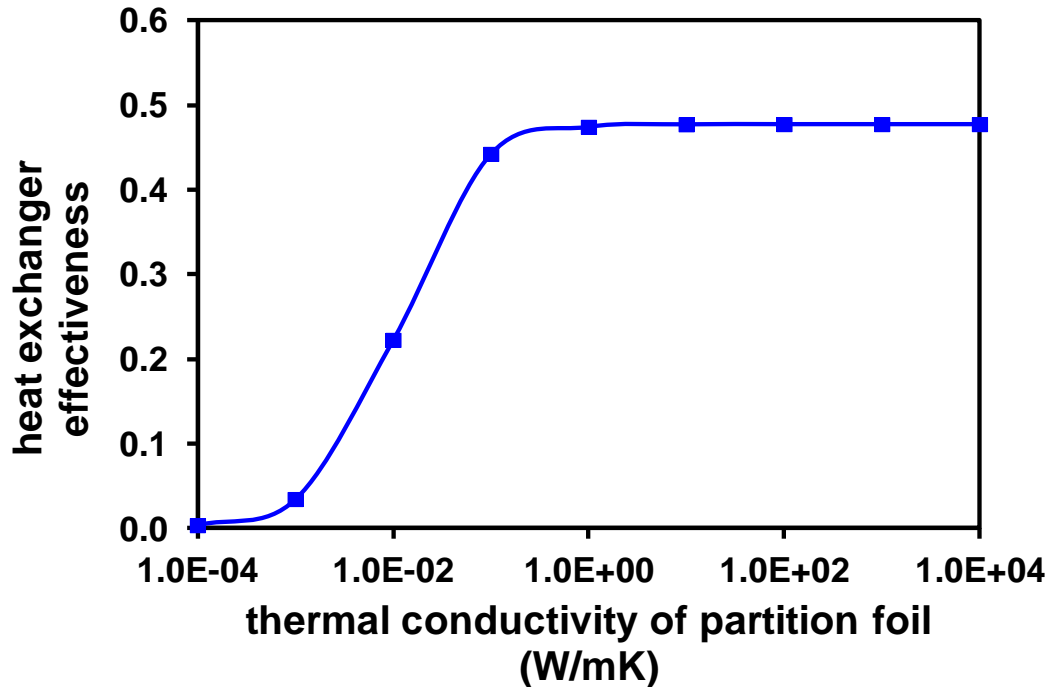


Figure 8-12: Heat exchanger effectiveness versus partition wall thermal conductivity for cocurrent flow arrangement at $Re=100$.

8.2.4 Comparison between simulation and experimental data

In this section the experimental data obtained for a double-layered microHEX with countercurrent flow arrangement presented in Chapter 7 are compared with the numerical data obtained with a 3D model of the microHEX. The mass flow rate is fixed at 1.0 kg/h and the thickness of partition foil is imposed to be equal to 100 μm . In order to reply numerically the cases in which the partition foils SS100, AL100 and C100 have been tested, the thermal conductivity of the foil has been imposed to be equal of 15, 150 and 400 $\text{W}/(\text{mK})$ in the numerical model. The comparison between the numerical results and the experimental data is plotted in Figure 8-13. It can be noted that the simulation roughly predicts the experimental trend, but with a certain underestimation in effectiveness, especially at large values of the wall thermal conductivity.

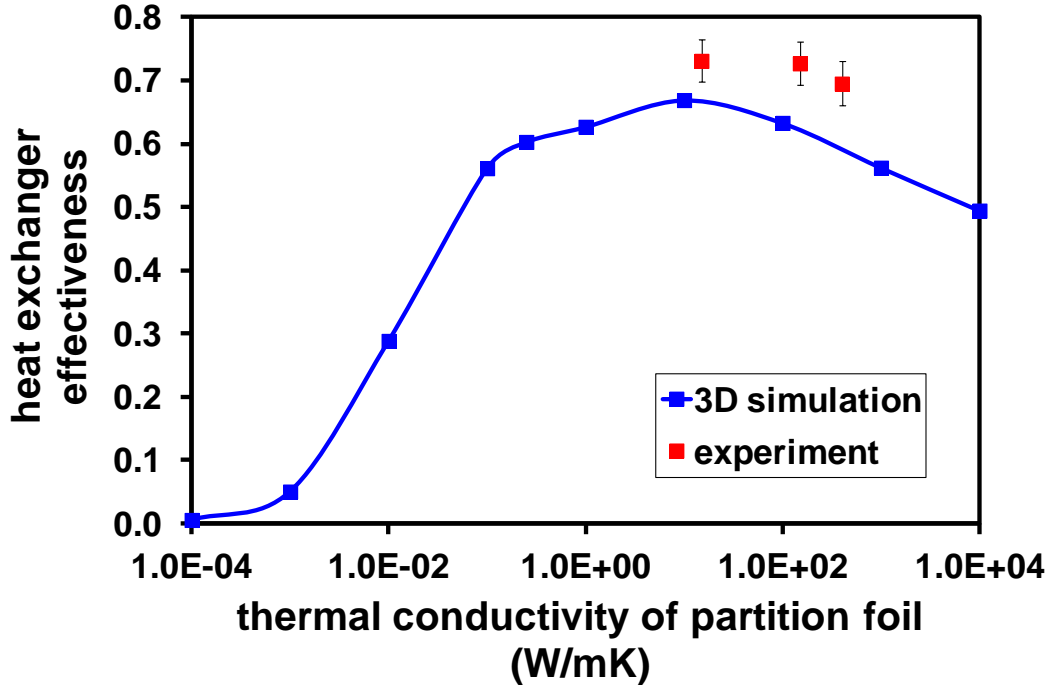


Figure 8-13: Comparison of heat exchanger effectiveness between simulation and experiment for a countercurrent double-layered microHEX with a balanced mass flow rate of 1.0 kg/h.

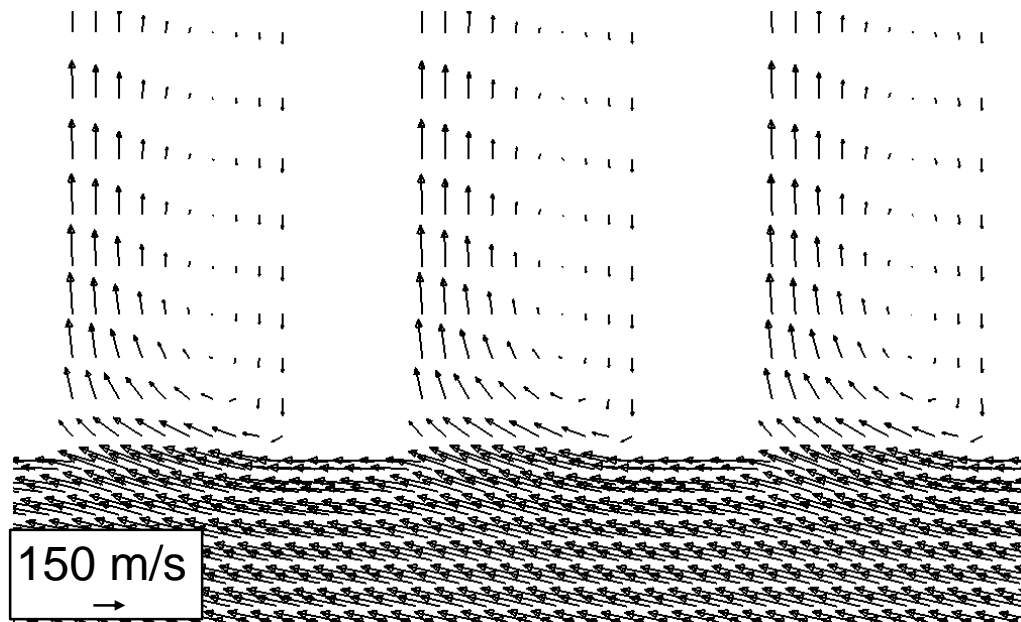
In order to explain this difference the 3D complete numerical model of a full layer by considering also the manifold connections (as shown in Section 6.5) is used in order to calculate the gas velocity distribution on the symmetric plane of the layer. Figure 8-14 shows the velocity vectors at different locations (inlet and outlet of the microchannels) of the layer in the case of an imposed feeding pressure of 500 kPa. By observing Figure 8-14(a), it can be found that in the distributing manifold very close to the inlets of microchannels, the flow velocity is not normal to the inlet cross section of the microchannels at all. It should be emphasized that this situation is quite typical for such distributing manifolds, as discussed in Chapter 6. Moreover, it is evident that in the entrance region of the microchannels, where the velocity vectors are forced to change direction due to the strong confinement of the solid walls, a backflow is generated and, as a consequence, vortices are present in the first part of the entrance region of the microchannels, as it can be clearly noticed in Figure 8-14(a). This effect linked to the presence of the manifolds is not taken into account in the 3D numerical simulation of the double-layered microHEX which has been used in order to obtain the results plotted in Figure 8-13. As explained in section 8.2, the 3D model considers only half of two microchannels and it is assumed that the gas flow enters the microchannels with a uniform velocity perpendicular to the inlet cross section.

The vortexes caused by the flow velocity re-distribution enhance the convective heat transfer coefficient in the entrance region of the channels and this fact, which is not taken into account in the numerical model used to obtain the data of Figure 8-13, can justify the underestimation of the effectiveness obtained numerically compared to the experimental data.

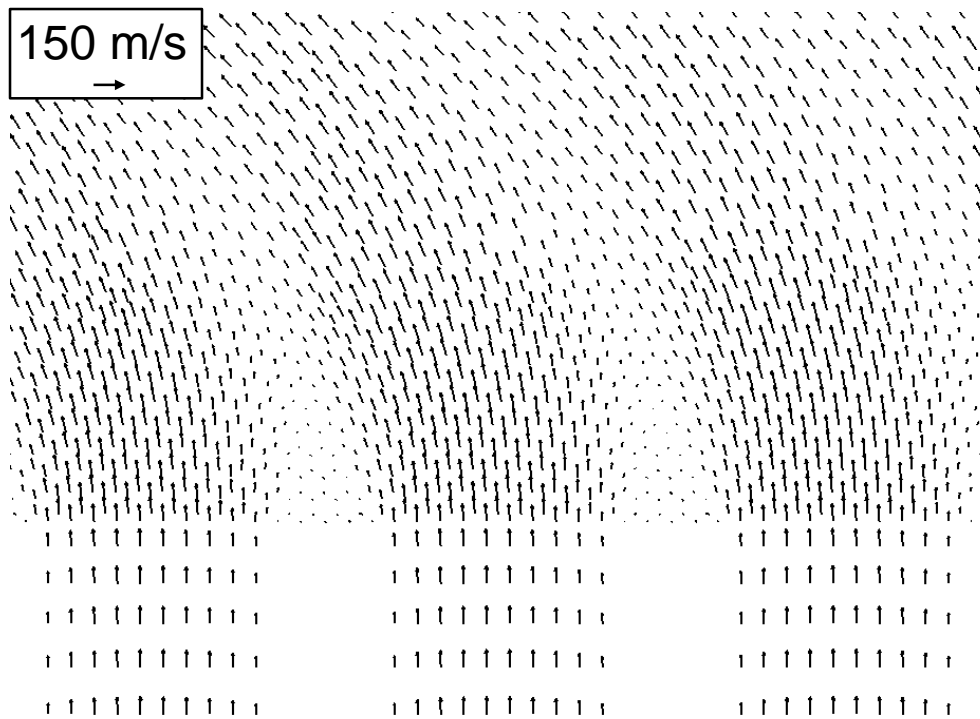
The results plotted in Figure 8-14(a) demonstrate that the presence of the manifolds can result in a series of non negligible effects which are difficult to account for in a numerical model in which only the parallel microchannels are considered. In other words, all the results of this thesis tend to demonstrate that in order to reproduce the experimental data obtained by testing a microHEX, great care must be taken in order to include and model the non-negligible effects which occur in experiment. As stressed in Chapter 6, the presence of the manifolds (especially the inlet manifold) has a strong impact on the mass flow rate distribution among the parallel channels and also on the velocity profiles within the channels.

After this first entrance region of the microchannels, the flow is laminarized and fully developed. Figure 8-14(b) shows the velocity vectors at the outlet section of microchannels and the collecting manifold. It is evident that at the outlet section, the velocity distribution keeps the classic parabolic profile. Therefore, at microchannel outlet section, the 3D model of double-layered microHEX should be able to simulate the real flow and heat transfer situation in experimental tests.

Of course, another reason responsible for the deviation in heat exchanger effectiveness can be the flow maldistribution among the microchannels, which occurs in practical tests but is neglected in the 3D numerical model. In fact, even if the test rig has been optimized in terms of flow distribution in the design phase, as described in Chapter 6, the influence of flow maldistribution cannot be considered completely negligible.



(a) microchannel inlets and part of distributing manifold



(b) microchannel outlets and part of collecting manifold

Figure 8-14: Velocity vectors at connecting manifolds and central microchannels (channel index: 66-68 out of 133) of the double-layered microHEX (feeding pressure at 500 kPa).

8.3 Simulation of the multi-layered microHEX

As shown in Section 8.1 not only the double-layered microHEX configuration has been studied numerically but also the complete multi-layered microHEX has been considered in order to put in evidence if the results obtained for a double-layered microHEX can be useful to predict what happens in a multi-layered device. The thermal boundary condition applied in the multi-layered model is slightly different from that adopted in the double-layered model. Because of the symmetry in both height and width in the multi-layered model, only a quarter of the microchannel was simulated for both hot flow and cold flow in order to reduce the computational cost. In addition, the solid part (both side walls and partition wall) of the multi-layered one is always made of homogeneous material.

In this section, the numerical results on a multi-layered microHEX will be discussed.

8.3.1 Temperature distribution

The temperature distribution on the right symmetric plane along the full length of microchannels is displayed in Figure 8-15 for three different magnitudes of wall thermal conductivity. The results have been obtained for a countercurrent arrangement and for a balanced mass flow rate of 1.0 kg/h.

The results plotted in Figure 8-15 highlight that, similar to the case of the double-layered microHEX, the temperature distribution highly depends on the foil thermal conductivity. At low thermal conductivity (Figure 8-15 (a)), the large thermal barriers prevents the heat exchange between the two flows. For a thermal conductivity equal to 1 W/mK (Figure 8-15 (b)), both flows experience large temperature change while the axial temperature difference in the foil is large, which means that the axial conduction along the wall is negligible. At very large values of the foil thermal conductivity (Figure 8-15 (c)), the temperature change of the flows become smaller again and the axial temperature gradient in the partition foil is very small.

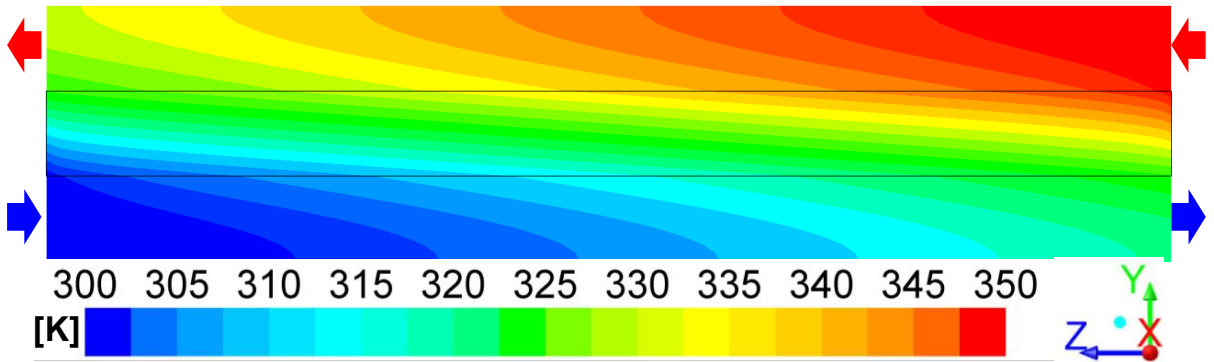
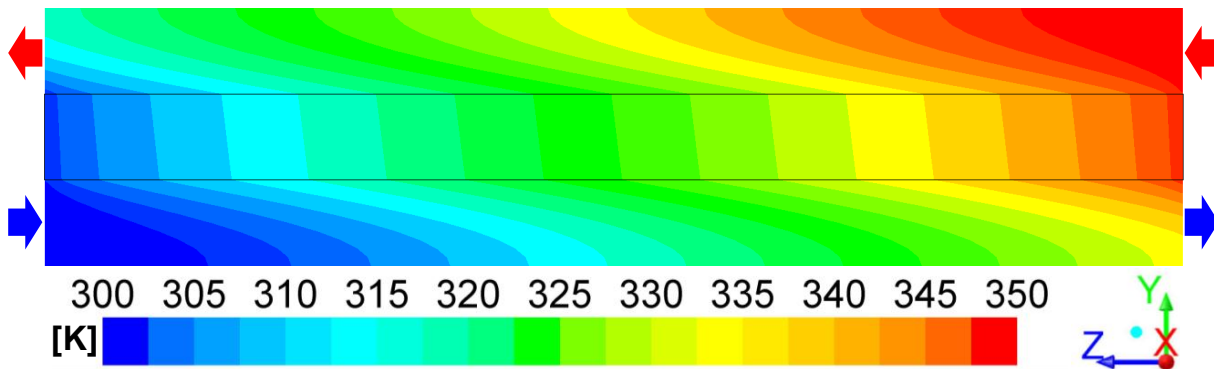
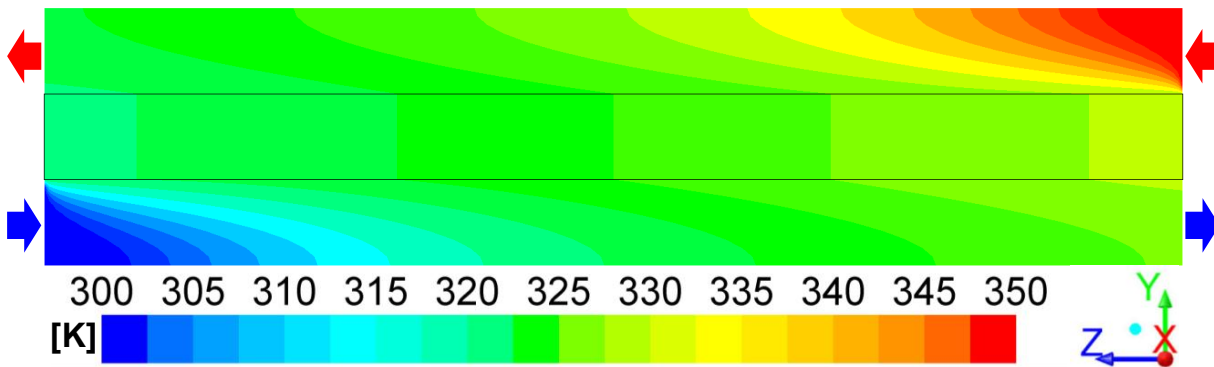
(a) $k=0.01 \text{ W/(mK)}$ (b) $k=1 \text{ W/(mK)}$ (c) $k=1000 \text{ W/(mK)}$

Figure 8-15: Temperature contour on the right vertical symmetric plane ($C_1H_1C_2H_2$) for three different thermal conductivities of solid walls (Black lines indicate the surfaces of solid walls).

Figure 8-16 shows the temperature contours on the left symmetric plane of the 3D model, which is the symmetric plane of the solid walls. For a low thermal conductivity of the partition wall, both lateral and axial temperature gradients are quite large due to its large thermal

resistance. For a thermal conductivity equal to 1 W/mK, the axial temperature difference is still large but the temperature difference across the partition foil is small due to the small thickness of the foil. When the wall thermal conductivity is extremely large, the wall temperature distribution tends to be uniform both in axial direction and across the foil.

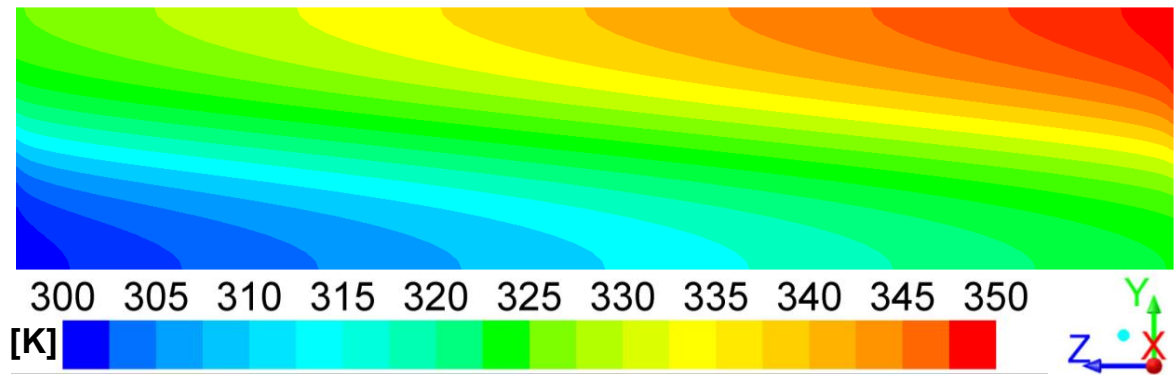
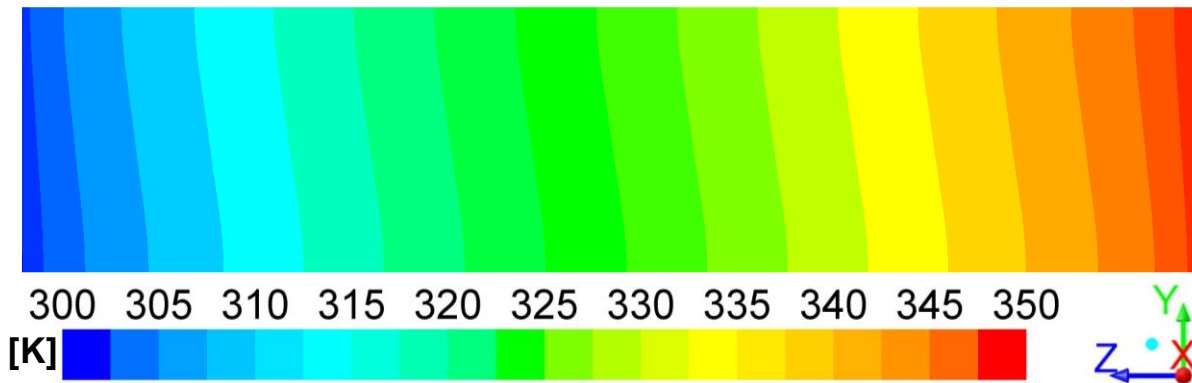
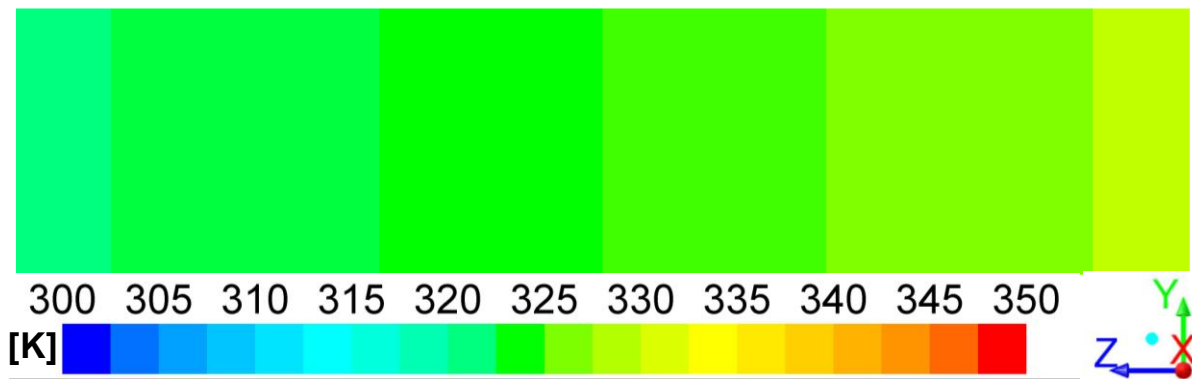
(a) $k=0.01$ W/(mK)(b) $k=1$ W/(mK)(c) $k=1000$ W/(mK)

Figure 8-16: Temperature contour on the left vertical symmetric wall ($A_1J_1A_2J_2$) for three different thermal conductivities solid walls.

8.3.2 Effectiveness of the multi-layered microHEX

A 3D simulation has also been carried out for the multi-layered microHEX in order to check the effect of the thermal conductivity of the partition foil on the effectiveness of the microHEX. The microHEX effectiveness of a countercurrent multi-layered heat exchanger with balanced mass flow rates is calculated as a function of the partition foil thermal conductivity, as shown in Figure 8-17. This is the first time, to the best of the author's knowledge, that the effectiveness-conductivity curve obtained by Stief *et al.* [147] by means of a simplified calculation based on a program developed more than a decade ago is checked by using a more accurate numerical model. The curve in Figure 8-17 is comparable to that obtained by Stief *et al.* [147], but the curve obtained with the present numerical simulation is characterized by a flatter region close to the maximum value of effectiveness in comparison with that made by Stief. In addition, the model proposed by Stief *et al.* [147] was based on a thickness of the partition foil of only 12 μm , which is too fragile to be applied in lab researches and engineering fields in terms of mechanical stability. The curve of Figure 8-17 on the contrary, is referred to a partition wall thickness of 100 μm which is more practical and applicable to various operative conditions.

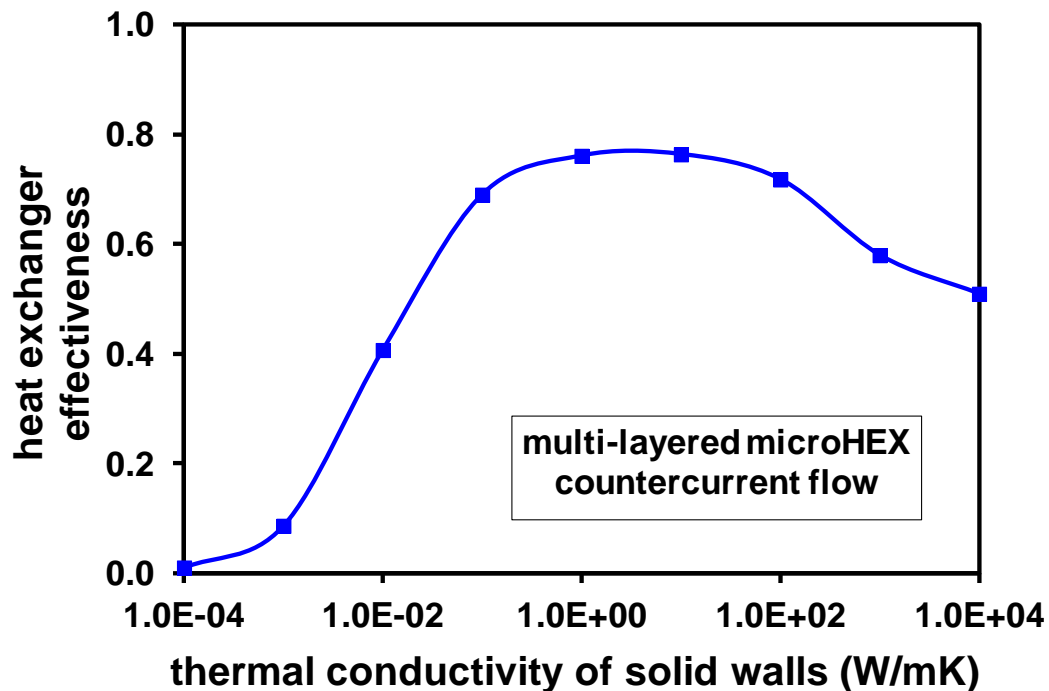


Figure 8-17: Heat exchanger effectiveness as a function of wall thermal conductivity for the multi-layered microHEX with countercurrent flow.

It is important to stress that the curve of Figure 8-17 is similar to the curves obtained in the previous sections of this chapter for a double-layered microHEX.

In each case, except for the case of the cocurrent flow arrangement, the effectiveness is characterized by a maximum which is due to the trade-off between the partition foil thermal resistance (very strong for low thermal conductivity) and the wall axial heat conduction (which prevails for large thermal conductivity). This means that it is always possible to optimize the microHEX effectiveness by selecting a specific material for the partition foil.

Of course, the heat exchanger effectiveness is not merely influenced by the thermal conductivity of the partition foil but it is also related to the thermal properties of the working fluids. In other words, the same micro heat exchanger may have completely different performance if the working fluid is changed from gas to liquid.

In order to verify this point a numerical simulation has also been carried out for the same geometry of the multi-layered microHEX by considering water as working fluid.

The comparison between the results obtained with water and with air is helpful to further understand the unique characteristics of gas flow microHEXs. Figure 8-18 compares heat exchanger effectiveness versus the thermal conductivity of the partition foil for both air flow and water flow. It is interesting to know that the range of conductivity corresponding to the maximum effectiveness is greatly shifted if the fluid is changed from air to water. For example, if glass (thermal conductivity around 1 W/(mK)) is used to manufacture the micro heat exchanger, the device will have an effectiveness of 78% with air flow. However, if water is used as working fluid, the effectiveness of the device reduces to only 50%.

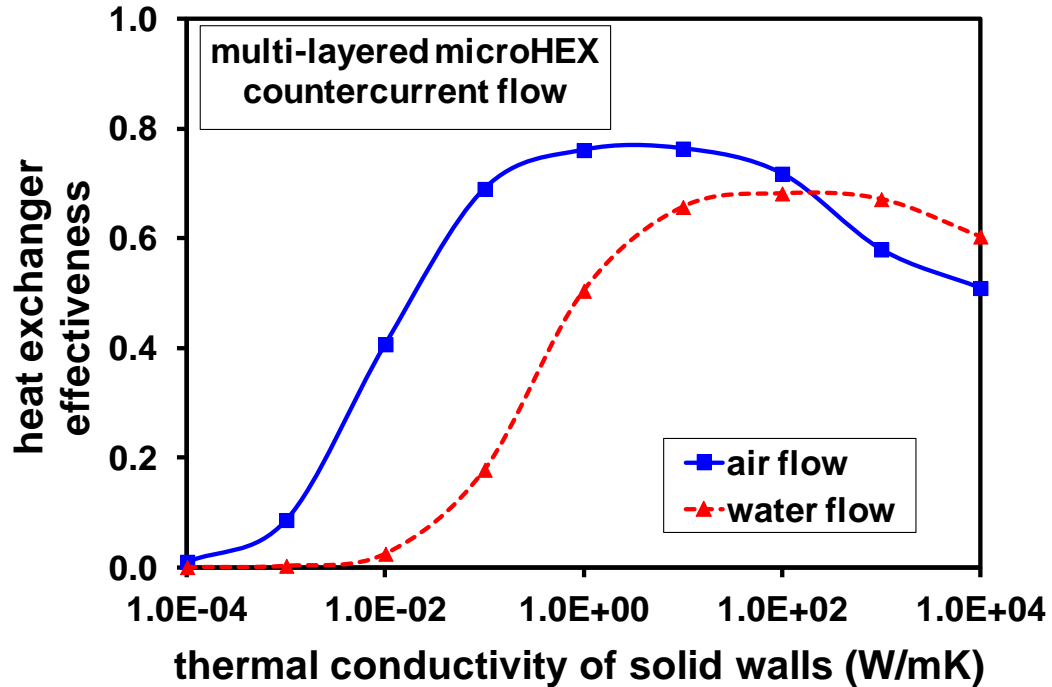


Figure 8-18: Heat exchanger effectiveness of a counter-current multi-layered microHEX with balanced mass flow rates as a function of wall thermal conductivity for air and water flows.

The difference in terms of effectiveness between the double-layered and the multi-layered microHEX is shown in Figure 8-19 for a counter-current flow arrangement with balanced mass flow rates.

For this comparison, a Reynolds number through the parallel microchannels equal to 550 for both devices has been set in the numerical simulation. It is evident that the difference in terms of effectiveness is very small for partition foils with very low or very high thermal conductivity. However, in the region in which the effectiveness is close to its maximum value, which is the region where the partition foil thermal conductivity is between 0.1 W/(mK) and 100 W/(mK), the difference in terms of heat exchanger effectiveness becomes fairly large. In this range, the effectiveness of the double-layered device is around 10% lower than that of the multi-layered one. In this comparison, the Reynolds number, the working fluid (air), the dimension and material of partition foil in both devices are exactly the same.

The only difference between the double-layered and the multi-layered 3D models is the solid material of the microchannel side wall, which is fixed as PEEK in the double-layered device for various values of conductivity of the partition foil but is the same as the material adopted for the partition foil in the multi-layered device. In addition, due to the different geometries of both

devices, the thermal boundary conditions are not exactly the same. In the multi-layered device, the top and bottom boundaries of the simulated element are symmetric due to the periodical stack of multi layers in height direction. However, in the double-layered device, there are only two flow layers which are packaged between thick plates with low thermal conductivities and further wrapped with thermal insulation material. Therefore, the top and bottom of the simulated element are assumed as adiabatic. As a result, it can be concluded that the thermal performance of the multi-layered microHEX is better than that of the double-layered device.

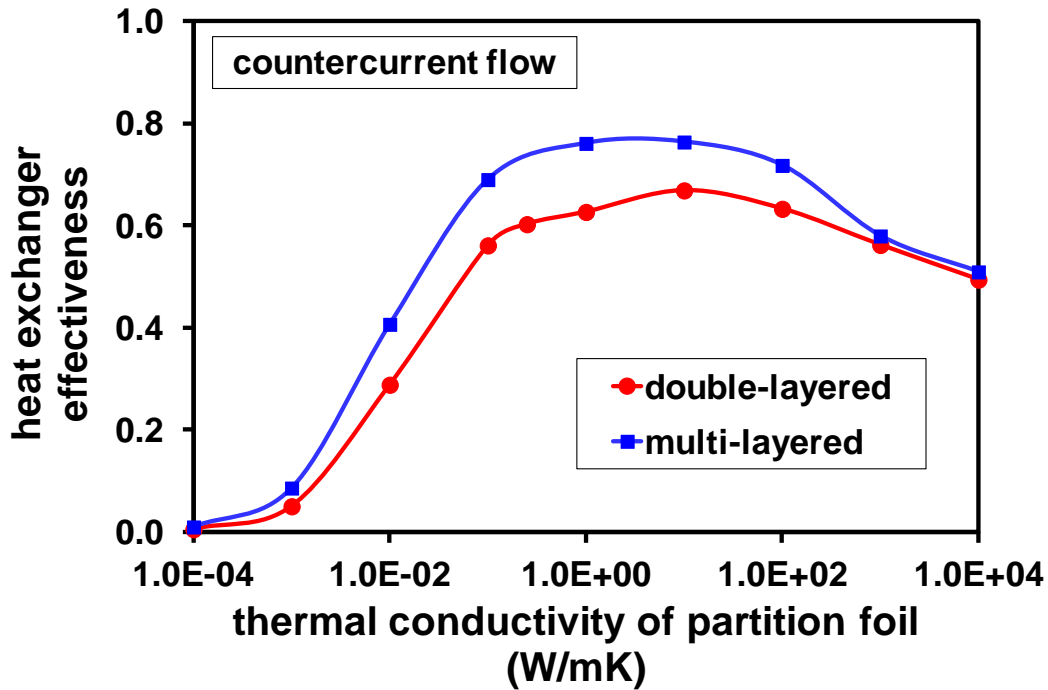


Figure 8-19: Comparison on thermal performance between double-layered and multi-layered microHEXs for countercurrent flow arrangement.

Figure 8-20 compares the thermal performance of a double-layered microHEX with that of a multi-layered microHEX by considering a cocurrent flow arrangement. Similar to the case of a countercurrent flow arrangement, the multi-layered microHEX is characterized by values of effectiveness larger than the values obtained for the double-layered microHEX due to wall materials and operating boundary conditions.

For values of the wall thermal conductivity very low (lower than 0.1 W/(mK)), the difference in terms of effectiveness between the two devices is low as in the case of the countercurrent flow arrangement. For wall thermal conductivity larger than 1 W/(mK), the conductivity of the

partition foil does not influence the effectiveness of both devices any more due to the uniform temperature along the partition foil in the axial direction..

In the case of the multi-layered microHEX, when the foil thermal conductivity becomes larger than 1 W/(mK) the effectiveness tends to the asymptotic value of 50%. This result is in agreement with the expected asymptotic value of the effectiveness of a cocurrent heat exchanger when NTU tends to ∞ (see Eq. (7.28)).

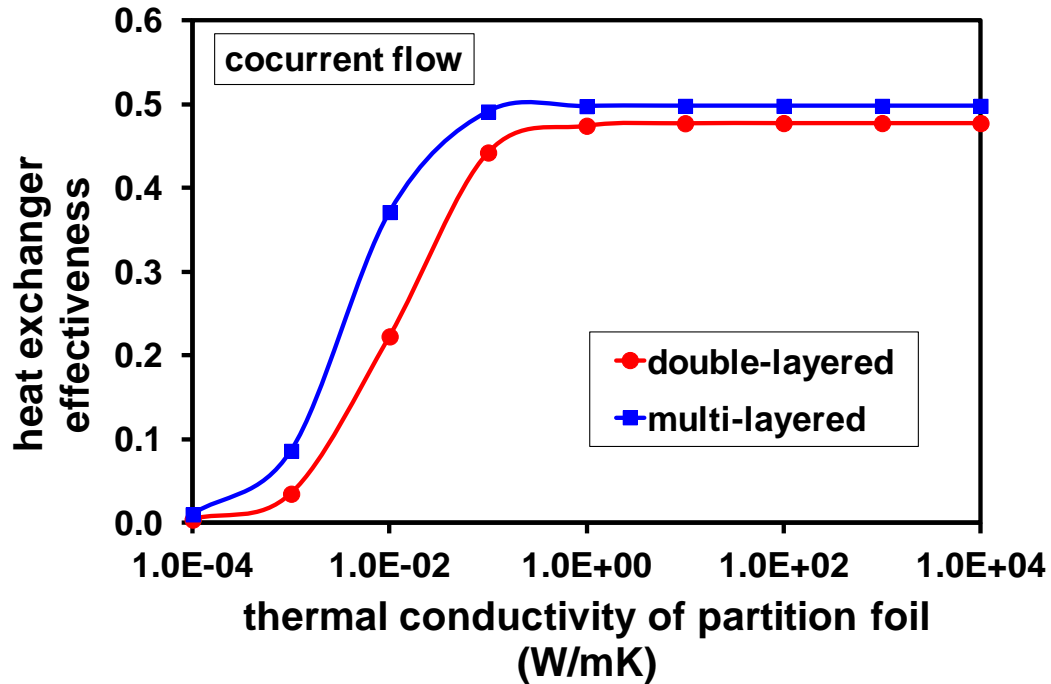


Figure 8-20: Comparison on thermal performance between double-layered and multi-layered microHEXs for cocurrent flow arrangement.

8.4 Conclusions

In this chapter the performance of the gas-to-gas microHEX has been numerically characterized by 3D computational simulation of a double-layered micro device and a multi-layered micro device.

The numerical data obtained from the double-layered microHEX have uncovered the typical temperature distribution inside both the flows and the solid walls of the device, which is generally challenging to obtain by experimental means. More specifically, for partition foil with low thermal conductivity ($k=0.01$ W/mK), the axial distribution of both hot and cold flows is quite linear but the local temperature difference between the two flows is very large, which

indicates very low heat exchange coefficient. When the thermal conductivity of the partition foil is moderate, the axial temperature distribution of both flows is still linear while the overall heat transfer coefficient of the microHEX is greatly increased. For very high thermal conductivity of the partition foil, the axial distribution of fluid temperature becomes strongly non-linear and the local heat transfer coefficient is not constant any more in axial direction. Moreover, the results highlight that the microHEX with partition wall of very large thermal conductivity does not increase the value of the overall heat transfer coefficient of the device.

The computational results obtained over an extensive range of the partition foil thermal conductivity (10^{-4} – 10^4 W/(mK)) evidence that for countercurrent flow arrangement, the optimal effectiveness can be achieved in the double-layered microHEX with partition foil thermal conductivity between 1 and 100 W/(mK), and in the multi-layered micro device with partition foil thermal conductivity from 0.1 to 100 W/(mK). On the contrary, in the case of cocurrent flow arrangement the value of effectiveness becomes stabilized at the maximum value when the partition foil thermal conductivity is larger than 1 W/mK, which is true for both the double-layered and the multi-layered devices.

In addition, the influence of other parameters on the thermal performance of the microHEX, such as mass flow rate, thickness of the partition foil and thermal properties of the fluid, have been numerically investigated in this chapter. The results confirm that an increase in the mass flow rate reduces the value of the microHEX effectiveness, which has also been evidenced by experimental data presented in Chapter 7. The range of partition foil thermal conductivity linked to optimal effectiveness can be narrowed by the increase in partition foil thickness, while a change in fluid thermal properties will shift the peak of the effectiveness-thermal conductivity curve.

The comparison between the numerical data and the experimental results underlines that the numerical model is able to predict the experimental trend of effectiveness as a function of partition foil thermal conductivity. The difference between the numerical and experimental values of effectiveness is mainly due to the vortexes generated in the manifolds connected to the parallel microchannels.

9 Conclusions and Outlook

9.1 Conclusions

This thesis deals with the analysis of the characteristics of gas forced convection through microchannels. Experimental investigation has been carried out by testing single microtubes, and then the experimental analysis has been extended to more complex microdevices, obtained by using a large number of parallel microchannels, as in the microHEXs. The analysis of the behavior of gas flow and heat transfer through single microtubes and through microHEXs has been conducted throughout this thesis by means of both experiment and simulation. The main conclusions of this thesis are summarized as follows:

In Chapter 2, the latest techniques developed for micro scale measurements of channel geometry, pressure, temperature and mass flow rate are critically reviewed by highlighting their advantages and restrictions when applied to gas micro flow and heat transfer. Meanwhile, the measurable ranges and typical uncertainties of these techniques are summarized by tabulating the original data quoted from various researchers.

The propagations of uncertainties for friction factor and Nusselt number have been analyzed in details in Chapter 3 in order to specify the influence of the accuracy of each single parameter in a specific test. It has been emphasized by the analysis that the accuracy of microchannel diameter measurement is most significant to the accurate experimental determination of the flow friction factor; while the key point to obtain the value of Nusselt number with high accuracy lies in the accuracy of fluid outlet temperature measurement. Based on this analysis, the test and measurement can be optimized by applying appropriated measurement strategies and using more precise measurement devices.

In Chapter 4 nitrogen flows through commercial stainless steel microtubes with various inner diameters (750 μm , 510 μm and 170 μm) have been experimentally characterized in terms of flow friction factor in laminar, transitional and turbulent regimes. The experimental results verify that the conventional theory in the prediction of friction factor still hold for isothermal laminar flows through microtubes. For heated gas flow at microscale, the tests have evidenced larger values of friction factor than those of isothermal flow in laminar regime, and a larger value of correction factor to account for the heating effects has been proposed by analyzing the

experimental data. In addition, the results underline non-negligible flow compressibility effects even in laminar regime ($Re \sim 1200$), and the outlet Mach number has been found to be more accurate than the average Mach number in order to fully take into account the influence of compressibility effects on the flow friction factor.

In Chapter 5 the characteristics of gas forced convection through the same three microtubes as tested in Chapter 4 have been investigated by combining experimental tests with numerical simulation. As the total uncertainty of the Nusselt number is highly sensitive to the uncertainty of the gas exit temperature measurement, a numerical simulation suggests that great care must be taken to the design of the exit section of the microtube in order to have an accurate estimation of gas exit temperature, especially for gas flows at low Reynolds numbers and through microtubes of small inner diameters. The results underline strong conjugate heat transfer due to significant axial conduction in the solid wall, which leads to non-linear distribution of bulk temperature along the heating length under H boundary conditions. By fully considering this effect in the evaluation of the Nusselt number, the classical Gnielinski correlation has been found to be able to predict the experimental data in laminar and transitional regimes. When the flow compressibility becomes significant, larger values of the Nusselt number have been evidenced due to extra heat transfer from the wall linked to the fluid internal energy conversion.

Chapter 6 focuses on the design of a microHEX for gas flow by considering the influences of wall axial conduction, the manifold configuration and the magnitude of the operating pressure on the performance of the device. The impact of the manifold configuration on the flow distribution has been numerically examined for five types of manifold, and the one that offers the most uniform flow distribution has been applied to the present microHEX. A full layer of the microHEX has been simulated in order to obtain the distribution of mass flow rate, flow velocity and pressure inside this device under different values of feeding pressure. The analysis of the numerical results improves the accuracy of the experimental test in which the positions of pressure measurement at both inlet and outlet of the parallel microchannels are carefully determined by the simulation data so that the values of the measured pressure are representative of the average inlet and outlet pressure of the 133 microchannels.

In Chapter 7, the double-layered microHEX for gas flow has been investigated experimentally by analyzing the influences of wall axial conduction, flow arrangement, mass flow rate, thickness and thermal conductivity of the partition foil on the thermal performance of the

microdevice. The experimental results show that the distributing and collecting manifolds have much larger pressure losses than the typical pressure drop along the microchannels. This fact suggests that the fluid-dynamic design of the microHEX manifolds should be of primary importance for the optimization of the performance of such micro device.

The data obtained from the tests have evidenced strong dependence of the overall heat transfer coefficient on the thermal conductivity of the partition foil, which is especially true for the case of countercurrent and cross flow arrangement. In addition, by increasing the mass flow rate the overall heat transfer coefficient and the volumetric heat exchange rate are increased, but this meanwhile results in lower heat exchanger effectiveness. The experimental results confirm that the effectiveness of microHEX with countercurrent and cross flow arrangements is highly dependent on the axial conduction in the partition wall, while in the case of cocurrent flow arrangement the influence of wall axial conduction on the microHEX effectiveness is insignificant. The highest effectiveness of the microHEX has been achieved in the countercurrent flow arrangement while cocurrent flow arrangement leads to lowest effectiveness for the same mass flow rate. However, the difference in the effectiveness of microHEX with different flow arrangement becomes smaller at larger mass flow rate.

In Chapter 8, the thermal performance of the microHEX has been investigated by 3D numerical simulation, which reproduces the test rig configuration as well as the operating conditions applied in the previous chapter. The numerical results show the temperature distribution in both the fluids and solid walls for an extensive range of solid wall thermal conductivity. The influences of solid wall thermal conductivity, partition foil thickness, flow arrangements and operating mass flow rate on the microHEX effectiveness have been numerically investigated. It has been confirmed that the experimental trend of effectiveness as a function of partition foil thermal conductivity is in agreement with the prediction of the numerical model used in this chapter.

To conclude very briefly, firstly, the present study on gas forced convection at microscale underlines that the flow friction factor, the Nusselt number and the microHEX effectiveness determined experimentally are in agreement with the prediction of the conventional theory on the basis that the experiment is carefully designed, the measurements are accurate and the possible effects are correctly and accurately evaluated. Throughout the study in this thesis, efforts have been devoted with the aim to check the validity and applicability of both the conventional theory

and the new correlations proposed during the last decades for the analysis of the frictional behavior and the convective heat transfer of gas micro flows. The results obtained in this thesis can be used in order to give a physical explanation to some non-physical results appeared in literature by highlighting the role of the main scaling effects which can play a dominant role on the characteristics of gas forced convection in microchannels.

Then, the influence of wall axial conduction has been evidenced and emphasized as very important in most cases of gas forced convection through both microtubes and microHEXs; neglecting this point may lead to unreasonable thermal analysis of gas force convection at micro scale.

Lastly, the results obtained in this thesis demonstrate that the numerical simulation obtained by using CFD codes can be very useful in order to optimize the design of the experiments, to check the validity of the measurements, and to better understand the mechanisms of gas flow forced convection at microscale during the post-processing of the experimental data.

9.2 Future work

While the present experimental study on gas forced convection through microtubes has been extended from laminar regime to transitional and part of turbulent regimes, the research on the double-layered microHEX has been carried out under Re smaller than 2000 in general. Therefore, the double-layered device can be further investigated with turbulent flows, where the influence of flow compressibility can be important.

Further work is also foreseen on the experimental investigation of the multi-layered micro heat exchanger, which has been designed and is being microfabricated during the writing of this thesis. The results can be compared with those obtained from the double-layered device as well as the numerical data on the multi-layered model presented in this thesis.

In addition, it will be very interesting to explore numerically the influence of wall thermal conductivity on the performance of a cross flow microHEX, as the numerical models presented in this thesis focus only on countercurrent and cocurrent flow arrangements. The model on cross flow arrangement may require far more computational resource due to lack of symmetries in the geometry and boundary conditions.

Bibliography

- [1] P. Tabeling, *Introduction to microfluidics*. Oxford University Press, 2005.
- [2] M. Madou, *Fundamentals of microfabrication: the science of miniaturization*. CRC Press, 2002.
- [3] G. L. Morini, “Single-phase convective heat transfer in microchannels: a review of experimental results,” *International Journal of Thermal Sciences*, vol. 43, no. 7, pp. 631–651, 2004.
- [4] S. Colin, “Gas microflows in the slip flow regime: A critical review on convective heat transfer,” *Journal of Heat Transfer*, vol. 134, no. 2, p. 020908, 2012.
- [5] A. A. Rostami, A. S. Mujumdar, and N. Saniei, “Flow and heat transfer for gas flowing in microchannels: a review,” *Heat and Mass Transfer*, vol. 38, pp. 359–367, 2002.
- [6] G. Hetsroni, A. Mosyak, E. Pogrebnyak, and L. Yarin, “Heat transfer in micro-channels: Comparison of experiments with theory and numerical results,” *International Journal of Heat and Mass Transfer*, vol. 48, no. 25-26, pp. 5580 – 5601, 2005.
- [7] R. Dey, T. Das, and S. Chakraborty, “Frictional and heat transfer characteristics of single-phase microchannel liquid flows,” *Heat Transfer Engineering*, vol. 33, no. 4-5, pp. 425–446, 2012.
- [8] S. Kandlikar, “History, advances, and challenges in liquid flow and flow boiling heat transfer in microchannels: A critical review,” *Journal of Heat Transfer*, vol. 2, p. 28, 2012.
- [9] P. Wu and W. Little, “Measurement of friction factors for the flow of gases in very fine channels used for microminiature joule-thomson refrigerators,” *Cryogenics*, vol. 23, no. 5, pp. 273 – 277, 1983.
- [10] K. Pong, C. Ho, J. Liu, and Y. Tai, “Non-linear pressure distribution in uniform microchannels,” in *International Mechanical Engineering Congress and Exposition*, vol. 197, pp. 51–56, 1994.
- [11] J. Jang and S. T. Wereley, “Pressure distributions of gaseous slip flow in straight and uniform rectangular microchannels,” *Microfluidics and Nanofluidics*, vol. 1, no. 1, pp. 41–51, 2004.
- [12] J. C. Harley, Y. Huang, H. H. Bau, and J. N. Zemel, “Gas flow in micro-channels,” *Journal of Fluid Mechanics*, vol. 284, pp. 257–274, 1995.
- [13] E. Arkilic, M. Schmidt, and K. Breuer, “Gaseous slip flow in long microchannels,” *Microelectromechanical Systems, Journal of*, vol. 6, no. 2, pp. 167–178, 1997.
- [14] P. Wu and W. A. Little, “Measurement of the heat transfer characteristics of gas flow in fine channel heat exchangers used for microminiature refrigerators,” *Cryogenics*, vol. 24, no. 8, pp. 415 – 420, 1984.
- [15] E. N. Sieder and G. E. Tate, “Heat transfer and pressure drop of liquids in tubes,” *Industrial & Engineering Chemistry*, vol. 28, no. 12, pp. 1429–1435, 1936.

- [16] H. Hausen, "Neue gleichungen fuer die waermeuebertragung bei freier und erzwungener stromung," *Allg. Waermetechnik*, vol. 9, pp. 75–79, 1959.
- [17] F. W. Dittus and L. M. K. Boelter, "Heat transfer in automobile radiators of the tubular type," *University of California (Berkeley) Publication in Engineering*, vol. 2, p. 443, 1930.
- [18] S. B. Choi, R. Barron, and R. Warrington, "Fluid flow and heat transfer in microtubes," in *American Society of Mechanical Engineers, Dynamic Systems and Control Division (Publication) DSC*, vol. 32, pp. 123–134, 1991.
- [19] D. Yu, R. Warrington, R. Barron, and T. Ameen, "An experimental and theoretical investigation of fluid flow and heat transfer in microtubes," in *Proceedings of ASME/JSME Thermal Engineering Joint Conf., Maui, HI*, 1995.
- [20] K. Hara, M. Inoue, and M. Furukawa, "Heat transfer in minichannel gaseous cooling," *Journal of Environment and Engineering*, vol. 2, pp. 525–534, 2007.
- [21] C.-W. Chen, T.-Y. Lin, C.-Y. Yang, and S. G. Kandlikar, "An experimental investigation on heat transfer characteristics of air and co2 in microtubes," in *Proceedings of the ASME 9th International Conference on Nanochannels, Microchannels, and Minichannels, June 19-22, Edmonton, Canada*, 2011.
- [22] C.-Y. Yang, C.-W. Chen, T.-Y. Lin, and S. G. Kandlikar, "Heat transfer and friction characteristics of air flow in microtubes," *Experimental Thermal and Fluid Science*, vol. 37, no. 3, pp. 12 – 18, 2012.
- [23] V. Gnielinski, "Ein neues berechnungsverfahren fuer die waermeuebertragung im uebergangsbereich zwischen laminarer und turbulenter roehrstromung," *Forschung im Ingenieurwesen*, vol. 61, no. 9, pp. 240–248, 1995.
- [24] K. Schubert, J. Brandner, M. Fichtner, G. Linder, U. Schygulla, and A. Wenka, "Microstructure devices for applications in thermal and chemical process engineering," *Microscale Thermophysical Engineering*, vol. 5, no. 1, pp. 17–39, 2001.
- [25] C. Harris, K. Kelly, T. Wang, A. McCandless, and S. Motakef, "Fabrication, modeling, and testing of micro-cross-flow heat exchangers," *Journal of Microelectromechanical Systems*, vol. 11, no. 6, pp. 726–735, 2002.
- [26] J. J. Brandner, E. Anurjew, L. Bohn, E. Hansjosten, T. Henning, U. Schygulla, A. Wenka, and K. Schubert, "Concepts and realization of microstructure heat exchangers for enhanced heat transfer," *Experimental Thermal and Fluid Science*, vol. 30, no. 8, pp. 801 – 809, 2006.
- [27] J. J. Brandner, L. Bohn, T. Henning, U. Schygulla, and K. Schubert, "Microstructure heat exchanger applications in laboratory and industry," *Heat Transfer Engineering*, vol. 28, no. 8-9, pp. 761–771, 2007.
- [28] B. Alm, U. Imke, R. Knitter, U. Schygulla, and S. Zimmermann, "Testing and simulation of ceramic micro heat exchangers," *Chemical Engineering Journal*, vol. 135, no. 1, pp. 179 – 184, 2008.
- [29] H. Cao, G. Chen, and Q. Yuan, "Testing and design of a microchannel heat exchanger with multiple plates," *Industrial & Engineering Chemistry Research*, vol. 48, no. 9, pp. 4535–4541, 2009.

- [30] N. Garcia-Hernando, A. Acosta-Iborra, U. Ruiz-Rivas, and M. Izquierdo, "Experimental investigation of fluid flow and heat transfer in a single-phase liquid flow micro-heat exchanger," *International Journal of Heat and Mass Transfer*, vol. 52, pp. 5433 – 5446, 2009.
- [31] B. Mathew and H. Hegab, "Experimental investigation of thermal model of parallel flow microchannel heat exchangers subjected to external heat flux," *International Journal of Heat and Mass Transfer*, vol. 55, pp. 2193 – 2199, 2012.
- [32] W. Bier, W. Keller, G. Linder, D. Seidel, K. Schubert, and H. Martin, "Gas to gas heat transfer in micro heat exchangers," *Chemical Engineering and Processing: Process Intensification*, vol. 32, no. 1, pp. 33 – 43, 1993.
- [33] F. Meschke, G. Riebler, V. Hessel, J. Schuerer, and T. Baier, "Hermetic gas-tight ceramic microreactors," *Chemical Engineering & Technology*, vol. 28, no. 4, pp. 465–473, 2005.
- [34] K. Koyama and Y. Asako, "Experimental investigation of heat transfer characteristics on a gas-to-gas parallel flow microchannel heat exchanger," *Experimental Heat Transfer*, vol. 23, pp. 130–143, 2010.
- [35] R. J. Kee, B. B. Almand, J. M. Blasi, B. L. Rosen, M. Hartmann, N. P. Sullivan, H. Zhu, A. R. Manerbino, S. Menzer, W. G. Coors, and J. L. Martin, "The design, fabrication, and evaluation of a ceramic counter-flow microchannel heat exchanger," *Applied Thermal Engineering*, vol. 31, pp. 2004 – 2012, 2011.
- [36] J. M. Commenge, L. Falk, J. P. Corriou, and M. Matlosz, "Optimal design for flow uniformity in microchannel reactors," *AIChE Journal*, vol. 48, no. 2, pp. 345–358, 2002.
- [37] R. Chein and J. Chen, "Numerical study of the inlet/outlet arrangement effect on microchannel heat sink performance," *International Journal of Thermal Sciences*, vol. 48, no. 8, pp. 1627 – 1638, 2009.
- [38] O. Tonomura, S. Tanaka, M. Noda, M. Kano, S. Hasebe, and I. Hashimoto, "Cfd-based optimal design of manifold in plate-fin microdevices," *Chemical Engineering Journal*, vol. 101, pp. 397 – 402, 2004.
- [39] S. Balaji and S. Lakshminarayanan, "Improved design of microchannel plate geometry for uniform flow distribution," *The Canadian Journal of Chemical Engineering*, vol. 84, no. 6, pp. 715–721, 2006.
- [40] C. Renault, S. Colin, S. Orieux, P. Cognet, and T. Tzedakis, "Optimal design of multi-channel microreactor for uniform residence time distribution," *Microsystem Technologies*, vol. 18, pp. 209–223, 2012.
- [41] S. Colin, "Rarefaction and compressibility effects on steady and transient gas flows in microchannels," *Microfluidics and Nanofluidics*, vol. 1, pp. 268–279, 2005.
- [42] T. Ewart, P. Perrier, I. Graur, and J. G. Meolans, "Mass flow rate measurements in gas micro flows," *Experiments in Fluids*, vol. 41, no. 3, pp. 487–498, 2006.
- [43] T. Ewart, P. Perrier, I. Graur, and J. G. Meolans, "Mass flow rate measurements in a microchannel, from hydrodynamic to near free molecular regimes," *Journal of Fluid Mechanics*, vol. 584, no. 1, pp. 337–356, 2007.

- [44] J. Pitakarnnop, S. Varoutis, D. Valougeorgis, S. Geoffroy, L. Baldas, and S. Colin, “A novel experimental setup for gas microflows,” *Microfluidics and Nanofluidics*, vol. 8, pp. 57–72, 2010.
- [45] A. Demsis, B. Verma, S. V. Prabhu, and A. Agrawal, “Experimental determination of heat transfer coefficient in the slip regime and its anomalously low value,” *Physical Review E*, vol. 80, no. 1, pp. 016311–8, 2009.
- [46] M. Knudsen, “Thermischer molekulardruck der gase in roehren und poroesen koerpern,” *Annalen der Physik*, vol. 336, no. 3, pp. 633–640, 1910.
- [47] I. Yasumoto, “Thermal transpiration effects for gases at pressures above 0.1 torr,” *The Journal of Physical Chemistry*, vol. 84, no. 6, pp. 589–593, 1980.
- [48] W. Jitschin and P. Rohl, “Quantitative study of the thermal transpiration effect in vacuum gauges,” *Journal of Vacuum Science Technology A: Vacuum, Surfaces, and Films*, vol. 5, no. 3, pp. 372–375, 1987.
- [49] D. York, A. Chambers, A. Chew, and A. Troup, “Measurement of thermal transpiration across an array of parallel capillaries using a differential capacitance manometer,” *Vacuum*, vol. 55, no. 2, pp. 133–139, 1999.
- [50] S. McNamara and Y. Gianchandani, “On-chip vacuum generated by a micromachined knudsen pump,” *Journal of Microelectromechanical Systems*, vol. 14, no. 4, pp. 741 – 746, 2005.
- [51] S. G. Kandlikar, D. Schmitt, A. L. Carrano, and J. B. Taylor, “Characterization of surface roughness effects on pressure drop in single-phase flow in minichannels,” *Physics of Fluids*, vol. 17, p. 100606, 2005.
- [52] G. H. Tang, Z. Li, Y. L. He, and W. Q. Tao, “Experimental study of compressibility, roughness and rarefaction influences on microchannel flow,” *International Journal of Heat and Mass Transfer*, vol. 50, no. 11-12, pp. 2282–2295, 2007.
- [53] S. G. Kandlikar, S. Joshi, and S. Tian, “Effect of surface roughness on heat transfer and fluid flow characteristics at low reynolds numbers in small diameter tubes,” *Heat Transfer Engineering*, vol. 24, no. 3, pp. 4–16, 2003.
- [54] M. Lorenzini, G. L. Morini, T. Henning, and J. Brandner, “Experimental uncertainties analysis as a tool for friction factor determination in microchannels,” *Proceedings of the Institution of Mechanical Engineers, Part C: Journal of Mechanical Engineering Science*, vol. 222, no. 5, pp. 817–827, 2008.
- [55] M. Lorenzini, G. L. Morini, and S. Salvigni, “Laminar, transitional and turbulent friction factors for gas flows in smooth and rough microtubes,” *International Journal of Thermal Sciences*, vol. 49, no. 2, pp. 248 – 255, 2010.
- [56] M. J. Kohl, S. I. Abdel-Khalik, S. M. Jeter, and D. L. Sadowski, “A microfluidic experimental platform with internal pressure measurements,” *Sensors and Actuators A: Physical*, vol. 118, no. 2, pp. 212–221, 2005.
- [57] G. Croce, P. D’agaro, and C. Nonino, “Three-dimensional roughness effect on microchannel heat transfer and pressure drop,” *International Journal of Heat and Mass Transfer*, vol. 50, pp. 5249 – 5259, 2007.

- [58] G. Croce and P. D'Agaro, "Numerical analysis of roughness effect on microtube heat transfer," *Superlattices and Microstructures*, vol. 35, pp. 601 – 616, 2004.
- [59] T.-Y. Lin and S. G. Kandlikar, "An experimental investigation of structured roughness effect on heat transfer during single-phase liquid flow at microscale," *Journal of Heat Transfer*, vol. 134, no. 10, p. 101701, 2012.
- [60] S. E. Turner, L. C. Lam, M. Faghri, and O. J. Gregory, "Experimental investigation of gas flow in microchannels," *Journal of Heat Transfer*, vol. 126, no. 5, pp. 753–763, 2004.
- [61] Y. Asako, K. Nakayama, and T. Shinozuka, "Effect of compressibility on gaseous flows in a micro-tube," *International Journal of Heat and Mass Transfer*, vol. 48, no. 23-24, pp. 4985 – 4994, 2005.
- [62] Z. Li, D. Du, and Z. Guo, "Investigation on the characteristics of frictional resistance of gas flow in microtubes," in *Proc. Symposium on Energy Engineering in the 21st Century*, vol. 2, pp. 658-664, 2000.
- [63] G. Bar-Meir, *Fundamentals of Compressible Fluid Mechanics*. Potto Project, 2007.
- [64] W. Shi, M. Miyamoto, Y. Katoh, and J. Kurima, "Choked flow of low density gas in a narrow parallel-plate channel with adiabatic walls," *International Journal of Heat and Mass Transfer*, vol. 44, no. 13, pp. 2555 – 2565, 2001.
- [65] V. Lijo, H. D. Kim, and T. Setoguchi, "Effects of choking on flow and heat transfer in micro-channels," *International Journal of Heat and Mass Transfer*, vol. 55, no. 4, pp. 701 – 709, 2012.
- [66] A. Luikov, V. Aleksashenko, and A. Aleksashenko, "Analytical methods of solution of conjugated problems in convective heat transfer," *International Journal of Heat and Mass Transfer*, vol. 14, no. 8, pp. 1047 – 1056, 1971.
- [67] R. Shah and A. London, *Laminar flow forced convection in ducts*. Advances in heat transfer: Supplement, Academic Press, 1978.
- [68] G. Maranzana, I. Perry, and D. Maillet, "Mini- and micro-channels: influence of axial conduction in the walls," *International Journal of Heat and Mass Transfer*, vol. 47, no. 17-18, pp. 3993 – 4004, 2004.
- [69] K. Koyama, *Experimental Investigation of Heat Transfer Characteristics on a Gas-to-Gas Parallel Flow Microchannel Heat Exchanger*. PhD thesis, Department of Mechanical Engineering, Tokyo Metropolitan University, 2010.
- [70] R. K. Shah and A. L. London, "Thermal boundary conditions and some solutions for laminar duct flow forced convection," *Journal of Heat Transfer*, vol. 96, no. 2, pp. 159–165, 1974.
- [71] H. Herwig and S. P. Mahulikar, "Variable property effects in single-phase incompressible flows through microchannels," *International Journal of Thermal Sciences*, vol. 45, no. 10, pp. 977 – 981, 2006.
- [72] S. P. Mahulikar and H. Herwig, "Physical effects in pure continuum-based laminar micro-convection due to variation of gas properties," *Journal of Physics D: Applied Physics*, vol. 39, no. 18, p. 4116, 2006.

- [73] H. Brinkman, "Heat effects in capillary flow," *Applied Scientific Research*, vol. 2, pp. 120–124, 1951.
- [74] C. P. Tso and S. P. Mahulikar, "Experimental verification of the role of brinkman number in microchannels using local parameters," *International Journal of Heat and Mass Transfer*, vol. 43, no. 10, pp. 1837 – 1849, 2000.
- [75] J. Judy, D. Maynes, and B. W. Webb, "Characterization of frictional pressure drop for liquid flows through microchannels," *International Journal of Heat and Mass Transfer*, vol. 45, no. 17, pp. 3477–3489, 2002.
- [76] G. Celata, G. Morini, V. Marconi, S. McPhail, and G. Zummo, "Using viscous heating to determine the friction factor in microchannels - an experimental validation," *Experimental Thermal and Fluid Science*, vol. 30, no. 8, pp. 725 – 731, 2006.
- [77] G. Tunc and Y. Bayazitoglu, "Heat transfer in microtubes with viscous dissipation," *International Journal of Heat and Mass Transfer*, vol. 44, no. 13, pp. 2395 – 2403, 2001.
- [78] N. G. Hadjiconstantinou, "Dissipation in small scale gaseous flows," *Journal of Heat Transfer*, vol. 125, no. 5, pp. 944–947, 2003.
- [79] J. Koo and C. Kleinstreuer, "Viscous dissipation effects in microtubes and microchannels," *International Journal of Heat and Mass Transfer*, vol. 47, no. 14-16, pp. 3159 – 3169, 2004.
- [80] J. van Rij, T. Ameel, and T. Harman, "The effect of viscous dissipation and rarefaction on rectangular microchannel convective heat transfer," *International Journal of Thermal Sciences*, vol. 48, no. 2, pp. 271 – 281, 2009.
- [81] G. L. Morini, "Viscous heating in liquid flows in micro-channels," *International Journal of Heat and Mass Transfer*, vol. 48, no. 17, pp. 3637 – 3647, 2005.
- [82] G. Morini, *Convective Heat Transfer in Microchannels*, in: *Encyclopedia of Microfluidics and Nanofluidics*, pp. 304–322. Springer Science, New York-Heidelberg, 2008.
- [83] J. Poiseuille, "Recherches experimentales sur le mouvement des liquides dans les tubes de tres petits diametres," *Comptes Rendus Hebdomadaires de l'Academie des Sciences*, vol. 11, pp. 961–967 and 1041–1048, 1840.
- [84] G. P. Celata, M. Cumo, S. J. McPhail, L. Tesfagabir, and G. Zummo, "Experimental study on compressible flow in microtubes," *International Journal of Heat and Fluid Flow*, vol. 28, no. 1, pp. 28–36, 2007.
- [85] Y. Zohar, S. Y. K. Lee, W. Y. Lee, L. Jiang, and P. Tong, "Subsonic gas flow in a straight and uniform microchannel," *Journal of Fluid Mechanics*, vol. 472, no. 1, pp. 125 –151, 2002.
- [86] G. L. Morini, M. Lorenzini, S. Colin, and S. Geoffroy, "Experimental analysis of pressure drop and laminar to turbulent transition for gas flows in smooth microtubes," *Heat Transfer Engineering*, vol. 28, no. 8-9, pp. 670–679, 2007.
- [87] G. L. Morini, M. Lorenzini, and S. Salvigni, "Friction characteristics of compressible gas flows in microtubes," *Experimental Thermal and Fluid Science*, vol. 30, no. 8, pp. 733 –

- 744, 2006. ECI International Conference on Heat Transfer and Fluid Flow in Microscale - Castelvechio Pascoli (Barga, Lucca), 25-30 September 2005.
- [88] L. Marino, "Experiments on rarefied gas flows through tubes," *Microfluidics and Nanofluidics*, vol. 6, no. 1, pp. 109–119, 2009.
- [89] J. Webster, *The measurement, instrumentation, and sensors handbook*. Springer, 1999.
- [90] S. Hsieh, H. Tsai, C. Lin, C. Huang, and C. Chien, "Gas flow in a long microchannel," *International Journal of Heat and Mass Transfer*, vol. 47, no. 17-18, pp. 3877–3887, 2004.
- [91] D. Du, Z. Li, and Z. Guo, "Friction resistance for gas flow in smooth microtubes," *Science in China Series E: Technological Sciences*, vol. 43, pp. 171–177, 2000.
- [92] C. Huang and J. Sullivan, "Psp measurement in microchannel flow," in *21st International Congress on Instrumentation in Aerospace Simulation Facilities*, (Japan), pp. 226–233, ICIASF'05, September 2005.
- [93] T. Liu and J. P. Sullivan, *Pressure and temperature sensitive paints*. Springer-Verlag, 2004.
- [94] T. Liu, B. Campbell, S. Burns, and J. Sullivan, "Temperature and pressure sensitive luminescent paints in aerodynamics," *Applied Mechanics Reviews*, vol. 50, no. 4, pp. 227–246, 1997.
- [95] J. H. Bell, E. T. Schairer, L. A. Hand, and R. D. Mehta, "Surface pressure measurements using luminescent coatings," *Annual Review of Fluid Mechanics*, vol. 33, no. 1, pp. 155–206, 2001.
- [96] H. Mori, T. Niimi, M. Hirako, and H. Uenishi, "Molecular number flux detection using oxygen sensitive luminophore," *Physics of Fluids*, vol. 17, no. 10, p. 100610, 2005.
- [97] Y. Matsuda, T. Uchida, S. Suzuki, R. Misaki, H. Yamaguchi, and T. Niimi, "Pressure-sensitive molecular film for investigation of micro gas flows," *Microfluidics and Nanofluidics*, vol. 10, pp. 165–171, 2011.
- [98] R. Baviere and F. Ayela, "Micromachined strain gauges for the determination of liquid flow friction coefficients in microchannels," *Measurement Science and Technology*, vol. 15, no. 2, pp. 377–383, 2004.
- [99] N. Nguyen, "Micromachined flow sensors—a review," *Flow Measurement and Instrumentation*, vol. 8, no. 1, pp. 7–16, 1997.
- [100] K. Petersen, J. Brown, and W. Renken, "High-precision, high-performance mass-flow sensor with integrated laminar flow micro-channels," in *Conference of Transducers '85: 1985 International Conference on Solid-State Sensors and Actuators*, pp. 361–363, IEEE, New York, NY, USA, 1985.
- [101] T. Lammerink, N. Tas, M. Elwenspoek, and J. Fluitman, "Micro-liquid flow sensor," *Sensors and Actuators A: Physical*, vol. 37-38, pp. 45–50, 1993.
- [102] A. Vittoriosi, J. J. Brandner, and R. Dittmeyer, "A sensor-equipped microchannel system for the thermal characterization of rarefied gas flows," *Experimental Thermal and Fluid Science*, vol. 41, pp. 112–120, 2012.

- [103] X. Zhang, H. Choi, A. Datta, and X. Li, "Design, fabrication and characterization of metal embedded thin film thermocouples with various film thicknesses and junction sizes," *Journal of Micromechanics and Microengineering*, vol. 16, no. 5, pp. 900–905, 2006.
- [104] H. Choi and X. Li, "Fabrication and application of micro thin film thermocouples for transient temperature measurement in nanosecond pulsed laser micromachining of nickel," *Sensors and Actuators A: Physical*, vol. 136, no. 1, pp. 118–124, 2007.
- [105] R. A. Bianchi, F. V. D. Santos, J. M. Karam, B. Courtois, F. Pressecq, and S. Sifflet, "Cmos-compatible smart temperature sensors," *Microelectronics Journal*, vol. 29, no. 9, pp. 627–636, 1998.
- [106] P. Miribel-Catala, E. Montane, S. A. Bota, M. Puig-Vidal, and J. Samitier, "Mosfet-based temperature sensor for standard bcd smart power technology," *Microelectronics Journal*, vol. 32, no. 10-11, pp. 869–873, 2001.
- [107] I. Y. Han and S. J. Kim, "Diode temperature sensor array for measuring micro-scale surface temperatures with high resolution," *Sensors and Actuators A: Physical*, vol. 141, no. 1, pp. 52–58, 2008.
- [108] R. Baviere, M. Favre-Marinet, and S. L. Person, "Bias effects on heat transfer measurements in microchannel flows," *International Journal of Heat and Mass Transfer*, vol. 49, no. 19-20, pp. 3325–3337, 2006.
- [109] R. Muwanga and I. Hassan, "Flow and heat transfer in a cross-linked silicon microchannel heat sink," *Journal of Thermophysics and Heat Transfer*, vol. 22, no. 3, pp. 333–341, 2008.
- [110] A. Mosyak, Z. Segal, E. Pogrebnyak, and G. Hetsroni, "Two- phase flow patterns and heat transfer in parallel microchannels," *Journal of Thermal Science*, vol. 11, pp. 353–358, 2002.
- [111] V. Hohreiter, S. Wereley, M. Olsen, and J. Chung, "Cross-correlation analysis for temperature measurement," *Measurement science and technology*, vol. 13, no. 7, p. 1072, 2002.
- [112] J. Sakakibara and R. Adrian, "Whole field measurement of temperature in water using two-color laser induced fluorescence," *Experiments in Fluids*, vol. 26, no. 1, pp. 7–15, 1999.
- [113] L. Schoeler, B. Lange, K. Seibel, H. Schaefer, M. Walder, N. Friedrich, D. Ehrhardt, F. Schoenfeld, G. Zech, and M. Boehm, "Monolithically integrated micro flow sensor for lab-on-chip applications," *Microelectronic Engineering*, vol. 78-79, pp. 164–170, 2005.
- [114] T. H. Kim and S. J. Kim, "Development of a micro-thermal flow sensor with thin-film thermocouples," *Journal of Micromechanics and Microengineering*, vol. 16, no. 11, pp. 2502–2508, 2006.
- [115] J. C. Shih, C.-M. Ho, J. Liu, and Y.-C. Tai, "Monatomic and polyatomic gas flow through uniform microchannels," in *ASME DSC*, vol. 59, pp. 197–203, 1996.
- [116] S. Colin, P. Lalonde, and R. Caen, "Validation of a Second-Order slip flow model in rectangular microchannels," *Heat Transfer Engineering*, vol. 25, pp. 23–30, Aug. 2010.

- [117] E. B. Arkilic, K. S. Breuer, and M. A. Schmidt, "Mass flow and tangential momentum accommodation in silicon micromachined channels," *Journal of Fluid Mechanics*, vol. 437, no. 1, pp. 29–43, 2001.
- [118] S. Tison, "Experimental data and theoretical modeling of gas flows through metal capillary leaks," *Vacuum*, vol. 44, pp. 1171–1175, Nov. 1993.
- [119] B. N. Taylor and C. E. Kuyatt, "Guidelines for evaluating and expressing the uncertainty of measurement results," *National Institute of Standards and Technology*, 1994.
- [120] A. Shapiro, *The dynamics and thermodynamics of compressible fluid flow*. 1953.
- [121] A. D. Ferguson, M. Bahrami, and J. R. Culham, "Review of experimental procedure for determining liquid flow in microchannels," in *Proceedings of ICMM 3rd International Conference on Microchannels and Minichannels*, no. 41855a, (Toronto), pp. 303–311, ASME, June 2005.
- [122] Z. Li, D. Du, and Z. Guo, "Experimental study on flow characteristics of liquid in circular microtubes," *Microscale Thermophysical Engineering*, vol. 7, no. 3, pp. 253–265, 2003.
- [123] H. Y. Wu and P. Cheng, "Friction factors in smooth trapezoidal silicon microchannels with different aspect ratios," *International Journal of Heat and Mass Transfer*, vol. 46, no. 14, pp. 2519 – 2525, 2003.
- [124] G. M. Mala and D. Li, "Flow characteristics of water in microtubes," *International Journal of Heat and Fluid Flow*, vol. 20, no. 2, pp. 142–148, 1999.
- [125] Y. Chen, S. Kang, W. Tuh, and T. Hsiao, "Experimental investigation of fluid flow and heat transfer in microchannels," *Tamkang Journal of Science and Engineering*, vol. 7, no. 1, pp. 11–16, 2004.
- [126] X. F. Peng, G. P. Peterson, and B. X. Wang, "Frictional flow characteristics of water flowing through rectangular microchannels," *Experimental Heat Transfer*, vol. 7, no. 4, pp. 249–264, 1994.
- [127] X. F. Peng and G. P. Peterson, "Convective heat transfer and flow friction for water flow in microchannel structures," *International Journal of Heat and Mass Transfer*, vol. 39, no. 12, pp. 2599 – 2608, 1996.
- [128] J. Maurer, P. Tabeling, P. Joseph, and H. Willaime, "Second-order slip laws in microchannels for helium and nitrogen," *Physics of Fluids*, vol. 15, no. 9, pp. 2613–2621, 2003.
- [129] S. E. Turner, H. Sun, M. Faghri, and O. J. Gregory, "Compressible gas flow through smooth and rough microchannels," in *International Mechanical Engineering Congress and Exposition: Heat Transfer Division*, no. 24145, (New York), pp. 1–4, 2001.
- [130] T. Araki, M. S. Kim, H. Iwai, and K. Suzuki, "An experimental investigation of gaseous flow characteristics in microchannels," *Microscale Thermophysical Engineering*, vol. 6, no. 2, pp. 117–130, 2010.
- [131] M. Lorenzini, G. L. Morini, T. Henning, and J. Brandner, "Uncertainty assessment in friction factor measurements as a tool to design experimental set-ups," *International Journal of Thermal Sciences*, vol. 48, no. 2, pp. 282 – 289, 2009.

- [132] J. J. Brandner, "Microstructure devices for process intensification: Influence of manufacturing tolerances and design," *Applied Thermal Engineering*, no. 0, p. In press, 2013.
- [133] V. Gesellschaft, *VDI Heat Atlas*. Springer, 2010.
- [134] W. Kays and A. London, *Compact Heat Exchangers*. McGraw-Hill, New York, third ed., 1984.
- [135] C. Colebrook, "Turbulent flow in pipes, with particular reference to the transition region between the smooth and rough pipe laws.," *Journal of the ICE*, vol. 11, no. 4, pp. 133–156, 1939.
- [136] G. Morini, M. Lorenzini, S. Salvigni, and M. Spiga, "Analysis of laminar-to-turbulent transition for isothermal gas flows in microchannels," *Microfluidics and Nanofluidics*, vol. 7, pp. 181–190, 2009.
- [137] C. Hong, Y. Asako, and I. Ueno, "Flow and heat transfer characteristics of turbulent gas flow in microtube with constant wall heat flux," in *1st European Conference on Gas Micro Flows, June 6-8, Skiathos Island, Greece, 2012*.
- [138] J. Lienhard IV and J. Lienhard V, *A heat transfer textbook*. Phlogiston Press, 3rd ed., 2003.
- [139] B. Spang, "Einfluß der thermischen randbedingung auf den laminaren wärmeübergang im kreisrohr bei hydrodynamischer einlaufströmung," *Heat and mass transfer*, vol. 31, no. 4, pp. 199–204, 1996.
- [140] S. Churchill and S. Zajic, "Prediction of fully developed turbulent convection with minimal explicit empiricism," *AIChE journal*, vol. 48, no. 5, pp. 927–940, 2004.
- [141] V. Gnielinski, "New equations for heat and mass transfer in turbulent pipe and channel flow," *International Chemical Engineering*, vol. 16, pp. 359–368, 1976.
- [142] C. Hong, T. Yamamoto, Y. Asako, and K. Suzuki, "Heat transfer characteristics of compressible laminar flow through microtubes," *Journal of heat transfer*, vol. 134, no. 1, pp. 011602, 2012.
- [143] S. M. Mori, S. and A. Tanimoto, "Steady heat transfer to laminar flow in a circular tube with conduction in the tube wall," *Heat Transfer-Japanese Res*, vol. 3, pp. 37–46, 1974.
- [144] C. Hong, Y. Asako, and J.-H. Lee, "Heat transfer characteristics of gaseous flows in micro-channel with constant heat flux," *International Journal of Thermal Sciences*, vol. 46, no. 11, pp. 1153 – 1162, 2007.
- [145] G. Croce and P. D'Agaro, "Compressibility and rarefaction effect on heat transfer in rough microchannels," *International Journal of Thermal Sciences*, vol. 48, no. 2, pp. 252 – 260, 2009.
- [146] Z. Y. Guo and X. B. Wu, "Compressibility effect on the gas flow and heat transfer in a microtube," *International Journal of Heat and Mass Transfer*, vol. 40, no. 13, pp. 3251 – 3254, 1997.
- [147] T. Stief, O.-U. Langer, and K. Schubert, "Numerical investigations of optimal heat conductivity in micro heat exchangers," *Chem. Eng. Technol.*, vol. 22, no. 4, pp. 297–303, 1999.

- [148] F. Kreith and D. Y. Goswami, *Handbook of Energy Efficiency and Renewable Energy*. CRC Press: Taylor & Francis Group, Boca Raton, FL, 2007.
- [149] J. J. Brandner, T. Gietzelt, T. Henning, M. Kraut, H. Moritz, and W. Pfleging, *Microfabrication in Metals and Polymers*. Wiley-VCH Verlag GmbH, 2008.
- [150] K. J. Hecht, S. Kohl, P. Pfeifer, and B. Kraushaar-Czarnetzki, “Boundary conditions in multiphase microchannel flows: The role of surface roughness,” in *Jahrestreffen Reaktionstechnik, Wuerzburg*, 10-12 May 2010.
- [151] A. Vittoriosi, J. J. Brandner, and R. Dittmeyer, “Experimental design with integrated temperature sensor in mems: an example of application for rarefied gases,” in *3rd Micro and Nano Flows Conf., Thessaloniki, GR*, August 22-24, 2011.
- [152] R. Shah and D. Sekulic, *Fundamentals of Heat Exchanger Design*. John Wiley & Sons, 2003.
- [153] S. J. Cartaxo and F. A. Fernandes, “Counterflow logarithmic mean temperature difference is actually the upper bound: A demonstration,” *Applied Thermal Engineering*, vol. 31, pp. 1172 – 1175, 2011.
- [154] *Ansys Fluent Manuals*. <http://www.ansys.com/Support/Documentation>.

Appendix A

Propagation of uncertainties on friction factor

Section one: incompressible flow

When the flow is incompressible and the fluid has constant properties, the friction factor can be calculated by using the Darcy-Weisback equation:

$$f = \frac{\rho d_h^5 \Delta p}{2L \dot{m}^2} \quad (\text{A.1})$$

In Eq. (A.1) the value of friction factor are directly related to the operating variables:

$$f = f(d_h, L, \Delta p, \dot{m}) \quad (\text{A.2})$$

The partial derivative of friction factor on each variable can be obtained analytically. Starting from hydraulic diameter, the derivative can be expressed as:

$$\frac{\partial f}{\partial d_h} = \frac{5\rho d_h^4 \Delta p}{2L \dot{m}^2} \quad (\text{A.3})$$

Substituting Eq. (A.1) into Eq. (A.3), the derivative can be simplified as:

$$\frac{\partial f}{\partial d_h} = \frac{5f}{d_h} \quad (\text{A.4})$$

Thus the coefficient in Eq. (3.6) can be calculated by

$$k_1 = \left| \frac{\partial f}{\partial d_h} \cdot \frac{d_h}{f} \right| = 5 \quad (\text{A.5})$$

Similarly, the derivative of friction factor on microchannel length can be deducted as:

$$\frac{\partial f}{\partial L} = -\frac{\rho d_h^5 \Delta p}{2L^2 \dot{m}^2} \quad (\text{A.6})$$

By substituting Eq. (A.1) into Eq. (A.6), the derivative can be simplified as:

$$\frac{\partial f}{\partial L} = -\frac{f}{L} \quad (\text{A.7})$$

The production of the derivative and the ratio of length to friction factor can be calculated as:

$$\frac{\partial f}{\partial L} \cdot \frac{L}{f} = -1 \quad (\text{A.8})$$

Therefore, the coefficient on length is

$$k_2 = \left| \frac{\partial f}{\partial L} \cdot \frac{L}{f} \right| = 1 \quad (\text{A.9})$$

From Eq. (A.1) the derivative of friction factor on pressure drop can be expressed as:

$$\frac{\partial f}{\partial \Delta p} = \frac{\rho d_h^5}{2L\dot{m}^2} \quad (\text{A.10})$$

The production of the derivative and the percentage of Δp over f is:

$$\frac{\partial f}{\partial \Delta p} \cdot \frac{\Delta p}{f} = \frac{\rho d_h^5 \Delta p^2}{2fL\dot{m}^2} \quad (\text{A.11})$$

Substituting Eq. (A.1) into Eq. (A.11), one can obtain

$$\frac{\partial f}{\partial \Delta p} \cdot \frac{\Delta p}{f} = 1 \quad (\text{A.12})$$

Or the coefficient on pressure drop is

$$k_4 = \left| \frac{\partial f}{\partial \Delta p} \cdot \frac{\Delta p}{f} \right| = 1 \quad (\text{A.13})$$

The derivative on mass flow rate is deducted as

$$\frac{\partial f}{\partial \dot{m}} = -\frac{\rho d_h^5 \Delta p}{4L\dot{m}^3} \quad (\text{A.14})$$

By using the expression of friction factor, the production can be calculated by

$$\frac{\partial f}{\partial \dot{m}} \cdot \frac{\dot{m}}{f} = -\frac{\rho d_h^5 \Delta p}{4fL\dot{m}^2} \quad (\text{A.15})$$

Substituting Eq. (A.1) into Eq. (A.15), the production can be further expressed as

$$\frac{\partial f}{\partial \dot{m}} \cdot \frac{\dot{m}}{f} = -2 \quad (\text{A.16})$$

Or the coefficient on mass flow rate is

$$k_6 = \left| \frac{\partial f}{\partial \dot{m}} \cdot \frac{\dot{m}}{f} \right| = 2 \quad (\text{A.17})$$

Section two: compressible flow with pressure drop and outlet pressure

When the flow is compressible, by measuring the pressure drop and outlet pressure the friction factor can be calculated by Eq. (3.3).

From Eq. (3.3) the derivative on hydraulic diameter can be deducted as

$$\frac{\partial f}{\partial d_h} = \frac{5\pi^2 d_h^4}{16RTL\dot{m}^2} (\Delta p^2 + 2\Delta p p_{out}) - \frac{2}{L} \ln \frac{p_{out} + \Delta p}{p_{out}} \quad (\text{A.18})$$

Substituting Eq. (3.3) into Eq. (A.18), one can obtain

$$\frac{\partial f}{\partial d_h} = \frac{5f}{d_h} + \frac{8}{L} \ln\left(1 + \frac{\Delta p}{p_{out}}\right) \quad (\text{A.19})$$

The production can be accordingly expressed as

$$\frac{\partial f}{\partial d_h} \cdot \frac{d_h}{f} = 5 + \frac{8d_h}{fL} \ln\left(1 + \frac{\Delta p}{p_{out}}\right) \quad (\text{A.20})$$

In order to simplify the expression in Eq. (A.20) and in the equations hereafter, two more dimensionless variables are introduced:

$$\frac{\Delta p}{p_{out}} = \alpha, \quad \frac{2d_h}{fL} = \beta \quad (\text{A.21})$$

By applying Eq. (A.21) to Eq. (A.20), the production can be simplified as

$$\frac{\partial f}{\partial d_h} \cdot \frac{d_h}{f} = 5 + 4\beta \ln(1 + \alpha) \quad (\text{A.22})$$

Or the coefficient on hydraulic diameter for compressible flow can be expressed by

$$k_1 = \left| \frac{\partial f}{\partial d_h} \cdot \frac{d_h}{f} \right| = 5 + 4\beta \ln(1 + \alpha) \quad (\text{A.23})$$

In a similar way, the derivative on length can be deduced as

$$\frac{\partial f}{\partial L} = -\frac{d_h}{L^2} \left[\frac{(p_{out} + \Delta p)^2 - p_{out}^2}{RT \left(\frac{4\dot{m}}{\pi d_h^2} \right)^2} - 2 \ln \frac{p_{out} + \Delta p}{p_{out}} \right] \quad (\text{A.24})$$

Substituting Eq. (3.3) into the equation above, we can obtain

$$\frac{\partial f}{\partial L} = -\frac{f}{L} \quad (\text{A.25})$$

Therefore, the coefficient on microchannel length is calculated by

$$k_2 = \left| \frac{\partial f}{\partial L} \cdot \frac{L}{f} \right| = 1 \quad (\text{A.26})$$

For compressible flow, the friction factor is a function of fluid temperature. The derivative on temperature can be obtained from Eq. (3.3), and is expressed as

$$\frac{\partial f}{\partial T} = -\frac{1}{T} \frac{\pi^2 d_h^5}{16RTL\dot{m}^2} (\Delta p^2 + 2\Delta p p_{out}) \quad (\text{A.27})$$

By using the expression of friction factor to the equation above, the derivative can be further expressed as

$$\frac{\partial f}{\partial T} = -\frac{1}{T} \left[f + \frac{2d_h}{L} \ln \left(1 + \frac{\Delta p}{p_{out}} \right) \right] \quad (\text{A.28})$$

Therefore the production of the derivative and the ratio of temperature to friction factor can be calculated by

$$\frac{\partial f}{\partial T} \cdot \frac{T}{f} = -1 - \frac{2d_h}{fL} \ln \left(1 + \frac{\Delta p}{p_{out}} \right) \quad (\text{A.29})$$

By using the introduced dimensionless parameters, Eq. (A.29) can be simplified as

$$\frac{\partial f}{\partial T} \cdot \frac{T}{f} = -1 - \beta \ln(1 + \alpha) \quad (\text{A.30})$$

Thus the coefficient on temperature is expressed by

$$k_3 = \left| \frac{\partial f}{\partial T} \cdot \frac{T}{f} \right| = 1 + \beta \ln(1 + \alpha) \quad (\text{A.31})$$

The derivative on pressure drop can be deducted as

$$\frac{\partial f}{\partial \Delta p} = \frac{\pi^2 d_h^5}{8RTL\dot{m}^2} (\Delta p + p_{out}) - \frac{2d_h}{L(p_{out} + \Delta p)} \quad (\text{A.32})$$

Using the expression of friction factor, the production for pressure drop is expressed by

$$\frac{\partial f}{\partial \Delta p} \cdot \frac{\Delta p}{f} = \frac{\pi^2 d_h^5}{8RTfL\dot{m}^2} (\Delta p^2 + \Delta p p_{out}) - \frac{2d_h \Delta p}{fL(p_{out} + \Delta p)} \quad (\text{A.33})$$

In order to use the two dimensionless variables, Eq. (A.33) can be mathematically transformed as

$$\frac{\partial f}{\partial \Delta p} \cdot \frac{\Delta p}{f} = 1 + \frac{1}{1 + 2 \frac{p_{out}}{\Delta p}} + \frac{2d_h}{fL} \left(1 + \frac{1}{1 + 2 \frac{p_{out}}{\Delta p}} \right) \ln \left(1 + \frac{\Delta p}{p_{out}} \right) - \frac{2d_h}{fL \left(1 + \frac{p_{out}}{\Delta p} \right)} \quad (\text{A.34})$$

The expression above can be therefore simplified as

$$\frac{\partial f}{\partial \Delta p} \cdot \frac{\Delta p}{f} = 1 + \frac{\alpha}{2 + \alpha} + \beta \left(1 + \frac{\alpha}{2 + \alpha} \right) \ln(1 + \alpha) - \beta \frac{\alpha}{1 + \alpha} \quad (\text{A.35})$$

Or the coefficient on pressure drop is expressed by

$$k_4 = \left| \frac{\partial f}{\partial \Delta p} \cdot \frac{\Delta p}{f} \right| = 1 + \frac{\alpha}{2 + \alpha} + \beta \left(1 + \frac{\alpha}{2 + \alpha} \right) \ln(1 + \alpha) - \beta \frac{\alpha}{1 + \alpha} \quad (\text{A.36})$$

The derivative of friction factor on the outlet pressure can be deduced as

$$\frac{\partial f}{\partial p_{out}} = \frac{\pi^2 d_h^5}{8RTL\dot{m}^2} \Delta p - \frac{2d_h}{L} \cdot \frac{\Delta p}{(p_{out} + \Delta p)p_{out}} \quad (\text{A.37})$$

The production on outlet pressure can be simply expressed by

$$\frac{\partial f}{\partial p_{out}} \cdot \frac{p_{out}}{f} = \frac{\pi^2 d_h^5}{8RTfL\dot{m}^2} \Delta p p_{out} - \frac{2d_h}{fL} \cdot \frac{\Delta p}{p_{out} + \Delta p} \quad (\text{A.38})$$

Eq. (A.38) can be changed into

$$\frac{\partial f}{\partial p_{out}} \cdot \frac{p_{out}}{f} = \frac{1}{1 + \frac{\Delta p}{2p_{out}}} + \frac{2d_h}{fL} \left(\frac{2}{2 + \frac{\Delta p}{p_{out}}} \ln \left(1 + \frac{\Delta p}{p_{out}} \right) + \frac{1}{1 + \frac{p_{out}}{\Delta p}} \right) \quad (\text{A.39})$$

By substituting Eq. (A.21) into the above equation, one can obtain

$$\frac{\partial f}{\partial p_{out}} \cdot \frac{p_{out}}{f} = \frac{1}{1 + \frac{\alpha}{2}} + \beta \left[\frac{2}{2 + \alpha} \ln(1 + \alpha) + \frac{\alpha}{1 + \alpha} \right] \quad (\text{A.40})$$

Therefore, the coefficient on outlet pressure can be expressed as

$$k_5 = \left| \frac{\partial f}{\partial p_{out}} \cdot \frac{p_{out}}{f} \right| = \frac{1}{1 + \frac{\alpha}{2}} + \beta \left[\frac{2}{2 + \alpha} \ln(1 + \alpha) + \frac{\alpha}{1 + \alpha} \right] \quad (\text{A.41})$$

The derivative of friction factor on mass flow rate is deduced from Eq. (3.3) as

$$\frac{\partial f}{\partial \dot{m}} = -\frac{\pi^2 d_h^5}{8RTL\dot{m}^3} (\Delta p^2 + 2\Delta p p_{out}) \quad (\text{A.42})$$

Further substituting Eq. (3.3) into the above equation, one obtains

$$\frac{\partial f}{\partial \dot{m}} = -\frac{2}{\dot{m}} \left(f + \frac{2d_h}{L} \ln \frac{p_{out} + \Delta p}{p_{out}} \right) \quad (\text{A.43})$$

The production on mass flow rate is accordingly calculated as

$$\frac{\partial f}{\partial \dot{m}} \cdot \frac{\dot{m}}{f} = -2 - \frac{4d_h}{fL} \ln \left(1 + \frac{\Delta p}{p_{out}} \right) \quad (\text{A.44})$$

This expression can be further simplified by using the two dimensionless variables:

$$\frac{\partial f}{\partial \dot{m}} \cdot \frac{\dot{m}}{f} = -2 - 2\beta \ln(1 + \alpha) \quad (\text{A.45})$$

The coefficient on mass flow rate is thus calculated by

$$k_6 = \left| \frac{\partial f}{\partial \dot{m}} \cdot \frac{\dot{m}}{f} \right| = 2 + 2\beta \ln(1 + \alpha) \quad (\text{A.46})$$

Section three: compressible flow with inlet pressure and outlet pressure

As demonstrated in Chapter 3, it is also possible to experimentally obtain the value of friction factor by using another measurement strategy which measures the inlet pressure and outlet pressure. The friction factor can be accordingly expressed as

$$f = \frac{d_h}{L} \left[\frac{p_{in}^2 - p_{out}^2}{RT \left(\frac{4\dot{m}}{\pi d_h^2} \right)^2} - 2 \ln \frac{p_{in}}{p_{out}} \right] \quad (\text{A.47})$$

From Eq. (A.47) it can be noted that friction factor is a function of the following operation variables:

$$f = f(d_h, L, T, p_{in}, p_{out}, \dot{m}) \quad (\text{A.48})$$

The derivative of friction factor on hydraulic parameter can be expressed as

$$\frac{\partial f}{\partial d_h} = \frac{5\pi^2 d_h^4}{16RTL\dot{m}^2} (p_{in}^2 - p_{out}^2) - 2 \ln \frac{p_{in}}{p_{out}} \quad (\text{A.49})$$

The production of derivative and the ratio of hydraulic diameter to friction factor can be calculated by

$$\frac{\partial f}{\partial d_h} \cdot \frac{d_h}{f} = \frac{5\pi^2 d_h^5}{16fRTL\dot{m}^2} (p_{in}^2 - p_{out}^2) - \frac{2d_h}{f} \ln \frac{p_{in}}{p_{out}} \quad (\text{A.50})$$

By substituting Eq. (A.47) into Eq. (A.50), one can obtain

$$\frac{\partial f}{\partial d_h} \cdot \frac{d_h}{f} = 5 + \frac{8d_h}{fL} \ln \frac{p_{in}}{p_{out}} \quad (\text{A.51})$$

In this case, the dimensionless variable α becomes

$$\frac{p_{in} - p_{out}}{p_{out}} = \alpha \quad (\text{A.52})$$

while the expression for β does not change.

By introducing these two variables, the production can be simplified as

$$\frac{\partial f}{\partial d_h} \cdot \frac{d_h}{f} = 5 + 4\beta \ln(1 + \alpha) \quad (\text{A.53})$$

Or the coefficient on hydraulic diameter can be calculated by

$$k_1 = \left| \frac{\partial f}{\partial d_h} \cdot \frac{d_h}{f} \right| = 5 + 4\beta \ln(1 + \alpha) \quad (\text{A.54})$$

The derivative on microchannel length is deducted from Eq. (A.47) as

$$\frac{\partial f}{\partial L} = -\frac{d_h}{L^2} \left[\frac{p_{in}^2 - p_{out}^2}{RT \left(\frac{4\dot{m}}{\pi d_h^2} \right)^2} - 2 \ln \frac{p_{in}}{p_{out}} \right] \quad (\text{A.55})$$

Substituting Eq. (A.47) into Eq. (A.55), the expression can be simplified as

$$\frac{\partial f}{\partial L} = -\frac{f}{L} \quad (\text{A.56})$$

Therefore, the production is calculated by

$$\frac{\partial f}{\partial L} \cdot \frac{L}{f} = -1 \quad (\text{A.57})$$

Or the coefficient on length is simply one:

$$k_2 = \left| \frac{\partial f}{\partial L} \cdot \frac{L}{f} \right| = 1 \quad (\text{A.58})$$

The derivative of friction factor on fluid temperature is deducted as

$$\frac{\partial f}{\partial T} = -\frac{1}{T} \frac{\pi^2 d_h^5}{16RTL\dot{m}^2} (p_{in}^2 - p_{out}^2) \quad (\text{A.59})$$

By substituting Eq. (A.47) into the above equation, one can obtain

$$\frac{\partial f}{\partial T} = -\frac{1}{T} \left[f + \frac{2d_h}{L} \ln \frac{p_{in}}{p_{out}} \right] \quad (\text{A.60})$$

The production on temperature is accordingly calculated as

$$\frac{\partial f}{\partial T} \cdot \frac{T}{f} = -1 - \frac{2d_h}{fL} \ln \frac{p_{in}}{p_{out}} \quad (\text{A.61})$$

Inserting the two dimensionless variables α and β , the production can be simplified as

$$\frac{\partial f}{\partial T} \cdot \frac{T}{f} = -1 - \beta \ln(1 + \alpha) \quad (\text{A.62})$$

Therefore, the coefficient on temperature can be expressed as

$$k_3 = \left| \frac{\partial f}{\partial T} \cdot \frac{T}{f} \right| = 1 + \beta \ln(1 + \alpha) \quad (\text{A.63})$$

The derivative on the inlet pressure is deduced as

$$\frac{\partial f}{\partial p_{in}} = \frac{\pi^2 d_h^5 p_{in}}{8RTL\dot{m}^2} - \frac{2d_h}{Lp_{in}} \quad (\text{A.64})$$

The production of derivative and the ratio of inlet pressure to friction factor is calculated by

$$\frac{\partial f}{\partial p_{in}} \cdot \frac{p_{in}}{f} = \frac{\pi^2 d_h^5 p_{in}^2}{8fRTL\dot{m}^2} - \frac{2d_h}{fL} \quad (\text{A.65})$$

By using the expression of friction factor, Eq. (A.65) can be further transformed as

$$\frac{\partial f}{\partial p_{in}} \cdot \frac{p_{in}}{f} = 2 \frac{p_{in}^2}{p_{in}^2 - p_{out}^2} \left(1 + \frac{2d_h}{fL} \ln \frac{p_{in}}{p_{out}} \right) - \frac{2d_h}{fL} \quad (\text{A.66})$$

Substituting the expressions of α and β , the production can be simplified as

$$\frac{\partial f}{\partial p_{in}} \cdot \frac{p_{in}}{f} = 2 + \frac{2}{\alpha^2 + 2\alpha} - \beta + 2\beta \left(1 + \frac{1}{\alpha^2 + 2\alpha} \right) \ln(1 + \alpha) \quad (\text{A.67})$$

Or the coefficient on inlet pressure is calculated by

$$k_4 = \left| \frac{\partial f}{\partial p_{in}} \cdot \frac{p_{in}}{f} \right| = 2 + \frac{2}{\alpha^2 + 2\alpha} - \beta + 2\beta \left(1 + \frac{1}{\alpha^2 + 2\alpha} \right) \ln(1 + \alpha) \quad (\text{A.68})$$

The derivative on the outlet pressure can be obtained from Eq. (A.47) as

$$\frac{\partial f}{\partial p_{out}} = -\frac{\pi^2 d_h^5}{8RTL\dot{m}^2} p_{out} + \frac{2d_h}{Lp_{out}} \quad (\text{A.69})$$

The production is accordingly expressed by

$$\frac{\partial f}{\partial p_{out}} \cdot \frac{p_{out}}{f} = -\frac{\pi^2 d_h^5}{8fRTL\dot{m}^2} p_{out}^2 + \frac{2d_h}{fL} \quad (\text{A.70})$$

By substituting Eq. (A.47) into the one above, the production can be transformed as

$$\frac{\partial f}{\partial p_{out}} \cdot \frac{p_{out}}{f} = -\frac{2p_{out}^2}{p_{in}^2 - p_{out}^2} \left(1 + \frac{2d_h}{fL} \ln \frac{p_{in}}{p_{out}} \right) + \frac{2d_h}{fL} \quad (\text{A.71})$$

It can be further simplified by using the two dimensionless variables:

$$\frac{\partial f}{\partial p_{out}} \cdot \frac{p_{out}}{f} = -\frac{2}{\alpha^2 + 2\alpha} [1 + \beta \ln(1 + \alpha)] + \beta \quad (\text{A.72})$$

And the coefficient on outlet pressure takes the form of

$$k_5 = \left| \frac{\partial f}{\partial p_{out}} \cdot \frac{p_{out}}{f} \right| = \frac{2}{\alpha^2 + 2\alpha} [1 + \beta \ln(1 + \alpha)] - \beta \quad (\text{A.73})$$

The derivative of friction factor on mass flow rate is deducted as

$$\frac{\partial f}{\partial \dot{m}} = -\frac{\pi^2 d_h^5}{8RTL\dot{m}^3} (p_{in}^2 - p_{out}^2) \quad (\text{A.74})$$

The production on mass flow rate is therefore expressed by

$$\frac{\partial f}{\partial \dot{m}} \cdot \frac{\dot{m}}{f} = -\frac{\pi^2 d_h^5}{8fRTL\dot{m}^2} (p_{in}^2 - p_{out}^2) \quad (\text{A.75})$$

By using the calculation of friction factor in Eq. (A.47), one can obtain

$$\frac{\partial f}{\partial \dot{m}} \cdot \frac{\dot{m}}{f} = -2 - \frac{4d_h}{fL} \ln \frac{p_{in}}{p_{out}} \quad (\text{A.76})$$

Hence the production can be simplified as

$$\frac{\partial f}{\partial \dot{m}} \cdot \frac{\dot{m}}{f} = -2 - 2\beta \ln(1 + \alpha) \quad (\text{A.77})$$

The coefficient related to mass flow rate take the form of

$$k_6 = \left| \frac{\partial f}{\partial \dot{m}} \cdot \frac{\dot{m}}{f} \right| = 2 + 2\beta \ln(1 + \alpha) \quad (\text{A.78})$$

Appendix B

Propagation of uncertainties on Nusselt number

The expressions of the coefficients k_1 to k_5 is deduced in this section based on the expression of Nusselt number in Eq. (3.8), where the fluid thermophysical properties are considered independent of temperature. Starting from the coefficient on microchannel length, it takes the general form of

$$k_1 = \left| \frac{\partial Nu}{\partial L} \frac{L}{Nu} \right| \quad (\text{A.79})$$

From Eq. (3.8) the derivative of Nusselt number on length can be expressed as

$$\frac{\partial Nu}{\partial L} = - \frac{\dot{m} c_{pf}}{\pi \lambda_f} \frac{T_{out} - T_{in}}{T_w - \frac{T_{out} + T_{in}}{2}} \quad (\text{A.80})$$

Substituting Eq. (3.8) and (A.80) into Eq. (A.79), we obtain

$$k_1 = 1 \quad (\text{A.81})$$

The general form of coefficient on mass flow rate is

$$k_2 = \left| \frac{\partial Nu}{\partial \dot{m}} \frac{\dot{m}}{Nu} \right| \quad (\text{A.82})$$

From Eq. (3.8) the derivative of Nusselt number on microchannel length can be expressed as

$$\frac{\partial Nu}{\partial \dot{m}} = \frac{c_{pf}}{\pi \lambda_f L} \frac{T_{out} - T_{in}}{T_w - \frac{T_{out} + T_{in}}{2}} \quad (\text{A.83})$$

Applying Eq. (3.8) and (A.83) to Eq. (A.82), the coefficient on mass flow rate is calculated as

$$k_2 = 1 \quad (\text{A.84})$$

The coefficient on flow outlet temperature by definition is

$$k_3 = \left| \frac{\partial Nu}{\partial T_{out}} \frac{T_{out}}{Nu} \right| \quad (\text{A.85})$$

From Eq. (3.8) the derivative of Nusselt number on outlet temperature is deduced as

$$\frac{\partial Nu}{\partial T_{out}} = \frac{\dot{m}c_{pf}}{\pi\lambda_f L} \frac{\left(T_w - \frac{T_{out} + T_{in}}{2}\right) + \frac{T_{out} - T_{in}}{2}}{\left(T_w - \frac{T_{out} + T_{in}}{2}\right)^2} \quad (\text{A.86})$$

By substituting Eq. (3.8) and (A.86) into Eq. (A.85), the coefficient can be expressed as

$$k_3 = \frac{T_{out} (T_w - T_{in})}{\left(T_w - \frac{T_{out} + T_{in}}{2}\right) (T_{out} - T_{in})} \quad (\text{A.87})$$

The coefficient on flow inlet temperature takes the form of

$$k_4 = \left| \frac{\partial Nu}{\partial T_{in}} \frac{T_{in}}{Nu} \right| \quad (\text{A.88})$$

The derivative in the equation above can be deduced as

$$\frac{\partial Nu}{\partial T_{in}} = \frac{\dot{m}c_{pf}}{\pi\lambda_f L} \frac{T_{out} - T_w}{\left(T_w - \frac{T_{out} + T_{in}}{2}\right)^2} \quad (\text{A.89})$$

By using the derivative and the calculation of Nusselt number, the coefficient on inlet temperature can be expressed as

$$k_4 = \frac{T_{in} (T_w - T_{out})}{\left(T_w - \frac{T_{out} + T_{in}}{2}\right) (T_{out} - T_{in})} \quad (\text{A.90})$$

The last coefficient is on the wall temperature and can be expressed as

$$k_5 = \left| \frac{\partial Nu}{\partial T_w} \frac{T_w}{Nu} \right| \quad (\text{A.91})$$

The derivative in Eq. (A.91) can be deduced from Eq. (3.8) as

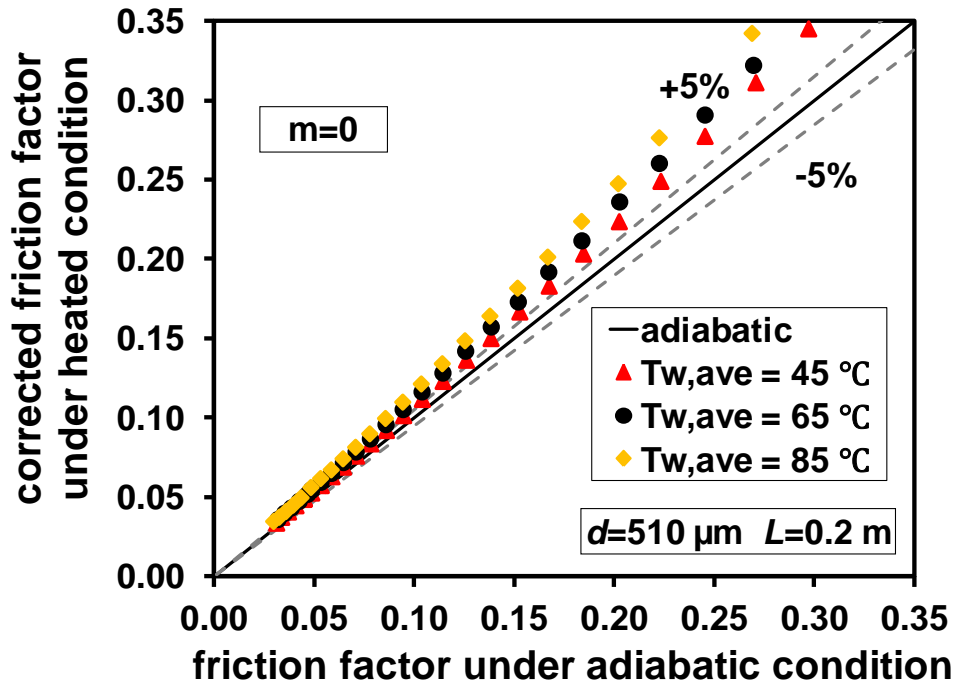
$$\frac{\partial Nu}{\partial T_w} = \frac{\dot{m}c_{pf}}{\pi\lambda_f L} \frac{-(T_{out} - T_{in})}{\left(T_w - \frac{T_{out} + T_{in}}{2}\right)^2} \quad (\text{A.92})$$

Inserting Eq. (3.8) and (A.92) into Eq. (A.91), the coefficient on microchannel wall temperature can be calculated by

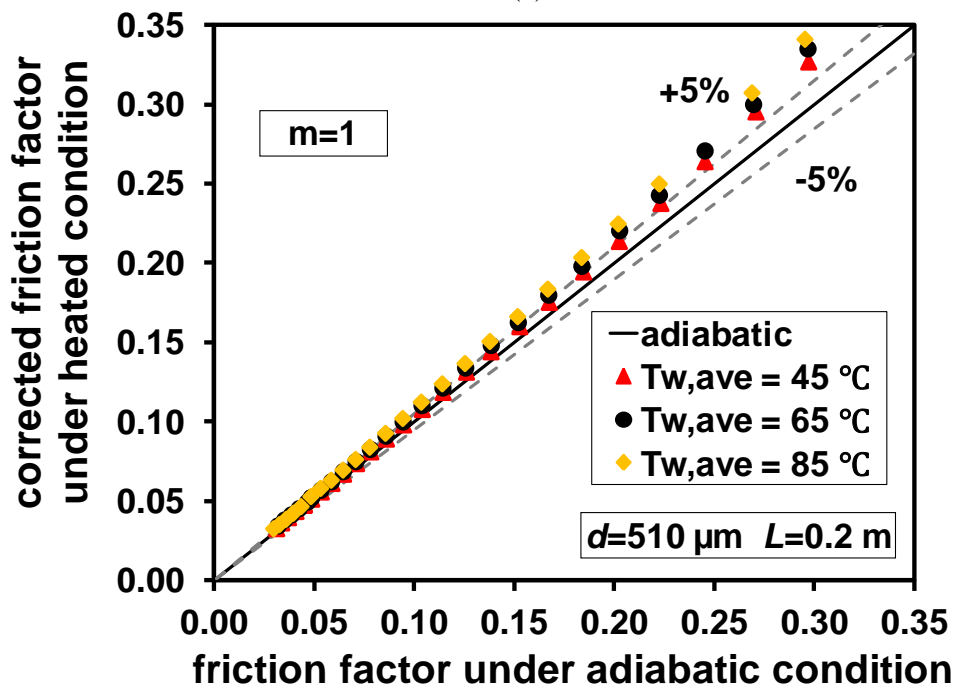
$$k_5 = \frac{T_w}{T_w - \frac{T_{out} + T_{in}}{2}} \quad (\text{A.93})$$

Appendix C

Figures of correction for friction factor under heated conditions



(a)



(b)

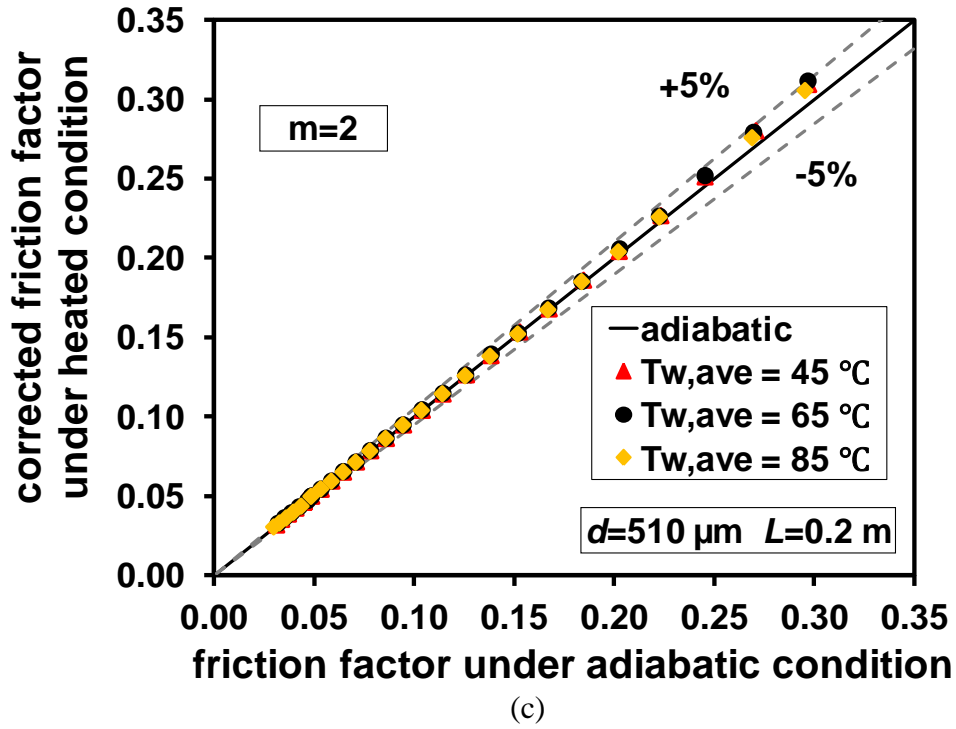
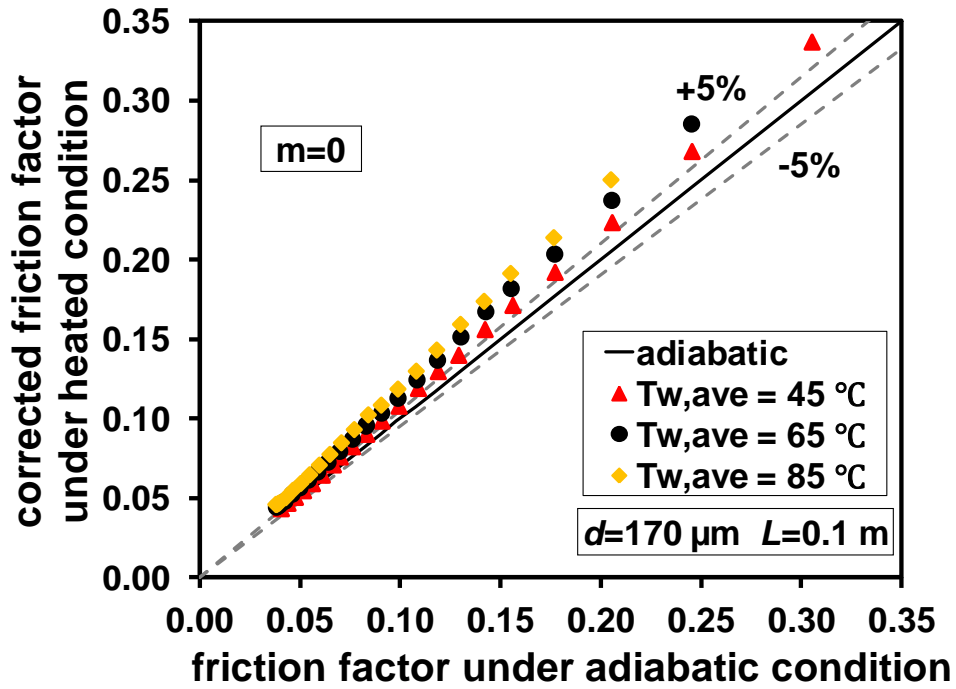
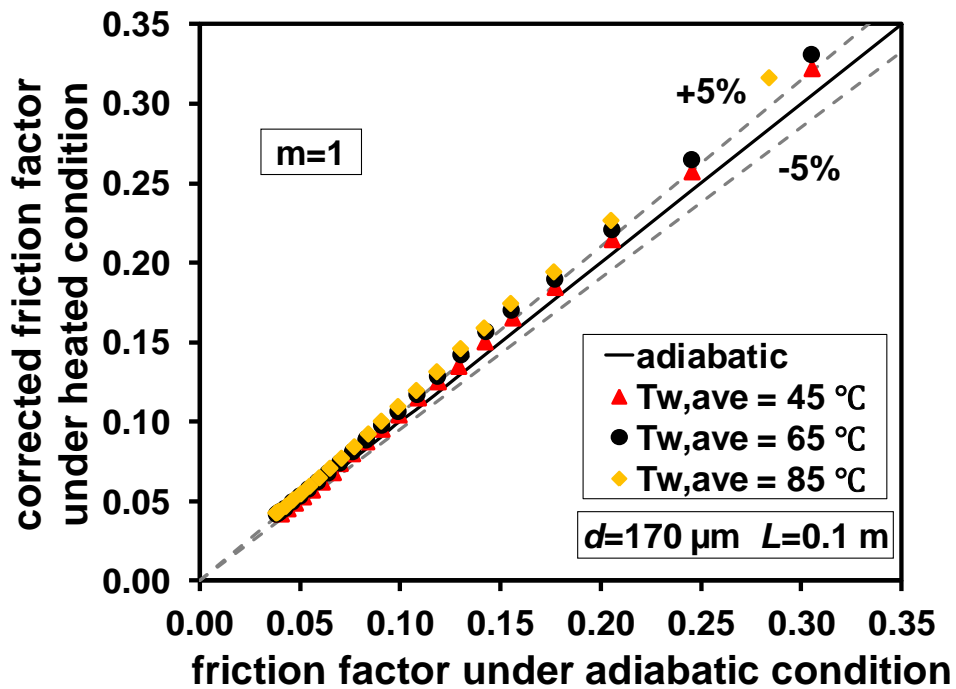


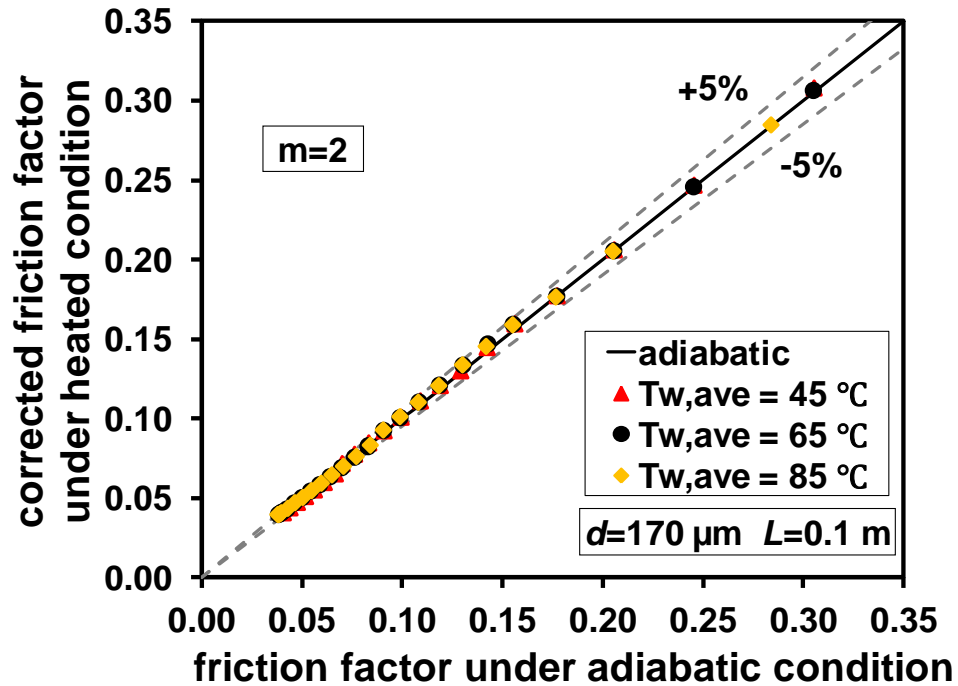
Figure A-1: Correction of the friction factors of heated flow through microtube #2: (a) $m=0$, no correction; (b) $m=1$, correction for macro flow; (c) $m=2$, suitable correction with minor deviation.



(a)



(b)



(c)

Figure A-2: Correction of the friction factors of heated flow through microtube #3: (a) $m=0$, no correction; (b) $m=1$, correction for macro flow; (c) $m=2$, suitable correction with minor deviation.

Curriculum Vitae

Yahui Yang

Dipartimento di Ingegneria Industriale (DIN)

Alma Mater Studiorum Università di Bologna, Viale Risorgimento 2, 40136 Bologna, Italy

Tel: +39 051 2090467 Fax: +39 051 2093296

E-mail: yahui.yang2@unibo.it

Research

08/2011 – 10/2012, IMVT, Karlsruhe Institute of Technology (KIT), Germany

- Marie Curie research fellow, GASMEMS network under 7th Framework Programme (FP7) of the European Commission (Marie Curie Actions)
- Main research topic: Design, experimental and numerical investigation on gaseous flow and heat transfer through micro heat exchangers

11/2009 – 07/2011, Lab of Microfluidics, DIENCA, Università di Bologna, Italy

- Marie Curie research fellow, GASMEMS network under 7th Framework Programme (FP7) of the European Commission (Marie Curie Actions)
- Main research topic: Experimentally and numerically study on the characteristics of gaseous flow and heat transfer through commercial microtubes

Education

11/2009 – present, Alma Mater Studiorum Università di Bologna

- Ph.D. study in mechanical engineering
- Research topic: Gas flow and heat transfer at microscale
- Supervisors: Prof. -Ing. Gian Luca Morini and Dr. -Ing. habil. Jürgen J. Brandner

09/2007 – 09/2009, Xi'an Jiaotong University

- Master study in mechanical engineering
- Title: Experimental and Numerical Study on Hydrodynamic Instabilities Driven by a Neutralization Reaction in Immiscible Liquid-liquid System
- Supervisors: Prof. Jiangtao Wu and Dr. Ying Shi

09/2003 – 07/2007, Xi'an Jiaotong University

- Bachelor study at School of Energy and Power Engineering
- Majored in Thermodynamics and Power Engineering

Publications

Journals

- [1] Morini, G. L. and Yang, Y., Guidelines for the determination of single-phase forced convection coefficients in microchannels, *ASME Journal of Heat Transfer*, accepted for publication.
- [2] Yang, Y., Morini, G. L., Chalabi, H., and Lorenzini, M., The effect on the Nusselt number of the non-linear axial temperature distribution of gas flows through commercial microtubes, *Heat Transfer Engineering*, in press.
- [3] Morini, G. L., Yang, Y., and Lorenzini, M., Experimental analysis of gas micro-convection through commercial microtubes, *Experimental Heat Transfer*, vol. 25, n° 3, pp. 151-171, 2012.
- [4] Morini, G. L., Yang, Y., Chalabi, H., and Lorenzini, M., A critical review of the measurement techniques for the analysis of gas microflows through microchannels, *Experimental Thermal and Fluid Science*, vol. 35, n° 6, pp. 849-865, 2011.

Conferences

- [5] Yang, Y., Gerken, I., Brandner, J. J., and Morini, G. L., Design and experimental investigation of a gas-to-gas counter flow micro heat exchanger, in *Proceedings of the 3rd European Conference on Microfluidics (Microfluidics2012)*, μ FLU12-57, Heidelberg, Germany, 2012.
- [6] Yang, Y., Hong, C., Morini, G. L., Asako, Y., Lorenzini, M., and Brandner, J. J., Transitional and turbulent convective heat transfer of compressible gas flow through microtubes, in *Proceedings of the ASME 2012 10th International Conference on Nanochannels, Microchannels and Minichannels (ICNMM2012)*, Puerto Rico, USA. ASME (Publisher), pp. ICNMM2012-73261, 2012.
- [7] Brandner, J. J., Vittoriosi, A., Yang, Y., and Morini, G. L., Microstructure devices for heat transfer studies in gas flows, presented at 28th International Symposium on Rarefied Gas Dynamics (RGD28), Zaragoza, Spain, July 9-13, 2012.
- [8] Yang, Y., Brandner, J. J., and Morini, G. L., Hydraulic and thermal design of a gas microchannel heat exchanger, in *Journal of Physics: Conference Series - Proceedings of 1st European Conference on Gas Microflows (GASMEMS2012)*, vol. 362, pp. 012023, 2012.
- [9] Yang, Y., Schakenbos, T., Chalabi, H., Lorenzini, M., and Morini, G. L., Compressible gas flow through heated commercial microtubes, in *Proceedings of 4th International Conference on Heat Transfer and Fluid Flow in Microscale (HTFFM-IV)*, Fukuoka, Japan, pp. HTFFM-IV-023:1-9, 2011.
- [10] Yang, Y., Morini, G. L., Chalabi, H., and Lorenzini, M., Non-linear temperature distribution of gas convection through commercial microtubes, in *Proceedings on CDROM of 3rd Micro and Nanoflow Conference (MNF2011)*, Thessaloniki, Greece, ISBN 978-1-902316-98-7, pp. MNF2011-17:1-8, 2011.

- [11] Yang, Y., Morini, G. L., Chalabi, H., and Lorenzini, M., Gas Flow Forced Convection through Commercial Microtubes, in Proc. of XXIX UIT National Conference, Turin, Italy, June 20-22, 2011.
- [12] Morini, G. L., Yang, Y., Chalabi, H., and Lorenzini, M., Experimental Analysis of Gas Flow Forced Convection in Microtubes, in Proceedings on CDROM of ASME 2011 9th International Conference on Nanochannels, Microchannels, and Minichannels (ICNMM2011), Edmonton, Canada, ASME (Publisher), pp. ICNMM2011-58190, 2011.
- [13] Yang, Y., Morini, G. L., Chalabi, H., and Lorenzini, M., Non-linear temperature distribution of gas convection through commercial microtubes, in Proceedings on CDROM of 3rd International GASMEMS Workshop (GASMEMS11), Bertinoro, Italy, pp. GASMEMS11-21:1-21, 2011.
- [14] Yang, Y., Morini, G. L., and Lorenzini, M., Experimental analysis of gas micro-convection through commercial microtubes, in Proceedings on CDROM of 2nd European Conference on Microfluidics (μ Flu'10), Toulouse, France, S. Colin and G. L. Morini (Eds.). SHF (Publisher), ISBN 978-2-906831-85-8, pp. μ FLU2010-50:1-18, 2010.
- [15] Yang, Y., Lorenzini, M., and Morini, G. L., A critical review of the measurement techniques for the analysis of gas microflows through microchannels, in Proceedings on CDROM of 2nd International GASMEMS Workshop (GASMEMS10), Les Embiez, France, pp. GASMEMS2010-HT04:1-20, 2010.